Protonation and Conformational Dynamics of Phytochrome Variants and Fluorescent Phytochromes

Dissertation

zur Erlangung des Grades eines

Doktors der Naturwissenschaften (Dr. rer. nat.)

am Fachbereich Physik

der Freien Universität Berlin

vorgelegt von

Maryam Sadeghi

Berlin 2022

Erstgutachterin: Frau Prof. Dr. Ulrike Alexiev

Zweitgutachter: Herr Prof. Dr. Joachim Heberle

Datum der Verteidigung: 16.11.2022

“Was uns nicht umbringt, macht uns stärker.”

Friedrich Nietzsche

“Climb Mount Fuji, O snail, but slowly, slowly.”

Kobayashi Issa

Kurzfassung

In dieser Arbeit wurden die biophysikalischen Eigenschaften von vier Phytochromen untersucht, um die Fluoreszenzverstärkung in Phytochrom-basierten Nahinfrarot-Fluoreszenzproteinen zu verstehen und den Beitrag der Protonierungsheterogenität zur Funktion der Phytochrome zu ermitteln. Phytochrome sind Rot/Fernrot-Photosensorproteine, die vor allem in Pflanzen aber auch in Bakterien, Pilzen und anderen Organismen vorkommen. Die in dieser Arbeit untersuchten Phytochrome sind Cph1 und Cph2, die aus Cyanobakterien stammen, als auch Agp1 und Agp2, die aus dem *Agrobacterium tumefaciens* stammen. Der Photosensor ist ein lineares Tetrapyrrol, welches in dem Photosensormodul (für Cph1, Agp1 und Agp2 als PGP für die PAS, GAF, und PHY-Domäne abgekürzt) gebunden ist.

Im ersten Teil (Kapitel 4 und 5) haben wir eine pH-Titration des linearen Tetrapyrrol-Chromophors im Pr (rot absorbierender) -Zustand verschiedener Cph1 PGP- und Agp1 PGP-Konstrukte durchgeführt. Darüber hinaus wurde die Rolle des Chromophortyps wie Biliverdin (BV) und Phycocyanobilin (PCB) bei der Phytochrom-Protonierungsheterogenität im Pr-Zustand unter Verwendung von kovalent und nicht-kovalent gebundenem PCB an Agp1 PGP V249C bzw. Wildtyp (WT) untersucht. Die strukturellen Veränderungen an verschiedenen Positionen in Cph1 PGP und Agp1 PGP wurden als Funktion des pH-Wertes mittels zeitaufgelöster Pikosekunden-Fluoreszenzanisotropie gemessen. Wir konnten zeigen, dass es nur bei Cph1 PGP eine direkte Korrelation zwischen der Deprotonierung des Chromophors und pH-abhängigen Konformationsänderungen gibt, nicht aber bei Agp1 PGP.

Im zweiten Teil (Kapitel 5 und 6) charakterisieren wir die Fluoreszenzeigenschaften mehrerer Varianten aus zwei verschiedenen Phytochrom-Familien: Phycocyanobilin-bindende Phytochrome (Cph1 und Cph2)) und Biliverdin-bindende Bakteriophytochrome (Agp1 und Agp2, sowie die Variante PAiRFP2),, unter Verwendung von stationärer und zeitaufgelöster Fluoreszenzspektroskopie. Die PCB-Addukte der PGP-Varianten von Agp1 wurden charakterisiert, um die Auswirkungen des Chromophortyps und der konservierten Aminosäuren in der Chromophor-Bindungstasche auf die Fluoreszenzquantenausbeute und die Fluoreszenzlebensdauer zu untersuchen. Unsere Ergebnisse zu Cph1 zeigten, dass die Kombination von Mutationen, von denen bekannt ist, dass sie die Fluoreszenz im cyanobakteriellen Phytochrom Cph1 verstärken, eine Fluoreszenzquantenausbeute von etwa 17 % ergibt. Außerdem bestätigten unsere Ergebnisse, dass die Fluoreszenzquantenausbeute von Phycocyanobilin-bindenden Phytochromen (Cph1&2) deutlich höher ist als die von Biliverdin-bindenden Bakteriophytochromen (Agp2 und PAiRFP2), wie in früheren Studien gezeigt wurde.

Abstract

In this thesis the biophysical properties of four phytochromes were investigated to understand the enhancement mechanism of fluorescence in phytochrome-based near-infrared fluorescent proteins and to understand the contribution of the protonation heterogeneity to the function of phytochrome. Phytochromes are red/far-red photosensor proteins found in many organisms, such as plants, bacteria or fungi. The investigated phytochromes are Cph1 and Cph2 from cyanobacteria, as well as Agp1 and Agp2 from the *Agrobacterium tumefaciens*. The photosensor itself is a linear tetrapyrrole, which is bound to the photosensor module of phytochrome comprising the PAS, GAF and PHY domain (in short PGP) for Cph1, Agp1 and Agp2.

In the first part (Chapter 4 and 5), we performed pH-titration of the linear tetrapyrrole chromophore in the Pr (red absorbing) state of different Cph1 PGP and Agp1 PGP constructs. Moreover, the role of the chromophore type such as biliverdin (BV) and phycocyanobilin (PCB) in phytochrome protonation heterogeneity in the Pr state was investigated using covalent and non-covalent PCB-binding to Agp1 PGP V249C and wild type (WT), respectively. The structural changes at various positions in Cph1 PGP and Agp1 PGP were measured as a function of pH using picosecond time-resolved fluorescence anisotropy. We showed that only in Cph1 PGP, a direct correlation of chromophore deprotonation with pH-dependent conformational changes was found, but not in Agp1 PGP.

In the second part (Chapter 6 and 7), we characterized the fluorescent properties of several variants from two different phytochrome families: phycocyanobilin-binding phytochromes (Cph1 and Cph2) and biliverdin-binding bacteriophytochromes (Agp1, und Agp2, as well as the variants of PAiRFP2), using steady-state and time-resolved fluorescence spectroscopy. The PCB adducts of Agp1 PGP variants were characterized to test the effect of chromophore type and conserved amino acids in the chromophore binding pocket on fluorescence quantum yield and fluorescence lifetime. Our results on Cph1 indicated that the combination of mutations known to enhance fluorescence in the cyanobacterial phytochrome Cph1 yield a quantum yield of about 17%. Also, our results confirmed a remarkable higher fluorescence quantum yield of phycocyanobilin-binding phytochromes (Cph1 and Cph2) compared to biliverdin-binding bacteriophytochromes (Agp2 and PAiRFP2), as it was shown in the previous studies.

Nomenclature

Agp1: Prototypical Phytochrome from *Agrobacterium tumefaciens*

Agp2: Bathy Phytochrome from *Agrobacterium tumefaciens*

ADC: **A**nalog-**D**igital- **C**onverter

BSA: **B**ovine **S**erum **A**lbumin

BV: **B**ili**v**erdin IX α

CBP: **C**hromophore **B**inding **P**ocket

CFD: **C**onstant **F**raction **D**iscriminator

Cph1: Phytochrome from Cyanobacteria *Synechocystis PCC 6803*

Cph2 *SyB*: *Synechococcus* Phytochrome *B*

Cph1PGP (PAS-GAF-PHY): Senseur module of Cph1

C-Terminus: Carboxy-Terminus

CW: **C**ontinuos **W**ave

DCM: 4-(**Dic**yanomethylene)-2-**m**ethyl-6-(4-dimethylaminostyryl)-4H-pyran

DTT: **D**i**t**hio**t**hreitol

EDTA: **E**thylene**d**iamine**t**etra**a**cetic acid

FNa: **F**luorescein Sodium (**N**atrium) **S**alt

FPs: **F**luorescent **P**roteins

FWHM: **F**ull **W**idth at **H**alf **M**aximum

GAF: c**G**MP-specific phosphodiesterase/**A**denylyl cyclase/**F**hlA-related domain

IA: **I**odo**a**cetamido

IAF: (5-) **I**odo**a**cetamido**f**luorescein

HK: **H**istidin**k**inase

HKRD: **H**istidine**k**inase **R**elated **D**omain

IRF: **I**nstrument **R**esponse **F**unction

LabVIEW: **L**aboratory **V**irtual **I**nstrumentation **E**ngineering **W**orkbench (program software)

MCP: **M**icro**c**hannel **P**late Photomultiplier

MW: **M**olecular **W**eight

NIF: **N**ear **Inf**rared

N-Terminus: Amino-Terminus

OD: **O**ptical **D**ensity

PAS: PERIOD/**A**RNT/**S**IMPLEMINDED-related domain

PCB: Phyco**c**yano**b**ilin

PΦB: Phytochromobilin

Pfr: **P**hytochrome **f**ar **r**ed

PHY: **Phy**tochrome-specific domain

Pr: **P**hytochrome **r**ed

RT: **R**oom **T**emperature

SDS: **S**odium **D**odecyl **S**ulfate

SDS-PAGE: **S**odium **D**odecyl **S**ulfate **P**olyacrylamide **G**el **E**lectrophoresis

SD: **S**tandard **D**eviation

TAC: **T**ime to **A**mplitude **C**onverter

TCEP: **T**ris(2-**c**arboxy**e**thyl) **phosphin**

TCSPC: **T**ime **C**orrelated **S**ingle **P**hoton **C**ounting

TiSa: **T**itan:**S**apphire Laser

Tris: Tris(hydroxymethyl)-aminomethan

UV: **U**ltra**v**iolet

VIS: **Vis**ible light

WL: **W**hite **L**ight

WT: **W**ild **T**ype

Contents

1 Introduction

1.1 Motivation

Life on Earth has developed over a billion years from the tiniest microbes. So far, the evolutionary theory, including natural selection, common descent, and speciation, can precisely explain the diversity of all organisms from their origins (Ayala and Coluzzi 2005). It has been found, during the evolutionary process, light has played an essential role, as all living species react to light, either as an energy or information source (Ruban 2014). The answers to the questions 'how can biological organisms absorb light' and 'how can light affect their function and development' are strongly related to our knowledge about photoreceptor proteins. Research on this group of proteins could provide a deeper understanding of the role of light in living creatures' mechanism. In general, proteins are made of long chains of amino acid residues. They perform a variety of functions within organisms, such as catalyzing metabolic reactions, DNA replication, responding to stimuli, providing structure to the cells and the organisms, transporting molecules from one location to another, or converting energy to be useable in the cells. The biological photoreceptors control

the physiological processes on the cellular level. They are composed of a protein matrix with a reaction center which is either a metal complex or an organic cofactor (Kennis and Mathes 2013).

This dissertation is focused on phytochromes, which are photoreceptor proteins and the photoreceptor proteins and belong to the class of bilin or open chain tetrapyrrole containing proteins. Phytochrome controls many developmental processes in the plants such as seed germination, de-etiolation, or flowering (Macháčková 1994). The discovery of the bacterial phytochrome (Hughes and Lamparter 1999) indicated the prokaryotic origin in this group of proteins which include two groups: prototypical and bathy phytochromes. Prototypical phytochromes, including Cph1 from the cyanobacterium *Synechocystis 6803* (Hughes and Lamparter 1999) and Agp1 from soil bacterium *Agrobacterium*act *tumefaciens* (Lamparter, Michael et al. 2002) act as photochemical switches that interconvert between stable red (Pr)- and metastable far-red (Pfr)-absorbing states induced by photoisomerization of the bilin chromophore after light activation. However, bathy phytochromes, including Agp2 from soil bacterium *Agrobacterium*act *tumefaciens,* interconvert between stable Pfr state and a metastable Pr state (Krieger, Molina et al. 2008). So far, details on the protein structure and the chromophore geometry have been extensively studied using X-ray crystallography for dark-adapted or thermally stable states of photosensor module (contains PAS-GAF-PHY domains) of Cph1 and Agp1 (Pr-state) (Essen, Mailliet et al. 2008, Nagano, Scheerer et al. 2016) and Agp2 (Pfr state) (Schmidt, Sauthof et al. 2018). Moreover, photoinduced reaction mechanisms, including proton translocations, have been discovered by spectroscopic techniques, such as (transient) absorption (van Thor, Borucki et al. 2001) , NMR (Song, Essen et al. 2012) , and vibrational spectroscopy (Escobar, Lang et al. 2017). These methods have significantly expanded the knowledge about the underlying molecular events and their dynamics.

The present thesis also contributes to a deeper understanding of the mechanism of the photoinduced processes of phytochromes, using time-resolved fluorescence spectroscopy methods (Sadeghi, Balke et al. 2020). Fluorescence spectroscopy and its applications have significantly evolved in the physical and life sciences during the past decades. This method has increasingly been used due to advances in time resolution, methods of data analysis, and improved instrumentation. Moreover, advances in laser and detector technology have increased the interest in fluorescence for clinical and analytical chemistry. With these advances, time-resolved measurements with enough resolution are favorable to study dynamic features of proteins.

Within this thesis the following results will be presented:

- Understanding the protonation heterogeneity and its correlation to the photoconversion in the photosensor module of phytochromes.
- Investigation of the protein dynamics proximal and distal to the linear tetrapyrrole in dependence on the chromophore deprotonation.
- Characterization of improved fluorescent phytochromes for *in situ* imaging

- Origin of fluorescence in fluorescent phytochromes, in particular, understanding the main factors that play a role in phycocyanobilin (PCB) binding and biliverdin (BV) binding fluorescent phytochromes.

1.2 Aims and approaches:

Aim 1. Understanding the protonation heterogeneity of the chromophore binding pocket in the Pr state and its relation to the photoconversion mechanism using two different phytochrome species Agp1 and Cph1.

Protonation heterogeneity first was observed in the Pr state of plant phytochrome (Sineshchekov 1995) (Schmidt, Gertsch et al. 1998), and later in Cph1 (Sineshchekov, Koppel' et al. 2002). In the thermodynamically stable Pr state of the photosensory module (PAS-GAF-PHY, PGP) of Cph1, two Pr ground states were found which are reflected by two chromophore p*K*-values of ~7.5 and ~9 (van Thor, Borucki et al. 2001, Escobar, Lang et al. 2017). It was revealed using resonance Raman/ultraviolet−visible spectroscopy and quantum mechanics/molecular mechanics (QM/MM) calculations, that the pH dependent equilibrium between Pr-I and Pr-II is dependent on the protonation state of histidine 260 (Escobar, Lang et al. 2017). Cph1 and Agp1 are both canonical phytochromes with about ~40% sequence homology but utilize different chromophores. Cph1 binds PCB in the GAF, Agp1 binds BV in the PAS domain. In contrast to the protonation mechanism in Cph1 and plant phytochrome, a pH dependent UV-vis absorption and RR spectroscopy study indicated the protonation homogeneity of Agp1 with only one p*K*-value (p*K* ~11), which was observed for chromophore deprotonation (von Stetten, Seibeck et al. 2007).

The following questions will be studied:

- Is protonation heterogeneity dependent on 1) the chromophore type, and 2) the ability of the phytochrome to photoconvert to the Pfr state?
- Is protonation heterogeneity still observed in the minimal photosensory module PAS-GAF (PG) of Cph1? Or in the other words, what are the effects of the PHY domain on protonation heterogeneity in the chromophore binding pocket?

These questions will be investigated by means of UV-vis absorption spectroscopy in steady-state and time-resolved measurement, to characterize the photoconversion from Pr to the Pfr state. The protonation heterogeneity will be determined by measuring the proton concentration in the aqueous bulk phase.

To observe the dependency of chromophore type and to test whether the homologous Pr ground state in Agp1 can be converted into a heterologous Pr state like in Cph1, a PCB binding site will be engineered into the GAF domain of Agp1 and the constructs, will be investigated. In addition, the mutations Y176H and Y263S known to inhibit photoconversion in Cph1 will be investigated in terms of protonation heterogeneity in the chromophore binding pocket.

Aim 2: Protonation-conformation coupling investigations in Cph1 and Agp1 phytochromes to identify possible correlations between chromophore deprotonation in the Pr state and protein dynamics in the different photosensory domains.

It has been shown for Cph1, which is more close to the plant phytochromes (Lagarias and Rapoport 1980), and for Agp1 that photoconversion of Pr to Pfr is associated with a release/recapture of protons from the solution phase (van Thor, Borucki et al. 2001, Borucki, von Stetten et al. 2005)(**Fig. 1-1**). Moreover, upon the photoconversion from Pr to Pfr, the tongue like hairpin protruding from the PHY domain to contact the chromophore bearing GAF domain, undergoes a sheet-to-helix transformation (**Fig. 1-1B**). This event has been observed in crystal structure of a bacteriophytochrome from *Deinococcus radiodurans* (Takala, Björling et al. 2014) and Agp2 PAiRFP2, which is locked in Meta-F state (Schmidt, Sauthof et al. 2018). Still, it is not fully understood how this remarkable event is initiated and how it can be reversed back to Pr state.

It was shown for Agp1 and Cph1 variants, the mutation of amino acids in the chromophore binding pocket (von Stetten, Seibeck et al. 2007) or in the PHY domain (Sadeghi, Balke et al. 2020) reduced the chromophore p*K* in their dark-adapted state (Pr state). The mutations of highly conserved amino acids in the chromophore binding pocket of Agp1, D197A and H250A decreased the chromophore p*K* from ~11 to ~7 and to ~9, respectively (von Stetten, Seibeck et al. 2007) . Also, it was shown for the photosensor module of Cph1, the mutation C371S and the biomolecular modification (fluorescein

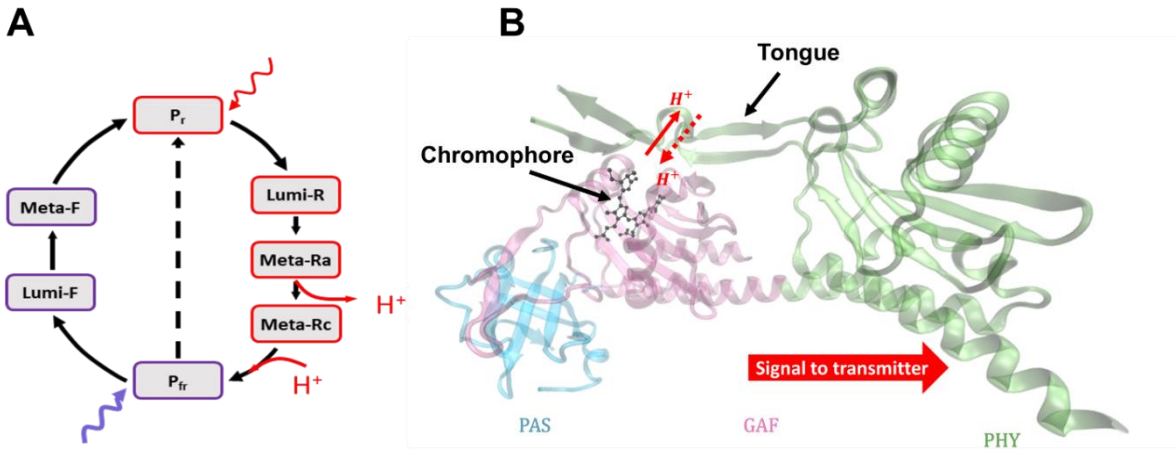

Figure 1-1: (A) Photoreaction cycle of Cph1. **(B)** Structural model of Cph1-PGP (PDB: 2VEA) the functional mechanism is indicated by the red arrows for protonation changes and the direction of signal transmission. Lumi-R, Meta-Ra and Meta-Rc are intermediate state.

labeling) at the PHY domain reduced the chromophore p*K* by half of a pH unit (Sadeghi, Balke et al. 2020).

The following questions will be investigated:

- Does the modification in the PHY domain of Agp1 affect the chromophore deprotonation, similar to what was observed in Cph1?
- How can the transient deprotonation of the chromophore in Cph1 affect the conformational dynamics of the protein at a far distance from the chromophore?
- Is the long-distance protonation-conformation coupling related to the protonation heterogeneity?

These questions will be investigated using UV-vis absorption spectroscopy and time-resolved fluorescence anisotropy spectroscopy. In order to investigate the corresponding protein structural changes, site-specific fluorescence labeling and time-resolved fluorescence anisotropy will be employed. pH-dependent time-resolved fluorescence anisotropy experiments will be performed in the Pr state of the labeled protein to probe the local protein dynamics and the structural changes within the picosecond time range.

In Cph1 PGP, wild type, and its mutants C371S and PG, and in Agp1 PGP, wild type and its mutants C279S, C295S, C279S/C295S/V364C were used for labeling with fluorescein as the reporter group. In addition, the variant V364C which is in the PHY domain equivalent to the residue C371 in Cph1, will be investigated.

Aim 3: Characterization of near-infrared fluorescent proteins (NIR-FPs) of biliverdin-binding bacterial phytochromes, Agp2/PAiRFP2 variants, and phycocyanobilin-binding cyanobacterial phytochromes, Cph1 and Cph2 variants, for in situ imaging.

Recently, several bacterial phytochrome proteins (BphPs) were employed for designing the optical molecular (optogenetic) tools for applications in mammals (Filonov, Piatkevich et al. 2011, Piatkevich, Subach et al. 2013) as well as in human cells (Kamper, Ta et al. 2018). In addition, several red fluorescent proteins **(**FPs) were developed based on plants and cyanobacterial phytochromes (Murphy and Lagarias 1997, Fischer and Lagarias 2004, Fischer, Rockwell et al. 2005, Wu, Chang et al. 2013). The directed evolution of FPs by random mutagenesis has been a popular approach in phytochromes to design a highly fluorescent mutant. However, the fluorescence quantum yield is different in PCB and BV chromophore binding proteins. For example, a previous study showed that the mutation Y176H in Cph1 inhibited the photoconversion to Pfr and enhanced the fluorescence quantum yield to about 14% (Fischer and Lagarias 2004). In contrast, 24 rounds of mutagenesis in bathy phytochrome Agp2 lead to the variant PAiRFP2 with a quantum yield of about 5% (Piatkevich, Subach et al. 2013). Time-resolved fluorescence characterization of these two groups of phytochromes will help to understand the different mechanism that enable fluorescence in BV and PCB binding fluorescent phytochromes.

The following questions will be investigated:

- Which mutations can improve fluorescent phytochromes in biliverdin-binding bacterial phytochromes and phycocyanobilin-binding cyanobacterial phytochromes?
- What can we learn from the correlation of the fluorescence quantum yield and lifetime in the different mutants?
- Are the fluorescence lifetime of different Cph1 variants the same *in vitro* and in *E.coli*?

These questions will be studied employing steady-state UV-vis absorption, steady-state fluorescence spectroscopy, time-resolved fluorescence spectroscopy, and fluorescence lifetime imaging microscopy (FLIM) to characterize the NIR-FPs. Also, for investigating the new NIR-FP variants as fluorescent tags for *in vivo* imaging, FLIM will be used to image *E.coli* cells expressing the relevant genes. Moreover, FLIM will be utilized for studying the NIR-FP Agp2 PAiRFP2 in crystals.

Aim 4: Elucidating the origin of fluorescence in fluorescent phytochromes.

Bilin chromophores such as biliverdin (BV) and phycocyanobilin (PCB) are highly sensitive to the environment (Falk 1989). In an aqueous solution, because of the unrestricted mobility of chromophore tetrapyrrole, the absorbed light is mainly dissipated through the radiation less processes. However, the deexcitation pathway becomes significantly modified when the bilin is incorporated into the protein such as phytochrome (Smith 2000, Montgomery and Lagarias 2002). In nature, phytochromes have evolved to increase the light absorption for photoconversion and signaling, and consequently, the fluorescence quantum yield of that process is minimized (Ihalainen, Takala et al. 2015). Therefore, higher fluorescence quantum yield in phytochrome may be achieved by disrupting the photoconversion by mutating the apoprotein (Fischer, Rockwell et al. 2005, Su and Lagarias 2007) or by altering the linear tetrapyrrole precursor chemical synthesis (Murphy and Lagarias 1997, Zienicke, Chen et al. 2011). Also, rigidifying the chromophore by binding to two cysteines can increase the fluorescence quantum yield in BphP (Buhrke, Tavraz et al. 2019). Also, locked chromophores in the phytochrome Agp1 enhanced the fluorescence quantum yield (Zienicke, Chen et al. 2011). The inhibition of photoconversion by low temperature or chromophore replacement correlates with an increase of Pr fluorescence, indicating that photoisomerization provides a significant route of energy dissipation (Zienicke, Chen et al. 2011).

Among the studied phytochromes which were designed as near infrared fluorescent proteins, the PCB-biding species revealed a higher fluorescence quantum yield compared to the BV-binding ones. For example, the substitution Y176H in Cph1 enhanced the fluorescence quantum yield by about 14% (Fischer and Lagarias 2004), while the equivalent variant Y165F in Agp2, increased the fluorescence by about 1% (Zienicke, Chen et al. 2011).To unravel the mechanism beyond the significant difference

in fluorescence quantum yield of these two groups of phytochromes (PCB and BV-binding) the following questions will be studied:

- How the type of chromophore such as BV or PCB, and the chromophore binding pocket, such as the hydrogen bond network and water molecule distribution can affect on the fluorescence quantum yield and the fluorescence lifetime of fluorescent phytochromes?
- Does tyrosine (Tyr) act as a fluorescence quencher of the linear tetrapyrrole in phytochrome?

These questions will be studied by means of site-directed mutagenesis, steady-state fluorescence spectroscopy, and time-resolved fluorescence spectroscopy to prepare and characterize respectively, the variants in the steady-state and time-resolved regime.

Agp1 PGP and its mutants Y166H, V249C, Y166H/V249C can bind to the PCB ligand. The mutant V249C provides the covalent binding site for PCB in the GAF domain. The steady-state and time-resolved fluorescence measurements of these variants will be compared to the results from Cph1 PGP WT and its variants Y176H (which is equivalent to Y166H in Agp1) to illustrate the role of chromophore type in fluorescence properties of the fluorescent phytochromes. Also, the variant F193Y was studied to elucidate the role of conserved tyrosine in fluorescence quantum yield in phytochromes. In order to study the quenching effect of tyrosine on the fluorescence emission of BV and PCB, the steady-state fluorescence, and the fluorescence lifetime of bovine serum albumin (BSA)+PCB and BSA+BV as a model binding protein for linear tetrapyrroles will be measured in different concentrations of Tyr in solution.

2 Fundamentals

2.1 Absorption of light

In modern theory, light (photons) is described in two ways: it can be regarded as an electromagnetic wave or as a particle. In the case of the particle description, the laws of quantum optics describe the behavior of photons as particles, particularly the interaction between photons and molecules. In the case of the electromagnetic wave description, the electromagnetic theory comprising Maxwell's equations describes photons' interaction as the electromagnetic wave with a medium.

The energy of a photon can be defined by

$$E = \hbar\nu \qquad 2\text{-}1$$

where ν is the frequency of the electromagnetic radiation of light and $\hbar$ is Plank's constant (6.626×10^{-34} J s). The velocity of light in vacuum c and the wavelength of the photon λ are related by

$$\nu = \frac{c}{\lambda} \qquad 2\text{-}2$$

In the medium, the absorption of a photon causes a transition from an energetic ground state to a particular excited state. Depending on the energy of light and on the chemical nature of the interacting compound, the excited states may differ very much in nature. While in general, an electron absorbs the photon with energy $\hbar\nu$ (**Eq. 2-1**) and jumps from an energetically more favorable state (E_1) to a state with higher energy (E_2) which is so-called electronic excitation. The energy difference will be defined by the Bohr-Einstein frequency relationship:

$$\Delta E = E_2 - E_1 = \hbar\nu \qquad 2\text{-}3$$

When the light is propagating in a medium as an electromagnetic wave, its propagation is written as

$$\mathrm{A}(\varphi) = \mathrm{A}_0(\varphi)\, \mathrm{e}^{\mathrm{i}(\omega t - \delta)} \qquad 2\text{-}4$$

where A is the amplitude, ω the circular frequency, t the time, δ is the phase angle and φ the polarization angle. The circular frequency is expressed by the wavelength λ and the refractive index n:

$$\omega = \frac{c}{\lambda n} \qquad 2\text{-}5$$

in case the medium absorbing the light, **Eq. 2-5** should be modified by replacing the reflective index n by its complex form n*:

$$\mathrm{n}^* = n + ik \qquad 2\text{-}6$$

where n and *k* always have non-negative values.

However, before finding the Maxwell equations and quantum optics laws, in 1729, Pierre Bouguer pointed out that the transmission of light through a substance has a logarithmic dependence on absorbance. Later, Johann Heinrich Lambert proposed that the absorbance was linearly proportional to the light pathlength l. August Beer in 1852, suggested that the absorbance is also linearly proportional to the concentration of the substance c. According to the conclusions given by these pioneers, the absorbance is then expressed as Bouguer- Lambert-Beer (BLB) law:

$$log_{10}\, \frac{I_0}{I} = \mathrm{A} = \varepsilon\, c\, l \qquad 2\text{-}7$$

where ε is the molar absorption coefficient, c the molar concentration of the absorbing compound and *l* is the path length of light within the absorbing medium.

The BLB law can be derived from electromagnetic theory and dispersion theory (Mayerhöfer, Pahlow et al. 2020). Moreover, a theoretical comparison between the BLB law and electromagnetic theory suggests

that the BLB law is approximately correct under certain circumstances, while it can be completely inappropriate under other conditions (Mayerhöfer, Pahlow et al. 2020).

2.1.1 Absorption of light by molecules

The absorbed energy level of a photon in the molecules is directly related to their chemical structure, which defines the energy level of electrons. Based on the molecular orbital theory, the atomic orbitals of all atoms in a molecule are considered together. The merging of the individual orbitals (s, p, d orbitals) is a so-called hybrid orbital, which can be described by bonding and antibonding states regarding the electronic interactions. Analogous to the designation of the s, p and d orbitals, they are designated as σ, π and δ (bonding) or σ^*, π^* and δ^* (antibonding) orbitals. π or π^* orbitals of several atoms can form a common conjugated system can overlap each other in which the electrons are delocalized over the entire area of the system.

The carbon compounds containing conjugated chains, i.e., long chains of alternating single and double bonds, which are characterized by a σ orbital and a π orbital, play a decisive role in the photoreceptors. Quantum mechanics can approximately estimate the energy level of electrons in the conjugated chain. For this purpose, the delocalized electrons are considered as particles in a one-dimensional box of the same length as the chain (L) (**Eq. 2-8**). The energy difference between the highest occupied molecular orbitals (HOMO) and the lowest unoccupied molecular orbitals (LUMO) can define the lowest possible absorption energy. There are 2n of π electrons occupying n molecule orbitals in the molecular ground state of the double bond carbon-carbon chain or 2n carbon atoms. Therefore, the energy gap is:

$$\Delta E = E_{n+1} - E_n \cong \frac{(2n+1)\hbar^2\pi^2}{2mL^2} \qquad 2\text{-}8$$

Electrons in the conjugated π-system, e.g., pigments, can capture a certain photon to resonate along with a certain distance of π-orbitals. As the conjugated π-system is longer, the pigment can absorb a photon with a longer wavelength. Since the length L increases approximately linearly with the number of C=C bonds n, this means that the energy ΔE of a photon absorbed in the HOMO–LUMO transition is approximately proportional to 1/n.

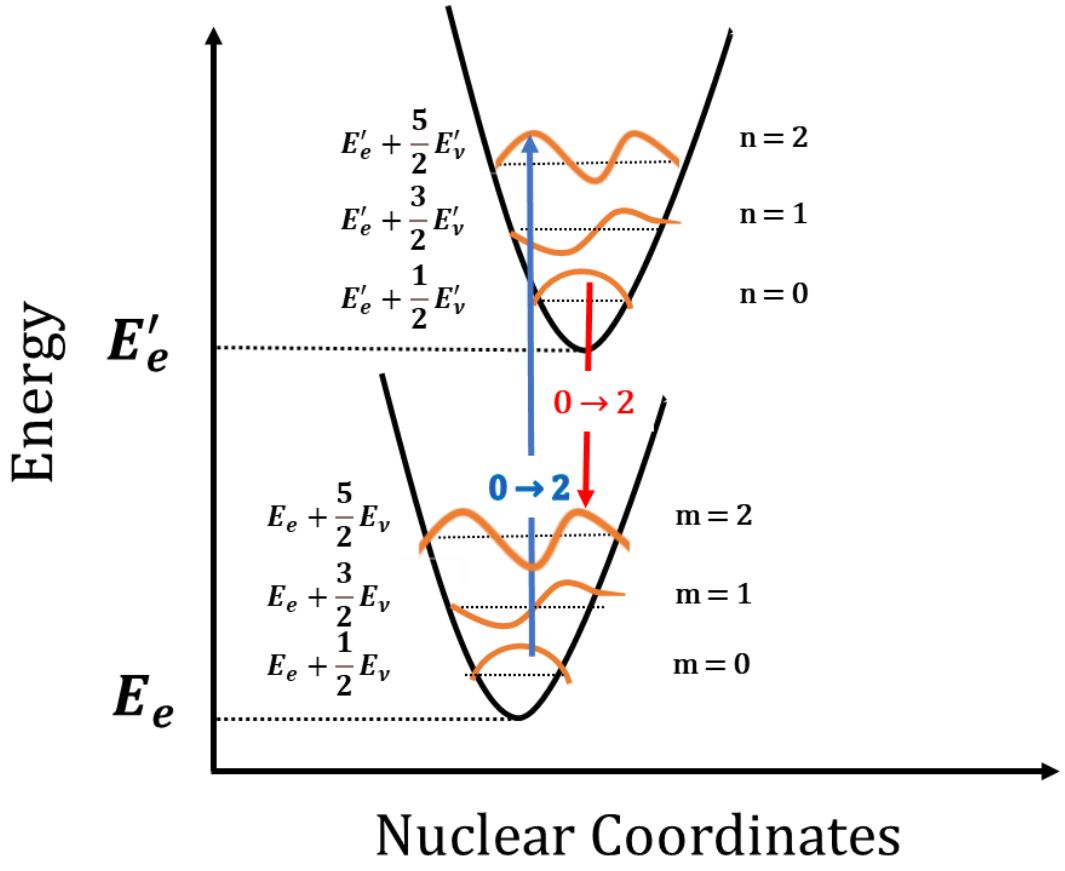

Figure 2-1: Illustration of the Franck-Condon principle alongside the assumption that the vibrational mode is dominant approximating to that of a simple harmonic oscillator. The orange curves denote the wavefunctions of each vibronic state. The intensity of lines spatially governed by the overlap of the vibrational wavefunctions denoted as blue arrow which is known as Franck Condon state. The blue absorption arrow 0-2 will give a strong band in the absorbance spectrum and the red emission arrow 0-2 will give a strong emission band in the emission spectrum because of the good overlap between the Franck Codon states.

The conjugated π-systems also can form a dipole as there is an uneven charge distribution which is characterized by the dipole moment. The dipole moment μ is the product of the charge (q) and the distance between the charge (r). The dipole moment operator $\vec{\mu}$ for a collection of charges will be the sum of each individual charge q_n multiplied by the distance of each individual charge r_n:

$$\vec{\mu} = \sum_n q_n r_n \qquad 2\text{-}9$$

In quantum mechanics the possibility of a transition from the ground eigenstate Ψ_i to first excited eigenstate Ψ_j is given by $\left|\vec{M}_{ij}\right|^2$, that the transition dipole moment for overall space will be (Limpouchová Z 1993):

$$\vec{M}_{ji} = \int \psi_j \vec{\mu} \psi_i \, dV \qquad 2\text{-}10$$

When a molecule is undergoing an electronic transition, such as ionization, the nuclear configuration of the molecule experiences no significant change. This is since nuclei are much more massive than electrons and the electronic transition takes place faster than the nuclei can respond. While when the nucleus realigns itself with the new electronic configuration, they must undergo a vibration. This assumption is known as the Franck-Condon principle. Based on Condon approximation the transition probability $\vec{M}_{ji}$ can be separated into electronic (e) and vibrational (ν) components which explain the transition probability of electron and proton respectively:

$$\vec{M}_{ji} = \int \psi_{je} \vec{\mu} \psi_{ie} \, dV \int \psi_{jv} \vec{\mu} \psi_{iv} \, dV \qquad 2\text{-}11$$

Since electronic transitions are very fast compared with nuclear motions, vibrational levels are favored when they correspond to a minimal change in the nuclear coordinates (**Fig. 2-1**). Thereby, the probability of an electronic transition from one vibrational energy to another will be more likely to occur if the vibrational wavefunctions of the two separate states of $\vec{M}_{ji}$ were overlapped (**Fig. 2-1**), these are known as Franck-Condon factors. Considering a molecule in which only the vibrational mode is dominant, therefore it approximates to a harmonic oscillation. According to the solutions of the simple harmonic oscillator in quantum mechanics, a state involving electronic and vibrational energy is referred to a vibrionic state. If the electronic energy of the ground state is E_e and the energy of the fundamental vibrational mode in the ground state is E_ν then the total energy E_t:

$$E_t = E_e + \left(m + \frac{1}{2}\right) E_\nu \qquad 2\text{-}12$$

where m=0,1, 2, … is the vibrational quantum number. An electronic excited state is characterized by certain basic properties, its energy, its multiplicity and its symmetry. To reach an electronic state higher than the ground state the fluorophore must first absorb light energy. Once energy is absorbed because the nuclear coordinates are unchanged the total energy of the excited state $E_{t:}$

$$E'_t = E'_e + \left(n + \frac{1}{2}\right) E'_\nu \qquad 2\text{-}13$$

where n=0,1, 2, is the vibrational quantum number, E_e' is the electronic energy in the excited state and E_v' is the energy of the fundamental vibrational mode in the excited electronic state.

2.2 Emission of light

The modern theory explains the emission of light by matter, based on electronic energy levels. An electron of relatively high energy may jump to a condition of lower energy, giving off the energy difference as electromagnetic radiation. The Jablonski diagram (**Fig. 2-3**) illustrates a molecule's electronic states and transitions between them. An electron can excite two different forms of a higher energy level: singlet (S) or triplet (T) states. Regarding the Pauli Exclusion principle, the single state contains the electrons' paired + ½ and − ½ spin states. In an excited singlet state, S_0 and S_1 in **Fig. 2-3**, the electron is promoted in the same spin orientation as in the ground state (paired). In a triplet excited state, T_1 in **Fig. 2-3**, an outer electron can go to a new orbital that has undergone a subsequent reversal in spin so that a former pair of electrons are now parallel. The difference between the spins of ground singlet, excited singlet, and excited triplet is shown in **Fig. 2-2**.

According to the quantum theory, the electron can be paired (+½ or –½); therefore, to have the parallel spin, the electron has to go through a 'forbidden' transition, which is less probable (**Fig. 2-2**). In contrast, the electrons can undergo 'intersystem crossing' between singlet and triplet states. The electrons can relax into the singlet vibrational ground states within picoseconds to respond to the interactions with surrounding environments. This process is so-called vibrational relaxation. Moreover, the vibrational states of two neighboring electronic singlet states can couple and go to a radiation-less transition called internal conversion and occur on a picosecond timescale. Electrons located in the vibrational ground state of S_1 have a relatively long residence time compared to vibrational states. Typical lifetimes of S_1 are in the order of nanoseconds, which leads to an accumulation of electrons. The transition between S_1 and the vibrational states of the electronic ground state is a radiative transition, named fluorescence. If it comes to a coupling

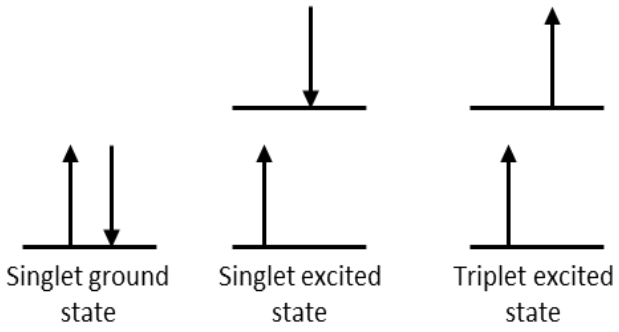

Figure 2-2: Spin in the ground and excited states

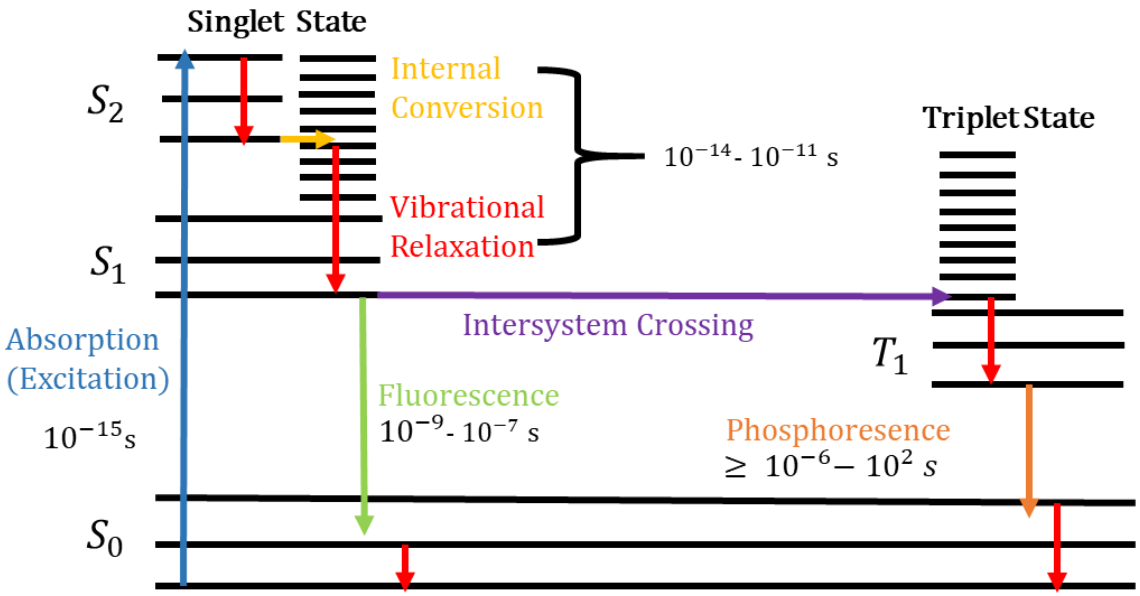

Figure 2-3: **Jablonski diagram, illustration of the relative positions of electronic states and possible transitions between them. S_0** is the electronic singlet ground state, **S_1** is the first excited singlet state, **T_1** the equivalent triplet state. Straight blue arrow indicates absorption of a photon, green arrow for the fluorescence emission, yellow arrow for the internal conversion, red arrow for the vibrational relaxation, and the orange arrow for the phosphorescence emission.

between the vibrational states of S_1 and the neighboring triplet state T_1, as it was mentioned earlier, a further transition can be observed, called intersystem crossing. The fast-vibrational relaxations lead to an accumulation of electrons, this time in T_1. While from quantum mechanics, the transitions into the electronic ground state are "forbidden," and the occurring transitions are longer than fluorescence. Typical lifetimes of T_1 range from milliseconds up to hours; the photon emission caused by these transitions is known as phosphorescence. Fluorescent molecules, called fluorophores, have characteristic properties that are correlated to their chemical structure and environment.

2.2.1 Fluorescence quantum-yield

The fluorescence quantum yield (Φ_f) is defined as the ratio of the rate of fluorescence emission to the rate of absorption. The fluorophore in the ground state F, after absorbing the light will excite to the emitting state F^*, which can be described by the mechanism below:

$$F + h\nu \rightarrow F^* \qquad rate = k_A n_F \qquad 2\text{-}14$$

where k_A is the rate constant for photon absorption. The emission of fluorescence is following:

$$F^* \rightarrow F + h\nu \qquad rate = k_r n_{F^*} \qquad 2\text{-}15$$

$$F^* \rightarrow F \qquad rate = k_{nr} n_{F^*} \qquad 2\text{-}16$$

where k_r is the rate constant for fluorescence emission, and k_{nr} is the sum of the fist-order rate constants for nonradiative decay modes, such as internal conversion and intersystem crossing (**Fig. 2-3**). The variables n_F and n_{F^*} are the number of fluorophores in the ground and excited state, respectively.

In the steady-state conditions, we can assume:

$$k_A n_F = (k_r + k_{nr}) n_{F^*} \qquad \left(\frac{dn_{F^*}}{dt} = 0\right) \qquad 2\text{-}17$$

Therefore n_{F^*} will be:

$$n_{F^*} = \frac{k_A n_F}{(k_r + k_{nr})} \qquad 2\text{-}18$$

The Φ_f formally defines as:

$$\Phi_f = \frac{k_r \, n_{F^*}}{k_A n_F} \qquad 2\text{-}19$$

If n_{F^*} is replaced by 2-19 the Φ_f will be:

$$\Phi_f = \frac{k_r}{k_r + k_{nr}} \qquad 2\text{-}20$$

Fluorophores that are rigid will have higher quantum yields as the bending or rotation of the bonds in a fluorophore can favor non-radiative pathways for de-excitation.

2.2.2 Fluorescence lifetime

When a fluorophore is excited by a short pulse rather than a continuous source, the decay of fluorophore after the short pulse is relaxed normally following a single exponential decay in solution. In general, the fluorescence lifetime is defined as the mean time elapsed between the activation of fluorophore (absorption of a photon) and emission of a photon from the fluorophore. If the transition to the ground state is only by photon emission, then the fluorescence lifetime will only depend on the radiative decay rate k_r :

$$\tau = \frac{1}{k_r} \qquad 2\text{-}21$$

As **Fig. 2-3**, the Jablonski diagram shows, non-radiative decay processes also are involved, such as internal conversion, intersystem crossing, excited state reactions and energy transfer. Therefore, the lifetime with considering the non-radiative decay k_{nr} will be:

$$\tau = \frac{1}{k_r + k_{nr}} \qquad 2\text{-}22$$

The term of non-radiative decay is strongly dependent on the environment, thereby the fluorescence lifetime will be sensitive to the environmental modification factors such as polarity, pH and conformation.

2.2.3 Fluorescence quenching

In general, the fluorescence quenching refers to the events, in which the fluorophore fluorescence intensity decreases due to the interaction with a quencher. The molecular contact between the fluorophore and quencher is essential for the quenching. A variety of processes can cause the quenching which are excited state reactions, the energy transfer, the complex formation, and collisional quenching. The intensity of fluorophore fluorescence can be quenched in two possible ways: 1. by ground-state quencher-fluorophore reactions which is called static quenching, 2. by excited-state quencher-fluorophore reactions which is called dynamic or collisional quenching. In dynamic quenching, excited-state molecule collides with quencher molecule and returns to ground state in non-radiative transitions.

When the quencher (Q) is present, another F^* decay mechanism is possible besides the mechanisms which were explained in **Eq. 2-15** and **Eq. 2-16**, and this mechanism known as quenching can be described fluorescence:

$$F^* + Q \rightarrow F + Q \qquad rate = k_q[Q]n_{F^*} \qquad 2\text{-}23$$

where k_q is the second-order constant for quenching and the product $k_q[Q]$ is pseudo-first order. Considering the existence of the quencher **Eq. 2-20** will be:

$$\Phi_f = \frac{k_r}{k_r + k_{nr} + k_q[Q]} \qquad 2\text{-}24$$

In static quenching, shift of the fluorophore's absorption spectrum by adding the quencher, shows the complex formation in the ground-state. This complex, after it absorbs light returns to the fundamental state

without emitting any photons. Combining the **Eq. 2-20**, which represents the quantum yield without quencher (Φ_f^0), and **Eq. 2-24** to derive the Stern-Volmer equation:

$$\frac{\Phi_f^0}{\Phi_f} = 1 + \frac{k_q[Q]}{k_r + k_{nr}} \quad 2\text{-}25$$

Constant K_{SV} is the Stern-Volmer quenching constant and can be defined as:

$$K_{SV} = \frac{k_q[Q]}{k_r + k_{nr}} \quad 2\text{-}26$$

In the more familiar form, Φ_f^0 and Φ_f are replaced by F^0 and F which are the intensity of fluorescence at a given wavelength, in the absence and present of Q respectively, and by inserting **Eq. 2-26** in **Eq. 2-25** yields:

$$\frac{F^0}{F} = 1 + K_{SV}\,[Q] \quad 2\text{-}27$$

Since the concentrations are proportional to the fluorescence intensities (I), **Eq. 2-27** can be written as

$$\frac{I_0}{I} = 1 + K_{SV}\,[Q] \quad 2\text{-}28$$

Therefore, plotting I_o / I = f ([Q]) yields a linear plot whose slope is equal to K_{SV} of the complex.

In the static quenching, fluorescence lifetime of fluorophore does not change upon increasing quencher concentration. This implies the following equation:

$$\frac{\tau_0}{\tau_{(Q)}} = 1 \quad 2\text{-}29$$

However, in the case of excited-state quencher-fluorophore reactions or dynamic quenching, considering the presence of the quencher, the lifetime in **Eq.2-22** will be written as:

$$\tau = \frac{1}{k_r + k_{nr} + k_q[Q]} \quad 2\text{-}30$$

where k_q [Q] is the rate constant for the quenching.

2.2.4 Fluorescence anisotropy

Fluorescence anisotropy or fluorescence polarization measures the changing orientation of a fluorescein molecule in space in a certain amount of time, regarding their respective absorption and emission dipole moments (**Eq.2-9**). Absorption and emission are defined by the specific alignment of the molecule's dipoles regarding to the electromagnetic wave polarization of excitation and emitted light, respectively. In the electronic ground state, the absorption dipole moments are randomly orientated. When a sample is excited with vertically polarized light, the absorption preferentially takes place by fluorophores in solution with an absorption dipole moment parallel to the plane of polarization of the excitation light (vertically in this case); this event is so-called photo-selection. The rotational motion of the fluorophore in solution, in most cases, has the main contribution to the depolarization of emitted photon, which depends on its size and shape and the viscosity of the solvent. The binding of a fluorophore to a target molecule e.g., biomolecules, will alter the rotational motion behavior of the fluorophore. Due to the higher molecular weight, the target-fluorophore complex moves slower. Slower movement means that the polarization of the light is conserved for a longer time. The fluorescence depolarization or anisotropy can contain information on the target molecule's size and internal flexibility.

The anisotropy is calculated by taking the ratio of the intensities as following:

$$r(t) = \frac{I_{\mathrm{VV}}(t) - I_{\mathrm{VH}}(t)}{I_{VV}(t) + 2GI_{VH}(t)} \qquad 2\text{-}31$$

where I_{VV} indicates the intensity with vertically polarized excitation and vertical polarization on the detected emission. I_{VH} indicates the intensity when using a vertical polarizer on the excitation and horizontal polarizer on the emission. G is a grating factor used as a correction for the instrument's differential transmission of the two orthogonal vector orientations and it is defined as:

$$\mathrm{G} = \frac{\mathrm{I_{HV}(t)}}{\mathrm{I_{HH}(t)}} \qquad 2\text{-}32$$

The initial anisotropy r_0 at time t =0 after excitation, can be define as:

$$\mathrm{r_0} = \frac{2}{5}\left(\frac{3\cos^2\beta - 1}{2}\right) \qquad 2\text{-}33$$

where β is the angle between the excitation and emission dipoles. According to the **Eq. 2-33,** r_0 has a maximum theoretical value of 0.4 when the excitation and emission dipoles are parallel (β = 0) and a minimum value of -0.2 when the excitation and emission dipoles are perpendicular (β = 90).

2.3 Phytochrome family

Phytochromes are photoreceptors that have been discovered first in plants (Butler 1959, Borthwick 1952), but are now known to be widely distributed among bacteria and fungi (Lamparter, Michael et al. 2003). In plants, phytochromes control the physiological processes, such as germination, de-etiolation, inhibition of stem and petiole elongation, Chloroplast development, Chlorophyll biosynthesis, leaf expansion, branching, flowering, and senescence (**Fig. 2-4**). In bacteria and cyanobacteria, phytochromes regulate not only phototaxis but also the composition of the light-harvesting complex. Finally, phytochrome is involved in the sexual development of fungi. To date, over 150 different phytochromes and phytochrome-related proteins have been characterized regarding to their expanded structural and spectroscopic variety all photoreceptors' proteins within the phytochrome family bind to an open-chain tetrapyrrole as a cofactor and photo-switchable sensor. Upon the light absorption, the phytochrome protein photo-converts between a dark-adapted state and a light induced state.

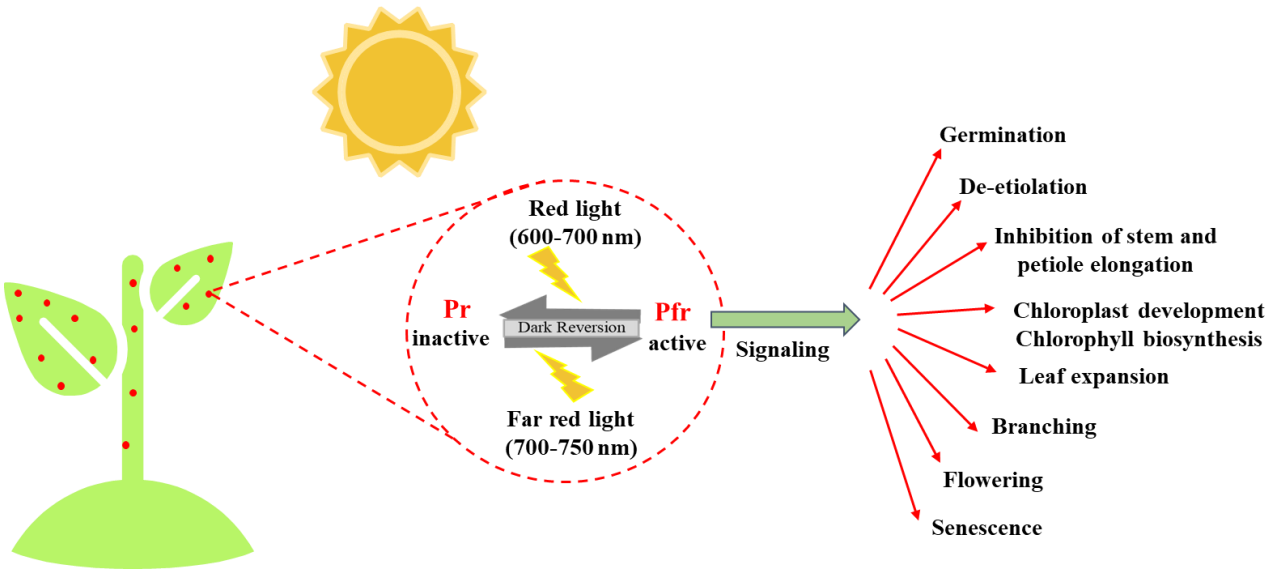

Figure 2-4: schematic diagram depicting the involvement of phytochromes in different stages of photomorphogenesis. The red dots represent phytochromes that are present ubiquitously in plants. Inactive phytochrome (red light-absorbing Pr form) can be converted to active phytochrome (far-red light-absorbing Pfr form) by absorbing red light. The Pfr form can be converted back to the Pr form upon absorbing far-red light or in the dark (known as dark reversion, or more recently, thermal reversion. The active Pfr form regulates various photomorphogenic development through other downstream components of the phytochrome- mediated light signaling pathway.

2.3.1 Protein domains of phytochromes

The most studied phytochromes consist of a sensor module and a regulatory module. The sensor module contains a PAS (PER/ARNT/SIM), GAF (derived from cGMP-specific phosphodiesterase cyanobacterial Adenylate-cyclase and form a hydrogen lyase transcription activator, FhlA) and PHY domain (Phytochrome domain), at the N-terminus and a regulatory module at the C-terminus which contains a histidine kinase. The sensor module converts the light signal into a conformational change of the protein and eventually activates the regulatory module. Some examples of the protein domain arrangement are displayed in **Fig. 2-5** The final signal transmission occurs at the C-terminal regulatory module using a histidine-kinase or related domain (HK or HKRD), in which it triggers the phytochrome catalytic activity. HK domain displays an ATP dependent phosphate transferase activity. The full sequence of canonical phytochromes is generally defined as PAS-GAF-PHY-HKRD construct. Bacterial and cyanobacterial proteins do not have PAS-domains in their C-terminus. The additional PAS domain in C-terminus play a crucial role in homodimerization of plant phytochrome. Chromophore attachment in plant and cyanobacterial phytochromes take place at a conserved cysteine in the GAF domain (phyA, Cph2-family

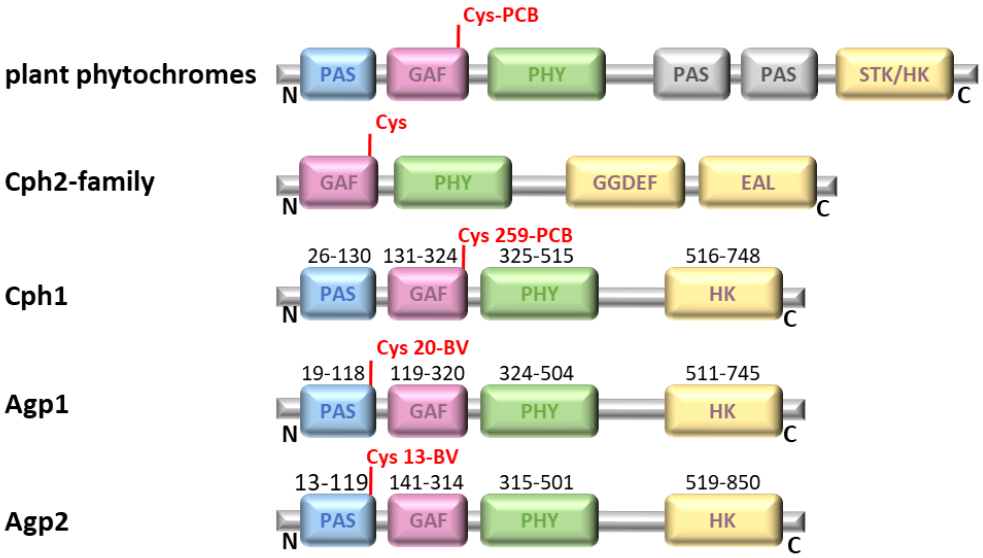

Figure 2-5: Protein domains in different phytochrome variants. The different domains PAS, GAF, PHY, HKRD and others are shown according to the N- to C-terminal phytochrome sequence. Almost all phytochrome variants hold only a single chromophore binding site at a conserved cysteine residue either at the PAS domain in the case of Agp1 and Agp2 or GAF domain in the case plant phytochrome and Cph1 and Cph2.

and Cph1 in **Fig. 2-5**). In contrast to that, the covalent chromophore attachment in bacterial phytochromes (Agp1 and Agp2) takes place at the PAS domain.

2.3.2 Chromophore and chromophore binding pocket (CBP)

The open chain tetrapyrrole binds to the sensor module of phytochrome. Upon red-light absorption, phytochrome undergoes an interconversion from Pr state to Pfr state. These two states can be considered as optical switches that are triggered by light absorption and Z/E isomerization of chromophore at the C-D methin bridge as the first step of photoconversion. Depending on the species, three different bilin (open chain tetrapyrrole) chromophores can be formed: biliverdin (BV), phycocyanobilin (PCB), or phytochromobilin (PφB). BV and PCB binding phytochromes were found in many bacteria, including cyanobacteria and in fungi. The chromophore is covalently attached to the phytochrome via a thioester bond to a cysteine. The cysteine can be in the GAF or in the PAS domain depending on the type of chromophore and the phytochrome. For example, PCB binds to the cysteine in the GAF domain in Cph1 (**Fig. 2-6**), and BV binds to the cysteine in the PAS domain in Agp1 and Agp2 (**Fig. 2-6**). Hydrogen bonds between the chromophore and chromophore binding pocket are present either directly between chromophore and amino acids or mediated by the water molecules.

Phytochromes sense light based on a linear tetrapyrrole chromophore with a highly conjugated π-system (Smith 2000). The open tetrapyrrole molecule variants such as BV and PCB are degradation products of the oxidative heme metabolism (**Fig. 2-7**). The first product is BV which is synthesized by enzymatic heme cleavage at the α-position (the α-position refers to the α carbon in organic molecules which is the first carbon atom that attaches to a functional group, such as a carbonyl). This reaction takes place at a

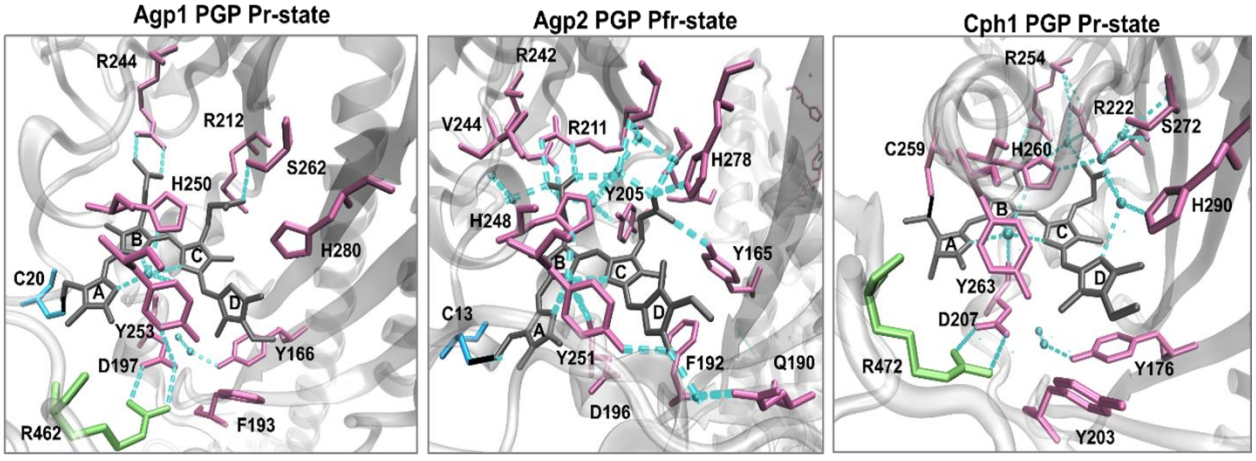

Figure 2-6: Chromophore binding pocket of BV and PCB-binding chromophore phytochromes. Agp1 PGP in the Pr state, PDB 5I5L (Nagano, Scheerer et al. 2016), Apg2 PGP in the Pfr state (Schmidt, Sauthof et al. 2018), and Cph1 PGP in the Pr state, PDB 2VEA (Essen, Mailliet et al. 2008).

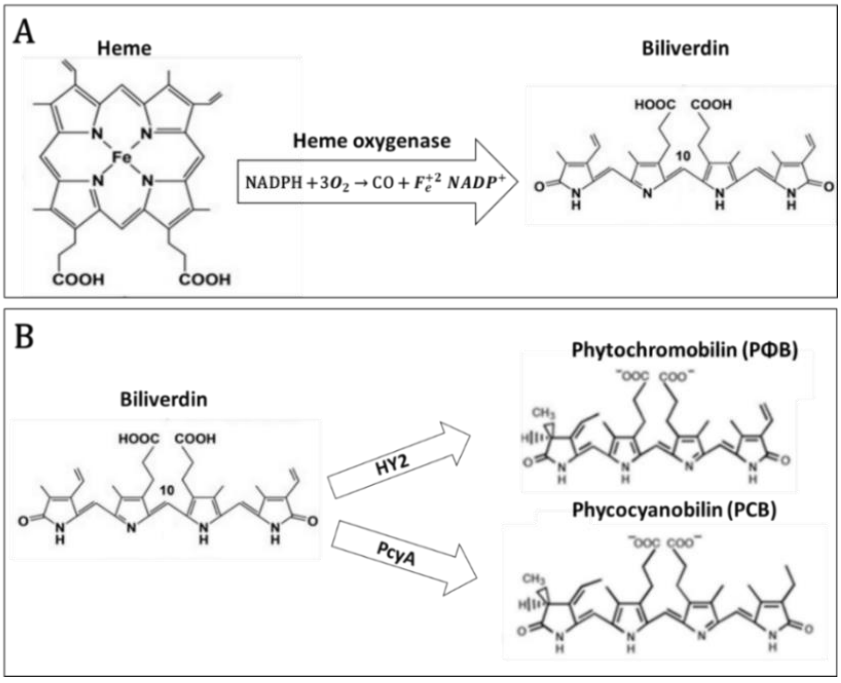

Figure 2-7: The reduction of heme to biliverdin BV by heme oxygenase, and reduction of biliverdine to PΦB and PCB by HY2 and PcyA,respectively.

ferredoxin-dependent heme oxygenase (HO or HOx) (**Fig. 2-7. A**) (Terry, Linley et al. 2002, Frankenberg and Lagarias 2003). In cyanobacteria BV is subsequently converted to PCB by the ferredoxin dependent bilin reductase of the PcyA family which it follows the four-electron reduction pathway (Frankenberg, Mukougawa et al. 2001)(**Fig. 2-7B**). Higher plants transform BV to phytochromobilin PΦB over a two-electron reduction pathway. Here, the enzymatic reaction involves a bilin reductase-phytochromobilin-synthetase (HY2) (Kohchi, Mukougawa et al. 2001) (**Fig. 2-7B**). In contrast to cyanobacteria and other photosynthetic organisms (Beale 1993), fungi and non-photo synthetic bacteria lack the ferredoxin-dependent phycobilin synthetase pathways of PCB reduction. In these organisms, BV was identified as native chromophore for bacterial phytochrome(Bhoo, Davis et al. 2001). **Fig. 2-6** shows the chromophore binding pocket of Agp1 and Cph1 in Pr state and Agp2 in Pfr state. Beside their different chromophores, the alignment of these two groups of phytochrome indicates the chromophore binding pocket amino acids are highly conserved except one or two amino acids. Also, there is a conserved water molecule which connects rings A, B, and C, and the amino acids tyrosine in Agp1, Agp2 and Cph1 (**Fig. 2-6**). In contrast to Agp1, Agp2 and Cph1 have other water molecules in their crystal structure of chromophore binding pocket. However, the water molecules are distributed differently in Agp2 and Cph1 (**Fig. 2-6**). In Cph1, a network of water molecules makes a hydrogen bond to the D-ring, this network is absent in Agp1 and Agp2,

and another water molecule network connects the propionate side chain C and B. In Agp2, there is a water molecule network that connects the propionate side chain C and B. The variations in the hydrogen binding network and water molecules distribution might explain the different properties of phytochromes.

2.3.3 Phytochrome photocycle

In prototypical phytochrome, the photocycle comprehends two photo-induced pathways: the Pr-to-Pfr and back reaction the Pfr-to-Pr (**Fig. 2-8. E**). The first step in both directions is a chromophore photo-isomerization at CD rings from Z/E to E/Z configuration which is in methine bridge C15=C16 double bond. In the Pr-to-Pfr transition, the chromophore photoisomerization triggers a larger conformational change in chromophore and the protein. The intermediate states formation is associated with protein refolding events as well as transient chromophore-proton translocation that precedes the formation of the Pfr state. In the last step a phytochrome specific peptide so-called tongue undergoes a secondary structure change from beta-sheet to α-helix (Takala, Björling et al. 2014). This event in prototypical phytochrome is associated with the activation of the output module (**Fig. 2-8E**), while in bathy phytochromes is going to deactivate the output module (in Pfr state) (**Fig. 2-8F**).

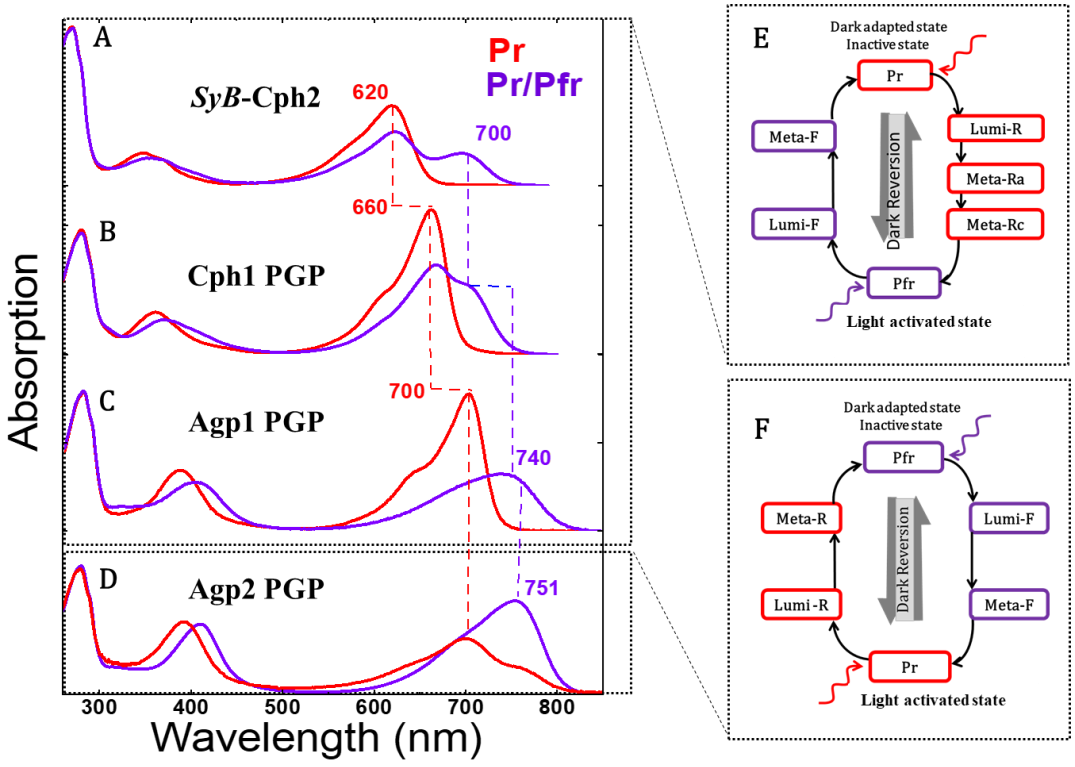

Figure 2-8: Absorption spectrum of prototypical phytochrome variants SyB-Cph2 (**A**), Cph1 PGP (**B**), Agp1 PGP (**C**), with the schematic photocycle from dark adapted state Pr to Pfr sate (**E**). Absorption spectrum of bathy phytochrome Agp2 PGP (**D**), with the schematic photocycle from dark adapted state Pfr to Pr sate (**F**). The absorption shown in purple for the Pr/Pfr state and in red for the Pr state.

The phytochrome photocycle and the corresponding parent and intermediate states are shown in **Fig. 2-8E** and **Fig. 2-8F** for prototypical and bathy phytochromes, respectively. In prototypical phytochromes the photoisomerization from the initial Pr state to Lumi-R takes place via a short-living excited state (excited state decay in 100-500 fs) within 20-100 ps (Kim, Rockwell et al. 2013). Lumi-R is associated with a very low quantum-yield since the steric constraints at the conical intersection of the Pr*/Lumi-R* potential surfaces favors the Pr back formation (Dasgupta, Frontiera et al. 2009). The Lumi-R intermediate subsequently decays thermally to the Meta-Ra species. The chromophore is found in a more relaxed ZZE-geometry and the pocket partially adapts to the photo-induced changes of the chromophore. Hence, protein residues reorient preparing the protein moiety to even larger structural changes. The Meta-Ra has a longer decay to back formation of Pr. Prior to the Pfr state formation, the chromophore is transiently deprotonated in the Meta-Rc state. Thus, losing its cationic nature at rings B and C and adopting a more distorted geometry. The protein moiety experiences long-range refolding events. The Meta-Rc lifetime is in the longer µs and lower ms range. In a similar way as in the Pr-to-Pfr reaction, the E/Z-photoisomerisation in the Pfr-to- Pr pathway leads to the formation of the Lumi-F intermediate (Chen, Lapko et al. 1997). Subsequent decay to the Meta-F also involves mayor residue reorientation as in the Meta-Ra intermediate. Unlike the forward reaction, a transient deprotonation of the chromophore at the Meta- F(a) level, has not yet been observed. Characterization of the reverse photoreaction is technically challenging; therefore, it is considerably less explored than the forward pathway.

UV-vis absorption of phytochrome indicates two different absorption spectra for Pr state and Pr/Pfr state, red and purple, in **Fig. 2-8A-D**, respectively. The dark-adapted state or thermally stable state, Pr in prototypical/Pfr in bathy phytochrome, can be formed by illumination with the far-red/red light for 2-5 min or alternatively resting in the dark for enough amount of time. The light activated state, Pfr in prototypical/Pr in bathy phytochrome, can be reached under the illumination of the red/far-red light. The absorption spectrum indicates three prominent bands: chromophore band, Soret band and protein band. The chromophore band variants among the phytochrome family regarding their type of chromophore e.g., BV or PCB, and the position of chromophore binding in the protein. Chromophore peak in PCB binding proteins such as Cph2-*SyB* and Cph1 (**Fig, 2-8A** and **B**, chromophore peak at 620 nm and 660 nm in Pr state, respectively) is blue-shifted compared to BV binding proteins such as Agp1 and Agp2 (**Fig. 2-8C** and **2-8D**,700 nm in Pr state).

2.3.4 Protonation heterogeneity

Among phytochrome family, protonation heterogeneity first was observed in the Pr state of plant phytochrome (Sineshchekov 1995, Schmidt, Gertsch et al. 1998), then later in Cph1 (Sineshchekov,

Koppel' et al. 2002). Moreover, a recent study showed the protonation heterogeneity is related to the structure heterogeneity which is directly related to the photoconversion and the protein signaling (van Thor, Borucki et al. 2001, Song, Essen et al. 2012, Escobar, Lang et al. 2017). For Cph1 and oat phyA3 (Pr-I and Pr-II), two specific Pr subpopulations were characterized by solid-state nuclear magnetic resonance (NMR) (Song, Psakis et al. 2011, Song, Essen et al. 2012). Also it was found different excited-state properties of Cph1 in Pr, (Kim, Rockwell et al. 2013) although conformational homogeneity in Pr was also reported using two-dimensional electronic spectroscopy. It was shown, because of the ionic status of the pyrrole water, the protonation states of His260 and His290 in Cph1 were different (Song, Essen et al. 2012). Furthermore, it was recently revealed using a combination of experiment and theory [resonance Raman/ultraviolet−visible spectroscopy and quantum mechanics/molecular mechanics (QM/MM) calculations] that the pH-dependent equilibrium between Pr-I and Pr-II is dependent on the protonation state of His260 (Song, Essen et al. 2012). His260 was identified, using QM/MM calculations, to be protonated and deprotonated in the Pr-I and -II states, respectively, whereas His290 was neutral in both. The authors proposed that a decrease in the p*K* of His260 during photo transformation is the driving force for proton release monitored in solution(Escobar, Lang et al. 2017). In contrast to the protonation mechanism in Cph1 and plant phytochrome, a pH dependent Uv-vis absorption, and RR spectroscopy indicated the protonation homogeneity of Agp1 (Borucki, von Stetten et al. 2005). However, the combined study of Raman spectroscopy and flash photolysis in Agp1 showed a strong similarity between Agp1 and plant phytochrome A that all pyrroles nitrogen are protonated during the chromophore isomerization (Borucki, von Stetten et al. 2005). Also, the authors showed the formation and decay of Meta-F are associated with proton release and uptake, respectively.

2.3.5 Fluorescent phytochrome

Modern biology investigation on phytochrome as a near-infrared (NIR) photoreceptor is essential to design optogenetic tools. So far, several types of naturally light-active proteins have been successfully used for optogenetic tools (Levskaya, Chevalier et al. 2005, Airan, Thompson et al. 2009, Levskaya, Weiner et al. 2009, Kennedy, Hughes et al. 2010, Strickland, Yao et al. 2010, Mattis, Tye et al. 2012). NIR (~650-900nm) light is favorable over shorter wavelengths for use in mammalian tissues (König 2000) due to its low absorbance by hemoglobin, melanin, and water. Also, tissue autofluorescence, light scattering and light absorption by lipids and fat are low in this range. (Wan, Parrish et al. 1981, Weissleder 2001, Byrnes, Waynant et al. 2005). Up to now, several bacterial phytochrome (Bph) fluorescence proteins (FPs) were employed for designing optical molecular tools for applications in mammals, (Shu, Royant et al. 2009, Filonov, Piatkevich et al. 2011, Piatkevich, Subach et al. 2013, Piatkevich, Subach et al. 2013) as well as human cells (Kamper, Ta et al. 2018) including PAiRFP1 and PAiRFP2, IFPs, iRFPs, IFP1.4, or SNFIP.

In addition, several red FPs were developed based on plant and cyanobacterial phytochromes (Murphy and Lagarias 1997, Fischer and Lagarias 2004, Fischer, Rockwell et al. 2005, Wu, Chang et al. 2013). The study and development on these groups of phytochromes would be important to have a higher NIR fluorescence for biotechnological and medical applications utilizing *in vivo* imaging.

The inhibition of photoconversion by low temperature increases Pr fluorescence, indicating that photoisomerization provides a major route of energy dissipation (Sineshchekov 1995, Sineshchekov 1998). Also, inhibition of photoconversion by "locked" chromophores enhanced fluorescence in the bacteriophytochromes Agp1 and Agp2 (Zienicke, Chen et al. 2011) . Assembling the phycoerythrobilin (PEB) chromophore to Agp1 and Agp2 enhanced the fluorescence quantum yield to ~50 % which is significantly high compared to the BV-binding in mutant variants (~ 1%) and locked chromophore BV (~ 2 %) (Zienicke, Chen et al. 2011) . The PEB chromophore has less conjugated π-system compared to BV (**Fig. 2-9**), that might reduce the energy dissipation after absorbing the light. The difference in the conjugated π-system distribution in BV and PCB (**Fig. 2-9**) also might be one of the reasons for the lower fluorescence quantum yield (Φ_f) of the BV-binding fluorescent phytochromes (Filonov 2011, Shu 2009) compared to the PCB-binding fluorescent phytochromes the orange/red wavelength region. Moreover, these results indicated the role of D-ring orientation in energy dissipation during the photoconversion. Similarly, rigidifying the chromophore by attaching the chromophore at two cysteines of the apoprotein increased the fluorescence quantum yield in a BphP iRFP variant (Buhrke, Tavraz et al. 2019). These results also show a tight coupling between the quantum efficiency of chromophore isomerization and fluorescence quantum yield of photoreceptor proteins (Ihalainen, Takala et al. 2015). As the protein environment has a critical role in defining the excited state lifetime and thereby the quantum efficiency of bilin photoisomerization (Slavov 2020), a higher fluorescence quantum yield in phytochromes may also be achieved by disrupting the photoconversion through appropriate apoprotein mutations (Fischer 2004, Fischer 2005). Directed evolution of FPs by random mutagenesis followed by screening for highly fluorescent mutants has been used to identify appropriate mutations. In pioneering work by the Lagarias group, the mutation Y176H in Cph1 showed a fluorescence quantum yield of about 14% at the expense of efficient photoconversion to Pfr (Fischer and Lagarias 2004). Interestingly however, the corresponding substitution failed to enhance fluorescence in bacteriophytochromes (Wagner.2008). Numerous rounds of mutagenesis using a similar approach led to a variant of the Rhodopseudomonas palustris bacteriophytochrome RpBphP2b with a quantum yield of about 6% after the introduction of no less than 13 mutations onto the PAS-GAF background (iRFP713) (Filonov, Piatkevich et al. 2011).

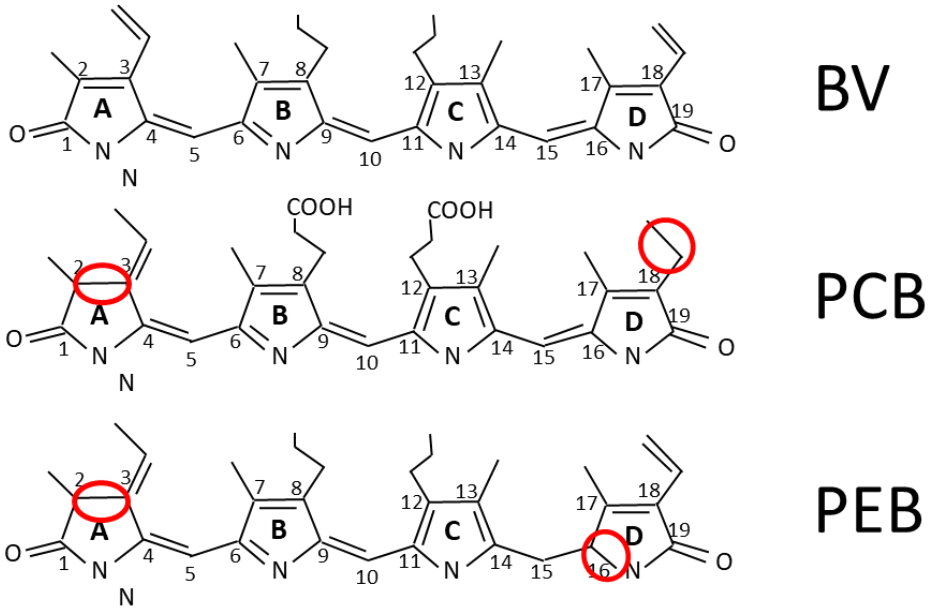

Figure 2-9: Chemical structure of biliverdin (BV), phycocyanobilin (PCB), and phycoerythrobilin (PEB). The lack of double bond in PCB and PEB compared to BV, are marked with red circle.

3 Material and Methods

3.1 Proteins used

Some of the samples were kindly provided by our collaboration partner (**Table 3-1)** and some other samples were generated during the thesis work in Prof. Alexiev lab (**Table 3-2**).

Table 3-1: List of investigated phytochrome proteins which were produced by the collaboration partners.

Protein	Organism	Cofactor	Domains	From
Agp1 WT	*Agrobacterium tumefaciens*	BV	PAS-GAF-PHY	AG Scheerer
Agp2 PGP WT	*Agrobacterium tumefaciens*	BV	PAS-GAF-PHY	AG Scheerer
Agp2 PGP V244F	*Agrobacterium tumefaciens*	BV	PAS-GAF-PHY	AG Scheerer
Agp2 PGP Y165F	*Agrobacterium tumefaciens*	BV	PAS-GAF-PHY	AG Scheerer
Agp2 PGP R211A	*Agrobacterium tumefaciens*	BV	PAS-GAF-PHY	AG Scheerer
Agp2 PGP PAIR2	*Agrobacterium tumefaciens*	BV	PAS-GAF-PHY	AG Scheerer
Agp2 PGP PAIR2 F244V	*Agrobacterium tumefaciens*	BV	PAS-GAF-PHY	AG Scheerer
Cph1 PG Y176H	*Synechocystis*	PCB	PAS-GAF	AG Hughes
Cph1 PG Y176H/Y263S	*Synechocystis*	PCB	PAS-GAF	AG Hughes
Cph1 PGP WT	*Synechocystis*	PCB	PAS-GAF-PHY	AG Hughes
Cph1 PGP C371S	*Synechocystis*	PCB	PAS-GAF-PHY	AG Hughes
Cph1 PGP Y176H	*Synechocystis*	PCB	PAS-GAF-PHY	AG Hughes
Cph1 PGP Y263F	*Synechocystis*	PCB	PAS-GAF-PHY	AG Hughes
Cph1 PGP Y176H/Y263F	*Synechocystis*	PCB	PAS-GAF-PHY	AG Hughes
Cph1 PGP Y176H/Y263S	*Synechocystis*	PCB	PAS-GAF-PHY	AG Hughes
Cph1 PG WT	*Synechocystis*	PCB	PAS-GAF	AG Hughes
Cph1 PG Y176H	*Synechocystis*	PCB	PAS-GAF	AG Hughes
Cph1 PG Y176H/Y263S	*Synechocystis*	PCB	PAS-GAF	AG Hughes

Table 3-2: List of proteins were generated in this work

Protein	Organism	Cofactor	Domains
Agp1 PGP WT	*Agrobacterium tumefaciens*	BV	PAS-GAF-PHY
Agp1 PGP WT	*Agrobacterium tumefaciens*	PCB	PAS-GAF-PHY
Agp1 PGP C279S	*Agrobacterium tumefaciens*	BV	PAS-GAF-PHY
Agp1 PGP C295S	*Agrobacterium tumefaciens*	BV	PAS-GAF-PHY
Agp1 PGP C279S /C295S	*Agrobacterium tumefaciens*	BV	PAS-GAF-PHY
Agp1 PGP C279S /C295S/V264C	*Agrobacterium tumefaciens*	BV	PAS-GAF-PHY
Agp1 PGP V249C	*Agrobacterium tumefaciens*	PCB	PAS-GAF-PHY
Agp1 PGP Y166H	*Agrobacterium tumefaciens*	BV	PAS-GAF-PHY
Agp1 PGP Y166H/V249C	*Agrobacterium tumefaciens*	PCB	PAS-GAF-PHY
Agp1 PGP F193Y	*Agrobacterium tumefaciens*	BV	PAS-GAF-PHY
Agp1 PGP F193Y	*Agrobacterium tumefaciens*	PCB	PAS-GAF-PHY

3.2 Protein mutagenesis and labeling

3.2.1 Plasmid maps

Plasmid maps are graphical representation of plasmids, that show the locations of major identifiable landmarks on DNA like restriction enzyme sites, gene of interest, plasmid name and length (**Fig. 3-1)**.

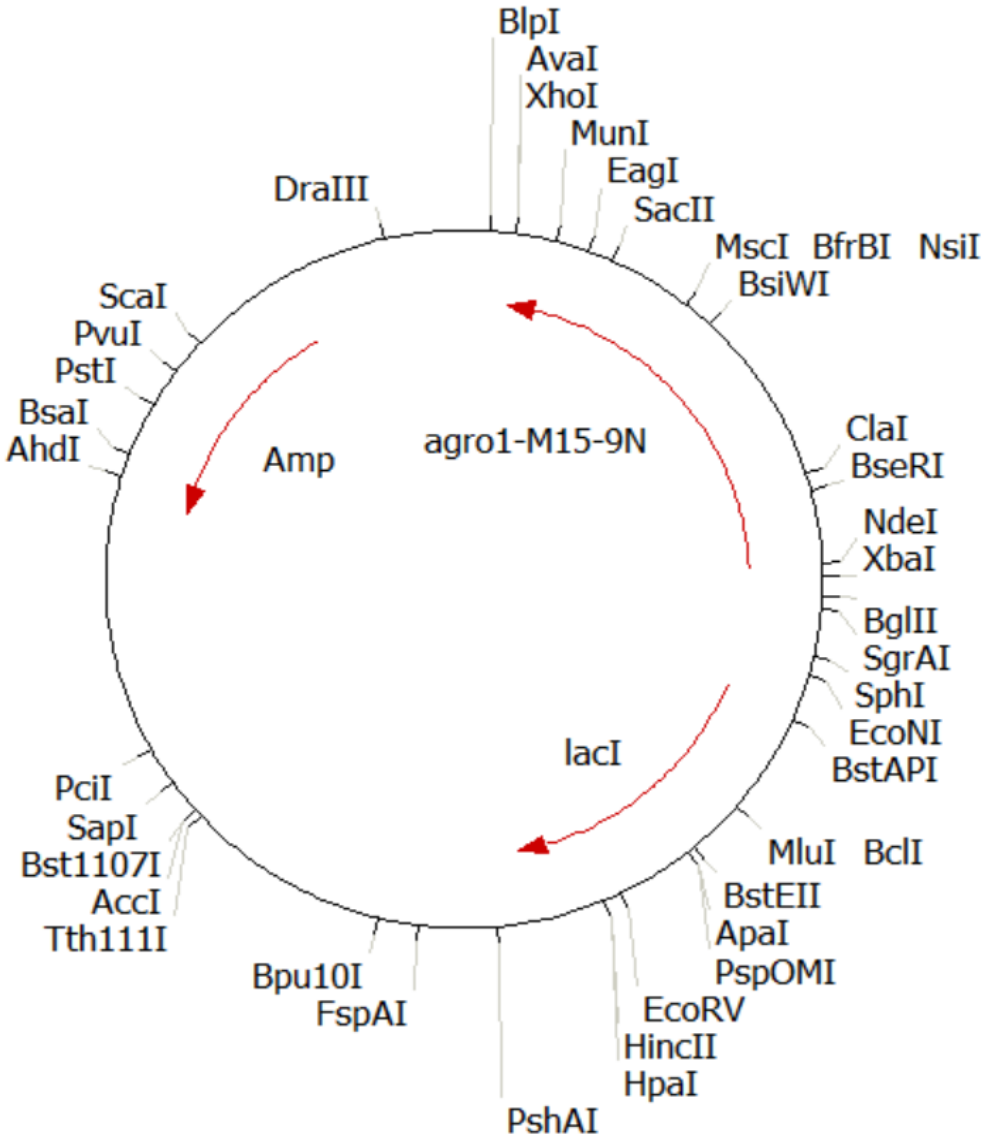

Figure 3-1: Map of the plasmid agro1-M15-9N, the plasmid was kindly provided from Prof. Hildebrand (TU Berlin) based on the original plasmid (Nagano, Scheerer et al. 2016). This plasmid as well as the plasmid without deletion of the first 9 N-terminal amino acids was used for the mutagenesis during the thesis work in Prof. Alexiev lab.

3.2.2 Quick exchange mutagenesis

Site-directed mutagenesis of Agp1 PGP and Cph1 PGP was carried out according to the Quik Change™ mutagenesis protocol (Agilent Technologies) albeit the enzymes were purchased from New England Biolabs. Mutagenesis reaction was always performed at 50 µl per reaction (**Table 3-3**). Composition of the reaction is as follows in **Table 3-3**. **Fig. 3-2** shows the schematic of PCR process according to **Table 3-4.**

Table 3-3: Quick exchange mutagenesis protocol.

Components	Volume (µl)
Milli-Q water	Adjusted for the reaction to be 50 µl
5x Phusion HF Buffer (New England Biolabs)	10
dNTP mix (10 mM) (New England Biolabs)	1
DMSO	3
Template parental plasmid	Adjusted to be 200 ng
Forward primer (10 µM) (EurofinsGenomics)	5
Reverse primer (10 µM) (EurofinsGenomics)	5
Phusion polymerase (New England Biolabs)	0.5

Table 3-4: Time cycle of PCR. **T*** is the specific annealing temperature for each set of the designed primers (see **Table 3-5**).

Cycle Step	Temperature	Time	Number of cycles
Initial denaturation	98°C	1 min	1
Denaturation	98°C	30 s	18
Annealing	**T***	30 s	
Extension	72°C	3:30 s	
Final Extension	72°C	5 min	1
	4°C	hold	

Table 3-5: List of primers. The primers were designed using program SECentral, and they were purchased from EurofinsGenomics company. All primes were dissolved with MQ water, the final concentration of each in MQ water is 100 µM and they stored in -20°C fridge.

primers	sequence	Length	Annealing Temperatu (T*)
Agp1 PGP C279S _f	CTTGATTGCCAGCCACCACGCGACACC	27	71.0
Agp1 PGP C279S _r	GGTGTCGCGTGGTGGCTGGCAATCAAG		
Agp1 PGP C295S _f	CGTACGTGAAGCCAGTGATTTTGCAGC	27	66.5
Agp1 PGP C295S _r	GCTGCAAAATCACTGGCTTCACGTACG		
Agp1 PGP V364C-f	CGCCCAGGCAAAGTGCTGCGCCATCCG	27	70.0
Agp1 PGP V364C-r	CGGATGGCGCAGCACTTTGCCTGGGCG		
Agp1 PGP V249C-f	GCGTATCGCCGTGTCATCTCGAATATATGC	30	68.1
Agp1 PGP V249C-r	GCATATATTCGAGATGACACGGCGATACGC		
Agp1 PGP Y166H-f	ACCGTACCCTGATCCATGATTTCGGACTG	29	68.1
Agp1 PGP Y166H-r	CAGTCCGAAATCATGGATCAGGGTACGGT		
Agp1 PGP F193Y-f	GTCGCCCGCCGGATAGCGAAGGCC	24	75
Agp1 PGP F193Y-r	GGCCTTCGCTATCCGGCGGGCGAC		

3.2.3 Transformation

Chemically competent *E. coli* cells (strain: DH5α) were transformed by heat-shock process to introduce a plasmid into the cell. For this purpose, 1 ng to100 ng of plasmid DNA in 1-5 µl volume was added to the 50 µl cells and gently mixed with pipette tips on ice. The mixture was incubated on ice for 30 minutes. The mixture was heat-shocked at 42°C for 35 seconds, and then cooled on ice for 5 minutes. 950 µl of super optimal broth (SOC) medium (**Table 3-6**) without an antibiotic was added and the culture was incubated at 37°C for 1 hour while shaken at 220 rpm (round per minute). 400 µl of the cell pellet was resuspended and plated onto Luria broth (LB) agar plate containing the appropriate selective antibiotics (**Table 3-7**).

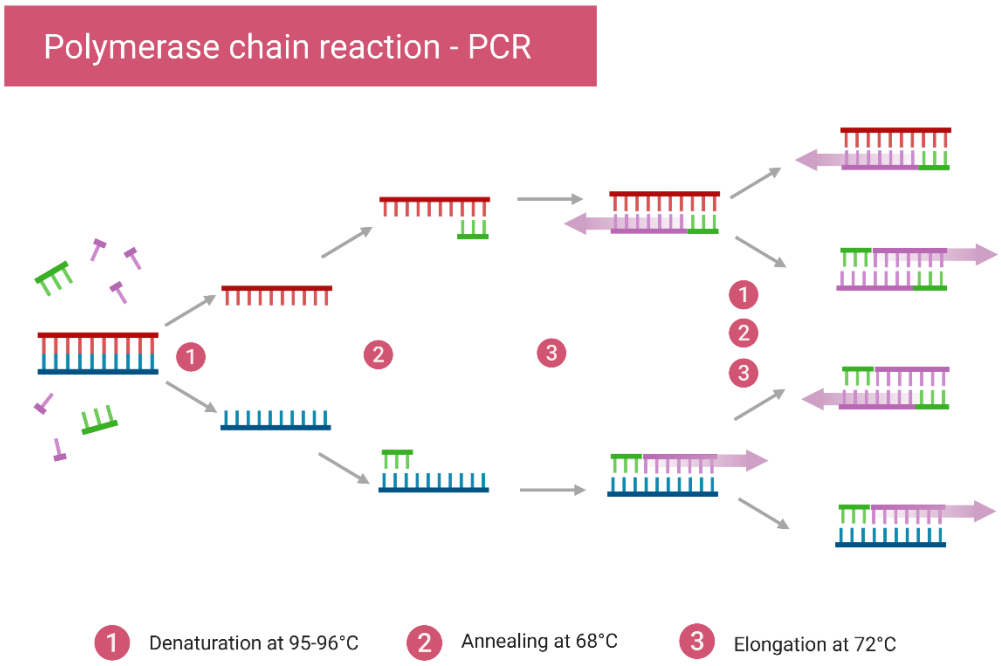

Figure 3-2: Schematic of the PCR process according to **Table 3-4**. The figure was created with BioRender.com

3.2.4 DNA sequencing

It is possible for a mutation to be inadvertently introduced because of replication error, therefore the correctness of the success of site-directed mutagenesis must be verified. Plasmid DNA samples were prepared using HiYield Plasmid Mini Kit (Agilent Technologies), according to the recommendation of the company (EurofinsGenomics) for DNA sequencing (15 µl of 50-100 ng/µl in Milli-Q water) before being shipped. Primers used for sequencing offered by Eurofins are designed to anneal to the T7 promoter.

3.2.5 Overnight culture

To express the protein, the plasmid was transformed to *E.coli* cell strain B L 21 (DE3). Then 1-6 ml of LB medium, containing appropriates antibiotic, was inoculated with a single colony of E. coli cells, from the glycerol stock. The culture was incubated overnight at 37°C while shaken at 145 rpm.

Table 3-6: List of used mediums

Medium	Components
super optimal broth (**SOC**)	purchased from New England Biolabs
Luria broth (**LB**) for overnight culture	10 g/l Tryptone, 10 g/l Nacl, 5 g/l Yeast
Luria broth (**LB**) for expression	10 g/lit Tryptone, 5 g/l Nacl, 5 g/l Yeast

Table 3-7: List of antibiotics

Plasmid	Antibiotic
agro1-M15-9N (for expression of apoprotein Agp1 PGP)	Ampicillin (Amp)
P83 (for expression of apoprotein Cph1 PGP)	Kanamycin (Kan)
P171 (expression of PCB)	Ampicillin (Amp)

3.2.6 Small scale test expression

Small scale test expressions were often carried out prior to large scale protein production. 30 ml of LB-Amp was inoculated with an overnight culture of the appropriate *E. coli* strain bearing the plasmid construct with 1/100 dilution. The cells were grown at 37°C and 200 rpm until absorption at wavelength at 600 nm reached 0.6. The culture was cooled in mixed ice and water. Protein expression was induced with 100 µM isopropyl β-d-1-thiogalactopyranoside (IPTG). The culture was incubated for 18 hours at 18°C and 120 rpm. Then the cells were collected by centrifugation at 5000 g for 20 minutes. The pellet was suspended in 10 ml of Basic buffer (50 mM NaCl, 50 mM Tris-HCl pH 7.8 at 20°C). Cells were lysed either by 3 cycles of freeze-thaw and/or 5 cycles of sonication for 30 seconds followed by a cooling period for 30 seconds. The cell lysate was centrifuged at 12000 g for 15 minutes. The supernatant was transferred into a fresh tube, and the insoluble pellet was resuspended in 500 ml of SDS loading solution (Coomassie Blue in 5% glycerol). The resuspended pellet was heated at 105°C for 5 minutes in a hot water bath. Soluble and insoluble fractions were analysed by SDS-PAGE (**Fig. 3-4**).

3.2.7 Large scale growth and induction

Typically, 250 ml of LB media (**Table 3-6**) with appropriate antibiotic were prepared in 1L baffled flasks. The media was inoculated with an overnight culture at 1/100 dilution. The culture was incubated at 30-37°C with 180-200 rpm until the OD at 600 nm reached 0.6. The cultures were cooled in ice. Expression

of the gene of the target protein was induced with IPTG at the final concentration of typically 50-100 µM. The culture was incubated for further 18 hours at 18°C and 120 rpm.

3.2.8 Sodium dodecyl sulfate polyacrylamide gel electrophoresis (SDS-PAGE)

Sodium dodecyl sulfate polyacrylamide gel electrophoresis (SDS-PAGE) is a method of separating molecules based on the difference of their molecular weight. At the pH in which gel electrophoresis is carried out the SDS molecules are negatively charged and bind to proteins in a set ratio, approximately one molecule of SDS for every 2 amino acids. In this way, the detergent provides all proteins with a uniform charge to mass ratio, independently of their original charge. Proteins bounds are destroyed by detergent, therefore the secondary, tertiary and/or quaternary structure denaturized and turned into the negatively charged linear poly peptide chains. When it is subjected to an electric field in PAGE, the negatively charged poly peptide chains travel toward the anode with different mobility. Their mobility, or the distance traveled by molecules, is inversely proportional to the logarithm of their molecular weight. By comparing the relative ratio of the distance traveled by each protein to the length of the gel one can make conclusions about the relative molecular weight of the proteins, where the length of the gel is determined by the distance traveled by a small molecule like a tracking dye. Molecules weight standards were used for comparison.

3.2.9 Protein purification

Cell disruption and lysate clearance. The overnight expression cell cultured was spinning down (10,000g, 20min, 4°C), then the pellets was resuspended in washing buffer (50mM Tris, 300mM NaCl, 5% glycerol, pH=7.8) and flash frozen in liquid Nitrogen and was stored at -86°C overnight. The next day the cell culture was defrosted and 2mg/ml lysozyme (Sigma-Aldrich), 60mg/ml DNAs (Sigma-Aldrich) and 0.5 mM phenylmethanesulfonyl fluoride (Pefabloc) (Sigma-Aldrich) was added to the solution, kept in ice for 30min, after 30 min 1mM $MgCl_2$ was added and kept in ice for 30min, after 30 min the cell culture solution is ready for sonication. The water bath sonication (Bandelin SONOREX) was done 5 times and each time was carried on for 2-3 min with 5 min rest in ice in between. The supernatant, which is contain the protein, was separated from the pellet by centrifuging (45,000g, 20min, 4°C). The protein purification was done using Ni-NTA (Nickel NTA) which refers to the coupled nickel^{2+} ion to Nitrilotriacetic acid (NTA). Ni-NTA can be coupled to agarose resin or magnetic beads for IMAC (Immobilized Metal Chelate Affinity Chromatography). This is a purification method to obtain functional His-tagged protein such as Agp1 and Cph1.The supernatant was loaded in 3 cm Ni-NTA (Cube Biotech) plastic column (Biorad) which is washed before three times with water and equilibrated with 10mM imidazole 50 mM Tris, 300 mM NaCl, 5% glycerol, pH=7.8 (**Fig. 3-3**). The blue color of Ni-NTA was changed to gray after loading the supernatant, that shows the His tag from protein is perfectly bound to the Ni NTA. Then the protein was washed with

10 mM imidazole 50 mM Tris, 300 mM NaCl, 5% glycerol, pH=7.8 and the absorption was measured at 280 nm of flow through, the column should be washed until the absorption of flow through at 280 nm be almost zero, this is the time for protein elution. The protein elution was done with 300 mM imidazole buffer (300 mM imidazole 50 mM Tris, 300 mM NaCl, 5% glycerol, pH=7.8).

The 300 mM imidazole buffer was added to the column slowly, and it was seen that the grey part in column was coming down by adding more elution buffer. The flow through was collected in 2 ml tubes (Eppendorf),

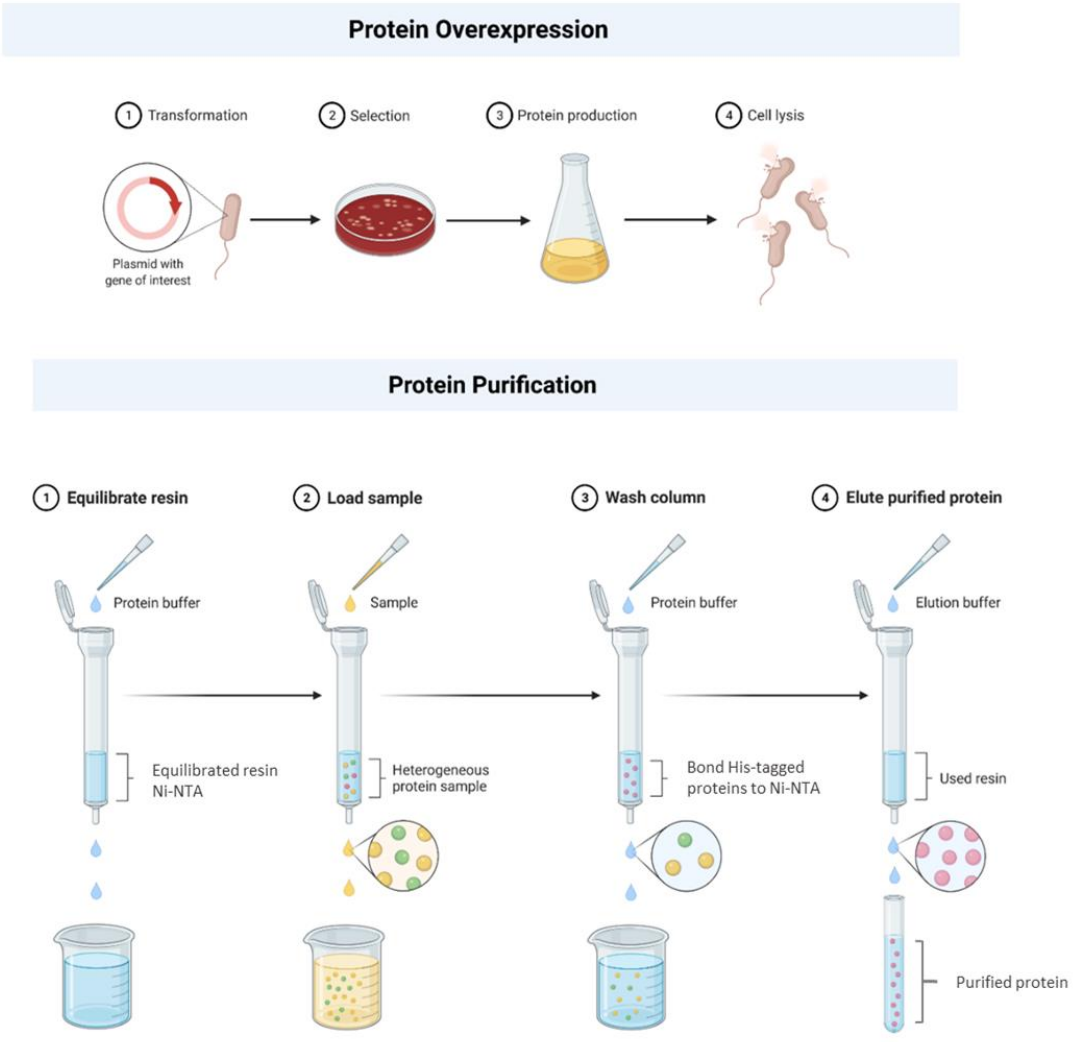

Figure 3-3: Schematic of protein production possess. The figure was created with BioRender.com

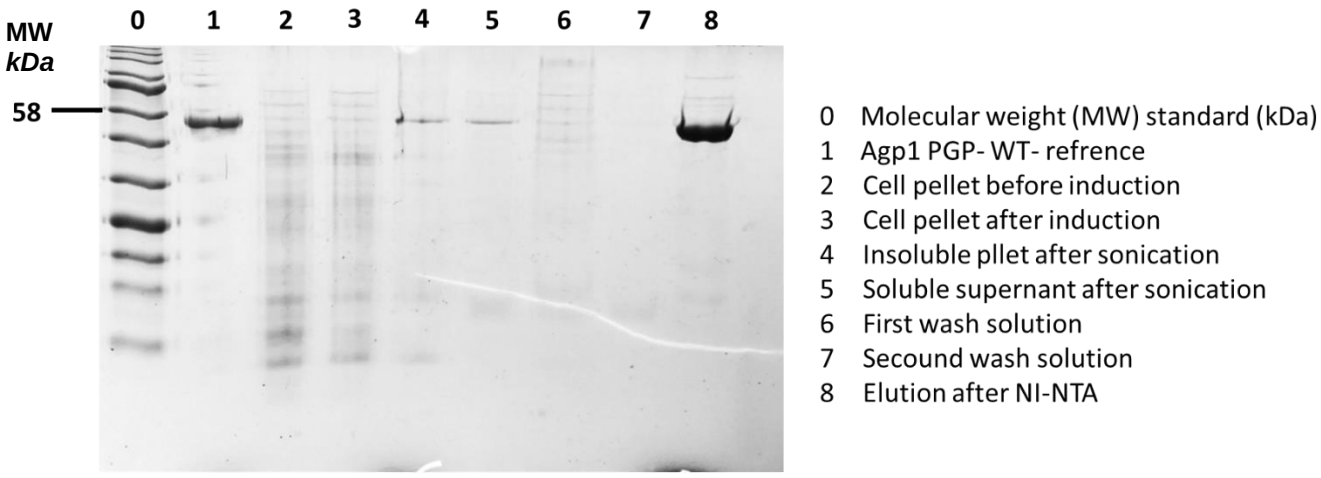

Figure 3-4: SDS-PAGE gel for analyzing the protein expression. MW molecular weight.

and the absorption was measured at 280 nm using Nanodrop (Thermo Scientific). **Fig. 3-5** shows the SDS-PAGE gel of each step: cell pellet before and after induction, insoluble pellet and soluble supernatant after sonication, first and second wash, and elution after Ni-NTA. Agp1 WT with a molecular weight of 54 *kDa* was used as a reference (**Fig. 3-4**).

Chromophore binding: PCB and BV were dissolved in dimethylformamide (DMF) and diluted to standard buffer to have only 0.1% DMF in final solution. 3-fold chromophore in standard buffer (300 mM NaCl, 50 mM Tris pH 7.8) and DDT (to have final concentration of 50 mM) were added to the apo-protein in dark,

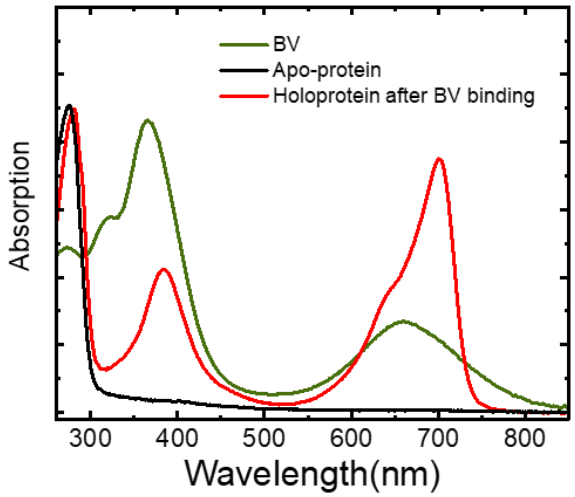

Figure 3-5: UV-vis absorption of BV and apo and holoprotein of Agp1 PGP. The spectra are normalized in the maximum absorption of the specific peak of 280 nm.

and it was stored over-night in ice. The purification was done using Sephadex G25 column (chromatographic methods). The quality of purification and the photoconversion was tested with UV-vis absorption (**Fig. 3-5**).

3.2.10 Site-directed labeling of proteins

Fluorescent dyes are the powerful tools to reveal different biophysical problems. The dyes act as a probe, which enable to reveal information about the direct environment of the probe. One method that accomplishes this and allows site-specific testing is the site-directed labeling of the proteins. The dye is bound to an amino acid of the protein. For this purpose, we can use the dyes with a molecular group which allows the dye to bind to a group of the protein or an amino acid. The linkers such as iodoacetamide or maleimide groups are the example of these molecular groups. These linkers bind specially to the SH group of cysteines and thus at a precisely defined position of the protein. However, each cysteine is a potentially possible target for the dye, which requires a careful characterization of the protein in advance. The process for labeling a protein with a dye is very simple in principle: the protein and the dye are incubated for a sufficient incubation time according to the required conditions, and the dyes which are not bound to the protein are separated. This is necessary because, the free dye not bound to the protein, would interfere during the measurement. The protein concentration to the dye concentration ratio, temperature, pH, salt concentration and the incubation time can influence on the rate of bond dyes to the proteins. A long incubation time as well as a high dye concentration increase the likelihood that the dye will nonspecifically bind to the protein. For this reason, the incubation time and dye concentration must be controlled to avoid nonspecific labelling. To label the proteins the cysteine is chemically reduced using Dithioreitol (DTT) to enable the reaction with the linker. After adding 1-fold protein and 2-fold DDT to 10-fold dye in dark (green background light) the final solution was superimposed with argon and protected from the light in a dark can. Free dyes were separated from the labeled protein by using 5 ml Sepharose (Sephadex G 25 fine) plastic column (Biorad). The column was rinsed three times with water and three times with buffer. Buffer or the mixture of substances, however, driven by the gravity, flow out of the column are collected in various fractions. As a rule, the column must be repeatedly rinsed with buffer after the addition of the mixture of substances so that the substances to be separated pass through the column. The labeling stoichiometry is highly dependent on the given reaction time, temperature, dye concentration and accessibility of the cysteine. It can be calculated as follows:

$$\frac{C_{Label}}{C_{Protein}} = \left(\frac{A_{Label}}{\varepsilon_{Label}}\right)\left(\frac{\varepsilon_{Protein,Pr}}{A_{Protein,Pr}}\right) \qquad 3\text{-}1$$

where C is concentration, A absorption, and ε extinction coefficient of the labeled dye (Label) and the protein. Pr refers to the Pr state of the protein.

3.2.11 Protein digestion with LysC and Trypsin

Purified Cph1 PGP [10 µg in 50 mM Tris-HCl (pH 7.8)] with 0.1% ProteasMax (Promega) was reduced with 2.5 mM DTT for 1 h at 37 °C and subsequently modified with 10 mM N-ethylmaleimide (NEM; Thermo-Scientific) at room temperature for 4 h. The reaction mixture was then diluted 4-fold with 25 mM Tris-HCl (pH 8.0) and 1 mM EDTA and then was digested with 0.5 µg of LysC (Promega) for 16 h at 37°C. One-fifth of the reaction mixture was purified by C18-ZipTip (Millipore) and analyzed by MALDI-TOF-MS (was performed by Dr. Chris Weise, Freie Universität Berlin Department of Biochemistry). One-half of the reaction mixture was supplemented with 0.5 µg of Trypsin-Gold (Promega) and digested for an additional 16 h at 37°C.

3.3 Steady-state absorption and fluorescence emission spectroscopy

UV-2450PC dual-beam UV-vis scanning spectrophotometer (Shimadzu, Japan) in parallel mode was used to perform steady-state absorption measurements. The sample was measured in 3×3 mm quartz cuvettes (Hellma, Germany). The concentration c of a given solution was defined using BBL law:

$$\boldsymbol{A_\lambda = \varepsilon_\lambda \times c \times d} \qquad 3\text{-}2$$

where ε_λ is the wavelength dependent molar extinction coefficient, A_λ is the optical density and d is the path length. Steady-state emission fluorescence measurements were recorded with a SPEX Fluoromax 3 spectrophotometer (HORIBA Jobin Yvon, Japan) in L-format configuration using the DataMax Software Version 2.20.

3.3.1 pH titration

The titration was performed by mixing a base buffer (Tris pH=11) and an acidic buffer (Tris/Hcl pH =5). The concentrated protein was added equally to each aliquot of buffer with desired pH. This way is safe due to the protein reaction to the high concentrated base or acid which results aggregation or denaturation of the protein. The concentration should be constant for each pH, this was in tracking by the absorption of the protein at 280 nm which is not affected by pH. The final pH was measured using the pH meter at 20°C. The pH meter was calibrated before measurement, using the solution of pH 7 and pH 10.

3.4 Transient absorption spectroscopy (Flash photolysis)

Transient flash absorption spectroscopy measures the difference in absorption within a period of time after the excitation of the molecule. Two different sources of light are used in this method of spectroscopy, one is usually a pulse laser to excite the sample, and the second is a continuous light source to measure the absorption changes. Here in this work, a new flash photolysis laser setup was used that was implemented during the doctoral work of Jens Balke in AG Alexiev. The excitation flash is generated by means of a pump laser Nd:YAG Laser (Surelite EX, Amplitude) which is excited at 355 nm. The laser pulse has a pulse length of approximately 3 ns, a high pulse energy of 230 mJ. To tune the emission wavelength an optical parametric oscillator (OPO) (Horizon, Amplitude) was used. In this work, the OPO emission was set to 640 nm with a pulse energy of 20-30 mJ. In order to resolve the changes in absorption, in time-resolved absorption spectroscopy the sample is irradiated with monochrome light with the intensity of I_0 before interacting with the sample and it is compared with the transient light as follows:

$$\Delta A = \ln\left(\frac{I_0}{I(t)'}\right) - \ln\left(\frac{I_0}{I(t)}\right) = \ln\left(\frac{I_0 \cdot I}{I' \cdot I_0}\right) = \ln\left(\frac{I(t)}{I'(t)}\right) \qquad 3\text{-}3$$

where I the intensity of light before the excitation and I' is the intensity of light after the excitation. If a photomultiplier is used to measure the light intensity, then in this case, **Eq. 3-3** can be written as:

$$\Delta A = \ln\left(\frac{V_0}{V}\right) \qquad 3\text{-}4$$

where the photomultiplier voltage before the excitation is V_0 and after the excitation is V, which is proportional to the light intensity I. The program uses a logarithmic time base which presents the transient absorption changes from the nanosecond to second time. The pulsed laser is controlled by a pulse generator (9200+ Sapphire, Quantum Composers) with constant flash lamp discharge signal. Using a constant time delay of 211 µs for the q switch signal to activate a single pulse allows for constant energy levels of the pulses. In the excitation beam path, a part of the laser beam is separated by means of a partially transparent mirror (5%) and directed onto a photodiode (DET 210, Thorlabs). If the beam hits the photodiode, a square-wave voltage pulse is given to National instrument card acting as the start signal. The excitation beam path is perpendicular to the measuring light beam path (**Fig. 3-6**). A 100 W halogen white lamp was used as the measuring light. An infrared filter (IF) and a monochromator ensure that only light of a certain adjustable wavelength hits the sample. The monochromatic light passes through a polarization filter and is focused on the sample by a lens. After passing through the sample, the measuring light is focused on a photomultiplier by another lens. In order to filter out any scattered radiation and the excitation laser flash, another monochromator is installed in front of the photomultiplier (**Fig. 3-6**) and also at the excitation wavelength

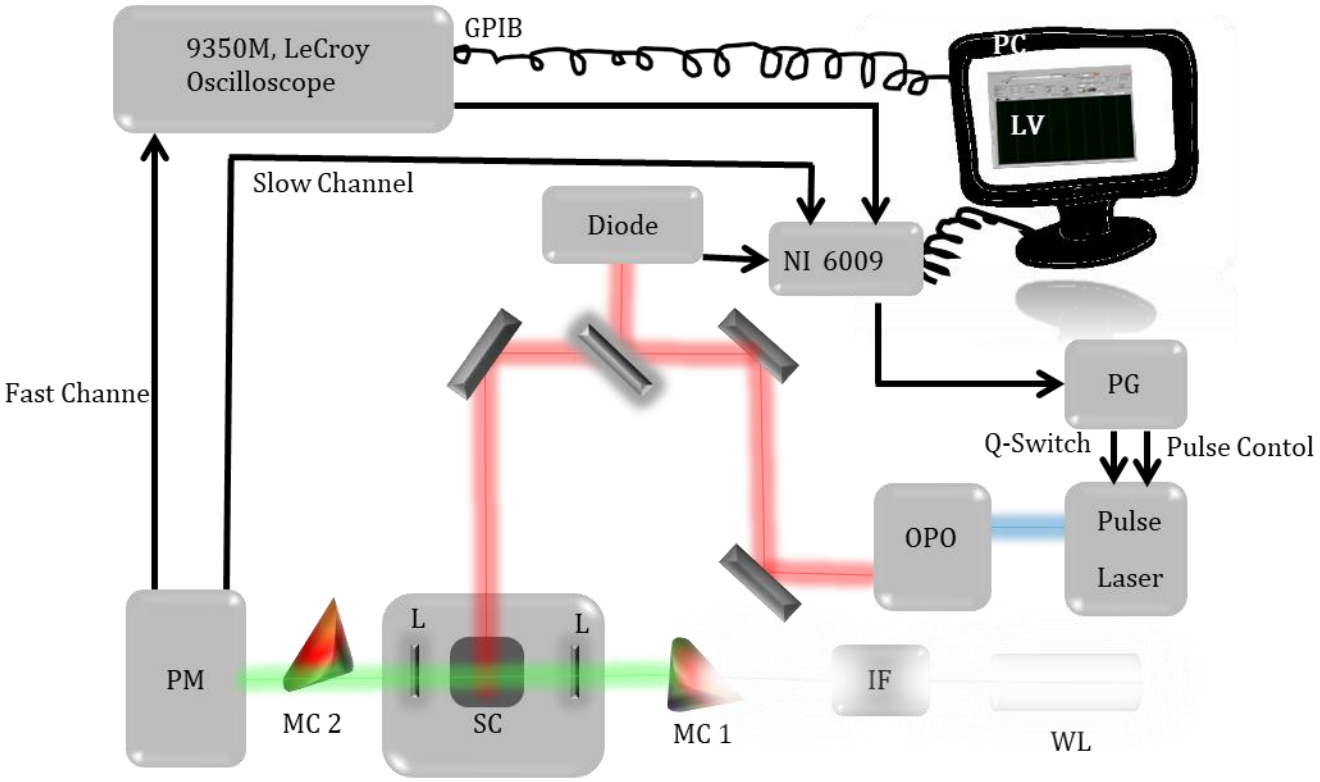

Figure 3-6: Schematic of the Flash Photolysis setup. The measurement is started at the same time as the laser excites the sample. The sample is irradiated with monochrome light and the change in its absorption is measured by a photomultiplier. The measuring beam path runs perpendicular to the excitation beam path. Abbreviations: general purpose interface bus (GPIB) optical parametric oscillator (OPO), pulse generator (PG), white lamp (WL), infrared filter (IF), monochromator (MC), lens (L), sample in cuvette (SC), photomultiplier (PM), National instrument card (NI), LabVIEW (LV). The laser setup was implemented by Jens Balke in AG Alexiev.

of 640 nm and the absorption wavelength of above 650 nm, long glass filer pass of LP655 was used. A photomultiplier tube (PMT, S4710, Hamamatsu) recorded changes at specific absorption. The photomultiplier translates the incoming light into a time dependent voltage signal. Two different channels are used for different time resolutions. Each of these channels is amplified separately and can be smoothed by a variable RC element. One of the two measurement channels, the "fast channel" of the flash photolysis measurement setup, is used for the measurements in the ns /µs range. The channel leads to a storage oscilloscope (9350M, LeCroy), which can record the voltage changes up to 500 MHz. This corresponds to a resolution Δt of up to 2 ns. The information is than passed on to the LabVIEW program using the National instrument card GPIB (general purpose interface bus). The second channel, the "slow channel", is measured by a measurement card (NI-6009, National Instrument) connected to the measurement computer with up to 48 kHz. This corresponds to a resolution Δt of approximately 20.83 µs. The time constant of the low-pass

filter can be changed for each channel independently of the other with twelve different settings. For the measurements in this work, the settings for the “fast channel” were 5 ns and for the “slow channel” 2 ns. The data are obtained from a LabVIEW measurement program (Frank Shüler Diploma 2011 and Jens Balke in AG Alexiev) averaged to 100 points per decade and added together. Several of these measurements were averaged to form a result graph.

3.5 Time-correlated single photon counting (TCSPC)

Time-correlated single-photon counting (TCSPC) is a very sensitive measuring method used in this study to determine fluorescence lifetime. In this process, the time difference is measured between starting the laser and when the photon is registered by detector. For this purpose, the fluorophore is irradiated with a pulsed light source which mostly is a laser with picosecond or femtosecond pulses and a repetition rate in the MHz range. The intensity of the laser is set in such a way that only one incident at the detector is happening every couple of hundred pulses by the laser. This assures the correct assignment of laser pulse and detector signal. From the activation time of the fluorophore, which can be obtained by a signal of the laser or a photodiode, and the detection time of the photon, the emission time of the photon can be

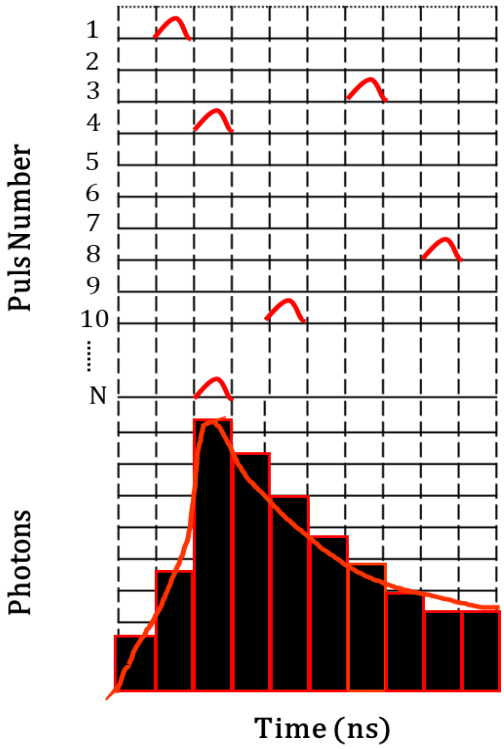

Figure 3-7: Illustration of the measurement principal of TCSPC. For each laser pulse, indicated by the period number, a maximum of one emitted photon per period is detected a certain time after excitation. The countering the corresponding channel is then increased by one. After many detected photons, the photon histogram represents the fluorescence decay curve. Adapted from (Becker, Su et al. 2012).

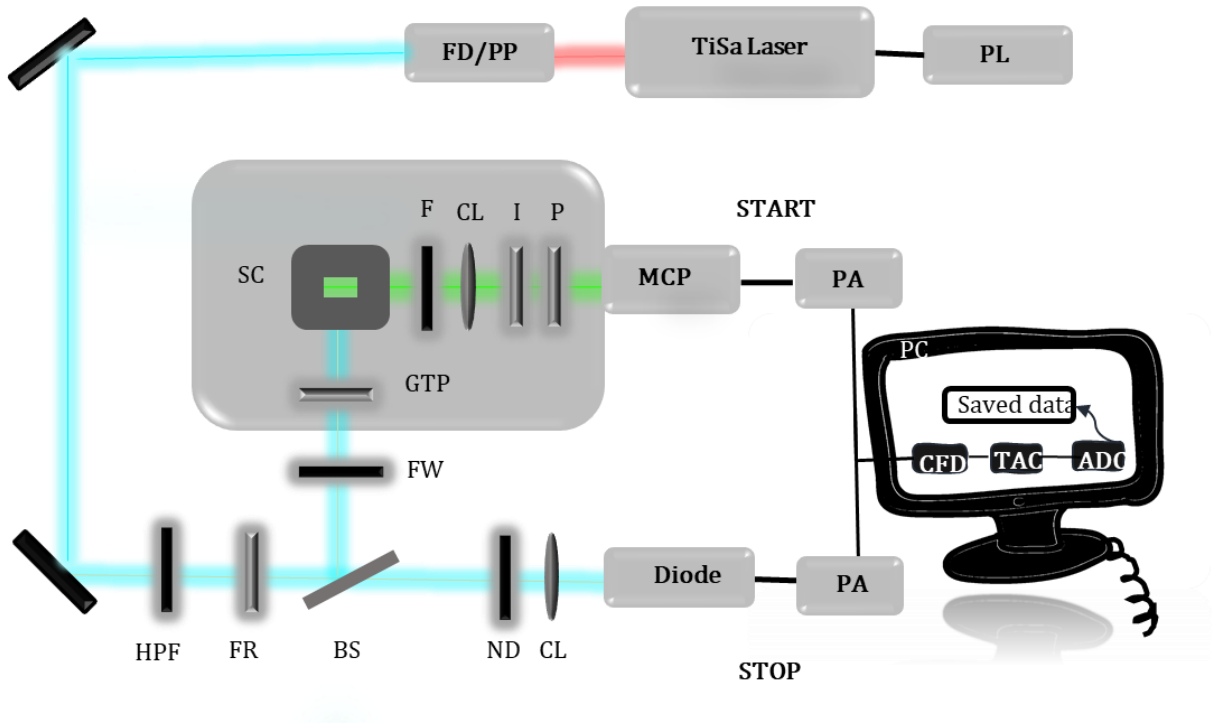

Figure 3-8: Schematic of the TCSPC setup employed. The pulsed laser beam is split into two individual pulses. One triggers a photodiode, while the other excites the sample. An emitted photon hits the detector, and the resulting signal is sent to the TCSPC electronics, where, together with the signal from the diode, the arrival time t of the photon is determined and placed into the intensity-time-histograms. Abbreviations: diode laser (DL), frequency doubler (FD), pulse picker (PP), high-pass filter (HPF), Fresnel rhomb (FR), beamsplitter (BS), neutral density filter (NDF), collimator lens (CL), neutral density filter wheel (FW), Glan-Thompson polarizer (GTP), sample chamber (SC), edge filter (F), iris diaphragm (I), polarizer (P), microchannel plate (MCP), preamplifier (PA), constant fraction discriminator (CFD), time-to-amplitude converter (TAC), analog-to-digital converter (ADC) (Alexiev, Rimke et al. 2003).

determined. After many repetition the course of the fluorescence decay and thus the fluorescence lifetime can be determined from the histogram (**Fig. 3-7**) of all collected times. In this work, a home-built ps-titanium sapphire (Tsunami, Spectra Physics) based TCSPC was use (Alexiev, Rimke et al. 2003). The laser is pumped by a 5 W Diode laser (Millenia Vs, Spectra) continuous wavelength laser at 532 nm. By mode coupling, 1.5 ps pulses are generated at 82 MHz. Appropriate pulses are selected, and the frequency is doubled, resulting in 488 nm pulses with a chosen repetition rate of 4 MHz. The laser beam is then directed to the sample located in a cuvette by means of several mirrors. During this time, they pass through a neutral density filter to reduce the intensity and to a Glan-Taylor polarization filter and a Fresnel rhombus switches the polarization of the excitation light from horizontal to linear vertical. To produce the above-described stop pulse, a small portion of the laser pulse is separated by a beam splitter and directed to a photodiode (DET 210, Thorlabs). The photodiode signal is pre-amplified (9369, EG G Ortec) and processed

by a TCSPC card (SPC-830, Becker Hickl) in the computer. The emitted photon from the sample is recorded under a 90° angle and after passing the long pass filter of 512 nm. A movable polarizer (Thorlabs) is used for detection of polarized light with fixed relation to the polarization of the excitation light, i.e., 0° meaning parallel and 90° meaning perpendicular, in order to measure time-dependent anisotropy. In the case of the fluorescence lifetime measurements, the movable polarizer sets to the so-called magic angle at 54.7°, in which light is transmitted independently of the polarization. At right angles to the sample there is a microchannel plate (MCP), which detect the emitted light and send the pre-amplified signal to the TCSPC card. In addition, polarization filter is in front of the MCP. The exact time of arrival of the photon is determined by constant fraction discriminators (CFD). Time to amplitude converter (TAC) is used to determine the start and stop time. An incoming signal triggers a capacitor to start charging and the second signal stops the charging process. Therfore, the charge on the capacitor is directly proportional to the delay time Δt between the two signals. Then the voltage values are sent to the analogue-digital converter (ADC) which are stored as Δt in a histogram. Even though the laser pulse is only 1-2 ps wide, the electronics additionally broaden the signal during processing, leading to a non-neglectable instrument response function (IRF) which is convoluted with the measured fluorescence decay. This is accounted for by recording scattered light pulses which are later used to deconvolute the fluorescence data. In our setup we achieve IRFs with typically FWHM of ~30-40 ps.

3.6 Fluorescence lifetime imaging microscopy (FLIM)

Time-resolved fluorescence measurements were conducted in a home-built FLIM setup (Alexiev, Volz et al. 2017, Volz, Brodwolf et al. 2018) with using time-correlated single-photon counting (TCSPC) method. We saw earlier, TCSPC setup was used for the solution samples in cuvettes (see **Fig. 3.8**), here this method is used to measure the fluorescence decay curves in a spatially resolved fashion, i.e., for each image pixel of a microscope image. For this purpose, the excitation light from a pulsed laser source of a tunable ps-supercontinuum laser (SuperK Extreme EUV3, NKT Photonics, Blokken, Denmark) 19.5 MHz, AOM UV-VIS Select (NKT Photonics, Birkerød, Dänemark) is coupled into a confocal scanning unit (DCS120, B&H, Berlin, Germany) and single emitted photons are registered at the detector (**Fig. 3.9**). In this method, the whole sample are not illuminated at once, while only a small portion of the sample (the confocal volume) is illuminated at a given time point. In order to gather information on the whole sample, the confocal volume should be moved across the sample, i.e., scanned (**Fig. 3.9**), and a measurement recorded for each spot. This can be achieved using a Glvo scanner that scan the illumination beam across the sample. The whole image can then be reconstructed from the sequential, individual pixel measurements. Moreover, the setup consists of an inverted Microscope (IX71, Olympus, Shinjuku, Japan), a hybrid PMT detector (HPM100-40, B&H) and TCPSC electronics (SPC150, B&H).

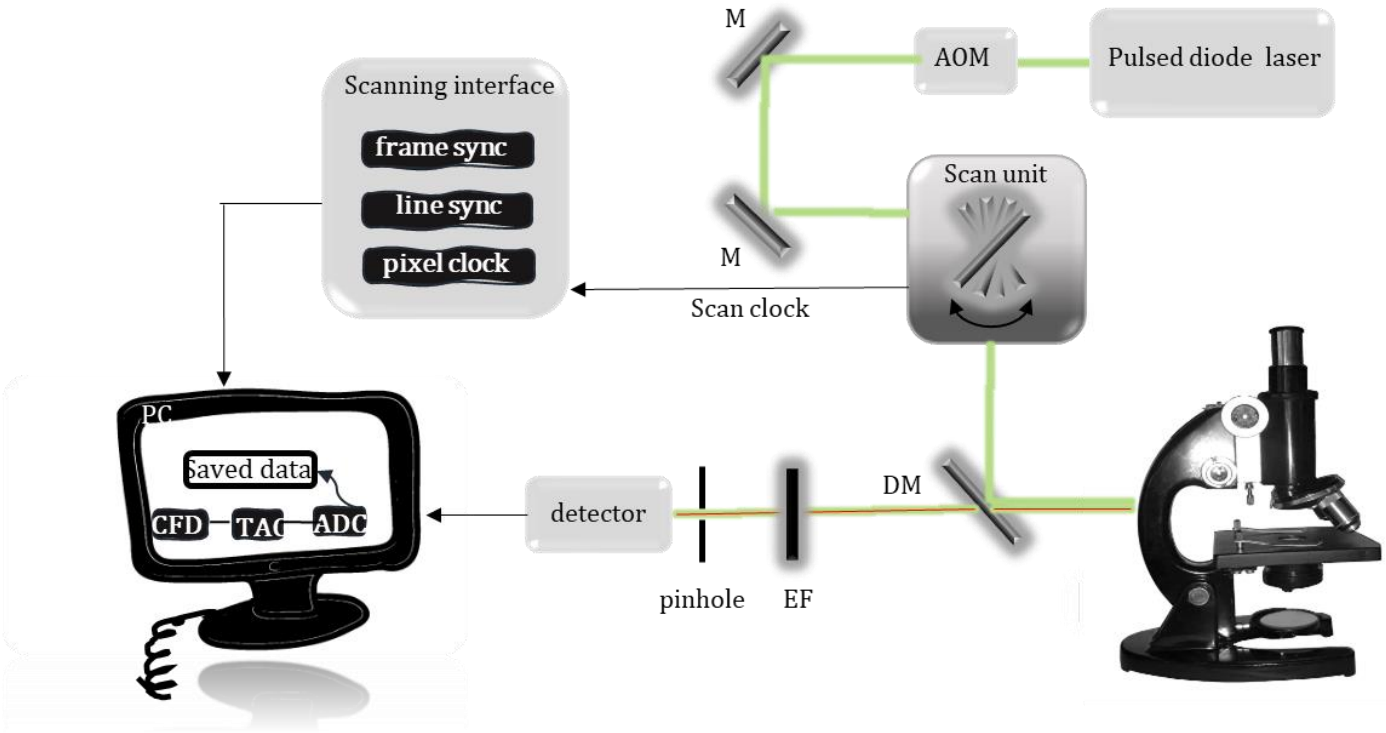

Figure 3-9: **Schematic of the FLIM setup employed.** A pulsed laser beam, from a pulsed diode laser can be coupled into the scan unit. Once coupled into the scan unit the beam is reflected off the dichroic mirror and coupled into the optical port of an Olympus IX-71 inverted microscope. The emission light passes through the dichroic mirror into the emission pathway. The emission light is focused onto a pinhole, thus suppressing out of focus light. The spectral detection range can be selected by a pair of emission filters placed into the light path before the detector. The signal from the detector is then sent to the CFD input of the measurement card. Abbreviations: mirror (M), dichroic mirror (DM), emission filters (EF) (Alexiev, Volz et al. 2017, Volz, Brodwolf et al. 2018)

The FLIM images were recorded using a 40× Objective (Olympus) resulting in a total field of view side length of 450 m. The fluorescent phytochromes were excited at 640 nm using an acousto-optical tunable filter (SELECT UV-VIS, NKT Photonics) at 19.5 MHz. Fluorescence emission was spectrally selected by a long-pass filter with λ_{em}>655 nm (BrightLine HC, Semrock, Rochester, NY). Emitted photons were collected into 1024-time channels with a channel width of 19.5 picoseconds.

3.7 Data analysis

3.7.1 pH-dependent absorption

pH-dependent absorption behavior of a molecule depends on its property regard to its different protonation states. This means the molecule have one or more than one group, in which a proton can associate or dissociate in each group. Due to the proton concentration of the environment, e.g., the pH value, the molecule will consequently be protonated or deprotonated. This can be described with the Henderson-Hasselbalch equation known as the "buffer equation", which results from the law of mass action and the concentration of the free protons in relation to the pK_a of the protonatable groups:

$$\mathrm{p}H = \mathrm{p}K_A + \log_{10}\frac{[A^-]}{[HA]} \qquad 3\text{-}5$$

where $[A^-]$ is the molar concentration of the deprotonated and $[HA]$ is the molar concentration of the protonated form. The pK_a value is thus the pH value at which the concentration of both forms is the same. Due to the different absorption properties of the different protonated forms, the pK_a value can be determined via the absorption spectra. A pH titration of the molecule with an adapted form of the Henderson-Hasselbalch equation follows as:

$$A = \frac{\Delta \mathrm{A}_{\max}}{1 + 10^{pK_A - pH}} + offset \qquad 3\text{-}6$$

where A denotes the measured absorbance (preferably at the maximum). The isosbestic point also results from the titration. This is the wavelength at which the protonated and deprotonated states absorb the light equally. In a titration all spectra, regardless of the pH value, have the same constant absorbance of the molecule at the isosbestic point, which means that all spectra intersect here.

3.7.2 Transient absorption flash photolysis

The absorption changes were recorded as voltage before excitation (U_0) and over time (U(t)). Then the data were processed in a self-written LabView program (by Jens Balke in AG.Alexiev) to calculate the changes in absorption over time (ΔA(t)) as

$$\Delta A(t) = ln\frac{U_0}{U(t)} \qquad 3\text{-}7$$

Single shot experiments are presented, and the transient is fitted by a sum of *n* exponentials with the time constants τ_n of the different intermediates and their respective amplitudes A_n

$$\Delta A(t) = \sum_n A_n e^{t/\tau_n}. \quad 3\text{-}8$$

3.7.3 Fluorescence lifetime fitting

The fluorescence lifetimes and their respective amplitudes follow from fitting I(t) with the model function:

$$I(t) = \sum_i \alpha_i e^{-\frac{t}{\tau_i}} \quad 3\text{-}9$$

where α_i represents the absolute amplitude of the individual lifetimes τ_i. However, for a better comparison between different data sets the absolute amplitudes are often replaced by the relative amplitudes α_i and **Eq.3-9** can be written as

$$I(t) = I_0 \sum_i \alpha_i e^{-\frac{t}{\tau_i}} \quad 3\text{-}10$$

with i the total number of decay components, τ_i the amplitude, and amplitude α_i after deconvolution with the IRF.(Kim, Winkler et al. 2007). The analysis of the time-resolved data (Alexiev and Farrens 2014, Volz, Krause et al. 2016) is based on the mean fluorescence lifetime τ_m calculated by

$$\tau_m = \sum_i^n \frac{\alpha_i \tau_i}{\sum_i^n \alpha_i \tau_i} \tau_i \quad 3\text{-}11$$

3.7.4 Fluorescence anisotropy

Fluorescence decay traces were fitted using **Eq. 3-10**, and fluorescence anisotropy time traces r(t) were calculated from $I_{\parallel}$ (t) and $I_{\perp}$ (t) using **Eq. 2-31**. Anisotropy fit data were acquired using the following model function using the software Globals (Laboratory for Fluorescence Dynamics, University of California, Irvine, CA)

$$r(t) = \sum_{i=1}^{3} \beta_i e^{-t/\phi_i} \quad 3\text{-}12$$

with the initial anisotropy (at t=0) $r_0 = (\beta_1 + \beta_2 + \beta_3)$ (for n =3,(Alexiev, Rimke et al. 2003), identifying the difference in excitation and emission dipole orientation. The rotational correlation times ϕ_1 and ϕ_2 describe the rotational motion of the label and the protein segment to which the labeled is attached. ϕ_3 describes the

rotational diffusion of the whole system. The amplitude ϕ_3 is a measure for the degree of sterically restriction of segment movement imposed by the surrounding constituents of the protein surface. The amplitudes ϕ_1 and ϕ_2 indicate the degree of depolarization of the anisotropy decay components with the correlation times ϕ_1 and ϕ_2, respectively. The conformational space of the protein segment is expressed as relative mobility using:

$$\beta_2' = \beta_2/(\beta_2 + \beta_3) \quad \text{3-13}$$

Assuming the transition dipole moment to diffuse freely inside a given cone with a semi cone angle Θ according to the wobbling-in-cone-model (Kinosita 1997, Schröder 2005), steric restriction can be estimated by

$$\beta_3/r_0 = [\frac{1}{2}\, cos\Theta(1 + \, cos\Theta\,)]^2 \quad \text{3-14}$$

Quality of the fit. The fitting was done by the software Globals (Laboratory for Fluorescence Dynamics, University of California, Irvine, CA). The quality of the respective fit is assessed from the residuals and by the value of the reduced χ^2_{red} as determined from

$$\chi^2_{red} = \frac{\chi^2}{N - M - 1} \quad \text{3-15}$$

Where N is the number of data points, M the number of parameters, and χ^2 as given by

$$\chi^2 \; = \sum_{t\,=\,0}^{N-1} (y_i - y\,(x_i\,, a_0 \ldots \; a_{M-1}))^2 \quad \text{3-16}$$

With the parameters a_i, and y_i and $y(x_i)$ an original data point and the corresponding fit point, respectively.

3.7.5 FLIM analysis

FLIM data were analyzed using self-written routines in C++ (Brodwolf, Volz-Rakebrand et al. 2020). The recorded fluorescence decay traces were fitted using a multiexponential model function. The recorded fluorescence decay traces were fitted using a multiexponential model function **Eq. 3-10** and with n the total number of decay components, τ_i the amplitude, and α_i the fluorescence lifetime of the ith component. The mean fluorescence lifetime τ_{mean} was calculated by **Eq. 3-11**.

3.7.6 Exhaustive error analysis

The fitting procedure above yields the fit parameters and an assessment of the quality of the fit. However, it does not give an accuracy for the individual parameters. The accuracy can be determined through an analysis of the confidence intervals. This must be performed separately for each parameter. The so-called exhaustive error analysis is based upon a sequential analysis of the quality of the fit when varying the parameter under investigation around its optimum value. The parameter under investigation is fixed at a certain value in the vicinity of the optimum and a χ^2_{red} minimization is conducted. Then, the value of the parameter under investigation is slightly shifted and fixed again and a further χ^2_{red} minimization is conducted. Ultimately, the χ^2_{red} can be plotted against the varied parameter and the confidence interval boundaries can then be determined from the intersection with the respective confidence interval level.

To ensure comparability of the confidence interval boundaries between different data sets, the respective χ^2_{red} and number of data points (N) need to be considered in the analysis. The confidence interval boundaries can be obtained from the intersection with the respective confidence interval level, determined from

$$\chi^2_{cl}\,(p,x) = \chi^2_{min} + \frac{\Delta\chi^2(p,x)}{N} \qquad 3\text{-}17$$

where χ^2_{cl} is the χ^2 value for which the parameter under investigation is contained with a given likelihood p. where χ^2_{cl} is the χ^2 value for r which the parameter under investigation is contained with a given likelihood p. The values used for the likelihood p, coincide with those used for the standard deviation σ of the Gaussian normal distribution, i.e., p = 68.27% corresponds to 1σ, p = 95.45% to 2σ and p = 99.73% corresponds to 3σ. The values for $\Delta\chi^2$(p, x) can be calculated from the cumulative χ^2 distribution function, and for a degree of freedom of 1 lead to the following values for the different likelihoods: $\Delta\chi^2$ (σ) = 1.00, $\Delta\chi^2$ (2σ) = 4.00 and $\Delta\chi^2$ (3σ) = 9.00 (Kim and Hanes 2012).The exhaustive error analysis was also performed using the software Globals (Laboratory for Fluorescence Dynamics, University of California, Irvine, CA).

4 Results and Discussion Part I:

Understanding the protonation heterogeneity and its correlation to the photoconversion in the photosensor module of phytochromes.

Part of the results shown in this chapter are published in M.Sadeghi, J.Balke, C. Schneider, S. Nagano, J. Stellmacher, G. Lochnit, C. Lang, C. Weise, J. Hughes, and U. Alexiev. *Transient Deprotonation of the Chromophore Affects Protein Dynamics Proximal and Distal to the Linear Tetrapyrrole Chromophore in Phytochrome Cph1*. Biochemistry 2020, 59, 9, 1051–1062 Publication Date: February 18, 2020, https://doi.org/10.1021/acs.biochem.9b00967

Both Cph1 and Agp1 are canonical bacterial phytochromes, which bind to the chromophore PCB and BV, respectively (**Fig. 4-1**). However the protonation heterogeneity was observed in the Pr state of Cph1 (Escobar, Lang et al. 2017, Sadeghi, Balke et al. 2020), similar to the plant phytochromes (Sineshchekov 1995), and no heterogeneity was observed in Agp1 (Borucki, von Stetten et al. 2005). To test the hypothesis that Pr protonation heterogeneity depends on the chromophore type, Agp1 PGP was genetically engineered for a covalent PCB-binding and was characterized. Further the results were compared to the non-covalent PCB-binding and covalent BV-binding. Also, the Cph1 mutants which are known to be poorly photoactive, such as Y176H (Fischer and Lagarias 2004) and Y263S, were characterized to examine the relation between the photoconversion ability to the Pfr state and the Pr protonation heterogeneity. Moreover, the protonation heterogeneity was investigated in Cph1 PG, which lacks the PHY domain, in order to test the effect of PHY domain deletion on Pr protonation heterogeneity.

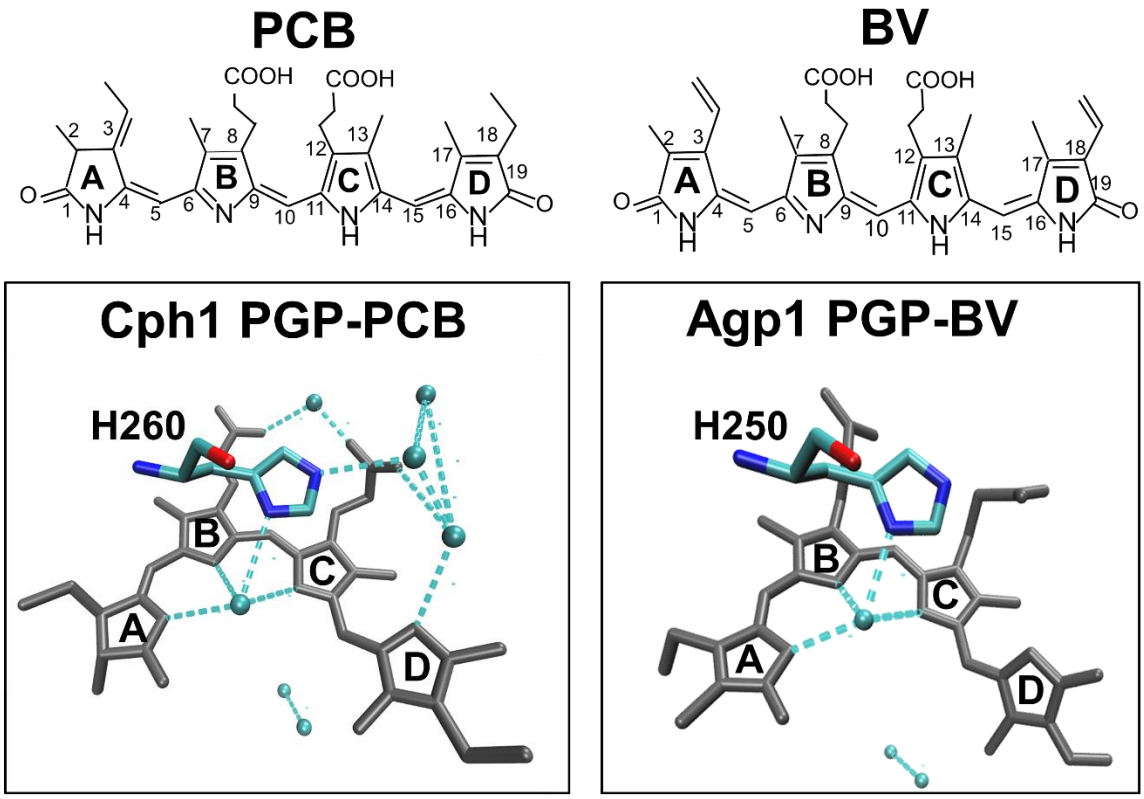

Figure 4-1: The top panel shows the chemical structure of PCB and BV according to (Lamparter, Michael et al. 2002). The lower panel depicts the structure of PCB in the chromophore binding pocket in Cph1 PGP (left) and the structure of BV in the chromophore binding pocket in the Agp1 PGP (right) including the water molecules (cyan spheres) and the conserved His (H260 in Cph1 and H250 in Agp1). Hydrogen bonds are shown as dashed cyan lines. Cph1 PGP PDB: 2VEA, Agp1 PGP PDB: 5I5L. The images of the chromophore binding pocket were created by VMD.

4.1 PCB adducts of Agp1 PGP WT (non-covalent) and Agp1 PGP V249C (covalent)

The variant Agp1 PGP V249C was created using site-directed mutagenesis as described in Material and Methods. This variant is aligned with residue C295 in Cph1 that provides a covalent bond to PCB in the GAF domain (Lamparter, Michael et al. 2003, Borucki, Seibeck et al. 2009). PCB and BV assembling was performed as described in Material and Method, and further the variants were characterized using UV-vis absorption spectroscopy. The protonation heterogeneity was investigated by determining the pH dependence of chromophore absorption using steady-state absorption spectroscopy.

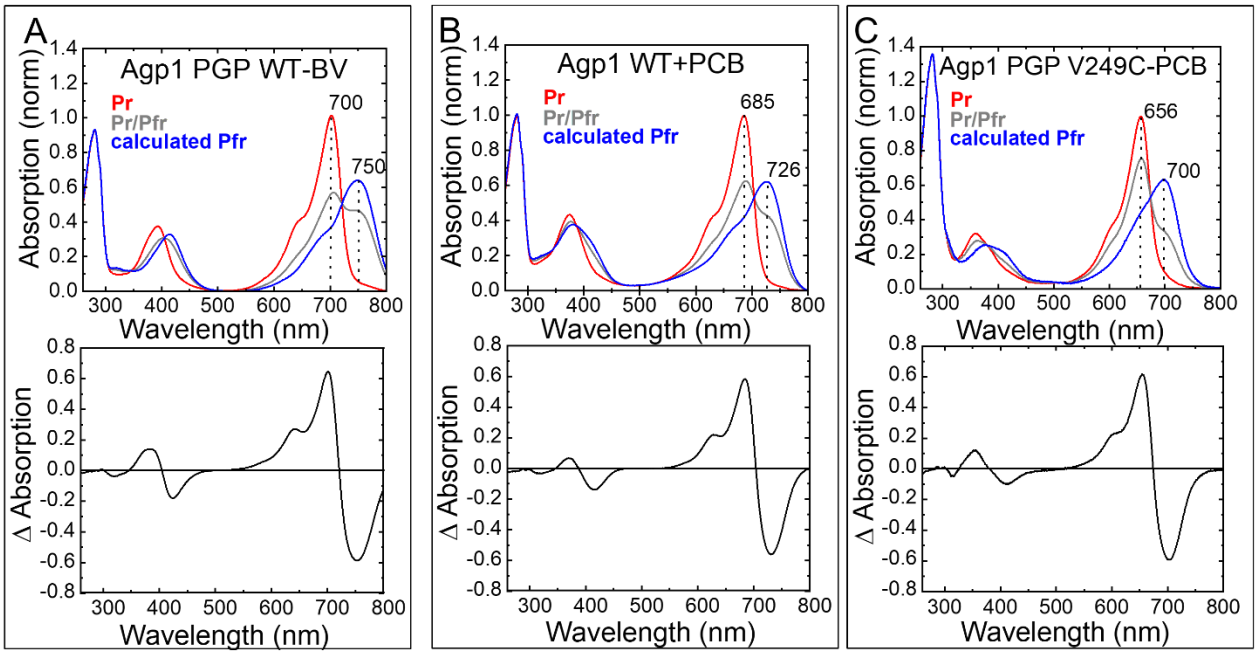

Figure 4-2: UV-vis absorption spectra of BV and PCB adducts of Agp1 PGP WT and variant V249C. Top panels show the Pr state of the adducts in red, the Pr/Pfr state in gray, and the calculated Pfr state according to **Eq. 4-1** in blue. The absorbance maximum at λ_{max}, Pr was normalized to 1. The lower panels show the absorption difference between the Pr state and the calculated (**Eq. 4-1**) Pfr state. **(A)** Agp1 PGP WT-BV (covalent assembling) **(B)** Agp1 PGP WT+PCB (non-covalent assembling) and **(C)** Agp1 PGP V249C-PCB (covalent assembling). Conditions: 50 mM Tris buffer pH 7.8, 300 mM NaCl, at 20ºC.

UV-vis absorption measurement for all the samples was performed under the same condition in buffer: 300 mM NaCl, 50 mM Tris/HCl pH 7.8, at 20ºC, and in background green light. The Pr state for Agp1 WT (BV) and for Agp1 WT+PCB was generated by saturating irradiation using a 784 nm LED (Conrad Electronic), or alternatively waiting long enough in the dark to have the back reaction to Pr. For the Pr/Pfr state a 735 nm LED (Conrad Electronic) was used. However, for Agp1 PGP V249C-PCB, a 735 nm LED (Conrad Electronic) was used to reach the Pr state and a 680 nm LED (Conrad Electronic) to reach Pr/Pfr, similar to the illumination process of Cph1 variants.

Fig. 4-2 shows the absorption spectra of Pr and Pr/Pfr forms of Agp1 PGP WT (BV), and PCB adducts of Agp1 PGP; WT (non-covalent) and V249C (covalent). The extinction coefficient of 90000±5000 $M^{-1}cm^{-1}$ was used for all the variants (Lamparter, Michael et al. 2002, von Stetten, Seibeck et al. 2007) (**Table 4-2**). The absorption spectra of the Pr forms of the covalent and non-covalent PCB adduct differ in the position of their chromophore band by ~ 30 nm (656 and 685 nm for the covalent and non-covalent PCB adduct, respectively), which are identical to that reported previously (Lamparter, Michael et al. 2003) (**Table 4-1**).

This blue shift is caused by saturation of the ring A ethylidene double bond of PCB upon covalent binding (Lamparter, Michael et al. 2003, Borucki, Seibeck et al. 2009). Replacing BV with PCB did not lead to a noticeable change in Agp1 PGP and its mutant variants regarding to the UV-vis spectra in Pr and Pr/Pfr states (**Fig. 4-2, Table 4-1**). **Table 4-1** provided the comparison of the chromophore peaks in Pr and Pfr states for Agp1 PGP with BV and PCB assembling and Cph1 PGP WT. As the Pfr state is not stable to directly measure the absorption spectra, the absorption spectra of the pure Pfr form were calculated under the following assumptions: (i) spectra of the pure Pr form are given by the non-irradiated samples. (ii) the irradiated sample contains Pr and Pfr. (iii) the Pfr form has an absorbance ratio A685 nm/A728 nm of 0.1 in the case of Agp1 WT+PCB (Zienicke, Molina et al. 2013). With these assumptions, data evaluation gave consistent results. When lower or higher A685 nm/A728 nm values were chosen, the calculated spectra had an aberrant shape. Thus, pure Pfr spectra were calculated according to

$$A_{Pfr} = \frac{A - f.A_{Pr}}{1 - f} \qquad 4\text{-}1$$

where *f* is the fraction of Pfr/Ptotal. This value was adjusted until A_{Pr}, A685 nm/A728 nm = 0.1 (Zienicke, Molina et al. 2013).

Table 4-1: Chromophore absorption maxima in nanometer for the red absorbing Pr and Pfr band of Agp1 is bound to BV and PCB and for Cph1 PGP WT is bound to PCB. The *f*-value for calculating the Pfr absorbance spectrum according to **Eq. 4-1** is given. *For comparison the values of Cph1 PGP WT from an earlier work (van Thor, Borucki et al. 2001).

Construct	$\lambda_{max(abs),Pr}$ (nm)	$\lambda_{max(abs),Pr}$ (nm)	*f*	Chromophore type
Agp1 PGP WT	700	750	0.30	BV
Agp1 PGP WT	685	728	0.35	PCB (non-covalent)
Agp1 PGP V249C	656	698	0.60	PCB (covalent)
Cph1 PGP WT*	658	704	0.68	PCB

Table 4-2: Extinction coefficients for Agp1 PGP variants.

Construct	ε at $\lambda_{max(abs),\ Pr}$ at pH 7.8 (M^{-1} cm^{-1})	Reference
WT-BV	90000 ± 5000	(Lamparter, Michael et al. 2002, von Stetten, Seibeck et al. 2007)
WT+PCB	90000 ± 5000	(Lamparter, Michael et al. 2002, von Stetten, Seibeck et al. 2007)
V249C-PCB	90000 ± 5000	(Lamparter, Michael et al. 2002, von Stetten, Seibeck et al. 2007)

pH-dependent UV-vis absorption.

pH-titration was carried out in 300 mM NaCl, 50 mM Tris/HCl buffer for pH 6.2- 9.5, or 100 mM Na_2CO_3/$NaHCO_3$ buffer for pH 9.5-10.8, at 20ºC. The pH was adjusted by adding the concentrated protein in 1 mM Tris/HCl pH 7.8 to the buffer with desired pH. The buffer solutions were prepared at the specific pH point by mixing 50 mM Tris and Tris/HCl for pH 6.2- 9.5 or using 100 mM Na_2CO_3/$NaHCO_3$ buffer at specific pH (9.5-10.8). The absorbance values were scaled to the extinction coefficient ε_{700nm}=90000$M^{-1}cm^{-1}$ for Agp1 PGP variants (Lamparter, Michael et al. 2002) (**Table 4-2**). The measurements were performed under the green light to avoid photoconversion of Pr. The pH titration curves were generated from the respective absorbance values at nine wavelengths 678 - 722 nm. A global fit of the Henderson−Hasselbalch equation (**Eq. 3-6**) was performed using Origin Pro 2019 (OriginLab) and the fit results are summarized in **Table 4-3**. The absorption of the deprotonated chromophore at high pH was estimated to 20% of the maximum absorption of the respective wavelength (von Stetten, Seibeck et al. 2007). **Fig. 4-3** shows the absorption spectra of PCB binding to Agp1 PGP WT (non-covalent binding) and Agp1 PGP V249C (covalent binding), as well as BV binding to Agp1 PGP WT (covalent) at different pH values. The dash black line in **Fig. 4-3** indicated that the maximum absorption wavelength is not pH-dependent in none of the studied cases. However, regarding to the covalent binding of PCB in Agp1 PGP V249C-PCB, a pH-dependence of chromophore λ_{max} was expected for this variant, as it was observed in Cph1 PGP (van Thor, Borucki et al. 2001). Corresponding closely to an earlier study (von Stetten, Seibeck et al. 2007) one p*K* was obtained for Agp1 PGP WT (BV) with p*K* value of 10.70 ± 0.02 (**Fig. 4-3A**. **Table 4-3**).

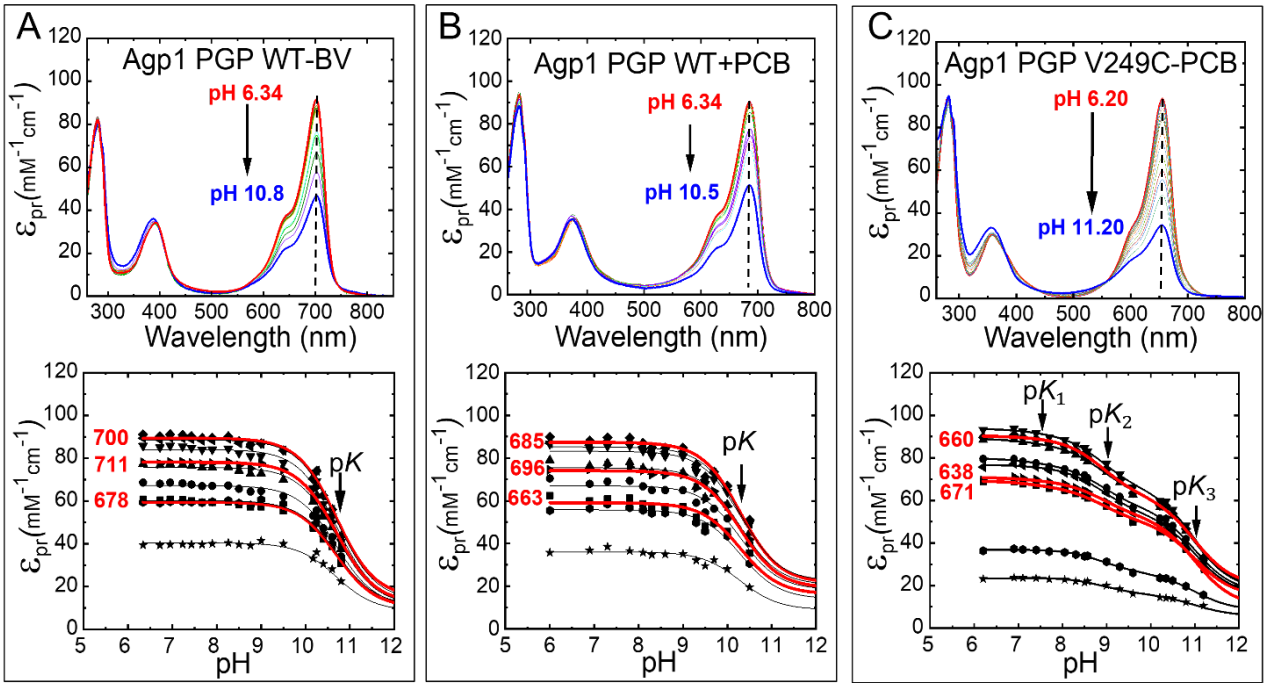

Figure 4-3: pH dependent UV-vis absorption spectra of Agp1 PGP wild type and its variants in Pr. The top panels show the absorption spectra at different pH-values, the direction of the pH-titration is indicated by the black arrow for Agp1 PGP WT-BV **(A)**, Agp1 PGP WT+PCB **(B)**, and Agp1 PGP V249C-PCB **(C)**. The bottom panels show the respective titration data at eight wavelengths. Agp1 PGP WT-BV: 678 (■), 683.5 (●), 689 (▲), 694.5 (▼), 700 (♦), 705.5(◄), 711(►), 716.5 (⬣), and 722 nm (★). Selected fit curves at 678, 700, and 711 nm are marked in red. Agp1 PGP WT+PCB: 663 (■), 668.5 (●), 674 (▲), 679.5 (▼), 685 (♦), 690.5(◄), 696(►), 701.5 (⬣), and 707 nm (★). Selected fit curves at 663, 685, and 696 nm are marked in red. Agp1 PGP V249C-PCB: 638 (■), 643.5 (●), 649 (▲), 654.5 (▼), 660 (♦), 665.5(◄), 671(►), 676.5 (⬣), and 682 nm (★). Selected fit curves at 638, 660, and 671 nm are marked in red. The pH-dependence was fitted by the Henderson−Hasselbalch equation (**Eq. 3-6**) using Origin Pro 2019 (OriginLab) and the fit results are summarized in **Table 4-3**. The absorption of the deprotonated chromophore at high pH was estimated to 20% of the maximum absorption of the respective wavelength) (von Stetten, Seibeck et al. 2007) Conditions: 300 mM NaCl, 50 mM Tris/HCl buffer for pH 6.2- 9.5, or 100 mM Na_2CO_3/$NaHCO_3$ buffer for pH 9.5-10.8, at 20ºC.

Table 4-3: Chromophore p*K* values of Agp1 PGP variants. The spectra and titration curves are shown in **Fig. 4-3**. The standard error is given.

Constructs	pK_1	pK_2	pK_3
	Agp1 PGP		
WT-BV	-	-	10.70 ± 0.02
WT+PCB	-	-	10.31 ± 0.02
V249C-PCB	7.3 ± 0.50	8.90 ± 0.06	11.00 ± 0.03
	***Cph1 PGP**		
in vitro PCB assembling	7.55 ± 0.05	9.5 ± 0.30	-
in vivo PCB assembling	7.6 ± 0.10	9.04 ± 0.02	-

*The values of Cph1 PGP shown for the comparison from (van Thor, Borucki et al. 2001) for *in vitro* PCB assembling and (Escobar, Lang et al. 2017) for *in vivo* PCB assembling .

For Agp1 PGP WT non-covalent PCB-binding, p*K* value of 10.31 ± 0.02 was obtained (**Fig. 4-3B**) which is lower than than the p*K* value of Agp1 PGP BV (**Table 4-3**). The p*K* shift is about 0.4 unit (**Table 4-3**). The evaluation of pH titration of the covalent PCB-binding of Agp1 PGP V249C indicated three p*K* with values of 7.3 ± 0.5, 8.90 ± 0.06, and 11.00 ± 0.03. The first and second p*K* values considering the error value range, are close to the p*K* values which were obtained for Cph1 PGP WT (*in vivo* PCB assembling) (Escobar, Lang et al. 2017). Combination of experiment and theory (resonance Raman/UV-vis spectroscopy and QM/MM calculations) revealed for Cph1 PGP WT that the first p*K* is related to the His260 deprotonation (**Fig. 4-1**), which shows the equilibrium between Pr-I and Pr-II (Escobar, Lang et al. 2017). This led to the proposal that a lowering of the p*K* of His260 during photo transformation is a driving force for proton release monitored in solution (van Thor, Borucki et al. 2001). This residue is conserved in the chromophore binding pocket of Agp1 as well (His 250, **Fig. 4-1**). The covalent PCB assembling of Agp1 V249C seems to lead to the deprotonation of His 250 which was not observed in non-covalent PCB assembling as well as Agp1 PGP WT (BV). The second p*K* of Cph1 PGP indicates the chromophore deprotonation, which was obtained with different p*K* values for *in vivo* PCB assembling and *in vitro* PCB assembling, 9.04 ± 0.02, and 9.5 ± 0.30, respectively (**Table 4-3**). However, the first p*K* was the same in both cases, considering the given error values (**Table 4-3**). Regarding *in vitro* PCB assembling of Agp1 V249C, it was expected that the second p*K* to be closer to the value from *in vitro* PCB assembling of Cph1 PGP, while it is closer to the value of *in vivo* PCB assembling of Cph1 PGP (**Table 4-3).** The CD spectra of non-covalent PCB adducts showed high similarities with those of the covalent BV adducts (Borucki,

Seibeck et al. 2009). In comparison, the covalent PCB adduct revealed a significant difference in those of non-covalent PCB adducts (Borucki, Seibeck et al. 2009). The resonance Raman spectroscopy study on Agp1 PGP V249C-PCB indicated the high vibrational similarity in HOOP and C=C stretching region of this variant to the plant phytochrome phyA (Velazquez Escobar, von Stetten et al. 2015). Also, they showed the structural heterogeneity of the Pfr state of this variant similar to the PCB and PΦB-binding phytochromes such as Cph1 and plant phytochrome. However, there has not been any study on the structure heterogeneity of this variant in Pr state as it was proved for Cph1 and plant phytochromes. The previous resonant Raman spectroscopic studied on the PCB adducts of phytochrome illustrated the similar spectroscopic features of all studied cases including Agp1 V249C-PCB binding, which confirmed the important role of chromophore and chromophore position in the vibrational signature of phytochromes in Pfr state (Velazquez Escobar, von Stetten et al. 2015).

4.2 Cph1 PGP variants Y176H and Y263S

Fig. 4-4A, B shows the location of Y176 and Y263 in the chromophore binding pocket of Cph1 PGP. These two tyrosines are conserved among the phytochrome family. In the Pr state, Y263 has a hydrogen bond to the structure water molecule, which connects rings A, B and C, and Y176 has a hydrogen bond to two structure water molecules (**Fig. 4-4A, B)**. However, Y176 can make a hydrogen bond with the ring D after photo-flipping in the Pfr state (Song, Psakis et al. 2011). It has been shown that the mutation of Y176 to histidine can interfere with the photoconversion (Fischer and Lagarias 2004). In this present section, first the variants Y176H and Y263S were characterized using steady-state and time-resolved absorption spectroscopy. Then protonation heterogeneity was investigated using pH-dependent steady-state absorption spectroscopy.

Steady-state absorption characterization.

UV-vis absorption measurement for all the samples was performed under the same condition in buffer: 300 mM NaCl, 50 mM Tris/HCl pH 7.8, at 20ºC, and in background green light. The extinction coefficient of the variants and their reference were summarized in **Table 4-4**. The UV-vis absorption of Y176H and Y263S variants in the illuminated state indicated that the photoconversion is interfered and trapped in a Pr-like state (**Fig. 4-4.C**, **D**), in agreement with a previous work (Fischer and Lagarias 2004). These variants can form the dark-adapted state similar to the wild type, while the maximum absorption 16 nm is blue shifted to 642 nm. The circular dichroism (CD) spectroscopy indicated a hypsochromic shift under denaturing acidic condition of Cph1 WT as isomerization results in the photo-flip of D-ring (Song, Psakis et al. 2014). The acid denaturation assay confirms for the variant Y263F after red light irradiation, like the WT, a 15Za to 15Ea geometry change takes place (Song, Psakis et al. 2014). In contrast, the Pr-like

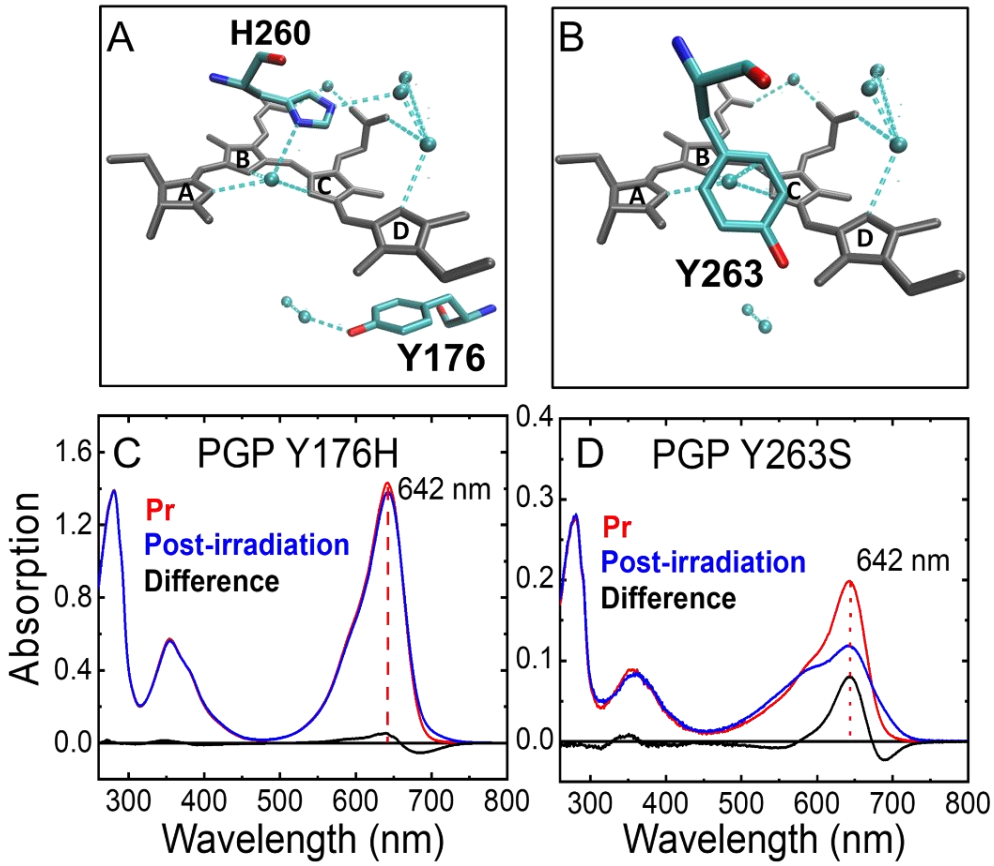

Figure 4-4: Top panels show the chromophore binding pocket of PCB in Cph1 PGP including the water molecules and the residues **(A)** H260 and Y176 and the residue **(B)** Y263. Cph1 PGP PDB: 2VEA. The images were created by VMD. The bottom panels show the absorption spectra of the dark-adapted (Pr) state in red, the red illuminated state with LED 730 nm in blue, and the difference absorption between the dark and illuminated state in black for (**C)** Cph1 PGP Y176H and (D) Cph1 PGP Y263S. Conditions: 300 mM NaCl, 50 mM Tris buffer pH 7.8, at 20ºC.

absorption peak of Cph1 PGP Y176H hardly changes upon irradiation, Pfr formation is almost undetectable as previously shown (Fischer and Lagarias 2004, Fischer, Rockwell et al. 2005). The absorption maximum of the Pr-like state under acid-denatured conditions is identical to that of WT, indicating *15Za* geometry. After red light irradiation followed by denaturation the spectra were virtually unchanged, consistent with the loss of photoconversion. Additionally, the CD signal for Cph1 PGP Y176H in the Pr state is identical to that of WT in Pr state (Nagano, Sadeghi et al 2022), indicating that the chromophore *D*-ring is still α-facial. The lack of photoconversion in Cph1 PGP Y176H shows the important role of position Y176 in the early Pr to Pfr photoconversion events, in agreement with the pioneering work on this Cph1 variant (Fischer and Lagarias 2004, Fischer, Rockwell et al. 2005) and work on homologous mutants in plant phytochromes (Su and Lagarias 2007) and bacteriophytochrome from *Deinococcus radiodurans* (*Dr*BphP) (Wagner, Zhang et al. 2008).

Table 4-4: Extinction coefficients of Cph1 variants.

Construct	ε at $\lambda_{max(abs),\ Pr}$ at pH 7.8 (M^{-1} cm^{-1})	Reference
PGP WT	85000	(Escobar, Lang et al. 2017, Sadeghi, Balke et al. 2020)
PGP Y176H	73000	(Fischer and Lagarias 2004)
PGP Y263S	86000	S. Nagano, personal communication
PG WT	41500	(Sadeghi, Balke et al. 2020)

Time-resolved absorption characterizations.

In addition to the steady-state absorption characterization, the time-resolved absorption spectroscopy was utilized to follow photoconversion directly (**Fig. 4-5)**. Photo-transformation properties of the variants Cph1 PGP WT, Y263S and Y176H were studied with respect to their kinetic and spectral characteristics during the Pr to Pf transition by flash-photolysis measurements. The samples were excited in the dark-adapted Pr-state with a single 3 ns laser pulse at the excitation wavelength λ_{ex}= 640 nm. The samples were measured under the same conditions: 40 µM WT (Y263S or Y176H) in 150 mM NaCl, 50 mM Tris buffer pH 7.8, 20°C.

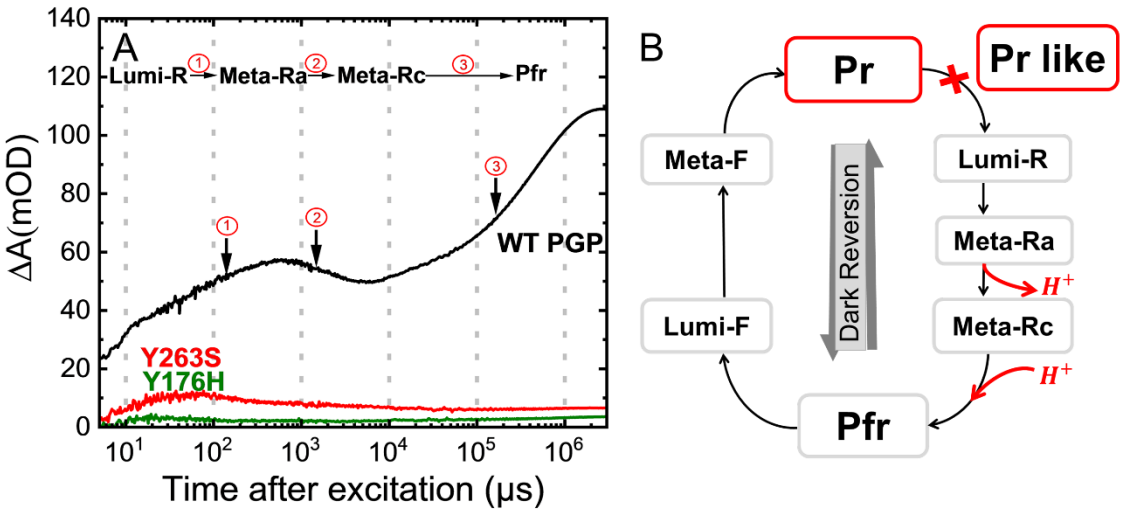

Figure 4-5: (A) Flash photolysis absorption difference transients of Cph1 PGP WT and the mutants Y176H and Y263S at 705 nm. Cph1 PGP WT is shown in black, Y263S in red and Y176H in green. The samples were excited in the dark-adapted Pr-state with a single 3 ns laser pulse at the excitation wavelength λ_{ex}= 640 nm. The different steps of the photocycle are indicated. Measurement conditions: 40 µM WT (Y263S or Y176H) in 150 mM NaCl, 50 mM Tris buffer pH 7.8, 20°C. **(B)** Photocycle scheme of cyanobacterial phytochromes from Pr to Pfr state, including the intermediate states Lumi-R, Meta-Ra, and Meta-Rc, and from Pfr to the Pr state, including the intermediate states Lumi-F and Meta-F. The photocycle of the mutant variants Y176H and Y263S is stopped mainly in a Pr-like state and the photoconversion is not completed as indicated by the red cross.

Table 4-5: Fit results of absorption difference Pr →Pfr transients of Cph1 PGP WT and variants with a sum of 5 exponentials as shown in Fig. 4-5 A. The standard error is given. For comparison the time constants in **Fig. 4-5**, time traces are shown for these samples at the characteristic wavelength 705 nm. The absorbance difference transient shows that photoconversion is blocked early on in both Y176H and Y263S mutants. Moreover, the time trace was fitted exponentially using origin program based on **Eq. 3-8**. *The transient results of WT at 705 nm from an earlier work (van Thor, Borucki et al. 2001) are given and show the agreement with literature values.

Cph1 PGP	τ_1 (µs)	τ_2 (µs)	τ_3 (ms)	τ_4 (ms)	τ_5 (ms)
WT	7.9 ± 0.3	149 ± 4	2.1 ± 01	21 ± 2	483 ± 5
Y263S	4.4 ± 0.8	200 ± 15	-	15 ± 3	310 ± 50
WT*	4.9	190	2.4	36	460

In **Fig. 4-5**, time traces are shown for these samples at the characteristic wavelength 705 nm. The absorbance difference transient shows that photoconversion is blocked early on in both Y176H and Y263S mutants. Moreover, the time trace was fitted exponentially using Origin program based on **Eq. 3-8** as described in Material and Methods. The fit results of WT and the variant Y263S were summarized in **Table. 4-5**. For wavelengths close to λ_{max} of Pr the measuring light contributed to the Pr to Pfr transition in the slowest time domain (>500 ms), therefore the analysis was limited to a 500-ms time window. The slow time constant was consequently τ_5 (~ 500 ms) less determined than the time constants of the faster components.

pH dependent UV-vis absorption.

pH-titration was carried out in 300 mM NaCl, 50 mM Tris/HCl buffer for pH 6.2-9.5, or 100 mM Na_2CO_3/$NaHCO_3$ buffer for pH 9.5-10.8, at 20ºC. The pH was adjusted by adding the concentrated protein in 1 mM Tris/HCl pH 7.8 to the buffer with desired pH. The buffer solutions were prepared at specific pH point by mixing 50 mM Tris and Tris/HCl for pH 6.2-9.5 or using 100 mM Na_2CO_3/$NaHCO_3$ buffer at specific pH (9.5-10.8). The absorbance values for each variant were scaled to the extinction coefficient values listed in **Table 4-4**. The measurements was performed under the green light to avoid photoconversion of Pr (van Thor, Borucki et al. 2001). The pH titration curves were generated from the respective absorbance values at nine wavelengths 638 - 682 nm. A global fit of the Henderson−Hasselbalch equation (**Eq. 3-6**) was performed. **Fig. 4-6A** shows the absorption spectra of Cph1 PGP at different pH-values. These data were measured and evaluated by Constantin Schneider (Sadeghi, Balke et al. 2020) and shown here for a comparison. Titration curves from the absorbance changes at nine distinct wavelengths were used to calculate the p*K* values in the Pr state. Two p*K*-values were obtained for Cph1 PGP which agrees with an earlier study (Escobar, Lang et al. 2017) (**Fig. 4-6A**). However, as it was discussed above the second p*K* value is different for PCB-assembling *in vivo* and *in vitro* (**Table 4-3**). **Fig. 4-6B, C** shows the pH-dependent absorption of Y176H and Y263S, respectively. The dashed black line in **Fig. 4-6** indicated pH-dependency of maximum absorption wavelength of Cph1 PGP WT, and pH-independency of this value for Y176H and Y263S. Moreover, the absorption spectra of Y263S variant shows an increase of absorption in the range of 500-580 nm by increasing pH, this phenomenon was observed earlier for *Deinococcus radiodurans* (Rumfeldt, Takala et al. 2019). They revealed the pH-dependency of *Dr*-PSM variant Y263F is simplified due to remove of the hydroxyl group of this residue (Y263-OH), which indicated the role of this group in protonation asymmetry and complexity in WT.

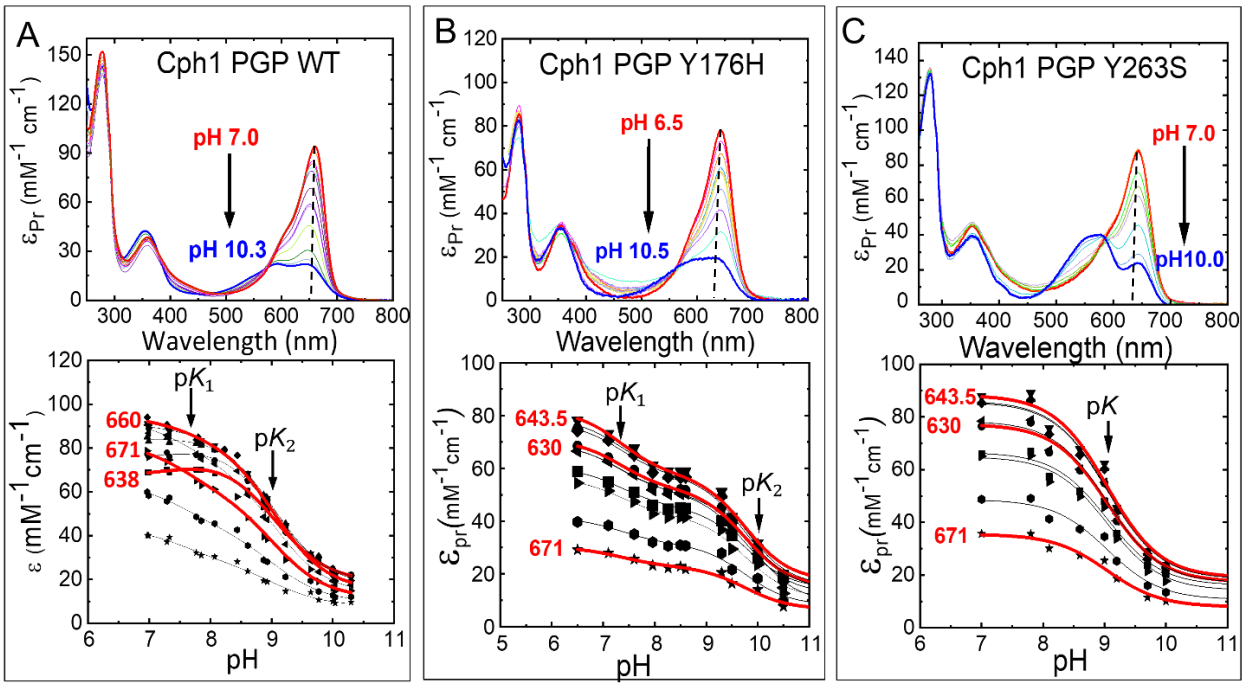

Table 4-6: Absorption spectra of the Pr state of (A) Cph1 PGP WT, (B) Cph1 PGP Y176H, and (C) Cph1 PGP Y263S. The top panels show the absorption spectra at different pH, and the direction of the pH-titration is indicated by the black arrow. The bottom panels depict the respective titration data at nine different wavelengths Cph1 PGP WT**:** 638 (■), 643.5 (●), 649 (▲), 654.5 (▼), 660 (♦), 665.5(◀), 671(▶), 676.5 (⬣), and 682 nm (★). Selected fit curves at 638, 660, and 671 nm are marked in red. Cph1 PGP mutants Y176H and Y263S: **(**622 (■), 630 (●), 638 (▲), 643.5 (▼), 649 (♦), 654.5 (◀), 660 (▶), 666 (⬣), and 671 nm (★)). Selected fit curves at 643.5, 630 and 671 nm are marked in red. The pH-dependence was fitted by the Henderson−Hasselbalch equation (**Eq. 3-6**) in Origin Pro 2019 (OriginLab) and the resulting p*K* values are summarized in **Table 4-7.** Conditions: buffer 300 mM NaCl, 50 mM Tris/HCl at 20ºC. The pH dependent absorption of Cph1 PGP WT was measured by Constantin Schneider in AG Alexiev.

The global fit of the pH curves at nine distinct wavelengths yields two p*K* values for Y176H, pK_1=7.3±0.1 , pK_2=9.76 ± 0.04, and one p*K* value for Y263S p*K*=9.04 ± 0.03 (**Table 4-6**). The first p*K* in Y176H is close to the first p*K* of WT (**Table 4-6**). As we discussed earlier, this p*K* represents the deprotonation of residue His260 (Escobar, Lang et al. 2017). **Fig. 4-4A** shows the location His260 and Tyr176 in the chromophore binding pocket including the water molecule network. It seems that the mutant Y176H did not influence the hydrogen bond connection between His260 and the chromophore or the water molecule. Therefore, this residue still would have the same function in the mutant Y176H similar to WT. However, it shows a different protonation behavior compared to WT, as the pH-curves at difference wavelength are not as complex as WT (**Fig. 4-6A-C** lower panels). We saw earlier this different protonation heterogeneity behavior in Agp1 PGP V249C, in which more than one p*K* was obtained.

It has been shown for Cph1 PGP that a complex titration behavior reflects the protonation equilibrium between Pr-1 and Pr-II via deprotonation of residue His260 (van Thor, Borucki et al. 2001, Escobar, Lang et al. 2017). However, the results from present study show, the protonation heterogeneity can be independent of the complex behavior of the pH-dependent absorption at different wavelengths, and it reflects another event that might be related to the photo-conversion of the protein, as the photoconversion is stopped in a Pr-like state. In the case of Agp1 PGP V249C, that allows the photoconversion, this complexity might be changed due to the different hydrogen bonds and water molecules network in Agp1 PGP (**Fig. 4-1**). As it was shown in **Fig. 4-1**, Cph1 PGP has a more complex water molecule network compared to Agp1, in which the ring D, is connected to the His 260 and the other three rings, A, B, and C, through this network. Mutant Y176H can obviously affect this network due to the direct connection of Tyr 176 to the ring D, thereby the photoconversion is blocked in this mutant. Also, the higher chromophore p*K* value in Y176H compared to WT can be the result of different charge state of histidine compared to tyrosine, which lead to a more positive electrostatic potential in the chromophore binding pocket.

Tyr 263 and His 260 both are connected to a structure water molecule that connected rings A, B and C (**Fig4-4**). The mutation Y263S can affect this network and most importantly the protonation function of His260. This might be a reason that this variant did not show the protonation heterogeneity as His260 might be de-protonated at different pH range. However, the crystal structure of Cph1 PGP Y263F illustrated that this substitution has not changed the structure water molecules network around the D-ring (Mailliet, Psakis et al. 2011). Also, the crystal spectroscopic studies (Mailliet, Psakis et al. 2011) concluded the structure heterogeneity of this variant, although they didn't solve the crystal structure of each subunit.

Table 4-6: The fit results of pH dependent absorption of Cph1 PGP variants. The spectra are shown in **Fig. 4-6**. The standard error is given.

Construct	**pK_1**	**pK_2**
*Cph1 PGP WT	7.6 ± 0.1	9.04 ± 0.02
Cph1 PGP Y176H	7.3 ± 0.1	9.76 ± 0.04
Cph1 PGP Y263S	-	9.04 ± 0.03

*The data shown from (Escobar, Lang et al. 2017) for a comparison .

4.3 Cph1 PG

The highly conserved GAF and PHY photosensory domains in plant and cyanobacterial phytochromes are essential for phytochrome photochemical and photophysical properties (Wu and Lagarias 2000, Oka, Matsushita et al. 2004). In most of the studied phytochrome families, the PHY domain reveals an important role in photoconversion and signaling. A tongue-like hairpin loop (β-sheet conformation in Pr) extending from the PHY to the GAF domain was suggested to play an essential role through sheet-to-helix conversion in conformational changes associated with photoconversion and subsequent signal transmission (Takala, Björling et al. 2014, Schmidt, Sauthof et al. 2018). Thereby, removing the PHY domain would lead to a major change in the function of the protein. The construct Cph1 PG was used to investigate the effect of PHY domain deletion on protonation heterogeneity. First, it was characterized using steady-state UV-vis spectroscopy. Then protonation heterogeneity was studied using the pH-dependent steady-state absorption spectroscopy.

UV-vis absorption measurement was performed in buffer: 300 mM NaCl, 50 mM Tris/HCl pH 7.8, at 20ºC, and in background green light. The absorption of this construct in dark adapted state and in post-irradiation with LED 680 nm (Conrad Electronic), indicates photoconversion inhibition, in which the Pfr state is not formed in this construct (**Fig. 4-7**). The maximum absorption is not red shifted by red light illumination, while it stayed at 645 nm with a decrease in the chromophore absorption (**Fig. 4-7**).

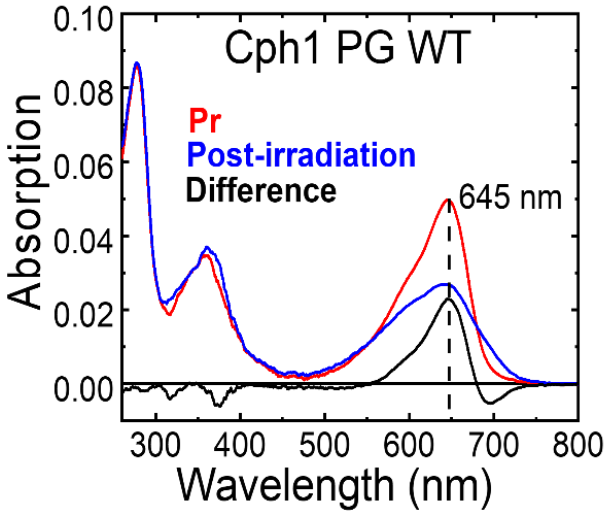

Figure 4-7: UV-vis absorption spectra of Cph1 PG WT. The Pr state of the variants is shown in red, the spectrum after the illumination with LED 680 nm in blue, and the difference absorption spectrum in black. The photoconversion is not completed in this construct and the maximum absorption at 645 nm (dashed line) is shown. Condition: 20 µM of protein in 300 mM NaCl, 50 mM Tris buffer pH 7.8, at 20ºC.

pH dependent UV-vis absorption.

pH-titration was carried out at 20°C in 50 mM Tris/HCl buffer including 300 mM NaCl. The pH was adjusted by adding the concentrated protein in 1 mM Tris/HCl pH 7.8 to the buffer with desired pH. The buffer solutions were prepared at specific pH point by mixing 50 mM Tris and Tris/HCl to have pH from 7 to 9. The Pr state was generated by saturating irradiation using a 735 nm LED. The absorbance values were scaled to the extinction coefficient $\varepsilon_{645\,nm}$ = 41500 M^{-1} cm^{-1} (**Table 4-4**). The measurements was performed under the green light to avoid photoconversion of Pr (van Thor, Borucki et al. 2001). The pH titration curves were generated from the respective absorbance values at nine wavelengths 638 - 682 nm. A global fit of Henderson−Hasselbalch equation (**Eq. 3-6**) was performed.

Fig. 4-8 shows the absorption spectra of Cph1 PG at different pH-values. Interestingly, only a single p*K*-value was apparent from Cph1 PG pH-titration with a value of 8.12 ± 0.06. This p*K* was attributed to chromophore deprotonation which agrees with the absence of a complex wavelength-dependent titration behavior as shown in **Fig. 4-8** by the red highlighted titration curves. Special emphasis is laid on the absence of the absorbance decrease at 638 nm at low pH values for Cph1 PG (**Fig. 4-8**), as we have seen earlier for variants Y176H and Y263S (**Fig. 4-6**). However, in the titration of Cph1 PGP WT, this fact was indicative of a complex titration behavior that stems from the protonation equilibrium between Pr-1 and Pr-II (Sadeghi, Balke et al. 2020). As we discussed earlier this complexity is not necessarily related to the protonation heterogeneity, e.g., in the case of Y176H showed two p*K*, while it lacks this complexity.

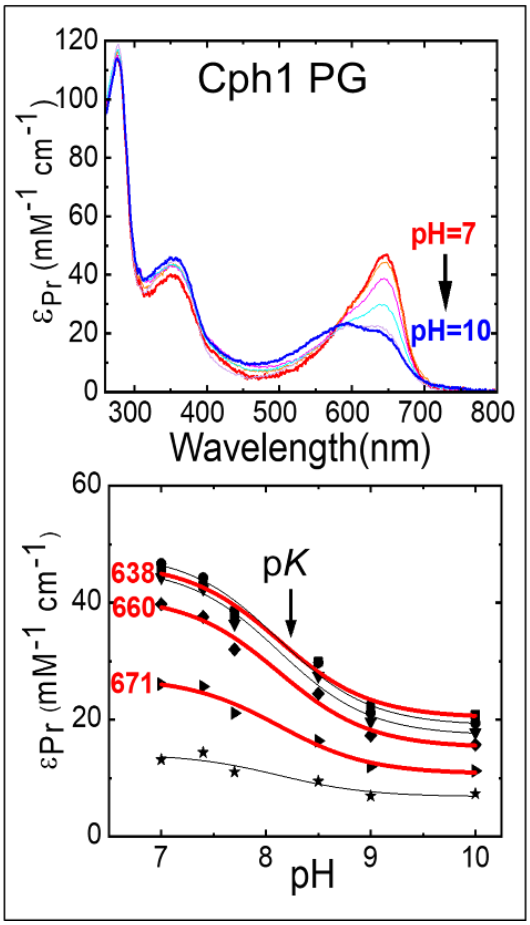

Figure 4-8: pH-dependence of Pr absorption spectra of the Cph1 PG. The top panel shows the pH dependent absorption spectra, the direction of the pH-titration is indicated by the black arrow. The bottom panel shows the respective titration data at six wavelengths (638 (■), 645 (●), 654 (▲), 660 (♦), 671 (▼), and 682 nm (★)). Selected fit curves at 638, 660, and 671 nm are marked in red. The pH-dependence was fitted by the Henderson−Hasselbalch equation (**Eq. 3-6**) in Origin Pro 2019 (OriginLab). The fit yields the following p*K* value of 8.12±0.06. Condition: 300 mM NaCl, 50 mM Tris pH 7.8, at 20ºC.

4.4 Conclusion

The protonation heterogeneity was observed in covalent PCB assembling of Agp1 PGP V249C. In contrast to Agp1 PGP (BV) and Agp1 WT+PCB, UV-vis absorption of the Pr state of Agp1 PGP V249C-PCB (covalent bond) at different pH points indicated the protonation heterogeneity of this variant as was observed for Cph1 PGP. However, V249C-PCB revealed a different protonation heterogeneity behavior compared to Cph1 PGP WT, these differences are as following:

- The chromophore maximum absorption wavelength ($\lambda_{max\ at\ chromophore\ peak}$) of chromophore in Agp1 PGP V249C-PCB is not pH-dependent, while $\lambda_{max\ at\ chromophore\ peak}$ is blue shifted with increasing pH in the case of Cph1 PGP (van Thor, Borucki et al. 2001).
- Three p*K* values were obtained for Agp1 PGP V249C-PCB, while two p*K* values were obtained in the case of Cph1 PGP.

In conclusion, replacing BV chromophore with PCB during the evolution of phytochrome seems to evolve a more advanced photo-biochemical mechanism in the protein by developing the protonation heterogeneity.

The protonation heterogeneity in Cph1 PGP is related to the His260 hydrogen bonds connection and not dependent on the photoconversion. pH-dependent chromophore absorption of two variants of Cph1 PGP, Y176H and Y263S which do not complete the photoconversion, revealed a protonation heterogeneity of variant Y176H with two p*K*, (**Table 4-6**) and a protonation homogeneity of variant Y263S with one p*K* (**Table 4-6**). As it was shown for Cph1 PGP WT, His260 reflects the lower p*K* besides the chromophore p*K* (higher p*K* or the second p*K*), which resulted in the protonation heterogeneity of this construct (Escobar, Lang et al. 2017). Thereby a different hydrogen bonds connection of this residue with chromophore, the conserved water molecule, and the other conserved amino acids in the chromophore binding pocket in these two different mutants lead to the change its protonation function. The mutant Y176H does not effect the protonation heterogeneity, as the mutant has a negligible effect on His260 and its connections. On the other hand, the mutant Y236S destroyed the protonation heterogeneity due to the lack of the connection of Ser263 and His260 via a conserved water molecule. Note, the mutant Y176H reveals a different protonation behavior compared to WT. In contrast to WT whose $\lambda_{max\ at\ chromophore\ peak}$ is blue shifted with increasing pH (van Thor, Borucki et al. 2001), the $\lambda_{max\ at\ chromophore\ peak}$ in Y176H is not pH dependent.

The deletion of PHY domain in Cph1 PGP destroyed the protonation heterogeneity. UV-vis absorption of the Pr state of Cph1 PG at different pH values showed a protonation homogeneity of this construct and yielded only one p*K*. Also, the p*K* value of this PG variant is lower than that of the PGP construct. Removing the PHY domain will consequently delete the tongue-like hairpin loop (β-sheet conformation in Pr) which extends to the GAF domain. The residue Arg472 located in the chromophore binding pocket belongs to the PHY domain (see chapter 2, **Fig. 2-6**). Arg472 makes a salt bridge to Asp207, furthermore the residue Asp207 is connected to the same conserved water molecule as His260 and Tyr263, and to which, as well as ring A, B, and D are connected (see chapter 2, **Fig. 2-6**). Removing the PHY domain and consequently the deletion of the strong salt bridge between Asp207- Arg472 might lead to the following consequences:

- Redistribution of the electrostatics in the chromophore binding pocket, as a positive amino acid (Arg472) is removed, might reduce the chromophore p*K* from 9.04 to 8.12.
- The H-bond network in the chromophore binding pocket including the His260 connection with the chromophore and the conserved water molecule will be interfered. This might be a reason that the first p*K* which refers to the deprotonation of His 260 was not observed in Cph1 PG.

5 Results and Discussion Part II: Study of the protonation-conformation coupling in Cph1 and Agp1 phytochrome and identification of possible correlations between chromophore deprotonation in the Pr state and protein dynamics in the different photosensory domains.

.

Part of the results shown in this chapter are published in M.Sadeghi, J.Balke, C. Schneider, S. Nagano, J. Stellmacher, G. Lochnit, C. Lang, C. Weise, J. Hughes, and U. Alexiev. *Transient Deprotonation of the Chromophore Affects Protein Dynamics Proximal and Distal to the Linear Tetrapyrrole Chromophore in Phytochrome Cph1*. Biochemistry 2020, 59, 9, 1051–1062 Publication Date: February 18, 2020, https://doi.org/10.1021/acs.biochem.9b00967

Despite of numerous research works on structure and function of phytochrome, still there are many unanswered fundamental questions regarding the phytochrome light activation mechanism. For example, still, it is not fully understood how the structural changes in Pr and Pfr are triggered by the light-induced isomerization of the chromophore, although structural differences between Pr and Pfr have been identified in bacteriophytochrome (Takala, Björling et al. 2014). Time-resolved fluorescence anisotropy enables a variety of experiments in which dyes can be used to monitor the conformational dynamics of the protein at a specific location. In this respect, the fluorescence labeling of the different phytochrome constructs provides the opportunity to study local conformational changes that would be hard to study in a crystal structure. Several studies on phytochrome have revealed that proton translocation has a crucial role in coupling chromophore and protein conformational changes (van Thor, Borucki et al. 2001, Borucki, von Stetten et al. 2005, Velazquez Escobar, Piwowarski et al. 2015).

This chapter aims to test the hypothesis whether chromophore deprotonation is coupled to the conformational changes in the different domains, i.e., whether the long-range conformational changes exist and whether a long-range H-bond network connects the PHY domain. The hypothesis will examine for two groups of phytochrome family, photosensor modules of Cph1 and Agp1 which both canonical bacterial phytochromes, binding to the chromophore PCB and BV, respectively. Nanosecond structural dynamics in these variants at the site of fluorescence sensor attachment were investigated by time-resolved fluorescence anisotropy and site-directed fluorescence labelling. Time-correlated single photon counting (TCSPC) and the performed analysis of the anisotropy were described in Material and Methods.

5.1 Covalent labeling of Cph1 and Agp1 with fluorescence sensor dye

5.1.1 Cph1 variants and their spectroscopic characterization

The labeling was performed as described in Material and Methods. The labeling stoichiometry (LS) was calculated using **Eq. 3-1.** The SDS-PAG gel was running to show a covalent bond of the dye to the protein (**Fig. 5-1.C**). In all the labeled proteins, the maximum absorption of -AF is red shifted (~7 nm) compared to the free dye (maximum absorption of free IAF in standard buffer is at wavelength of 490 nm). Cph1 PGP has six natural cysteines, in which C259 is connected to the chromophore and it is not accessible to the dye. While the other five cysteines C49, C120, C289, C305 and C371 can be accessible to the dye (**Fig. 5-1. A**). The LS were between 80 to 100% in Cph1 PGP and the variants. The mass spectrometry indicates the labeling of C120 and C371 in Cph1 PGP WT-AF, and C305 in Cph1 PGP C371S-AF (see the **Fig. A1**, **Table A1)**.

pH-dependence of UV-vis absorption of IAF. IAF absorption is strongly pH dependent (**Fig. 5-2**). The pH-dependence was performed in buffer 300 mM NaCl, 1 mM Tris, at 20ºC. The pH was adjusted using small aliquot of HCl. The maximum absorption at 490 nm (**Fig. 5-2** below panel) was fitted by the Henderson−Hasselbalch equation (**Eq. 3-6**) using Origin Pro 2020 (OriginLab). The obtained p*K* value is 6.45 ± 0.04. A previous study reported this p*K* value for 150 mM NaCl, 6.23 ± 0.01 (Möller and Alexiev 2009). The extinction coefficient of IAF at pH 7.2 is 85000 $M^{-1}cm^{-1}$ according to the provider Invitrogen.

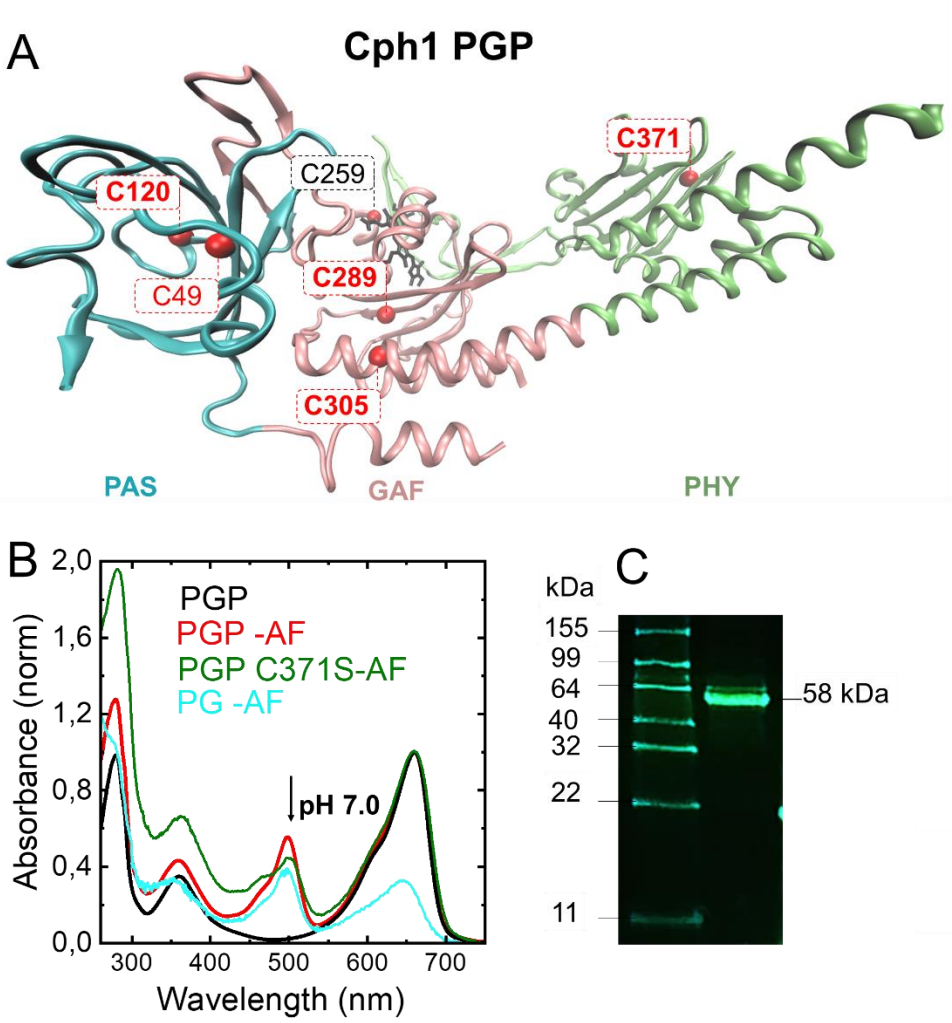

Figure 5-1: Labeling Cph1 PGP with IAF. (A) Structural model of Cph1 PGP (PDB code 2VEA) with accessible cysteines to -AF covalent bond, indicated in red, the Cys is attached to PCB chromophore in black. The PAS, GAF, PHY domains are colored in blue, pink, and green, respectively. The figure was generated by VMD. **(B)** Pr absorption spectrum of Cph1 PGP and Cph1 PGP-AF at pH 7, normalized to the chromophore peak at 658 nm. The labeling stoichiometry is ~75%. **(C)** Tricine-SDS-PAGE gel showing covalent labeling by the fluorescent band of Cph1 PGP-AF at 58 kDa.

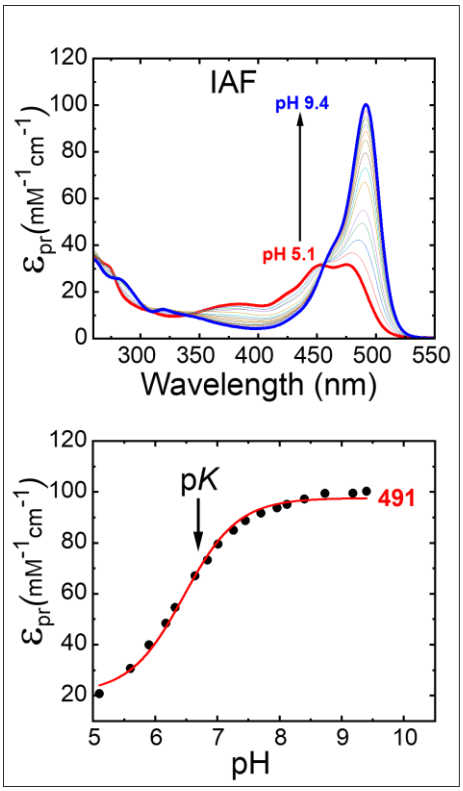

Figure 5-2: pH dependent UV-vis absorption of IAF. The top panel shows the absorption spectra at different pH-values, the direction of the pH-titration is indicated by the black arrow. The bottom panel shows the respective titration data at 491 nm. The pH-dependence was fitted by the Henderson−Hasselbalch equation (**Eq. 3-6**) using Origin Pro 2020 (OriginLab)**.** The obtained p*K* value is 6.45 ± 0.04. The extinction coefficient of IAF at pH 7.2 is 85000 $M^{-1}cm^{-1}$ according to the provider Invitrogen. Conditions: 300 mM NaCl, 1 mM Tris, at 20ºC.

pH-dependence of UV-vis absorption of Cph1 PG-AF. Fig. 5-3A shows the absorption spectra of fluorescein-labeled Cph1 PGP at different pH-values. These data were measured and evaluated by Constantin Schneider (Sadeghi, Balke et al. 2020). Titration curves from the absorbance changes at nine distinct wavelengths were used to calculate the p*K* values in the Pr state. Two p*K*-values were obtained for Cph1 PGP-AF which agrees with an earlier study (Escobar, Lang et al. 2017) (**Fig. 5-3A**). The lower value reflects the protonation equilibrium of H260 with a p*K*-value of 7.6 ± 0.1 that controls the Pr-I/Pr-II transition, and the higher value reflects the equilibrium between Pr-II and the deprotonated chromophore state (Pr-DPC) with a p*K* value of 8.28 ± 0.02 when fluorescein is attached in the PHY domain (**Fig. 5-3A**). Although, the first p*K* value of Cph1 PGP-AF is in line with published data for the Pr-I/Pr-II substate equilibrium of Cph1 PGP WT (Escobar, Lang et al. 2017), the second p*K* differs significantly from the p*K*-value of 9.04 ± 0.02, which was reported previously for Pr chromophore deprotonation (Escobar, Lang et

al. 2017). It has been shown that the C→S substitution in the distant PHY domain (C371S) in Cph1 PGP also reduces the chromophore p*K* to 8.37± 0.03 (**Table 5-1**) (Sadeghi, Balke et al. 2020). Moreover, the labeling of this construct in GAF domain leads to a more downshift of p*K* to 8.10 ± 0.08 (**Table 5-1**) (Sadeghi, Balke et al. 2020). The p*K* values of labeled and non-labeled Cph1 PGP variants are summarized in **Table 5-1**, as well as the calculated ΔpK_{DPC} values for the different constructs with respect to Cph1 PGP WT. These results clearly indicated of existing a long-range effect in all studied Cph1 PGP variants, leading to the significant changes in the chromophore p*K* (Sadeghi, Balke et al. 2020).

In order to compare the chromophore protonation changes as a result of the fluorescein labeling in the PAS/GAF domain, the construct Cph1 PG was evaluated which lacks PHY domain. pH-titration of this variant was carried out at 20°C in 50 mM Tris/HCl buffer including 300 mM NaCl. The pH was adjusted by adding the concentrated protein in 1 mM Tris/HCl pH 7.8 to the buffer with adjusted pH. The buffer solutions were prepared at specific pH point by mixing 50 mM Tris and Tris/HCl to have pH from 7 to 9. The Pr state was generated by saturating irradiation using a 735 nm LED. The absorbance values were scaled to the extinction coefficient $\varepsilon_{645\,nm} = 41500\ M^{-1}\ cm^{-1}$ for Cph1-PG (Sadeghi, Balke et al. 2020). The measurements were performed under the green light to avoid photoconversion of Pr (van Thor, Borucki et al. 2001). The pH titration curves were generated from the respective absorbance values at nine wavelengths 638 - 682 nm. A global fit of the Henderson−Hasselbalch equation (**Eq. 3-6**) was performed. **Fig. 5-3B** shows the absorption spectra of fluorescein-labeled Cph1 PG at different pH-values. Titration curves from the absorbance changes at nine distinct wavelengths were used to calculate the p*K* values in the Pr state. Similar to the non-labeled Cph1 PG (see chapter 4, **Fig. 4-7**), only a single p*K*-value was apparent from Cph1 PG-AF pH-titration, with a value of 7.20 ± 0.04. As we saw earlier for PGP variants, here also the labeling of PG construct consequences a further substantial decrease of chromophore deprotonation by ~ 0.9 pH units compared to the underivatized construct (**Table 5-1**). As it was discussed earlier in chapter 4, truncation of the PHY domain appears to abolish the ground-state Pr heterogeneity in the CBP (**Fig. 4-7**) and p*K* was attributed to only chromophore deprotonation. This assignment is in agreement with the absence of a complex wavelength-dependent titration behavior as shown in **Fig. 5-3B** by the red highlighted titration curveswhich was observed for the titration of Cph1 PGP (Sadeghi, Balke et al. 2020). It should be taken into account that the absorbance decrease at 638 nm at low pH values for Cph1 PG and Cph1 PG-AF (**Fig. 5-3B**) is missing.

Similar to the Cph1 PGP C371S-AF (Sadeghi, Balke et al. 2020) Cph1 PG-AF also displays different p*K*-value for chromophore deprotonation (**Table 5-1**). This fact confirms the sensitivity of the H-bond network in the chromophore binding pocket to the protein changes in the GAF domain.

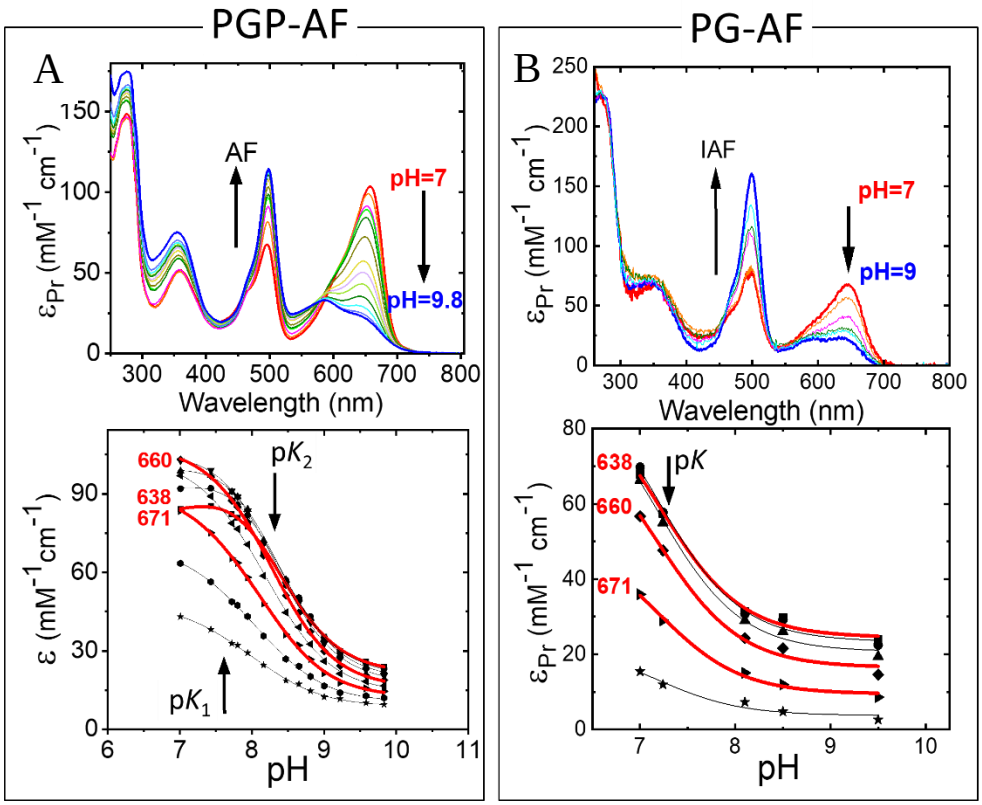

Figure 5-3: pH-dependence of Pr absorption spectra of Cph1 PG-AF (**A**) The absorption spectra at different pH, the direction of the pH-titration is indicated by the black arrow. (**B**) The respective titration data at six wavelengths are shown (638 (■), 645 (●), 654 (▲), 660 (♦), 671 (▼), and 682 nm (★)). The selected fit curves (638, 660, and 671nm) are marked in red. The pH-dependence was fitted by the Henderson−Hasselbalch equation (**Eq.3-6**) (Origin Pro 2019, OriginLab), and the fit yields the following values: p*K*= 7.20±0.04, i.e., smaller than p*K* of 7.5 given the uncertainty due to the number of data points. The standard error is given. The data for Cph1-PGP-WT-AF are given for comparison. These data were measured and evaluated by Constantin Schneider (Sadeghi, Balke et al. 2020). Conditions: 300 mM NaCl, 50 mM Tris/HCl, at 20ºC.

Table 5-1: p*K* comparison of chromophore deprotonation of different AF-labeled and unlabeled Cph1 variants. The fit error is given.

Cph1	Chromophore pK_{DPC}	ΔpK_{DPC}[a]
PGP wt	9.04± 0.02	-
PGP-C371S	8.37± 0.03	-0.67± 0.05
PG	8.12± 0.06	-0.92± 0.08
PGP-AF (labeling in PHY/PAS)	8.28 ± 0.02	-0.76± 0.04
PGP- C371S-AF (labeling in GAF)	8.10± 0.08	-0.94± 0.10
PG-AF (labeling in PAS-GAF)	7.20± 0.04	-1.84± 0.06

[a]ΔpK_{DPC} values were calculated for the different constructs with respect to PGP WT. PGP: PAS-GAF-PHY. PG: PAS-GAF. The standard error is given.

5.1.2 Agp1 variants and their spectroscopic characterization

Agp1 PGP have less cysteines compared to Cph1 PGP (**Fig. 5-4**), which makes it easier to have a single cysteine mutant in order to have a site-specific labeling with IAF. Agp1 PGP has three cysteine, C20 in PAS domain which provides a covalent bond to BV, and C279 and C295 in GAF domain are presumably accessible to IAF (**Fig. 5-4**). C279 is located in beta-sheet, neighboring H280 (a residue in CBP), and C295 is located at the beginning of the long helix which connect GAF and PHY domains (**Fig. 5-4**). The single cysteine variants of Agp1 PGP were created using site-directed mutagenesis as described in Material and Methods. The double mutants C279S/C295S was characterized using UV-vis absorption and the Raman Resonance (RR) and the results were compared to the WT. The RR spectra was measured and evaluated by Anastasia Kraskov in TU Berlin. The results showed a close similarity between the double mutant and WT, which indicates that there is no obvious effect of C → S mutation in Agp1 PGP. Further the single cysteine variant V364C (**Fig. 5-4**) was created, in which V346 is aligned with C371 in Cph1 PGP.

The labeling was performed as described in Material and Methods. The labeling stoichiometry (LS) was calculated by **Eq. 3-1.** The SDS-PAG gel was running to show a covalent bond of the dye to the protein (The data is not shown). In all the labeled proteins, the maximum absorption of -AF is red shifted compared to the free dye (maximum absorption of free IAF in standard buffer is at wavelength 490 nm). However different labeled position indicated a different red shift, 12 nm for WT-AF, 15 nm for C279-AF, 11 nm for C295-AF, and 8 nm for V364C-AF. The LS were between 80 to 110% in Agp1 PGP WT and the variants (**Fig. 5-6**).

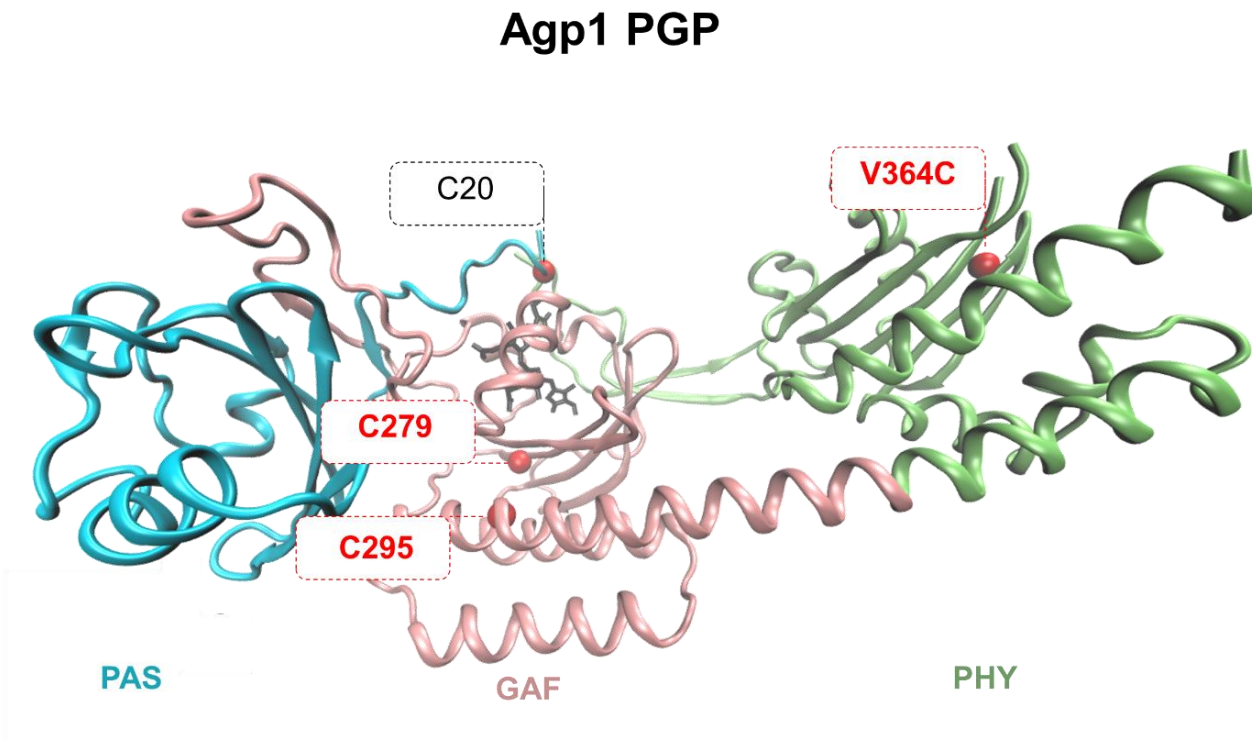

Figure 5-4: Agp1 PGP structure and single cysteine mutants. Structural model of Agp1 PGP (PDB code 5I5L) with accessible single cysteines for fluorescence labeling which are indicated in red, the PCB chromophore attached to Cys20 and Cys20 in black. In WT, two cysteines C295 and C279 are accessible. To introduce single accessible cysteine variants in Agp1, the following mutants were constructed: C297S/C295, C295S/C279, C279S/C295S/V364C. The PAS, GAF, PHY domains are colored in blue, pink, and green, respectively. The figure was generated by VMD.

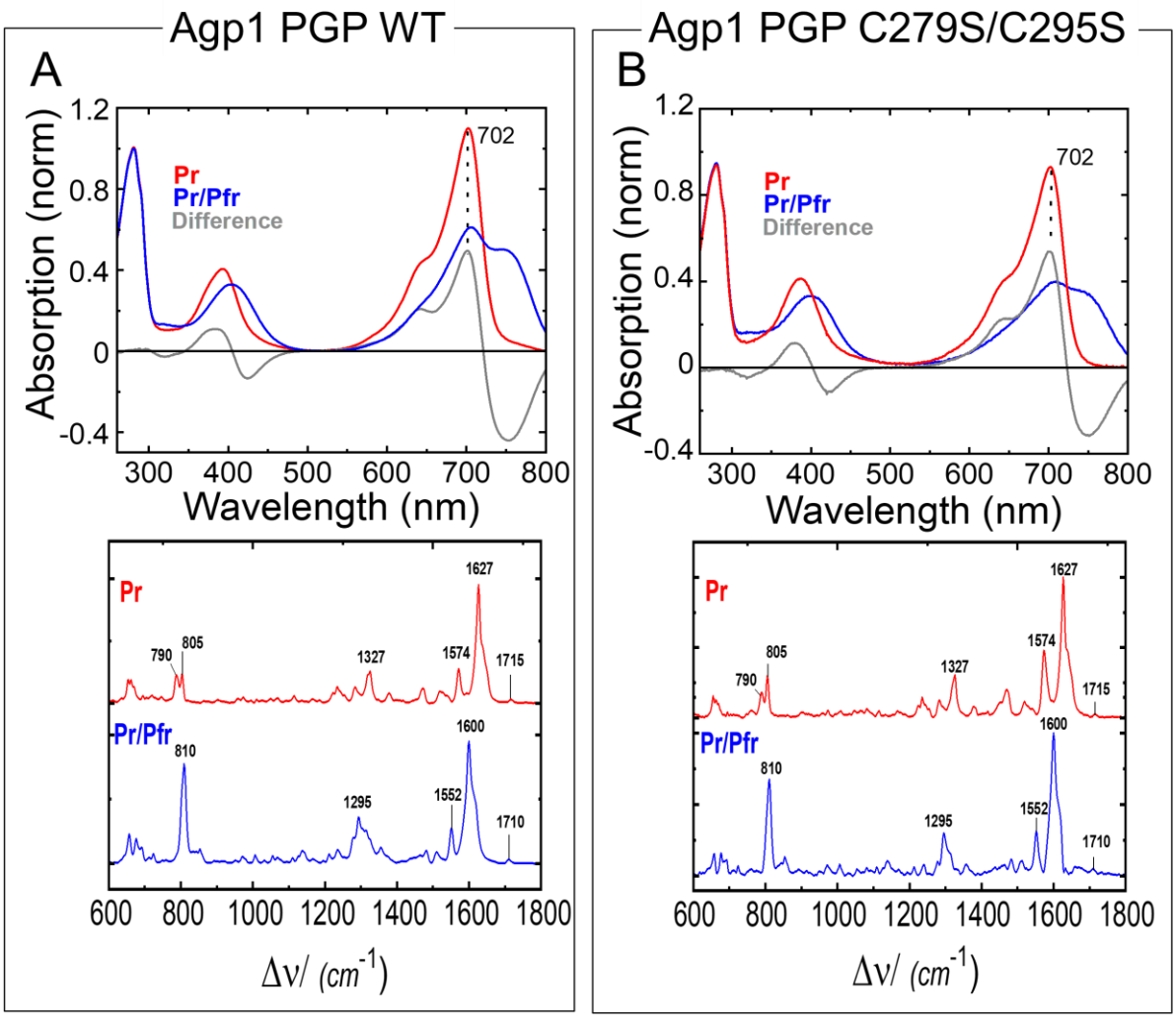

Figure 5-5: Characterization of the cysteine less variant (CS variant) of Agp1 PGP. Top panel shows the UV-vis absorption, Pr state in red, Pr/Pfr state in blue, and the difference in black. The lower panel indicates the Raman Resonance (RR) spectroscopy, Pr state in red and Pr/Pfr state in blue for Agp1 PGP WT (A) and Agp1 PGP C279S/C295S (B). The RR spectra was measured by Anastasia Kraskov in TU Berlin. Conditions: 300 mM NaCl, 50 mM Tris, pH 7.8 at 20ºC.

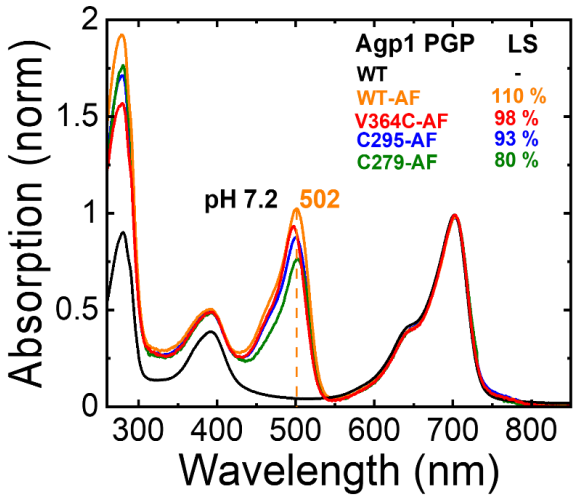

Figure 5-6: Labeling of Agp1 PGP single cysteine mutants with IAF. Pr absorption spectrum of Agp1 PGP and labeled variants at pH 7.2, normalized to the chromophore peak at 70 nm, WT in black, WT-AF in orange, V364C-AF in red, C295-AF in blue, and C297-AF in green. The labeling was performed as described in Material and Methods and the labeling stoichiometry (LS) was calculated according to **Eq. 3-1,** with yielded LS of 110 %**,** 98%, 93 %, and 80 % for WT-AF, V364C-AF, C295-AF, and C297-AF. Conditions: 300 mM NaCl, 50 mM Tris, pH 7.2 at 20ºC.

pH-dependence of UV-vis absorption of Agp1 PGP variants. A pervious study on Agp1 PGP showed that a single-site mutation of negatively and positively charged residues in highly conserved positions in the chromophore binding pocket (D197 and H250, respectively) to a neutral amino acid (alanine) resulted in a large chromophore p*K*-downshift from p*K*~11 to p*K*=7.6 (D197A) and to p*K*=9.2 (H250A) (von Stetten, Seibeck et al. 2007). Moreover, we saw earlier for Cph1 PGP and PG variants, that the distal and proximal protein modifications resulted in a long-range effect, which was observed as significant chromophore p*K* changes (**Table 5-1**) (Escobar, Lang et al. 2017, Sadeghi, Balke et al. 2020). To test whether the chromophore p*K* in Agp1 PGP is also affected by the protein modification in far-distance, pH-dependent chromophore absorption spectra of the single cysteine variants, both non-labeled and -AF labeled, were characterized.

pH-titration was carried out in 300 mM NaCl, 50 mM Tris/HCl buffer for pH 6.2- 9.5, or 100 mM Na_2CO_3/$NaHCO_3$ buffer for pH 9.5-10.8, at 20ºC. The pH was adjusted by adding the concentrated protein in 1 mM Tris/HCl pH 7.8 to the buffer with desired pH. The buffer solutions were prepared at specific pH point by mixing 50 mM Tris and Tris/HCl for pH 6.2- 9.5 or using 100 mM Na_2CO_3/$NaHCO_3$ buffer at specific pH (9.5-10.8). The absorbance values were scaled to the extinction coefficient ε_{700nm}=90000 $M^{-1}cm^{-1}$ for Agp1 PGP variant (Lamparter, Michael et al. 2002). The measurements were performed under the green light to avoid photoconversion of Pr. The pH titration curves were generated from the respective

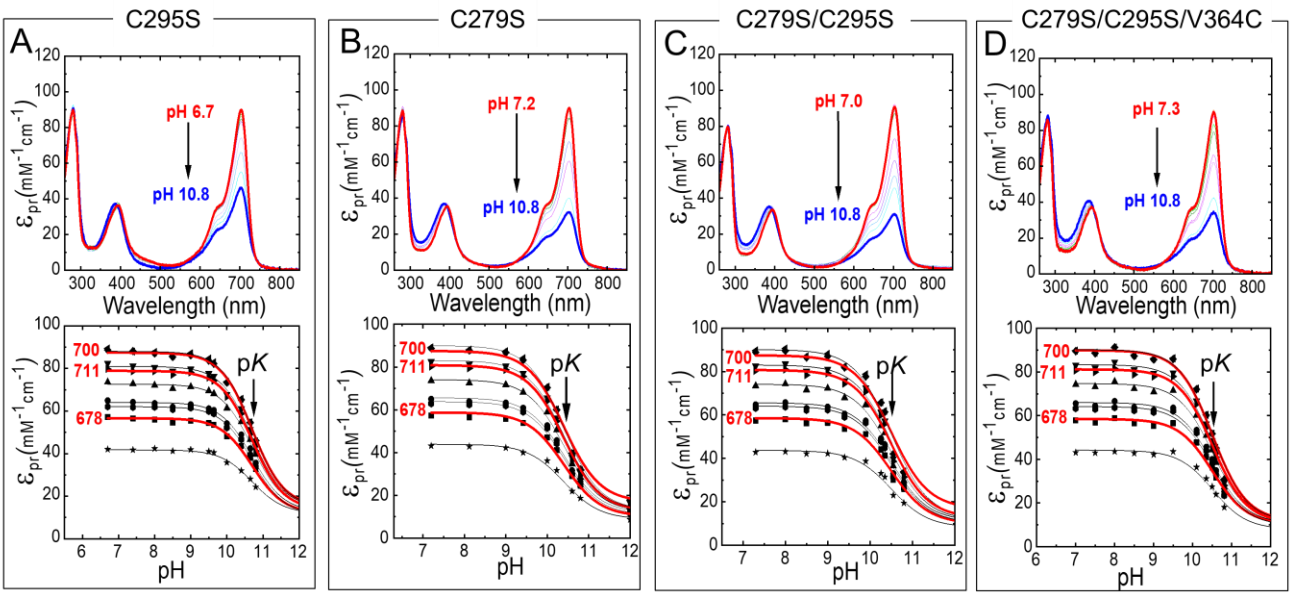

Figure 5-7: **pH dependent UV-vis absorption of Agp1 PGP and its variants.** pH dependent UV-vis absorption spectra of Agp1 PGP mutants in Pr. The top panels show the absorption spectra at different pH-values, the direction of the pH-titration is indicated by the black arrow for C295S (**A**), C279S (**B**), C279S/C295S (**C**), C279S/C295S /V364C (**D**). The bottom panel shows the respective titration data at nine wavelengths 678 (■), 683.5 (●), 689 (▲), 694.5 (▼), 700 (♦), 705.5(◄), 711(►), 716.5 (⬣), and 722 nm (★). Selected fit curves at 678, 700, and 711 nm are marked in red. The pH-dependence was fitted by the Henderson−Hasselbalch equation (**Eq.3-6**) using Origin Pro 2019 (OriginLab) and the fit results are summarized in **Table 5-2.** The absorption of the deprotonated chromophore at high pH was estimated to 20% of the maximum absorption of the respective wavelength (von Stetten, Seibeck et al. 2007), Conditions: 300 mM NaCl, 50 mM Tris/HCl buffer for pH 6.2- 9.5, or 100 mM Na_2CO_3/$NaHCO_3$ buffer for pH 9.5-10.8, at 20ºC.

absorbance values at nine wavelengths 678 - 722 nm. A global fit of the Henderson−Hasselbalch equation (**Eq. 3-6**) was performed. **Fig. 5-7** and **Fig-5-8** show the absorption spectra of Agp1 PGP, and Agp1 PGP-AF variants at different pH-values, respectively. To evaluate the effect of electrostatic charge of the protein segment that contain the bond IAF, on fluorescein p*K*, further the maximum absorption at IAF in Agp1 PGP-AF variants was fitted to calculate the p*K* of labeled IAF at different labeling positions (**Fig. 5-8** bellow panels). The results are summarized in **Table 5-2** and **Table 5-3**.

Corresponding closely to a previous study, the pH titration of Agp1 PGP WT indicated of only one p*K* with a value of 10.70 ± 0.02, however this value is lower than the one was reported before with a p*K* value of 11.1 (von Stetten, Seibeck et al. 2007). This difference in p*K* values might be related to the different protein purification or BV-assembling methods, or the accuracy of the pH-titration process and instruments such as pH meter, or the data evaluation, as the error fit was not reported, it is hard to judge the data analysis preciseness. The mutation C → S in GAF domain in β-sheet (C279S) resulted in a downshift of

chromophore p*K* with 0.3 pH units to a value of 10.40 ± 0.02. The Cys mutation in long-helix (C295S) resulted in a p*K* with a value of 10.70 ± 0.02 which is equal to the one that was calculated for WT (**Table 5-2**). The effect of this Cys mutation in both positions in the GAF domain leads to a small drop of the chromophore p*K* with 0.2 pH unit to a p*K* value of 10.51 ± 0.02, which is mostly related to the modification in the β-sheet versus than in long-helix regarding the single mutations results. C279 is neighboring H280, which is in the chromophore binding pocket of Agp1 PGP (see chapter 2, **Fig 2-6**). It has been shown the mutation H → A can result in a large p*K* shift to 8.8 due to the removed of the positive charge of the amino acid His. However, Cys and Ser are both polar and uncharged amino acids, thereby the mutant C → S is not leading to a big change in the chromophore p*K* as observed for the mutant H → A. However, because of the difference in polarity of these two amino acids and the local electrostatic charge, the mutant C → S can also change chromophore p*K*, as we saw earlier for Cph1 PGP (Sadeghi, Balke et al. 2020). The mutant C295S in Agp1 seems to not change the polarity and electrostatics of the local environment in the long helix in GAF domain, thereby this variant has no effect on the chromophore deprotonation. The labelling with IAF at these positions in the GAF domain (C279-AF in β-sheet and C295-AF in long-helix), influenced only in the β-sheet the chromophore deprotonation p*K* with a downshift of 0.2 pH unit to a value of 10.49 ± 0.02 in C295S/C279-AF. And the chromophore p*K* remained unchanged for the labeling in the long-helix in C279S/C295-AF with a p*K* value of 10.45 ± 0.03. However, the same labeling in the GAF domain of Cph1 PGP resulted a larger p*K* shift, 0.4 pH point for C371S-AF and 0.9 pH point for PG-AF. Also, in contrast to Cph1 PGP, the labelling of the PHY domain in single cysteine variant V364C-AF, leads only to a minor change in BV chromophore p*K* by a downshift of about 0.1 pH unit (**Table 5-2**) and thereby does not indicate a long-range H-bond network connecting the chromophore binding pocket and the β-sheets of the PHY domain. Likewise, the V → C substitution in position 364 (V364C) in the β-sheet of the PHY domain did not effect the chromophore p*K* (**Table 5-2**), in contrast to the C → S mutation at the corresponding site in Cph1 (C371S), which resulted in a drop of ~0.7 pH units (**Table 5-1**) (Sadeghi, Balke et al. 2020).

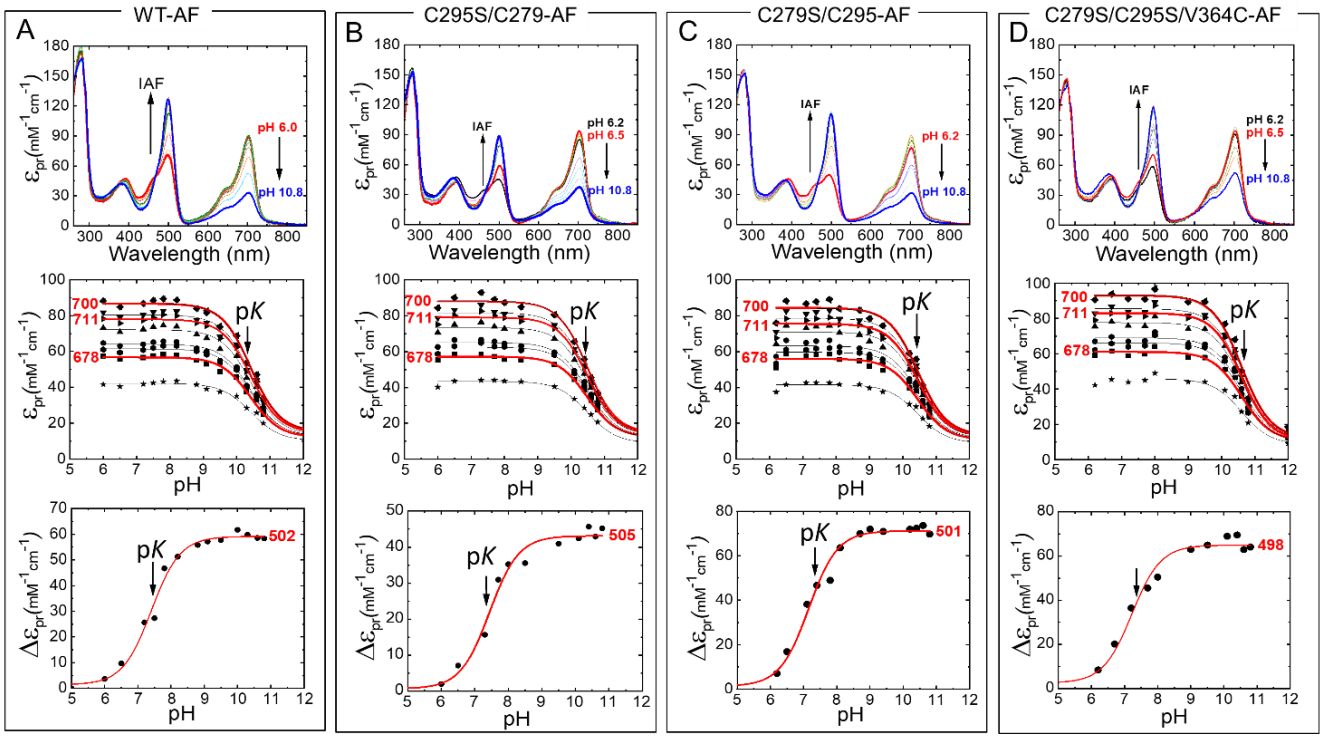

Figure 5-8: pH dependent UV-vis absorption. pH dependent UV-vis absorption spectra of Agp1 PGP-AF mutants in Pr. The top panel shows the absorption spectra at different pH-values, the direction of the pH-titration is indicated by the black arrow for WT-AF (**A**), C295S/C279-AF (**B**), C279S/C295-AF(**C**), C279S/C295S /V364C-AF (**D**). The middle panel shows the respective titration data at nine wavelengths 678 (■), 683.5 (●), 689 (▲), 694.5 (▼), 700 (♦), 705.5(◄), 711(►), 716.5 (⬣), and 722 nm (★). Selected fit curves at 678, 700, and 711 nm are marked in red. The bottom panel shows the respective titration data at 502 nm **(A)**, 505 nm **(B)**, 501 nm (**C**), 498 nm (**D**). The pH-dependence was fitted by the Henderson−Hasselbalch equation (**Eq. 3-6**) using Origin Pro 2019 (OriginLab) and the fit results for middle panels are summarized in **Table 5-2** and **Table 5-3.** The absorption of the deprotonated chromophore at high pH was estimated to 20% of the maximum absorption of the respective wavelength (von Stetten, Seibeck et al. 2007), Conditions: 300 mM NaCl, 50 mM Tris/HCl buffer for pH 6.2- 9.5, or 100 mM Na_2CO_3/$NaHCO_3$ buffer for pH 9.5-10.8, at 20ºC.

Table 5-2: The fit results of the pH dependent BV chromophore absorption (p*K*-values) of Agp1 PGP and Agp1 PGP-AF variants from the spectra and fits shown in Fig. 5-7 and 5-8. The standard error is given.

Agp1	Chromophore pK_{DPC}	ΔpK_{DPC}[a]
PGP WT	10.70 ± 0.02	0
PGP C295S	10.70 ± 0.01	0 ± 0.03
PGP C279S	10.40 ± 0.02	-0.3 ± 0.03
PGP C279S/C295S	10.51 ± 0.02	- 0.19 ± 0.04
PGP C279S/C295S/V364C	10.50 ± 0.02	- 0.20 ± 0.04
PGP WT-AF (labeling in GAF)	10.42 ± 0.02	- 0.28 ± 0.04
PGP C295S/C279-AF (labeling in β-sheet of GAF)	10.49 ± 0.02	- 0.21 ± 0.04
PGP C279S/C295-AF (labeling in long helix of GAF)	10.45 ± 0.03	- 0.25 ± 0.05
PGP C279S/C295S/V364C-AF (labeling in β-sheet of PHY)	10.60 ± 0.03	- 0.09 ± 0.05

[a] ΔpK_{DPC} values were calculated for the different constructs with respect to PGP WT. PGP: PAS-GAF-PHY. PG: PAS-GAF. The standard error is given.

Table 5-3: The fit results of the pH dependent fluorescein absorption (p*K*-values) as obtained from Agp1 PGP-AF variants. The spectra are shown in **Fig. 5-8**. The standard error for the p*K* is given. The λ_{max} values of the alkaline band of fluorescein are shown together with the polarity (according to Alexiev et al. Biochemistry 1994).

Agp1	p*K*	$\lambda_{\max\,(-AF)}$ (nm)	Polarity
PGP WT-AF (labeling in GAF)	7.4 ± 0.1	502	hydrophobic
PGP C295S/C279-AF (labeling in β-sheet of GAF)	7.4 ± 0.1	505	hydrophobic
PGP C279S/C295-AF (labeling in long helix of GAF)	7.2 ± 0.1	501	hydrophobic
PGP C279S/C295S/V364C-AF (labeling in β-sheet of PHY)	7.2 ± 0.1	498	hydrophilic

5.2 Conformational dynamics of Cph1 and Agp1 as monitored by time-resolved fluorescence anisotropy

Fluoresceine labeling of the different Cph1 constructs provides the opportunity to study local conformational changes. The time-resolved fluorescence depolarization was employed to detect the nanoseconds structural dynamics of the protein (Alexiev, Rimke et al. 2003). The anisotropy decay curve of a bound fluorophore contains the information on global and local protein dynamics as well as on the protein structure and conformational changes (Alexiev, Rimke et al. 2003, Kirchberg, Kim et al. 2011, Alexiev and Farrens 2014).

5.2.1 Conformational dynamics of Cph1

First, the sensitivity of attached fluorescent probe to the protein dynamics in Cph1 PGP was evaluated. **Fig.5-9** shows the time-resolved anisotropy decay curve of free IAF, and **Fig. 5-10** shows the time-resolved anisotropy decay curve of Cph1 PGP-AF variants at pH 7.5. In contrast to the anisotropy of free IAF, the anisotropy decay of fluorescein attached to Cph1 PGP variants displays a complex decay behavior. This complex behavior is resulted by the motion of the protein segment to which the probe is attached. Analysis of the anisotropy decay curves (**Fig. 5-10**) was performed as described (Alexiev, Rimke et al. 2003). The main decay components were assigned to the dynamics of (i) the fluorescent dye itself with a correlation time ϕ_1 in the 100–300 ps range, (ii) the protein segment to which the dye is bound (β-sheet in WT-AF, and helix in C371S-AF) (ϕ_2), and (iii) a rotational correlation time (ϕ_3) of about 30 ns that reflects the overall tumbling of the protein and the amplitude β_3 represents a measure of steric hindrance of protein segment motion (**Table 5-4**).

At pH 7.5, the protein segment motion is described by a correlation time ϕ_2=1.3 ns for WT-AF, and 0.80 ns and 0.58 ns for C371S-AF, and PG-AF, respectively. The corresponding amplitude (β_2) is a measure of the conformational space movement of the protein segment to which the probe is attached (**Table 5-4**), which can be expressed as the half cone angle θ (**Eq. 3-14)** in the context of the wobbling-in-a-cone model (Schröder, Alexiev et al. 2005).

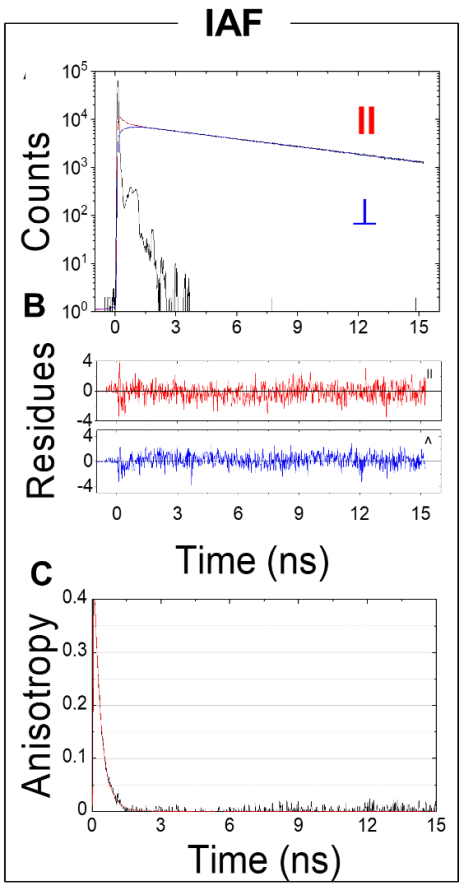

Figure 5-9: **The lifetime decay and fitting curves of free IAF.** (**A**) The raw data and fitting curves in parallel (red) and in perpendicular (blue). (**B**) The residue for the parallel (red) and perpendicular (blue). (**C**) The anisotropy curve in black and the fitting curve in red. Conditions: 150 mM NaCl, 50 mM Tris/HCL, pH 8 at 19ºC.

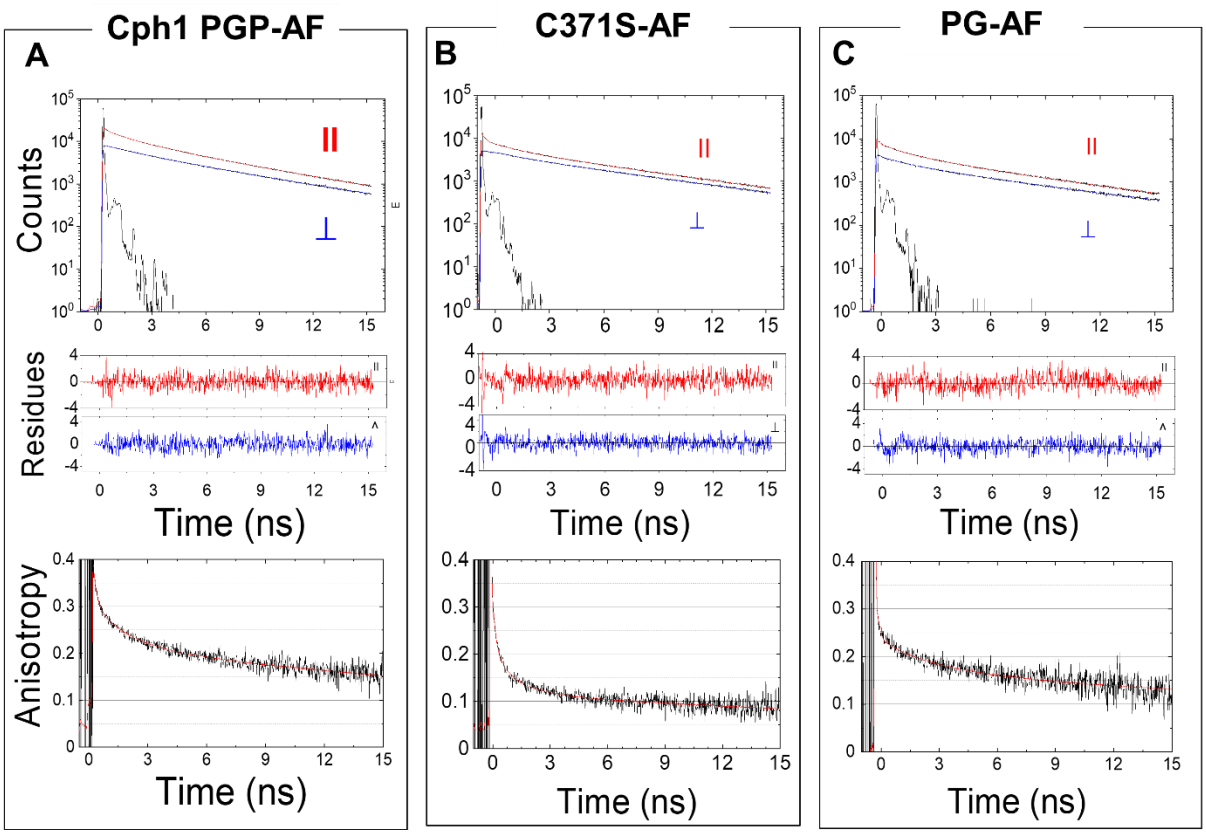

Figure 5-10: Time-resolved anisotropy curve of Cph1 PGP-AF variants. The fit curve and residuals are shown. Fit parameters are summarized in **Table 5-4**. Conditions: 150 mM NaCl, 50 mM Tris/HCL, pH 7.5 at 19ºC.

Table 5-4: **Time-resolved anisotropy fit results of Cph1-PGP variants**. r_0 is initial anisotropy and the amplitudes β_1, β_2 and β_3 indicate the degree of depolarization of the anisotropy decay components with the correlation times ϕ_1, ϕ_2 and ϕ_3. The reduced χ_2 (χ_{red}^2) is given as a measure of the goodness of the fit.

Cph1	r_0	ϕ_1(ns)	ϕ_2 (ns)	ϕ_3 (ns)	β_1	β_2	β_3	χ_{red}^2
PGP WT-AF (C371-AF) (labeling in PHY/PAS)	0.35	0.08	1.30	30	0.091	0.060	0.199	1.26
PGP C371S -AF (labeling in GAF)	0.39	0.10	0.80	30	0.176	0.067	0.149	0.92
PG-AF (labeling in PAS-GAF)	0.34	0.05	0.58	15	0.085	0.054	0.200	1.00

pH-dependence of conformational dynamics and structural constraints in Cph1 constructs. Fig. 5-11A, C, and E show the pH-dependent anisotropy curves of labeled Cph1 variants. All samples are measured under the same conditions, in 150 mM NaCl, 50 mM Tris, at 19ºC. The curves were evaluated as described in Material and Methods. The fit results are summarized in **Table 5-6**. For further evaluation the titrations curves of β-sheet flexibility expressed as the relative mobility $\beta_2' = \beta_2/(\beta_2 + \beta_3)$ (red data points in **Fig. 5-11B, D, and F**) and the segment steric restriction expressed by β_3 (black data points in **Fig. 5-11B, D, F**) were globally fitted according to the Henderson-Hasselbalch equation (Origin Pro 2019, OriginLab). The respective p*K*-values (**Fig. 5-11**) can be compared to those which were obtained from pH-dependent UV-vis absorption (**Table 5-5**).

The anisotropy curves of Cph1 PGP-AF were measured at 5 different pH-values between pH 6.6 and pH 9.4. As the mass spectroscopy proved (**Fig. A1**, **Table A1**), the reporter group located in the β-sheet in the chromophore distant PHY (position 371) and PAS (position 120) domains (**Fig. 5-11A**). Data analysis revealed only small changes in the rotational correlation times for β-sheets with 1.4 ± 0.1 ns (**Table 5-6**). However, the amplitudes of the anisotropy decay components and, in particular the steric restriction of the strand movement changed significantly with pH (**Table 5-6**). The global fit of the β-sheet mobility, i.e., the conformational space of strand movement and the steric restriction of movement in Cph1 PGP yielded a p*K* of 8.2 ± 0.2. This result indicated that the conformational changes occurred in the β-sheets in the chromophore distant PAS/PHY domains is pH-dependent.

Fig. 5-11C, D show the respective data for Cph1 PGP C371S-AF, with labeling in position 305, in the long helix connecting the GAF and PHY domains (C305-AF). The observed rotational correlation time for the long helix in GAF is 0.8 ± 0.2 ns (**Table 5-6B**) and shows no pH dependency. Similar to Cph1 PGP WT-AF (**Fig. 5-11A, B**), the amplitudes of the anisotropy decay components, and in particular the steric restriction of segmental mobility are highly pH-dependent (**Table 5-6B**), indicating an increase in helix mobility (conformational space) with increasing pH. The global p*K* of the pH-dependency of conformational change around the long helix in the GAF domain is p*K* = 8.0 ± 0.2 (**Fig. 5-11D).** However, the comparison results of WT-AF and C371S-AF indicated that the pH-dependency of steric restriction of helix (at location of C305-AF) motion are smaller than those were observed for β-sheets (at location of C371-AF). Also, the values reflect a lower steric restriction of motion in this region of the GAF domain (**Fig. 5-11D**) compared to the PAS/PHY domain β-sheet (**Fig. 5-11B**).

It has been subjected in phytochrome photoconversion that a tongue-like hairpin loop (β-sheet conformation in Pr) which extends from the PHY to the GAF domain plays an essential role through sheet-to-helix conversion (Takala, Björling et al. 2014, Schmidt, Sauthof et al. 2018). However, it is still an open question how the tongue refolds upon Pfr formation, and, even more intriguingly, how that process is reversed by

photoconversion back to Pr. Removing the PHY domain will cause the deletion of tongue in Cph1 PG construct. To test the effect of this deletion on the conformational flexibility of the PAS-GAF bidomain, compared to PGP construct when tongue is present, the labeled of truncated construct Cph1 PG with fluorescein was investigated. **Fig. 5-11E** shows the time-resolved anisotropy curves between pH 7 and 10. The data show a pH-dependency of conformational change with a p*K* of 7.5 ± 0.2 (**Fig. 5-11F**). The measured rotational correlation time of the protein segment labeled in the PG construct is 0.5 ± 0.1 ns (**Table 5-6C**), close to the value obtained for position 305 in the connecting helix of the PGP C371S construct. In the PG-construct, similar to the PGP-constructs, chromophore deprotonation leads to an increase in protein mobility. The respective p*K*-values of the chromophore deprotonation (pK_{DPC}) are depicted alongside with the structural models on the right side of **Fig. 5-11**.

For all studied Cph1 PGP variants, the anisotropy decay behaved similarly as a function of pH (**Fig. 5-11**), a higher protein mobility (less steric restriction) with increasing pH. However, there are some distinguished differences, such as the amplitudes of the steric restriction at pH 7 that clearly stems from the different labeling positions, and the p*K*-values of the conformational transitions (**Fig. 5-11, Table 5-5**). The p*K*-values of the conformational transition are interestingly correlated to the respective chromophore p*K*-values (**Table 5-5**). This will imply a casual interaction between the chromophore deprotonating and the conformational dynamic of proximal and distal protein. This interaction is facilitated by the charge propagation along the protein which is resulted of the change in the H-bond network from the CBP to the rest of the protein towards the PHY domain. This process can perform mechanically and through electrostatic force propagation between charged amino acids, as well as by the rearrangement of the H-bond network, including salt bridges. Thereby, we can suggest that extended H-bond networks exist that connect distal and proximal sites in the protein to the CBP. *Vice versa*, changes in the H-bond network in the CBP through chromophore deprotonation result in a higher protein mobility in both the PAS, GAF and the PHY domain.

Table 5-5: p*K* comparison of the chromophore deprotonation and protein conformational changes of different AF-labeled. The fit error is given.

Cph1	Chromophore pK_{DPC}	p*K* of conformational change
PGP-AF (labeling in PHY/PAS)	8.28 ± 0.02	8.2± 0.2
PGP- C371S-AF (labeling in GAF)	8.10± 0.08	8.0± 0.2
PG-AF (labeling in PAS-GAF)	7.20± 0.04	7.5± 0.2

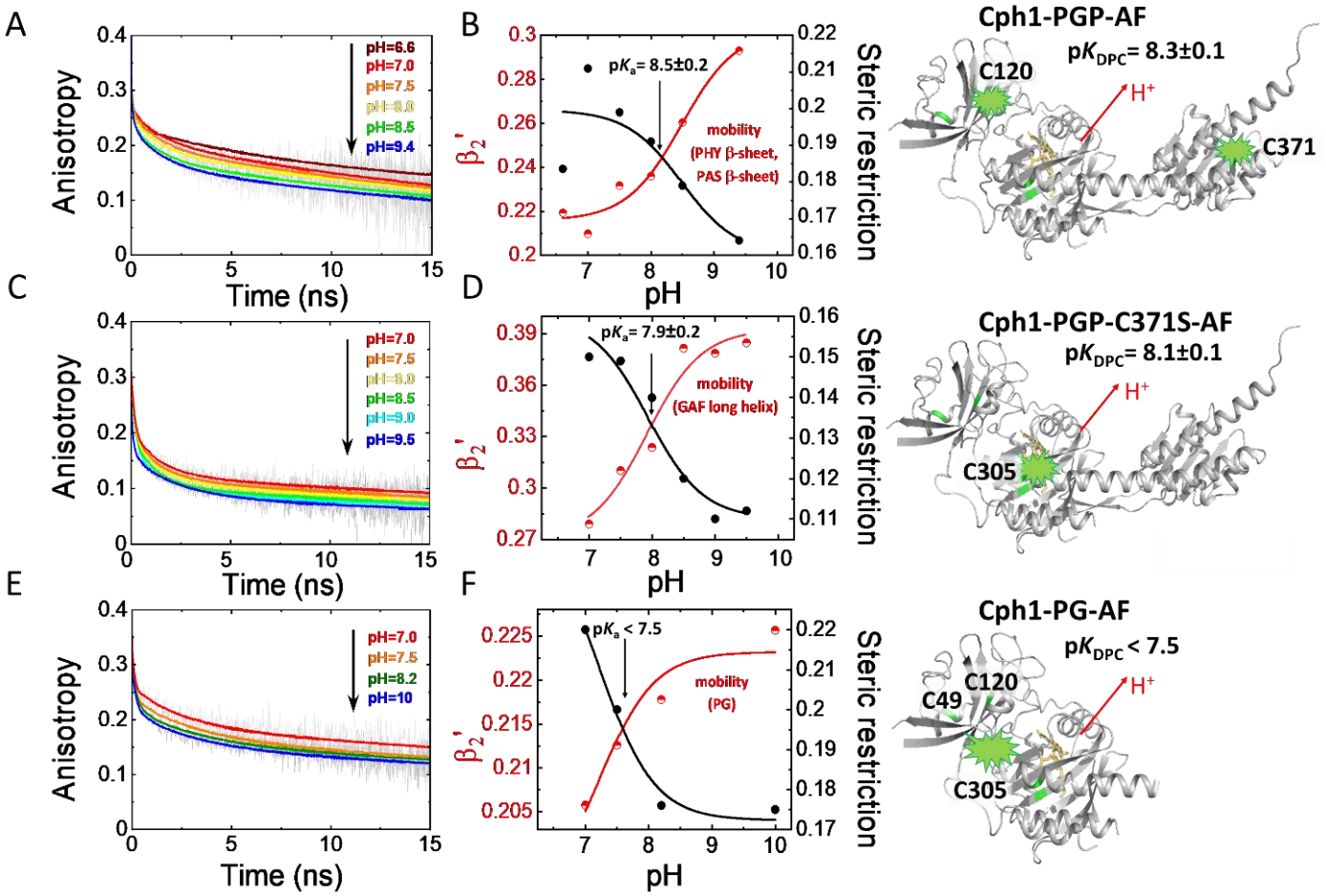

Figure 5-11: pH-dependent time-resolved fluorescence anisotropy data for Cph1 variants. (**A, C, E**) show the anisotropy decay curves (grey) and the respective fits (colored) at different pH-values. (**B, D, F**) show the titrations curves of β-sheet flexibility expressed as the relative mobility $\beta_2' = \beta_2/(\beta_2 + \beta_3)$ (red data points) and of segment steric restriction expressed by β_3 (black data points). The global fit curves according to the Henderson-Hasselbalch equation (**Eq. 3-6**, fitted with Origin Pro 2019, OriginLab) used to calculate the p*K* values are shown. The respective p*K*-values are given. (**A, B**) Cph1 PGP-AF, (**C, D**) Cph1 PGP-C371S-AF, and (**E, F**) Cph1 PG-AF. The p*K*-values of chromophore deprotonation are depicted alongside with the structural models at the right. The labeling positions are indicated by a green star. Anisotropy fit values are summarized in **Table 5-6.** Conditions: 150 mM NaCl, 50 mM Tris, at 19ºC.

Table 5-6: Time-resolved anisotropy fit results of Cph1-PGP (**A**) WT-AF, (**B**) C371S-AF, (**C**) PG-AF. r_0 is initial anisotropy and the amplitudes β_1, β_2 and β_3 indicate the degree of depolarization of the anisotropy decay components with the correlation times ϕ_1, ϕ_2 and ϕ_3. The reduced χ_2 (χ_{red}^2) is given as a measure of the goodness of the fit. The corresponding fluorescence lifetimes of bound IAF were 0.2 ns, 1.3 ns, and 3.9 ns (pH 8). The fit error is 10%.

A.WT-AF

pH	r_0	ϕ_1(ns)	ϕ_2 (ns)	ϕ_3 (ns)[a]	β_1	β_2	β_3	χ_{red}^2
6.6	0.30	0.11	2.8	30	0.063	0.051	0.183	0.98
7.0	0.37	0.09	1.4	30	0.104	0.056	0.211	1.07
7.5	0.35	0.08	1.3	30	0.091	0.060	0.199	1.26
8.0	0.34	0.07	1.2	30	0.090	0.059	0.191	1.12
8.5	0.33	0.10	1.3	30	0.088	0.063	0.179	1.02
9.4	0.31	0.12	1.5	30	0.078	0.068	0.164	1.00

[a]The rotational correlation time of the whole protein was fixed to 30 ns. (mean ϕ_3-value from individual fits is 27±3.3 ns)

B. C371S-AF

pH	r_0	ϕ_1(ns)	ϕ_2 (ns)	ϕ_3 (ns) [b]	β_1	β_2	β_3	χ_{red}^2
7.0	0.38	0.11	0.9	30	0.176	0.058	0.150	0.99
7.5	0.39	0.10	0.8	30	0.176	0.067	0.149	0.92
8.0	0.39	0.10	0.8	30	0.181	0.067	0.140	0.93
8.5	0.37	0.08	0.7	30	0.178	0.074	0.120	0.95
9.0	0.37	0.11	1.0	30	0.201	0.067	0.110	0.97
9.5	0.28	0.07	1.0	30	0.098	0.070	0.112	1.10

[b]The rotational correlation time of the whole protein was fixed to 30 ns. (mean ϕ_3-value from individual fits is 33±3.1 ns)

C. PG-AF

pH	r_0	ϕ_1(ns)	ϕ_2 (ns)	ϕ_3 (ns)[c]	β_1	β_2	β_3	χ_{red}^2
7.0	0.38	0.03	0.37	15	0.103	0.057	0.220	0.93
7.5	0.34	0.05	0.58	15	0.085	0.054	0.200	1.00
8.2	0.30	0.09	0.60	15	0.075	0.049	0.176	1.01
10	0.30	0.07	0.55	15	0.073	0.051	0.175	1.04

[c]The rotational correlation time of the whole protein was fixed to 15 ns. (mean ϕ_3-value from individual fits is 17±3.0 ns)

5.2.2 Site-specific conformational dynamics of Agp1

Similar to Cph1 PGP-AF variants, first, the sensitivity of attached fluorescent probe to the specific position in Agp1 PGP was evaluated. **Fig 5-12** shows the time-resolved anisotropy decay curve of site-labeled variants of Agp1 PGP at pH 7.5. As we discussed above, the anisotropy decay of attached fluorescein in specific position of Agp1 PGP reveals a complex decay behavior, which is mostly resulted by the motion of the site-specific segment in the protein to which the probe is attached. Analysis of the anisotropy decay curves (**Fig. 5-12**) was performed as described (Alexiev, Rimke et al. 2003). The main decay components were assigned to the dynamics of (i) the fluorescent dye itself with a correlation time ϕ_1 in the 40–300 ps range, (ii) the protein segment to which the dye is bound (β-sheet or helix) (ϕ_2), and (iii) a rotational correlation time (ϕ_3) of about 30 ns that reflects the overall tumbling of the protein and whose amplitude β_3 represents a measure of steric hindrance of the protein segment's dynamic (**Table 5-7**).

At pH 7.5, the β-sheets motion is described by a correlation time ϕ_2=2.25 ns for C279-AF in the GAF domain, and 1.40 ns for V364C-AF in the PHY domain. At this pH, helix motion is indicated by ϕ_2 = 0.50 ns for C295-AF in GAF domain which is much faster than the β-sheet motion in the GAF or PHY domain (**Table 5-7**). This observation was consequently detected also for the motion of the probe itself, which has faster motion in helix in the GAF domain ($\phi_{1=}$ 40 ps for C295-AF) than β-sheet in GAF ($\phi_{1=}$ 310 ps for C279-AF), or β-sheet in the PHY domain ($\phi_{1=}$ 150 ps for V364C-AF). The corresponding amplitude (β_2) is a measure of the conformational space movement of the protein segment to which the probe is attached (**Table 5-7**), which can be expressed as the half cone angle θ in the context of the wobbling-in-a-cone model (Schröder, Alexiev et al. 2005).

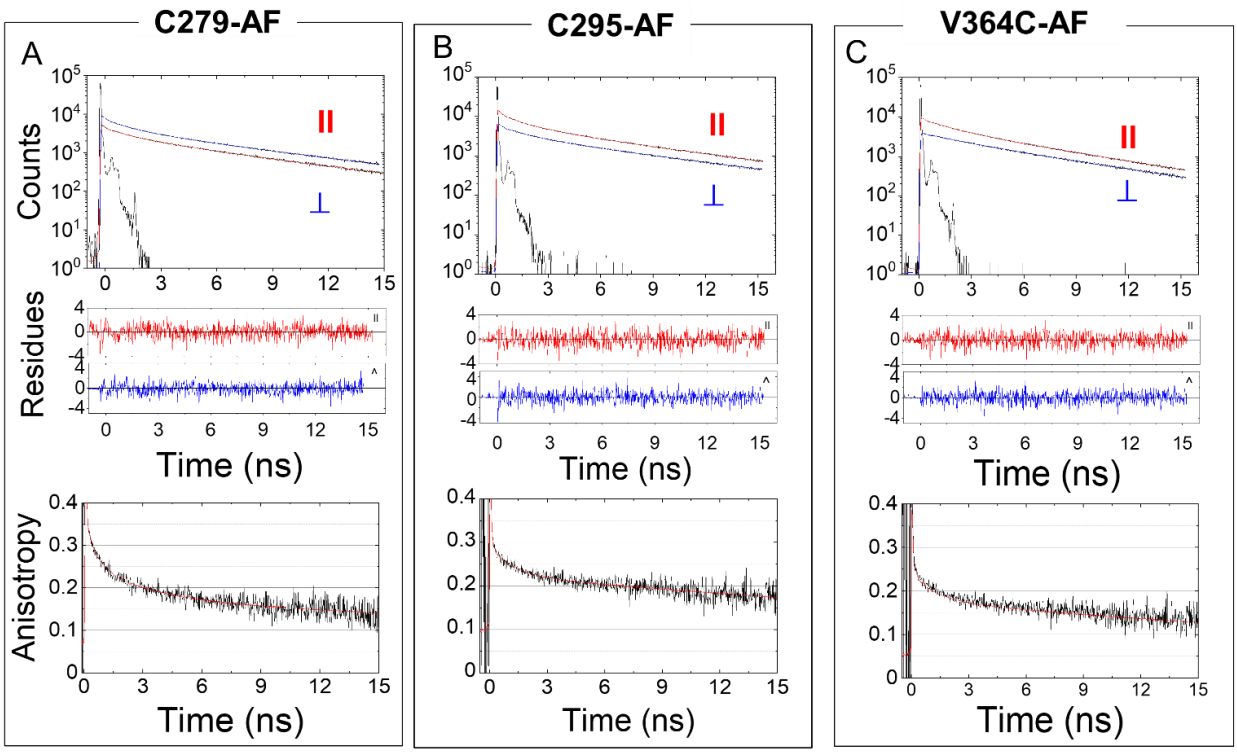

Figure 5-12: **Time-resolved anisotropy curve of Agp1 PGP-AF variants**. The fit curve and residuals are shown. Fit parameters are summarized in **Table 5-7**. Conditions: 300 mM NaCl, 50 mM Tris, pH 7.5 at 19ºC.

Table 5-7: Time-resolved anisotropy fit results of Agp1-PGP-AF variants. r_0 is initial anisotropy and the amplitudes β_1, β_2 and β_2 indicate the degree of depolarization of the anisotropy decay components with the correlation times ϕ_1, ϕ_2 and ϕ_3. The reduced χ^2 (χ_{red}^2) is given as a measure of the goodness of the fit. The corresponding fluorescence lifetimes of bound IAF were 0.2 ns, 1.3 ns, and 3.9 ns (pH 8). The fit error is 10%.

Agp1 PGP	r_0	ϕ_1(ns)	ϕ_2 (ns)	ϕ_3 (ns) [a]	β_1	β_2	β_3	χ_{red}^2
C279-AF (labeling in β-sheet of GAF)	0.34	0.31	2.25	30	0.070	0.071	0.199	1.04
C295-AF (labeling in long-helix of GAF)	0.34	0.04	0.50	30	0.054	0.055	0.231	1.01
C279S/C295S/V364C-AF (labeling in β-sheet of PHY)	0.34	0.15	1.40	30	0.059	0.085	0.199	0.94

[a]The rotation correlation of the whole protein was fixed at 30 nm.

pH-dependence of conformational dynamics and structural constraints in Agp1 constructs. Fig. 5-13A, C, E, G show the pH-dependent anisotropy curves of site specific labeled in Agp1 variants. All samples are measured under the same conditions, in 300 mM NaCl, 50 mM Tris, at 19ºC. The curves were evaluated as described in Material and Methods. The fit results are summarized in **Table 5-9**. For further evaluation the titrations curves of β-sheet flexibility expressed as the relative mobility $\beta_2' = \beta_2/(\beta_2 + \beta_3)$ (red data points in **Fig. 5-13B, D, F and H**) and of segment steric restriction expressed by β_3 (black data points in **Fig. 5-13B, D, F and H**) were globally fitted according to the Henderson-Hasselbalch equation (Origin Pro 2019, OriginLab). Further the respective p*K*-values from the protein conformation transition were compared to the chromophore p*K* (**Table 5-8**).

The anisotropy curves of Agp1 PGP WT-AF were measured at 6 different pH-values between pH 6.4 and pH 10.2 (**Fig. 5-13A**). Data analysis revealed only small changes in the rotational correlation times for protein segment with 0.9 ± 0.15 ns (**Table 5-9**). The respective data for site-specific labeling in GAF and PHY, also indicated of small changes in rotational correlation times of β-sheet in GAF with 1.4 ± 0.8 ns, β-sheet in PHY 1.7 ± 0.7 ns, and long-helix in GAF with 0.5 ± 0.2 ns. However, the amplitudes of the anisotropy decay components and, in particular the steric restriction of the strand movement changed significantly with pH (**Table 5-9**). The global fit of the protein segment mobility, i.e., the conformational space of strand movement and the steric restriction of movement in Agp1 PGP WT and the site-specific labeled variants yielded a p*K* of 9.0 ± 0.2 for WT-AF, 9.2 ± 0.1 for C279-AF (β-sheet in GAF), 9.7 ± 0.2 for C295-AF (long-helix in GAF), and 9.0 ± 0.2 for V364C-AF (β-sheet in PHY) (**Table 5-8**). While a pH dependence of the conformational dynamics in the CBP and the GAF domain as observed, only a residual dependence was observed for the PHY domain conformational dynamics. Most importantly, there is no correlation between the chromophore p*K* (~10.4-10.6) and conformational change (p*K*~8.8-9.4) (**Table 5-8**).

Table 5-8: p*K* comparison of the chromophore deprotonation and protein conformational changes of different AF-labeled. The fit error is given.

Agp1 PGP	Chromophore pK_{DPC}	p*K* of conformational change
WT-AF (labeling in GAF)	10.42 ± 0.02	9.0 ± 0.2
C279-AF (labeling in β-sheet of GAF)	10.49 ± 0.02	9.2 ± 0.1
C295-AF (labeling in long-helix of GAF)	10.45 ± 0.03	9.7 ± 0.2
C279S/C295S/V364C-AF (labeling in β-sheet of PHY)	10.60 ± 0.03	9.0 ± 0.2

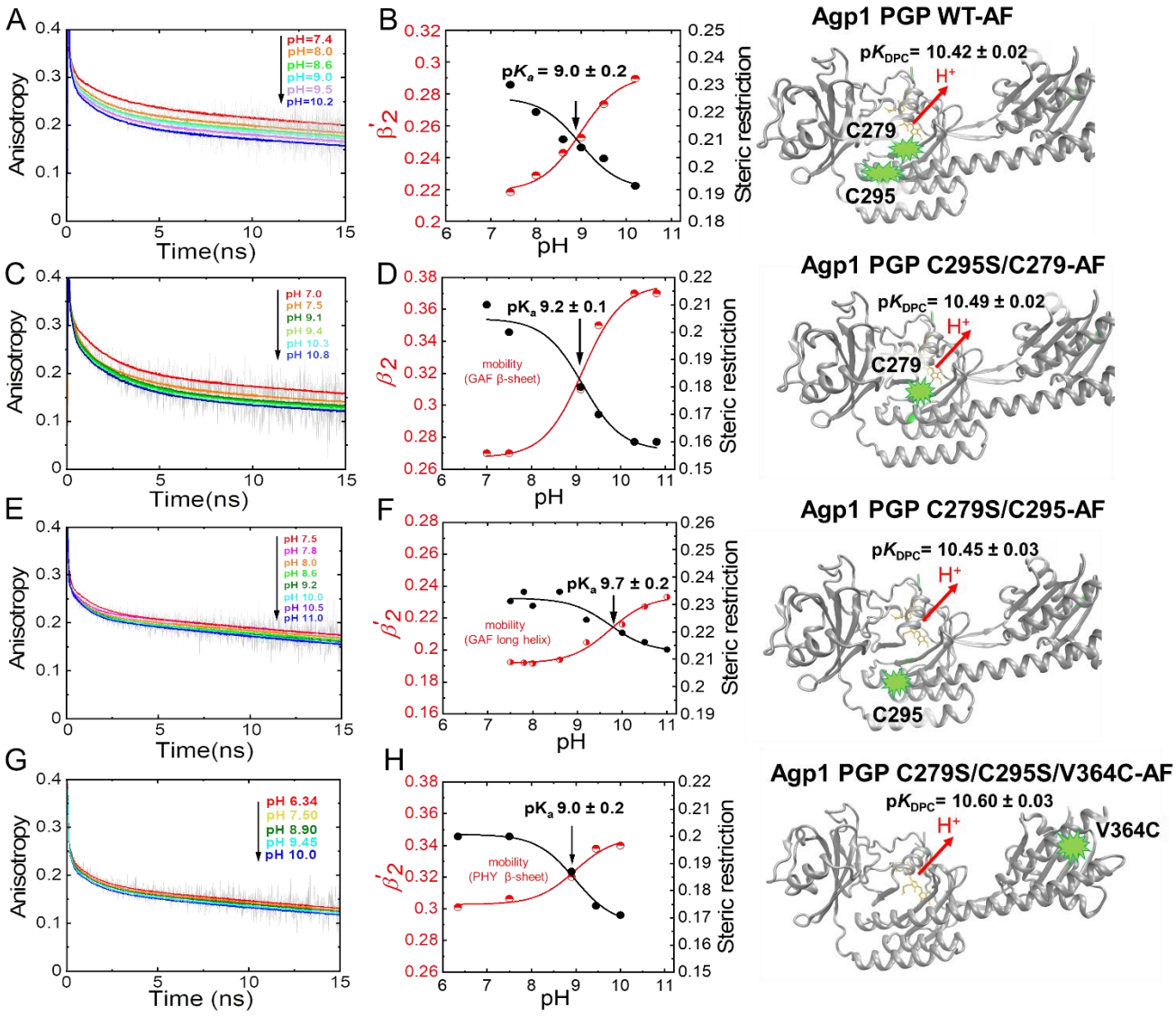

Figure 5-13: pH-dependent time-resolved fluorescence anisotropy data for Agp1 variants. (**A, C, E, G**) show the anisotropy decay curves (grey) and the respective fits (colored) at different pH-values. (**B, D, F, H**) show the titrations curves of β-sheet flexibility expressed as the relative mobility $\beta_2' = \beta_2/(\beta_2 + \beta_3)$ (red data points) and of segment steric restriction expressed by β_3 (black data points). The global fit curves according to the Henderson-Hasselbalch equation (**Eq. 3-6**, fitted with Origin Pro 2019, OriginLab) used to calculate the p*K* values are shown. The respective p*K*-values are given. (**A, B**) Agp1 PGP WT-AF, (**C, D**) Agp1 PGP C295S/C279-AF, (**E, F**) Agp1 PGP C279S/C295-AF, and (**G, H**) Agp1 PGP C279S/C295S/V364C-AF. The p*K*-values of chromophore deprotonation are depicted alongside with the structural models at the right. Anisotropy fit values are summarized in **Table 5-9.** Conditions: 300 mM NaCl, 50 mM Tris, at 19ºC.

Table 5-9: Time-resolved anisotropy fit results of Agp1-PGP-AF variants. WT-AF (**A**), C279-AF (**B**), C295-AF (**C**), and V364C-AF (**D**). r_0 is initial anisotropy and the amplitudes β_1, β_2 and β_3 indicate the degree of depolarization of the anisotropy decay components with the correlation times ϕ_1, ϕ_2 and ϕ_3. The reduced χ^2 (χ_{red}^2) is given as a measure of the goodness of the fit.

A. WT-AF

pH	r_0	ϕ_1(ns)	ϕ_2 (ns)	ϕ_3 (ns)[a]	β_1	β_2	β_3	χ_{red}^2
7.4	0.35	0.10	1.05	34.1	0.052	0.065	0.232	0.95
8.0	0.35	0.08	0.82	30.0	0.063	0.066	0.220	0.93
8.6	0.34	0.08	0.82	30.0	0.058	0.071	0.211	0.93
9.0	0.34	0.11	0.91	30.0	0.066	0.066	0.207	0.92
9.5	0.34	0.07	0.87	30.0	0.062	0.076	0.202	1.00
10.2	0.33	0.13	0.92	30.0	0.059	0.079	0.192	0.93

B. C279-AF

pH	r_0	ϕ_1(ns)	ϕ_2 (ns)	ϕ_3 (ns)[a]	β_1	β_2	β_3	χ_{red}^2
7	0.34	0.10	1.10	30	0.048	0.078	0.214	0.96
7.5	0.34	0.31	2.25	30	0.070	0.071	0.199	1.04
9.1	0.34	0.23	1.17	30	0.078	0.082	0.180	0.87
9.5	0.34	0.17	1.10	30	0.065	0.098	0.174	1.06
10.3	0.34	0.18	1.17	30	0.077	0.097	0.161	1.02
10.8	0.34	0.27	1.5	30	0.088	0.093	0.160	0.96

C. C295-AF

pH	r_0	ϕ_1(ns)	ϕ_2 (ns)	ϕ_3 (ns)[a]	β_1	β_2	β_3	χ_{red}^2
7.5	0.34	0.04	0.50	30	0.054	0.055	0.231	1.01
7.8	0.34	0.04	0.41	30	0.049	0.056	0.235	0.96
8.0	0.34	0.04	0.50	30	0.056	0.054	0.229	0.95
8.6	0.34	0.05	0.51	30	0.049	0.056	0.235	0.95
9.2	0.34	0.04	0.52	30	0.058	0.058	0.224	1.01
10.0	0.34	0.06	0.60	30	0.060	0.060	0.2196	0.96
10.5	0.34	0.07	0.70	30	0.060	0.063	0.2162	0.98
11.0	0.34	0.05	0.60	30	0.061	0.066	0.2135	0.94

D.V364C-AF

pH	r_0	ϕ_1(ns)	ϕ_2 (ns)	ϕ_3 (ns)[a]	β_1	β_2	β_3	χ_{red}^2
6.3	0.34	0.15	1.40	30	0.049	0.086	0.204	0.96
7.5	0.34	0.15	1.40	30	0.059	0.085	0.199	0.94
8.9	0.34	0.15	1.35	30	0.065	0.088	0.187	1.01
9.5	0.34	0.15	0.60	30	0.076	0.089	0.174	0.97
10.0	0.34	0.15	1.70	30	0.080	0.088	0.171	0.98

5.3 Conclusion

A correlation between the chromophore deprotonation and the conformation transition at different pH was only observed for Cph1 PGP and not for Agp1 PGP. For Cph1 PGP, we showed a direct correlation of the chromophore deprotonation with pH-dependent conformational changes in the various domains. Our results suggest that chromophore deprotonation is closely associated with a higher protein mobility (conformational space) both in proximal and in distal protein sites, implying a causal relationship that might be important for the global large protein arrangements and thus intramolecular signal transduction (Sadeghi, Balke et al. 2020). However, for Agp1, we did not observe a direct correlation of the chromophore deprotonation with pH-dependent conformational changes in distal (PHY) and proximal (CBP, GAF) domains, although the GAF domain displays a pronounced pH-dependent conformational change.

Deprotonation of an unknown residue in the chromophore binding pocket of Agp1 PGP might affect the conformational plasticity of the GAF domain. The p*K* of the pH-dependent conformational change in the CBP (pos. 279) and the GAF (pos. 295) domain is about 1.1-1.8 pH units lower (p*K* ~ 8.8-9.4) than the chromophore p*K* (~ 10.4-10.6). This suggests that another residue in the CBP deprotonates and affects the conformational plasticity of the GAF domain and more specifically in the CBP. This residue is a potential candidate for the transient deprotonation observed during the Pr to Pfr photoconversion. A p*K* of about 9 could be due to an elevated p*K* of one of the two conserved histidines in the CBP, but could also point, for instance, to a lysine or tyrosine deprotonation. Thus, while in Cph1 histidine deprotonation in the CBP affects PCB chromophore deprotonation spectra, another type of protonation heterogeneity is present in Agp1 that affects CBP conformational flexibility but not the chromophore deprotonation spectra. This type of protonation heterogeneity distinguishes Agp1 from Cph1 and might be correlated to the long-range H-bond networks observed in Cph1.

BV chromophore deprotonation is possibly not a requirement for the PHY domain conformational plasticity in Agp1. The absence of any effects of labeling in the PHY domain or V364C mutation on the chromophore p*K* indicates a different H-bond network compared to Cph1.

.

6 Results and Discussion Part III:

Fluorescent Phytochromes for *in situ* Imaging

Part of the results shown in this chapter are published in Soshichiro Nagano, Maryam Sadeghi, Jens Balke, Moritz Fleck, Nina Heckmann, Georgios Psakis & Ulrike Alexiev. *Improved fluorescent phytochromes for in situ imaging*. Scientific Reports volume 12, Article number: 5587 Publication Date: April 04, 2022, https://doi.org/10.1038/s41598-022-09169-x

This chapter aims to characterize the fluorescent properties of NIR-FPs* phytochrome variants, using fluorescence time-resolved spectroscopy and fluorescence time-resolved imaging. This characterization will be beneficial to apply the fluorescent phytochromes for in situ imaging. For this purpose, several mutants of two phytochrome species were investigated, which are known to enhance fluorescence. The studied mutants were selected from cyanobacterial phytochrome, Cph1 and Cph2 variants, and agrobacterium phytochrome, Agp2 variants. Further, the time-resolved fluorescence properties of a variant of Agp2 PGP, so-called PAiRFP2 was investigated in crystal and in solution to see the effect of the protein crystallization on fluorescence lifetime.
Moreover, the fluorescence lifetime of a Cph1 PG double mutants was measured *in vivo* and in *E.coli* cell.

* For the introduction of the near infrared fluorescent proteins (NIR-FPs) see chapter 2.

6.1 Single tyrosine mutation in Cph1 PGP

Previous works on bacterial phytochrome (Bph), cyanobacteria and plant phytochrome identified several conserved amino acids that can affect on photocycle, such as Y176 in Cph1 (Fischer and Lagarias 2004). Therefore, fluorescence is increased in phytochrome Y176H mutant with a fluorescence quantum yield of 0.1 in cyanobacteria (Fischer and Lagarias 2004). However, this mutant does not block Pfr formation and consequently it has not changed the fluorescence quantum yield in BV chromophore phytochrome family (Wagner, Zhang et al. 2008, Rockwell, Shang et al. 2009, Nieder, Stojković et al. 2013), despite the observation that the tyrosine side chain directly contacts the BV C-ring 12-propionate side chain in the crystal structure of the PaBphP Pfr state (Rockwell, Shang et al. 2009). They explained the different behavior of two group of phytochrome family has origin in characteristic feature of PCB/PΦB and BV chromophore which might be related to the different directions of bilin D-ring rotation account for these distinct classes of red/far-red photochemistry (Rockwell, Shang et al. 2009).

The residue Y176 in β1-strand of the GAF domain of cyanobacterial phytochrome Cph1 (**Fig. 6-1I**) acts as a molecular gate for the primary Z-to-E photoisomerization reaction of phytochrome's bilin prosthetic group via phenol ring rotation, this process would be significantly inhibited when tyrosine is replaced with histidine due to its highly H-bond imidazole moiety (**Fig. 6-1B**) (Fischer and Lagarias 2004). Also, the maximum chromophore absorption in the Pr state is blue-shifted from 658 nm in wide-type PGP (**Fig. 6-1A**) to 642 nm in mutant Y176H (**Fig. 6-1B**). Tyrosine 263 is a conserved amino acid among the phytochrome family; plants, cyanobacteria and bacterial phytochromes. It is placed in the chromophore binding pocket (CBP) and has the water interactions with the chromophore (**Fig. 6-1I**). The recent study on *Deinococcus radiodurans* shows the absence of the Tyr 263 hydroxyl destabilizes the β-sheet conformation of the tongue, also the water interactions are missing in Y263F which is consequently decreasing the photoconversion yield (Auldridge, Satyshur et al. 2012). The same mutant variant was studied in cyanobacterial phytochrome Cph1 and plant PhyB (Mailliet, Psakis et al. 2011, Auldridge, Satyshur et al. 2012, Sineshchekov, Mailliet et al. 2014). The residue Y263 in cyanobacterial phytochrome Cph1 (**Fig. 6-1I**) optimizes the photochemistry reactions at the prelumi-R to Lumi-R Step (Sineshchekov, Mailliet et al. 2014). Also, it was shown in *Deinococcus radiodurans* that Y263F prevent the Lumi-R formation (Takala, Lehtivuori et al. 2018). The mutant of this residue to serin and phenylalanine indicates that the photoconversion is partially taken place (**Fig. 6-1C and D**). However, the absorption shows different wavelength values of 651 nm and 642 nm in Pr maximum absorption for Y263F and Y263S, respectively.

The uncompleted photoconversion in Y176H increased the fluorescence quantum yield of mutants compare to WT.

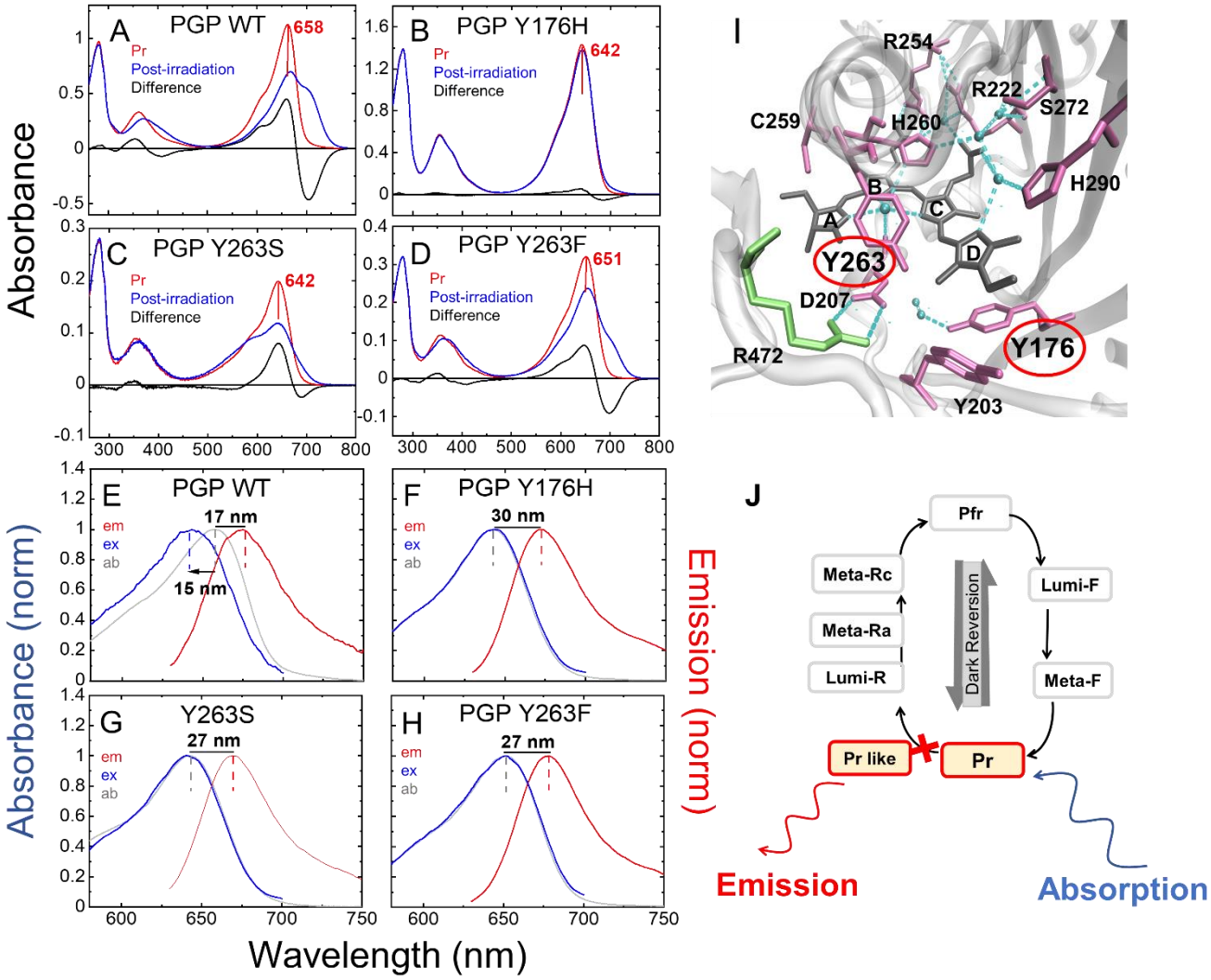

Figure 6-1: UV-vis absorption spectra of Cph1 PGP single tyrosine mutants. The dark-adapted (Pr state) and post-irradiation spectra (red light irradiated sample) are shown in red and blue, respectively. The difference spectra are shown in black. λ_{max} values for Pr are indicated. **(E-H)** Steady-state absorption, excitation, and emission spectra of Cph1 PGP single tyrosine mutants. The absorption (ab), excitation (ex) and emission (em) spectra are shown in grey, blue, and red, respectively. The Stokes shift ($\lambda_{max(em)}$- $\lambda_{max(ab)}$) is indicated. The blue shift between maximum excitation and absorption wavelength ($\lambda_{max(as)}$- $\lambda_{max(ex)}$) is indicated in (**E**). The values are summarized in **Table 6-1**. Conditions: 300 mM NaCl, 50 mM Tris pH 7.8, 20°C. The shown spectra were recorded by Soshihiro Nagano (University of Giessen). **(I)** Chromophore binding pocket of Cph1 PGP (PDB: 2VEA). The conserved tyrosine Y176 and Y263 are indicated with a red circle. (**J)** The photocycle from Pr to the Pfr state of Cph1 is shown. A complete photoconversion is inhibited in the mutants as indicated by a red cross, and a Pr-like state is assumed.

Table 6-1: Spectroscopic characteristics of phytochromes.

Cph1 PGP	$\lambda_{max(abs\_Pr)}$ (nm)	$\lambda_{max(em)}$ (nm)	Stokes shift (nm)	$^{*}\Phi_f$
WT	658	675	17	0.024 ± 001
Y176H	642	672	30	0.144 ± 002
Y263S	642	676	27	0.082 ±0 02
Y263F	651	669	27	0.125 ± 002

*Fluorescence quantum yield was calculated by Soshihiro Nagano (University of Giessen) and reported in (Nagano, Sadeghi et al.2022).

It was first reported by Fischer in 2004 that Y176H has quantum yield of 0.144 which is much higher than quantum yield of WT 0.024. **Fig. 6-1 E-H** shows the excitation, absorption and the emission of the wide-type and the single mutants. Although the wild type shows different spectra for excitation and absorption, the mutants have identical excitation and absorption spectra. We saw earlier in chapter four that the protonation heterogeneity was only observed for the Cph1 PGP WT and not for the variant Y263S. This event might be an explanation for the different excitation and absorption energy in WT. The stokes shift in WT is 17 nm which increases to 30 nm in mutant Y176H. The mutants Y263S and Y263F both has the stokes shift of 27 nm.

Fig. 6-2 shows the decay curves of Cph1 PGP wild type, and the single mutants. All samples were measured under the same conditions, in 150 mM NaCl, 50 mM Tris pH 8, at 19ºC with maximum excitation wavelength of λ_{ex} = 640 nm, and the emitted photons were collected at wavelength λ_{em}= 708±38 nm. The time-resolved fluorescence lifetime curves were fitted with two decay components according to **Eq. 3-10**, the fit results are summarized in **Table 6-2**, including lifetimes τ_i, amplitudes α_i, and the mean lifetime τ_{mean}. Cph1 PGP WT is naturally fluorescent with τ_{mean} = 0.86 ± 0.05 ns and Φ_f = 0.024 ± 001. The fluorescent affinity of this construct is significantly increased when Y176 is mutated to histidine, the weight mean lifetime and quantum yield are raised to 1.90 ± 0.05 ns and 0.144 ± 002, respectively. These results are in agreement with the recent works on this mutant for cyanobacteria and plan phytochrome (Fischer and Lagarias 2004). The single mutant Y263F was investigated before, regarding to the role of this mutant in

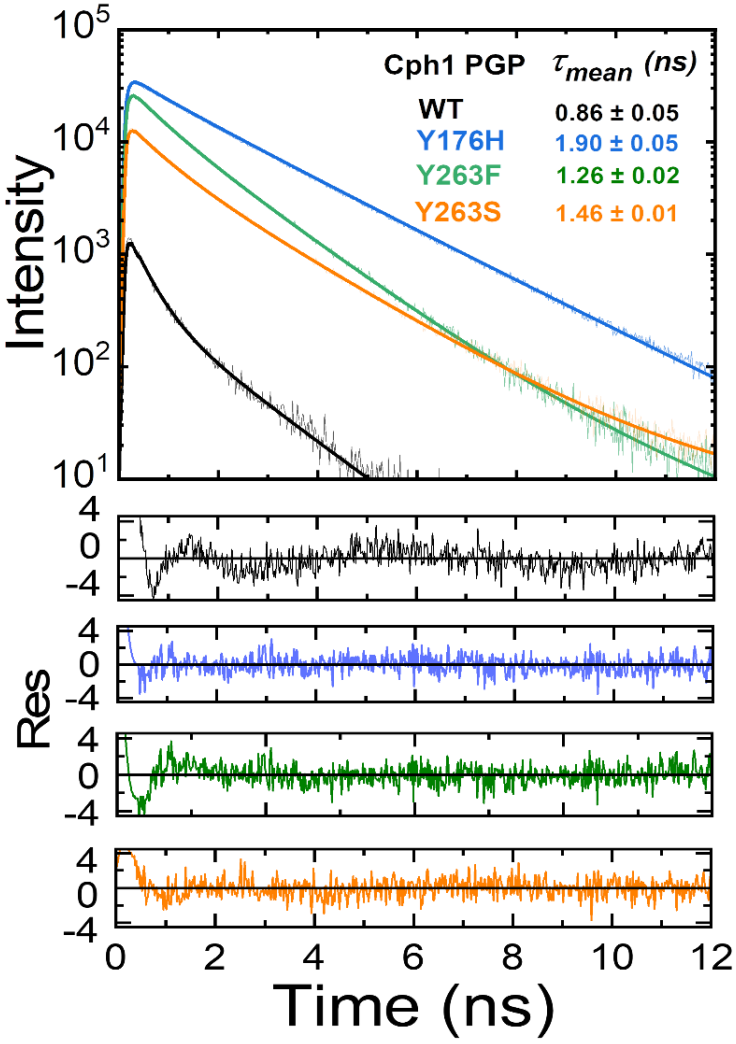

Figure 6-2: Fluorescence lifetime curves (excited state decays) of single tyrosine mutant proteins of Cph1 PGP. They are fitted to a multi- exponential decay function (**Eq.3-10**) and the fit is shown as a solid line. The residuals are shown below, and the mutant proteins are indicated by color as in the upper panel. The fluorescence lifetimes were measured in the FLIM setup, which is equipped with a white light laser system for tunable excitation. The deconvolution with the instrument response function and the temporal profile of the excitation pulse leads to the larger fit residuals in the time range up to 200 ps. The fluorescence lifetime decay fit results are summarized in **Table 6-2**. Conditions: 150 mM NaCl, 50 mM Tris pH 8, 19ºC; λ_{ex} = 640 nm, and λ_{em}= 708±38 nm.

the early step of photoconversion, the pre-lumi-R to Lumi-R Step (Sineshchekov, Mailliet et al. 2014). The fluorescence quantum yield Φ_f and lifetime for Y263F have a lower value compared to the single mutant Y176H, 0.82 ± 002, and 1.26 ± 0.02 ns, respectively.

Table 6-2: The fluorescence lifetime decay fit results. The lifetime components are τ_1, τ_2, and the related amplitudes α_1, α_2 and τ_{mean} is calculated as the population weighted mean lifetime according to the **Eq. 6-11**, and the reduced chi-square (χ_{red}^2) is given to judge the goodness of the fit.

Cph1 PGP	τ_1 (ns)	τ_2 (ns)	α_1 (%)	α_2 (%)	τ_{mean} (ns)	χ_{red}^2
WT	0.34 ± 0.01	1.30 ± 0.02	76.09 ± 1.36	23.91 ± 0.82	0.86 ± 0.05	0.93
Y176H	0.90 ± 0.05	2.00 ± 0.01	18.02 ± 0.90	81.98 ± 0.90	1.90 ± 0.05	1.27
Y263F	0.68 ± 0.01	1.47 ± 0.01	43.26 ± 0.56	56.74 ± 0.84	1.26 ± 0.02	1.14
Y263S	0.69 ± 0.03	1.76 ± 0.01	50.30 ± 0.90	49.70 ± 0.90	1.46 ± 0.01	1.19

Mutant Y263S has a lifetime of 1.46 ± 0.01 ns which is longer compared to Y263F. The WT was fitted with two components exponential fit, while the mutant Y176H could be fitted monoexponentially, as the first amplitude with a short lifetime (~18%) is low compared to the WT (~76 %) (**Table 6-2**). This might be related to the increasing the fluorescence quantum yield of Y176H in comparison to the WT. According to the **Eq. 2-20**, the fluorescence quantum yield can increase when the nonradiative rate is minimized, which is mostly related to the fluorophore interaction with its environment, such as hydrogen bond network and the chromophore isomerization. As we discussed earlier, the photoconversion is blocked in this mutant (Y176H), this might be a reason for reducing the interaction of the chromophore with its immediate environment and consequently, decreasing of the nonradiative rate. Moreover, this event also reduces the interaction complexity of the chromophore with hydrogen bond network in the chromophore binding pocket, which result of more homogeneous nonradiative decay rate. Therefore, the constructs with higher fluorescence quantum yield have mono-exponentially fit, which means of less interaction events with surrounding. For the mutants of Y263F, and Y263S the first and second amplitude are more in the same range (α_1 ~ 43-50%, α_1 ~ 50-56%, **Table 6-2**) compared to the WT (α_1 ~ 76%, α_1 ~ 24%, **Table 6-2**) that the first amplitude is about five times is bigger than the second amplitude. In this substitution, as the absorption also shows, the photoconversion is partially taken place, and it is not like the mutant Y176H which is trapped in Pr like state. If the first amplitude represents a specific biochemical process, it seems this event decreasing gradually from WT to the single mutants Y263F, Y263S and Y176H, while the second amplitude is increasing form WT to the single mutants. As we discussed earlier, the water molecule connection is missing in mutant Y263F, this can be a reason for minimizing the non-radiation rate, which increases the second lifetime with higher amplitude in two single mutants of Y263S and Y263F. The first

amplitude is reduced significantly in mutant Y176H (~18 %) compared to WT (~76 %). As we saw earlier in absorbance spectra of Y176H, the photoconversion is not taking place in this mutant, as well as the D-ring isomerization. The approximately mono-exponential decay of Y176H reveals this fact that the nonradiative rate related to first amplitude are significantly minimized. A previous time-resolved fluorescence study on Cph1 PGP WT and the mutant Y176H indicated a biexponential and mono-exponential for WT and Y176H, respectively (Fischer and Lagarias 2004). According to these results, it seems the first component reflects the events that happening next to ring-D and the connection with the conserved water molecule, which has high amplitude in WT with a low lifetime due to the high rate of the non-radiative decay (see **Table 6-2**).

6.2 Double tyrosine mutation of Cph1 PGP

The double mutant variants Cph1 PGP Y176H/Y263S and Cph1 PGP Y176H/Y263F show the same, blue-shifted absorption maximum of the chromophore peak in the Pr state, λ_{max} = 642 nm as the single mutant Cph1 PGP Y176H (**Fig. 6-3A, 6-3B, Table 6-3)**. Also, the photoconversion is inhibited in these variants similar to the single mutant Cph1 PGP Y176H (**Fig. 6-3A, 6-3B, Table 6-3).** The steady-state fluorescence characterization of the double mutants was performed to investigate the effect of combining mutations known to enhance fluorescence in Cph1 on fluorescence quantum yield. Both double tyrosine mutants have a synergistic effect on fluorescence, Cph1 PGP Y176H/Y263F and Cph1 PGP Y176H/Y263S, with fluorescence quantum yields of Φ_f = 0.160 ± 0.002 and Φ_f = 0.176 ± 0.002, respectively, both higher than the single tyrosine mutants Y176H, Y263S, and Y263F (**Table 6-3**).

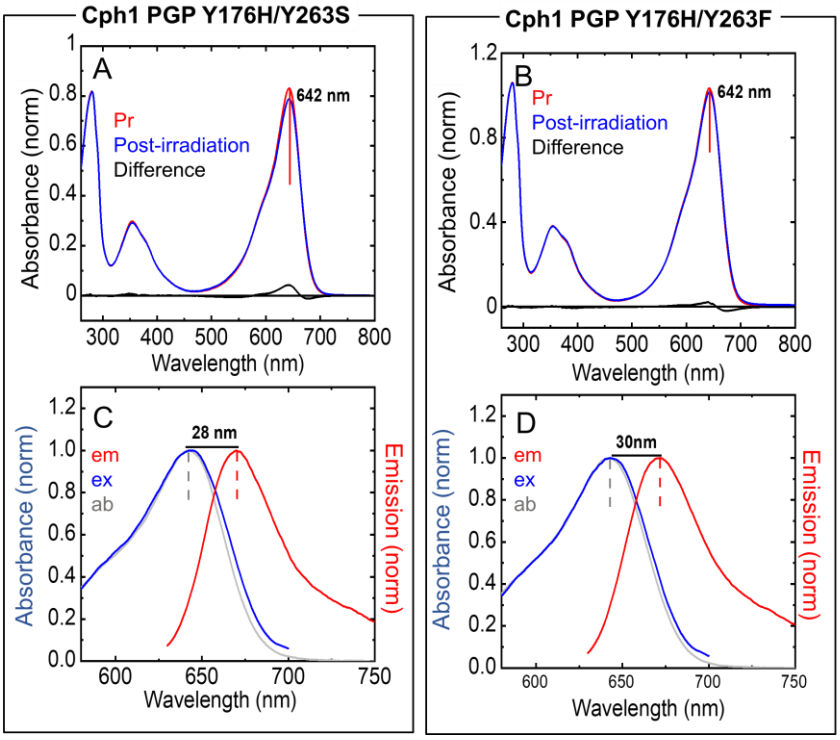

Figure 6-3: (A-B) UV-vis absorption spectra of Cph1 PGP double tyrosine mutants. The dark-adapted (Pr state) and post-irradiation spectra (red light irradiated sample) are shown in red and blue, respectively. The difference spectra are shown in black. λ_{max} values for Pr are indicated. **(C-D)** Steady-state absorption, excitation, and emission spectra of Cph1 PGP double tyrosine mutants. The absorption (ab), excitation (ex) and emission (em) spectra are shown in grey, blue, and red, respectively. The Stokes shift ($\lambda_{max(em)}$- $\lambda_{max(ab)}$) is indicated. The values are summarized in **Table 6-3**. Conditions: 300 mM NaCl, 50 mM Tris pH 7.8, 20°C. The shown spectra were recorded by Soshihiro Nagano (University of Giessen).

Table 6-3: Spectroscopic characteristics of of double tyrosine mutants of Cph1 PGP and the comparison with single tyrosin mutant Y176H.

Cph1 PGP	$\lambda_{max(abs\_Pr)}$ (nm)	$\lambda_{max(em)}$ (nm)	Stokes shift (nm)	$^{*}\Phi_f$
Y176H	642	672	30	0.144 ± 0.020
Y176H /Y263S	642	670	28	0.176 ± 0.002
Y176H /Y263F	642	672	30	0.160 ± 0.002

*Fluorescence quantum yield was calculated by Soshihiro Nagano (University of Giessen) and reported in (Nagano, Sadeghi et al.2022).

The fluorescence lifetime of all the samples were measured under the same conditions, in 150 mM NaCl, 50 mM Tris pH 8, at 19ºC with maximum excitation wavelength of λ_{ex} = 640 nm, and the emitted photons were collected at wavelength λ_{em}= 708±38 nm. The time-resolved fluorescence lifetime curves were fitted with two decay components according to **Eq. 3-10**, the fit results are summarized in **Table 6-4**, including lifetimes τ_i, amplitudes α_i , and the mean lifetime τ_{mean} . In contrast to higher fluorescence quantum yield of double mutants, the mean lifetime remains unchanged for the variant Y176H/Y263S with value of 1.92±0.01 ns and slightly increase for the variant Y176H/Y263F with value of 2.00 ± 0.01 ns (**Fig. 6-4, Table 6-4**). Regarding to the values of the first amplitude α_1 in **Table 6-4**, this value is reduced in double mutants, compared to the single mutants Y263S, and Y263F in **Table 6-2**. This result confirms a lower non-radiative rate of the first amplitude in the double mutant (~10-18 %) similar to single mutant Y176H (~ 18 %), which is caused by a less contribution of the chromophore with its immediate environment. Moreover, as we saw earlier, the mutants Y263F and Y263S didn't enhance the fluorescence quantum yield as much as variant Y176H. Also, the absorption shows, the photoconversion is partially taken place, while in Y176H the photoconversion is locked in Pr like.

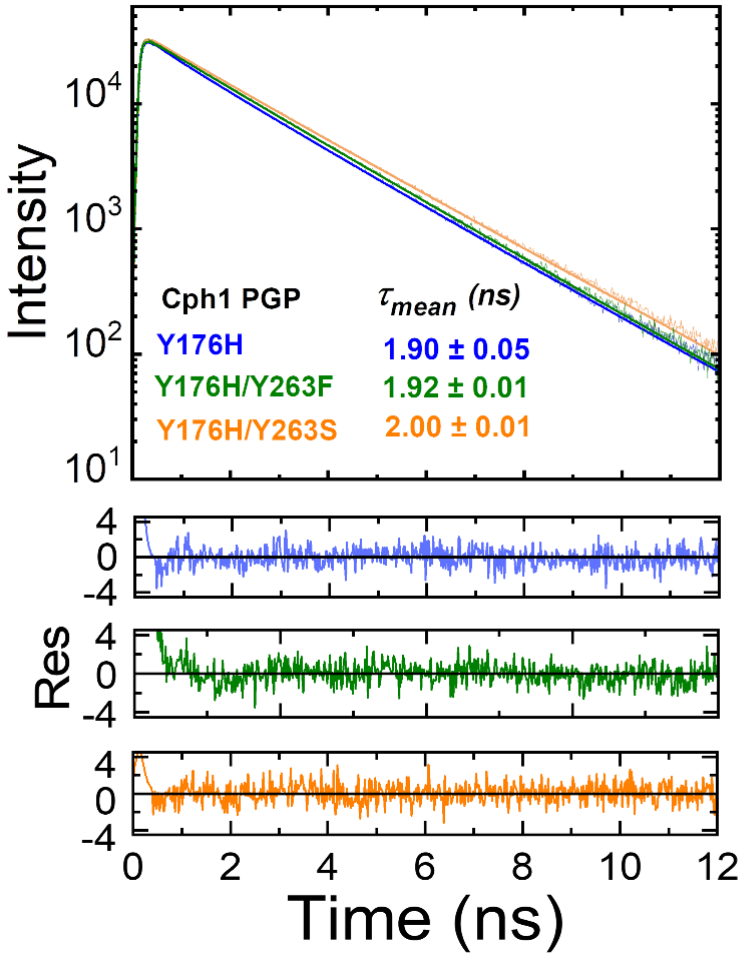

Figure 6-4: Fluorescence lifetime decays of Cph1 PGP double tyrosine mutant proteins are compared to the lifetime curve of the single tyrosine mutant Y176H. The residuals are shown , the different variants are indicated by color as in the upper panel. The curves were measured under the same conditions. The fluorescence lifetimes were measured in the FLIM setup, which is equipped with a white light laser system for tunable excitation. The deconvolution with the instrument response function and the temporal profile of the excitation pulse leads to the larger fit residuals in the time range up to 200 ps The fluorescence lifetime decay fit results are summarized in **Table 6-4**. Conditions: 150 mM NaCl, 50 mM Tris pH 8, 19ºC; λ_{ex}= 640 nm, and λ_{em} = 708±38 nm.

Table 6-4. The fluorescence lifetime decay fit results of Cph1 PGP double tyrosine mutant proteins are compared to fluorescence decay component of the single tyrosine mutant protein Y176H. The lifetime components τ_1, τ_2, and the related relative amplitudes α_1, α_2 are given. τ_{mean} is calculated as the population weighted mean lifetime according to the **Eq. 3-11**. The reduced chi-square (χ_{red}^2) is given to judge the goodness of the fit.

Cph1 PGP	τ_1 (ns)	τ_2 (ns)	α_1 (%)	α_2 (%)	τ_{mean} (ns)	χ_{red}^2
Y176H	0.90 ± 0.05	2.00 ± 0.01	18.02 ± 0.90	81.98 ± 0.90	1.90 ± 0.05	1.27
Y176H/Y263S	0.84 ± 0.08	2.06 ± 0.01	10.14 ± 0.97	89.86 ± 0.97	1.92 ± 0.01	1.14
Y176H/Y263F	0.42 ± 0.03	1.95 ± 0.00	8.64 ± 0.45	91.36 ± 0.45	2.00± 0.01	1.23

6.3 Cph1 PG WT and its variants

In plant and cyanobacterial phytochromes, highly conserved GAF and PHY photosensory domains appear essential to phytochrome photochemical and photophysical properties (Wu and Lagarias 2000, Oka, Matsushita et al. 2004). Among the phytochrome family, PHY domain specifically is essential for the photoconversion and signaling, therefore the absent of this domain can result the photoconversion inhibition. In this section Cph1 PG WT, in which this construct lacks the PHY domain, and its variants Y176H and Y176H/Y263S were investigated, to test the effect of removing the PHY domain on fluorescence quantum yield and fluorescence lifetime.

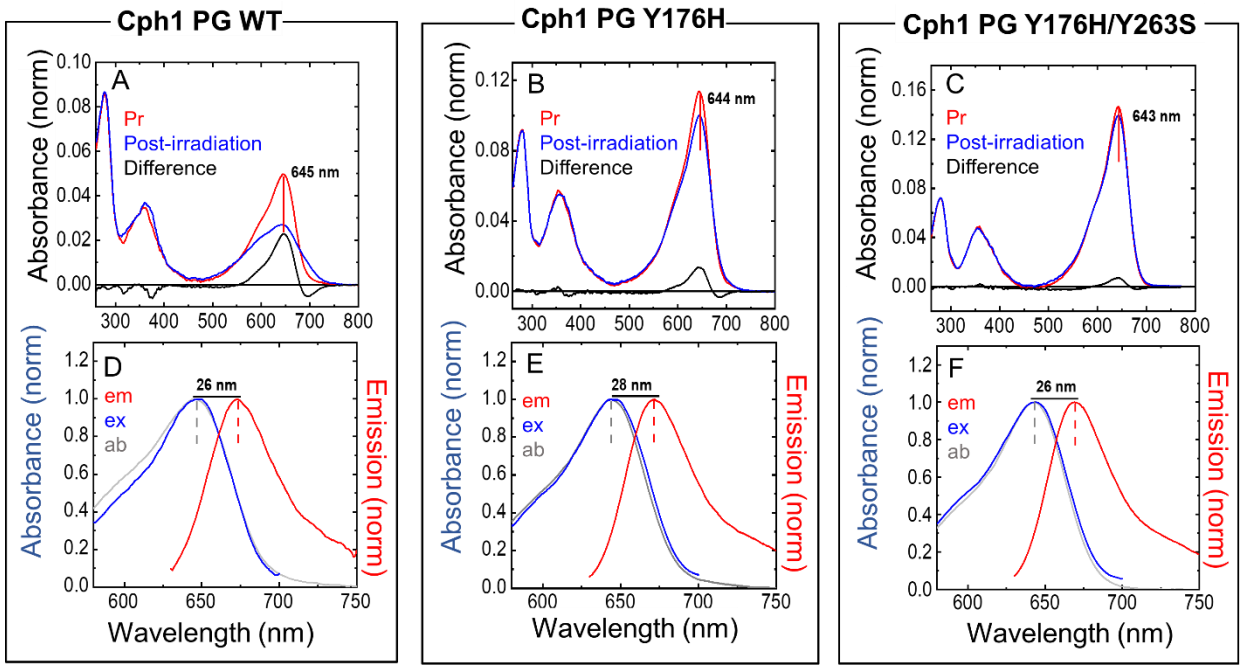

Figure 6-5: **(A-C)** UV-vis absorption spectra of Cph1 PG variants. The dark-adapted (Pr state) and post-irradiation spectra (red light irradiated sample) are shown in red and blue, respectively. The difference spectra are shown in black. λ_{max} values for Pr are indicated. All PG variant spectra indicate incomplete photoconversion and it seems these variants are locked in a Pr like state with the maximum absorption of 645, 644 and 643 nm for WT, Y176H and Y176H/Y263S, respectively. **(D-F)** Steady-state absorption, excitation, and emission spectra of Cph1 PG variants. The absorption (ab), excitation (ex) and emission (em) spectra are shown in grey, blue, and red, respectively. The Stokes shift ($\lambda_{max(em)}$- $\lambda_{max(ab)}$) is indicated. The values are summarized in **Table 6-5**. Conditions: 300 mM NaCl, 50 mM Tris pH 7.8, 20°C. The shown spectra were recorded by Soshihiro Nagano (University of Giessen).

Table 6-5: Spectroscopic parameters of Cph1 PG single and double tyrosine mutant proteins as shown in Fig. 6-5.

Cph1	$\lambda_{max(abs\_Pr)}$ (nm)	$\lambda_{max(em)}$ (nm)	Stokes shift (nm)	$^{*}\Phi_f$
PG WT	645	649	26	0.018± 0.001
PG Y176H	644	644	28	0.108 ± 0.002
PG Y176H /Y263S	643	644	26	0.171 ± 0.003

*Fluorescence quantum yield was calculated by Soshihiro Nagano (University of Giessen) and reported in (Nagano, Sadeghi et al.2022).

The UV-vis absorption shows for PG WT a hypochromic shift of 13 nm of the Pr absorption band with respect to its PGP WT counterpart (**Fig. 6-5A, Table 6-5**). The absorption maxima of both PG variants Y176H and Y176H/Y263S in the Pr state are blue shifted with λ_{max} values of 644 nm and 643 nm, respectively (**Fig. 6-5B**, **6-5C, Table 6-5)**. The photoconversion of Y176H single mutant behaved similarly in both PGP and PG constructs, however, the Pr peak showed a weaker photo bleach in the PGP background (3.7% *vs.* 11.9%) (Nagano, Sadeghi et al.2022). Y263S mutants in both constructs PGP and PG indicated similar photobleaching behavior to Y176H (~4.8%) (**Fig. 6-5C**). As we have seen earlier the uncompleted photoconversion can scientifically enhance the fluorescence emission e.g., in Y176H and Y263S, while in the case of PG WT, the fluorescence quantum yield is even reduced to 0.018 ± 0.001 compared to PGP construct (0.024 ± 0.001). However, a recent study on DrBphP and RpBphP3, revealed that the remove of the PHY domain could enhance Φ_f from 0.017 to 0.025 and from 0.043 to 0.055, respectively (Toh, Stojkovic et al. 2011, Takala, Lehtivuori et al. 2018). The variants Cph1 PG Y176H and Y176H/Y263S both enhance the quantum yield compared to PG WT to 0.108 ± 0.002 and 0.171 ± 0.003, respectively. While, in variant Y176H similar to WT, the quantum yield is lower in the equivalent variant in PGP construct. In the case of double mutants Y176H/Y263S the quantum yield is equal, in the range of error values, in both PGP and PG construct, 0.176 ± 0.002 and 0.171 ± 0.003, respectively.

The fluorescence lifetime of all the samples were measured under the same conditions, in 150 mM NaCl, 50 mM Tris pH 8, at 19ºC with maximum excitation wavelength of λ_{ex} = 640 nm, and the emitted photons were collected at wavelength λ_{em}= 708±38 nm. The time-resolved fluorescence lifetime curves were fitted with two decay components according to **Eq. 3-10**, the fit results are summarized in **Table 6-6**, including lifetimes τ_i, amplitudes α_i, and the mean lifetime τ_{mean}. **Fig. 6-6** illustrated the comparison of the lifetime in PGP and PG construct, WT and their variants.

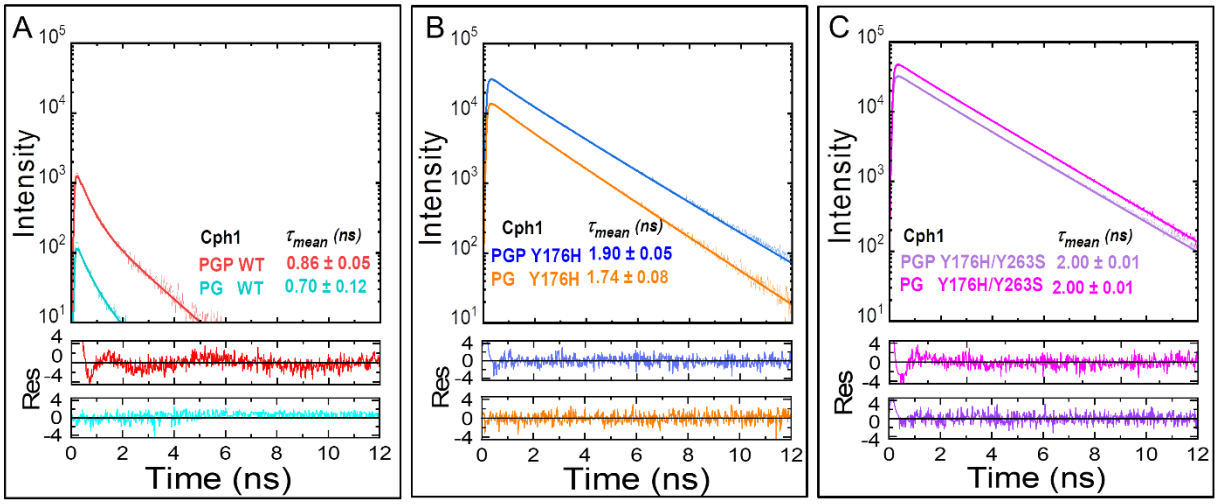

Figure 6-6: Fluorescence lifetime decays of Cph1 PG WT and its variants are compared with Cph1 PGP WT and the respective PGP variants. (**A**) WT (**B**) Y176H (**C**) Y176H/Y263S. The residuals are shown, the different variants are indicated by color as in the upper panel. The fluorescence lifetimes were measured in the FLIM setup, which is equipped with a white light laser system for tunable excitation. The deconvolution with the instrument response function and the temporal profile of the excitation pulse leads to the larger fit residuals in the time range up to 200 ps. The fluorescence lifetime decay fit results are summarized in **Table 6-6**. The curves were measured under the same conditions. Conditions: 150 mM NaCl, 50 mM Tris pH 8, 19ºC; λ_{ex} = 640 nm, and λ_{em} = 708±38 nm.

Table 6-6: The fluorescence lifetime decay fit results of phytochromes of Cph1 PGP single and double tyrosine mutant proteins. The lifetime components with τ_1, τ_2, and the related relative amplitudes α_1, α_2 are given. τ_{mean} is calculated as the population weighted mean lifetime according to the **Eq. 3-11.** The reduced chi-square (χ_{red}^2) is given to judge the goodness of the fit.

Cph1	τ_1 (ns)	τ_2 (ns)	α_1 (%)	α_2 (%)	τ_{mean} (ns)	χ_{red}^2
PG WT	0.19 ± 0.20	0.86 ± 0.02	61.32 ± 1.74	38.68 ± 2.32	0.70 ± 0.12	0.94
PG Y176H	0.70 ± 0.04	1.87± 0.006	15.23 ± 0.41	84.77 ± 0.82	1.74 ± 0.08	1.11
PG Y176H/Y263S	0.76 ± 0.05	2.050 ± 0.004	8.70 ± 0.48	91.30 ± 0.97	2.00 ± 0.01	1.32

The fit result of PG variants is summarized in **Table 6-6**. The mean lifetime of PG WT and the variant Y176H are 0.70 ± 0.12 and, 1.74 ± 0.08 ns, respectively, which are shorter than PGP WT and PGP Y176H. However, the double mutant Y176H/Y263S has the same mean lifetime in both constructs with the value of 2.00 ± 0.01 ns. The first amplitude has larger value in WT (~ 61 %), compared to the mutants (~8-15%) as we saw earlier for PGP constructs. However, the ratio between two amplitudes is smaller in PG construct (~1.5), in comparison to PGP (~3.1), in which PG has lower first amplitude value and larger second amplitude (α_1 ~ 61 %, α_2 ~ 39 %, **Table 6-6**). This result was expected considering the earlier discussion, the inhibition of the photoconversion can reduced the nonradiative rate which led to decreasing of the first amplitude with a shorter lifetime and increasing the second amplitude with a longer lifetime. However, the mean lifetime of PG (0.70 ns) construct is shorter than the PGP (0.86 ns) construct.

6.4 *SyB*-Cph2 WT and its variant D86H

The construct *SyB*-Cph2 has only GAF and PHY domain. UV-vis absorption indicated the *SyB*-Cph2 PG fragments indicate the maximum absorption of the chromophore in the Pr state is 632 nm for WT, 631 nm for the variant D86H. Photoconversion to Pfr takes place in the WT (**Fig. 6-7A**), but not in the D86H mutant (**Fig. 6-7B**), in agreement with a previous report (Ulijasz, Cornilescu et al. 2008).

Although SyB-Cph2 WT indicated a complete photoconversion, this construct is naturally fluorescent with considerably a high quantum yield of 0.124 ± 0.003 compared to Cph1 PGP (0.024 ± 001) and PG (0.018±0.001) wild type construct. The steady-state fluorescence properties of *SyB*-Cph2 GP D86H variant was characterized in a previous work (Ulijasz, Cornilescu et al. 2008). They reported this variant "five times more fluorescent" than Cph1 PGP Y176H. However, we reported the value of Φ_f = 0.202 ± 0.003 for this variant (**Table 6-7**) which is two times more fluorescent than Cph1 PGP Y176H (Nagano, Sadeghi et al.2020). The different results might be because of the used excitation wavelengths which was 360 nm in the Ulijasz study (Ulijasz, Cornilescu et al. 2008) *vs*. 610 nm here and in Maillet *et al*. To check this possibility, Soshihiro Nagano (University of Giessen) measured emission spectra based on both excitation wavelengths, adjusting the dilution appropriately to give similar absorbances at the excitation wavelength (Nagano, Sadeghi et al.2022). This measurement showed that the used excitation wavelength has a minimal effect. Considering the Kasha's rule, the fluorescence only occurs from the S_1 excited state to the S_0 ground state (**Fig. 2-3**) which indicates that fluorescence is independent of excitation wavelength for the same fluorescence state. Therefore, we can assume that the Soret band around 350 nm corresponds to an S_2 state that can favorably relax to S_1 which it agrees with Kasha's rule. The samples in Ulijasz *et al*. work, were standardized at an absorbance of $A_{\lambda max,\ red}$ = 0.6, which makes it hard to estimate the differences in red/Soret

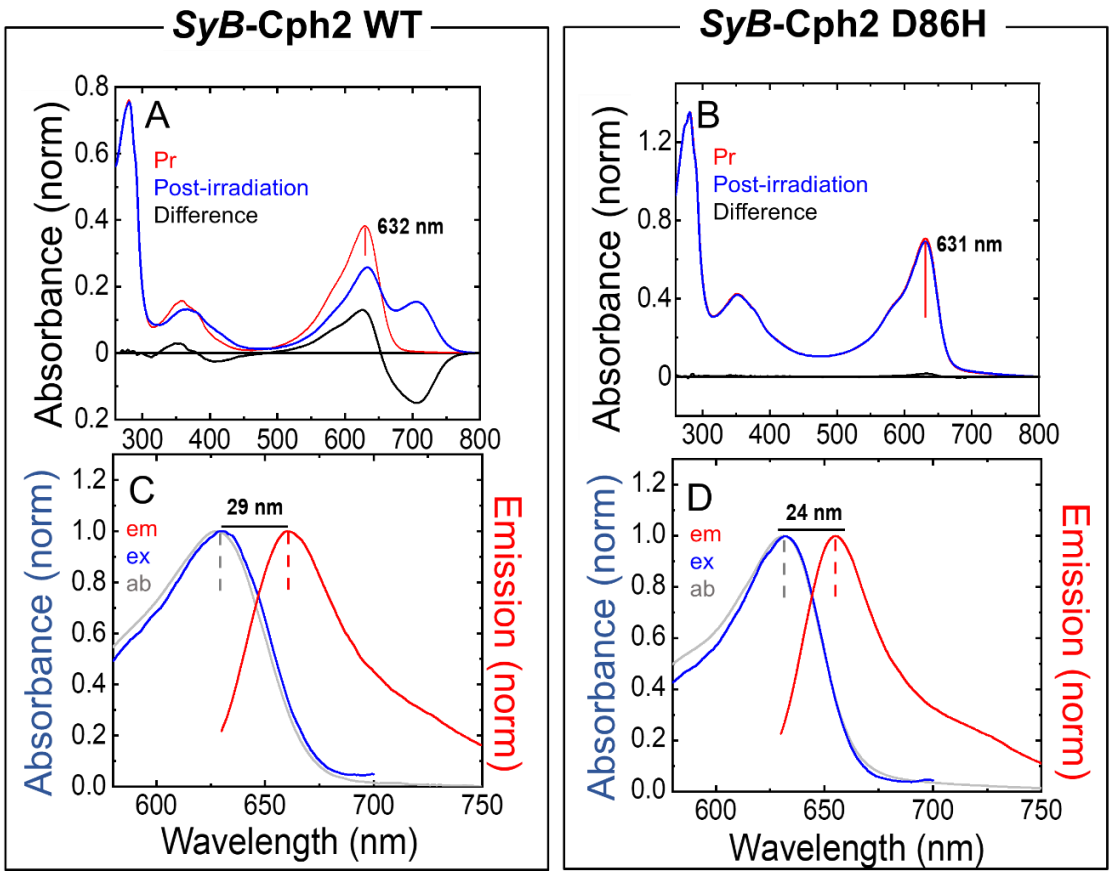

Figure 6-7*:* **(A-B)** UV-vis absorption spectra of SyB-Cph2 WT and its mutant D86H. The dark-adapted (Pr state) and post-irradiation spectra (red light irradiated sample) are shown in red and blue, respectively. The difference spectra are shown in black. λ_{max} values for Pr are indicated. D86H spectra indicates incomplete photoconversion and it seems these variants are locked in a Pr like state with the maximum absorption 631. **(C-D)** Steady-state absorption, excitation, and emission spectra of SyB-Cph2 WT and its mutant D86H. The absorption (ab), excitation (ex) and emission (em) spectra are shown in grey, blue, and red, respectively. The Stokes shift ($\lambda_{max(em)}$- $\lambda_{max(ab)}$) is indicated. The values are summarized in **Table 6-7**. Conditions: 300 mM NaCl, 50 mM Tris pH 7.8, 20°C. The shown spectra were recorded by Soshihiro Nagano (University of Giessen).

band oscillator ratios between different holoproteins when exciting the Soret band at 360 nm. However, still there is clearly a different excitation and biased quantification which cannot explain the discrepancy in fluorescence quantum yield of the *SyB*-Cph2 GP D86H construct from the oscillator ratio. The differences in fluorescence quantum yield might derives from using a much higher concentration of the sample than given in the paper due to a dilution error (Nagano, Sadeghi et al.2022). It should also be considered a large difference between excitation and absorption spectrum of *SyB*-Cph2 GP D86H shown by Ulijasz *et al.* which such differences are perhaps not impossible, while unusual. However, the excitation and absorption

Table 6-7: Spectroscopic parameters of SyB-Cph2 WT and the variant D86H as shown in Fig. 6-7.

SyB-Cph2	$\lambda_{max(abs\_Pr)}$ (nm)	$\lambda_{max(em)}$ (nm)	Stokes shift (nm)	$^{*}\Phi_f$
WT	632	631	29	0.124 ± 0.003
D86H	632	632	23	0.202 ± 0.003

*Fluorescence quantum yield was calculated by Soshihiro Nagano (University of Giessen) and reported in (Nagano, Sadeghi et al.2022).

spectra of *SyB*-Cph2 GP D86H reported here and in (Nagano, Sadeghi et al.2022) are similar at a low protein concentration (**Fig. 6-7. D**). On the other hand, by increasing the sample concentration to ~30 µM (~1.5 mg/ml or higher), it is possible to reproduce an artefactual excitation spectrum like the work of Ulijasz *et al.* (Nagano, Sadeghi et al.2022). This measurement showed, such artifacts in fluorescence spectroscopy can arise in high concentration samples because of the excitation light gradients and fluorescence reabsorption, which should be included into the calculation of the fluorescence quantum yield. Therefore, the fluorescence quantum yield of *SyB*-Cph2 GP D86H considering this error should be about 20% (0.202 ± 0.003) (**Table 6-7**), not 60% as published (Ulijasz, Cornilescu et al. 2008). The fluorescence lifetime of all the samples were measured under the same conditions, in 150 mM NaCl, 50 mM Tris pH 8, at 19ºC with maximum excitation wavelength of λ_{ex} = 640 nm, and the emitted photons were collected at the wavelength λ_{em}= 708±38 nm. The time-resolved fluorescence lifetime curves were fitted with two decay components according to **Eq. 3-10**, the fit results are summarized in **Table 6-8**, including lifetimes τ_i, amplitudes α_i, and the mean lifetime τ_{mean}. Time-resolve fluorescence characterization of *SyB*-Cph2 GP WT and its mutant D86H in the Pr state (**Fig. 6-8**) gave the mean lifetime of about 2.07 ± 0.01ns which is much larger values than for Cph1 WT. The variant D86H indicated a larger mean lifetime compared to the WT, with value of 2.60 ± 0.01ns (**Table 6-7** and **Table 6-8**). Opposite to Cph1 PGP WT and Cph1 PG WT, *SyB*-Cph2 GP WT indicates a low first amplitude (~10 %) and higher second amplitude (~90%) which led to a considerably higher mean lifetime of this construct. The earlier discussion does not apply here, as the *SyB*-Cph2 GP WT carries the photoconversion. Minimizing the nonradiative rate might be because of removing the PAS domain or different photoconversion mechanisms in *SyB*-Cph2 GP. However, recent works on some cyanobacterial phytochrome suggest that the PAS domain does not contribute residues that directly participate in the primary photoisomerization process (Montgomery and Lagarias 2002). Among

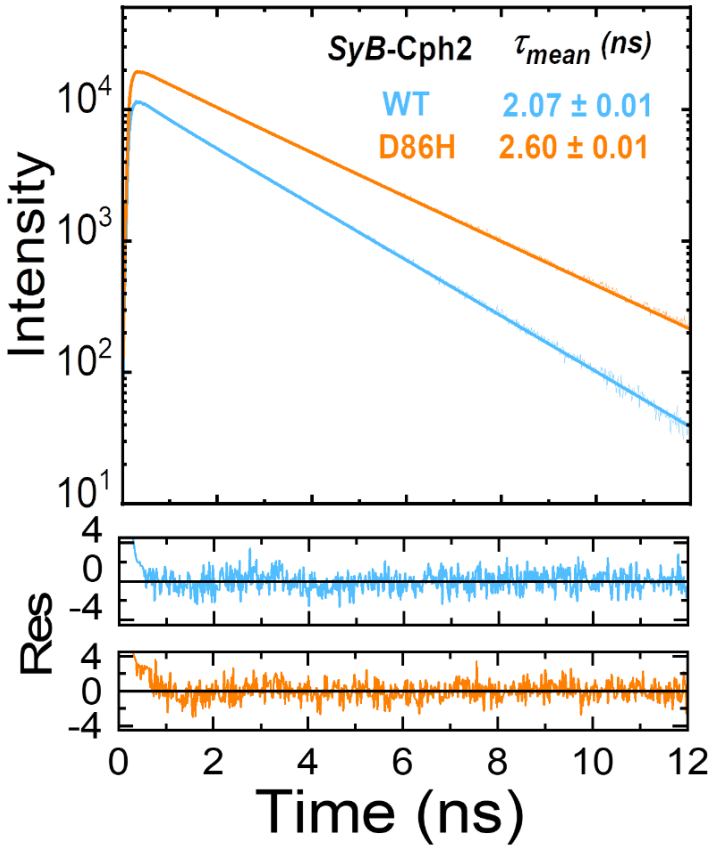

Figure 6-8: Fluorescence lifetime curves of *SyB*-Cph2 WT and the variant D86H. The mean fluorescence lifetime is indicated. The residuals are given in the lower panel, WT and the variant D86H are indicated by color as in the upper panel. The curves were measured under the same conditions. The fluorescence lifetimes were measured in the FLIM setup, which is equipped with a white light laser system for tunable excitation. The deconvolution with the instrument response function and the temporal profile of the excitation pulse leads to the larger fit residuals in the time range up to 200 ps. The values are summarized in **Table 6-8**. Conditions: 150 mM NaCl, 50 mM Tris pH 8, 19ºC; λ_{ex} = 640 nm, and λ_{em} = 708±38 nm.

the fluorescent protein, *SyB*-Cph2 GP wild type and mutant D86H have the longest fluorescence lifetime, which makes this protein appropriate for the optogenetic tools. The lifetime decay of *SyB*-Cph2 WT and its mutant are mono-exponentially as the first amplitude is smaller than the second one ($\alpha_1 \sim 8$ %, $\alpha_2 \sim 92$ %, **Table 6-8**). The increase in fluorescence quantum yield of *SyB*-Cph2 might be because of its lower absorption coefficient compared to Cph1 PGP.

Table 6-8: The fluorescence lifetime decay fit results. The lifetime components are τ_1, τ_2, and the related amplitudes α_1, α_2 and τ_{mean} is calculated as the population weighted mean lifetime according to the **Eq.3-11**, and the reduced chi-square (χ_{red}^2) is given to judge the goodness of the fit.

SyB-Cph2	τ_1 (ns)	τ_2 (ns)	α_1 (%)	α_2 (%)	τ_{mean} (ns)	χ_{red}^2
WT	0.60 ± 0.05	2.12 ± 0.005	9.36 ± 0.49	90.64 ± 0.50	2.07 ± 0.01	1.11
D86H	0.91 ± 0.01	2.65 ± 0.01	7.50 ± 0.62	92.50 ± 3.12	2.60 ± 0.01	1.23

6.5 Agp2 PGP WT and its variants

The steady-state and time-resolved fluorescence properties of Agp2 PGP variants were investigated. The studied variants are V244F, R211A and Y165F, which are indicated in the crystal structure image of Agp2 PGP in **Fig. 6-9J.** Recent study on Agp2 PGP mutants of R211A, Y165F, H278A, and F192A, revealed no effect of these variants on the BV structure in the dark-adapted state, Pfr state, including the characteristic Pfr properties of bathy phytochromes, such as the protonated propionic side chain of ring C of BV (Kraskov, Nguyen et al. 2020). While the mutants R211A, Y165H showed that the photocycle is locked in the meta-F intermediate state, and they avoid forming the Pr state (Schmidt, Sauthof et al. 2018). This is proved by weak deprotonation of the propionic side chain of the BV-ring C and the lack of keto-enol tautomerization at the carbonyl group of ring-D (Kraskov, Nguyen et al. 2020). UV-vis spectroscopic kinetic measurements showed an extremely slow dark reversion of Y165F variant compared to R211A which behaves similar to the wild type (Kraskov, Nguyen et al. 2020). These results show how the residue Y165 helps to conduct the immediate deprotonation of the ring C propionic side chain, while R211 locks the deprotonated propionate residue thus preventing it from re-protonation in a reverse process (Kraskov, Nguyen et al. 2020).

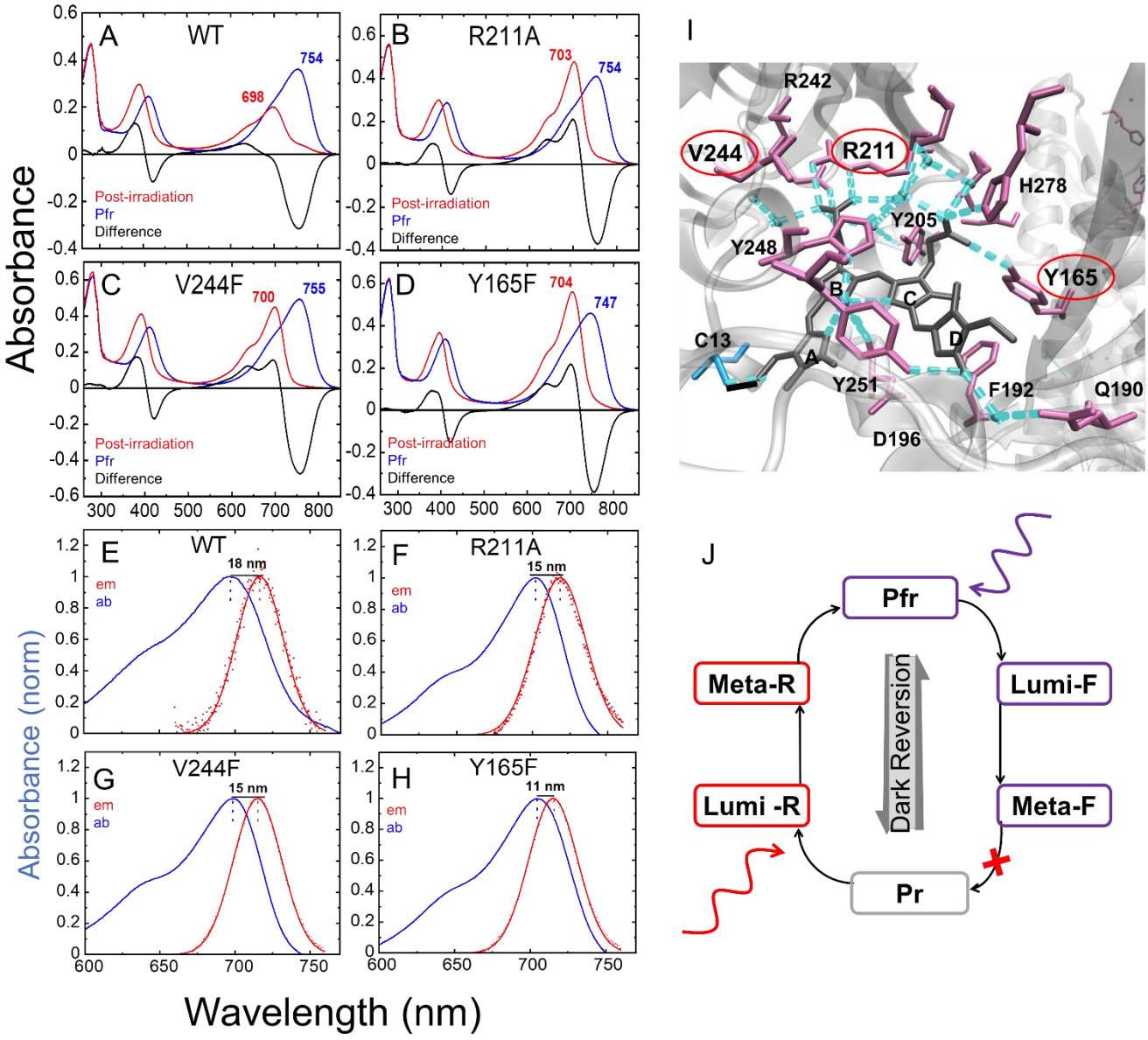

Figure 6-9: (**A-D**) UV-vis absorption spectra of Agp2 PGP variants. The dark-adapted (Pfr state) and (far-red light irradiated sample) are shown in blue and red, respectively. The difference spectra are shown in black. λ_{max} values for Pfr and post-irradiation spectra are indicated. (**E-H**) Steady-state absorption, excitation, and emission spectra of Agp2 PGP variants. The absorption (ab) and emission (em) spectra are shown in blue and red, respectively. The emission spectra (dotted line) were fitted by a gaussian (solid line) to obtain the lmax values. The Stokes shift ($\lambda_{max(em)}$- $\lambda_{max(ab)}$) is indicated. The values are summarized in **Table 6-9**. Conditions: 150 mM NaCl, 50 mM Tris pH 7.8, 20°C. (**I**) Chromophore binding pocket Agp2 PGP (PDB: 6G1Y). The residues Y165, V244, and R211 are indicated with a red circle. (**J**) The photocycle from Pfr to the Pr state in Agp2 is shown. In the mutants the photoconversion is stopped in Meta-F and this is indicated by a red cross (Schmidt 2018).

UV-vis absorption measurements of all studied constructs were performed under the same conditions; in buffer 300 mM NaCl, 30 mM HEPES 7.8, 20°C. The protein was measured in ambient green light for a dark-adapted state, and it was illuminated for 1 min, using LED 780 nm to measure the illuminated state. As Agp2 WT and R211A show a fast-dark reversion, the absorption measurement of the illuminated state was carrying on while the sample was illuminated, due to have a complete absorption spectrum for the illuminated state. **Fig. 6-9A-D** show the absorption of Agp2 PGP WT and the mutants, dark-adapted state (Pfr) in blue, illuminate state in red and the difference spectra in black. The maximum absorption of WT in the Pfr is 754 nm which is identical to the mutant R211A. This value is slightly changed in V244F to 755nm, while it is about 7 nm blue-shifted to 747 in Y165F. The maximum absorption in the Pr state for WT, and the variants R211A, and Y165F are almost the same with values of 703 nm and 704 nm, respectively. However, it is different for V244F with value of 700 nm. The hydrogen bond network of Agp2 PGP in Pfr indicates the hydrogen bond between Y165 and propionate side chain C (**Fig. 6-9I**), while this hydrogen bond is removed in Meta-F form or Pr form (Schmidt, Sauthof et al. 2018). The lack of this hydrogen bond between the F165 and ring C might be the reason for the blue-shift maximum absorption in the Pfr state of Y165F compared to WT, while there is no obvious change in the Pr maximum absorption compared to R211A (**Fig. 6-9B, 6-9D**). However, as we discussed earlier based on RR spectroscopy research, this variant does not influence on the BV structure in the Pfr state which includes the protonated propionic side chain of ring C of BV, but a different absorption in the Pfr state compared to WT was observed (**Fig. 6-9A, 6-9D**). The same argument will be applied to the variant V244F, when it is in the Pfr state this residue does not have any hydrogen bond with chromophore, therefore it has identical maximum absorption as WT. While the maximum absorption of this mutant in the Pr state has about 4 nm blue-shifted compared to WT. This might be caused by dislocation of this residue to the chromophore, although in this case there was not any formed hydrogen bond between F244 and the chromophore in the crystal structure of PAiRFP2 (Schmidt, Sauthof et al. 2018). **Fig. 6-9E-H** shows the normalized absorption and emission spectra of Agp2 WT and its variants. The conditions for measuring the emission spectra were similar to UV-vis measurement. The fluorescence emission was recorded between 600-760 nm, with excitation wavelength of 640 nm. The stokes shift was indicated in **Fig. 6-9E-H,** which is 18 nm for WT, 15 nm for mutants R211A and V244F and 11 nm for Y165F. The steady-state characterization results are also summarized in the **Table 6-9**. Further, the fluorescence quantum yield was calculated using the ratio of the integral of non-normalized emission spectra, and the absorption at the excitation wavelength. The fluorescens quantum yield was calculated using based **Eq 2-20,** and PAiRFP2 with $\Phi_f = 0.047$ was used as the respected reference. The fluorescence quantum yield of WT is 0.003 which is about two time higher than the

fluorescens quantum yield was reported before (Zienicke, Chen et al. 2011). The mutations of R211A, Y165F, and V244F increase the FQY about 2, 2.5, and 3-fold, respectively (**Table 6-9**).

Table 6-9 : Spectroscopic parameters of Agp2 PGP WT and its variants as shown in Fig. 6-9.

Protein	$\lambda_{max(abs\_Pr)}$ (nm)	$\lambda_{max(abs\_Pfr)}$ (nm)	$\lambda_{max(em)}$ (nm)	Stokes shift (nm)	Φ_f
WT	698	754	716	18	0.003
R211A	703	754	718	15	0.006
V244F	700	755	715	15	0.009
Y165F	704	747	715	11	0.007

Table 6-10: The fluorescence lifetime decay fit results of Agp2-PGP WT and mutants for the data shown in Fig. 6-10. The lifetime decay components with τ_1, τ_2, and the related relative amplitudes α_1, α_2 are given. τ_{mean} is calculated as the population weighted mean lifetime according to the **Eq.3-11** And the reduced chi-square (χ_{red}^2) is given to judge the goodness of the fit.

Agp2-PGP	τ_1 (ns)	τ_2 (ns)	α_1 (%)	α_2 (%)	τ_{mean} (ns)	χ_{red}^2
WT	0.16	0.47	81.36	18.64	0.28	0.98
R211A	0.30	0.54	62.60	37.40	0.43	1.20
V244F	0.30	0.60	67.30	32.70	0.45	1.47
Y165F	0.29	0.60	66.70	33.30	0.44	1.39

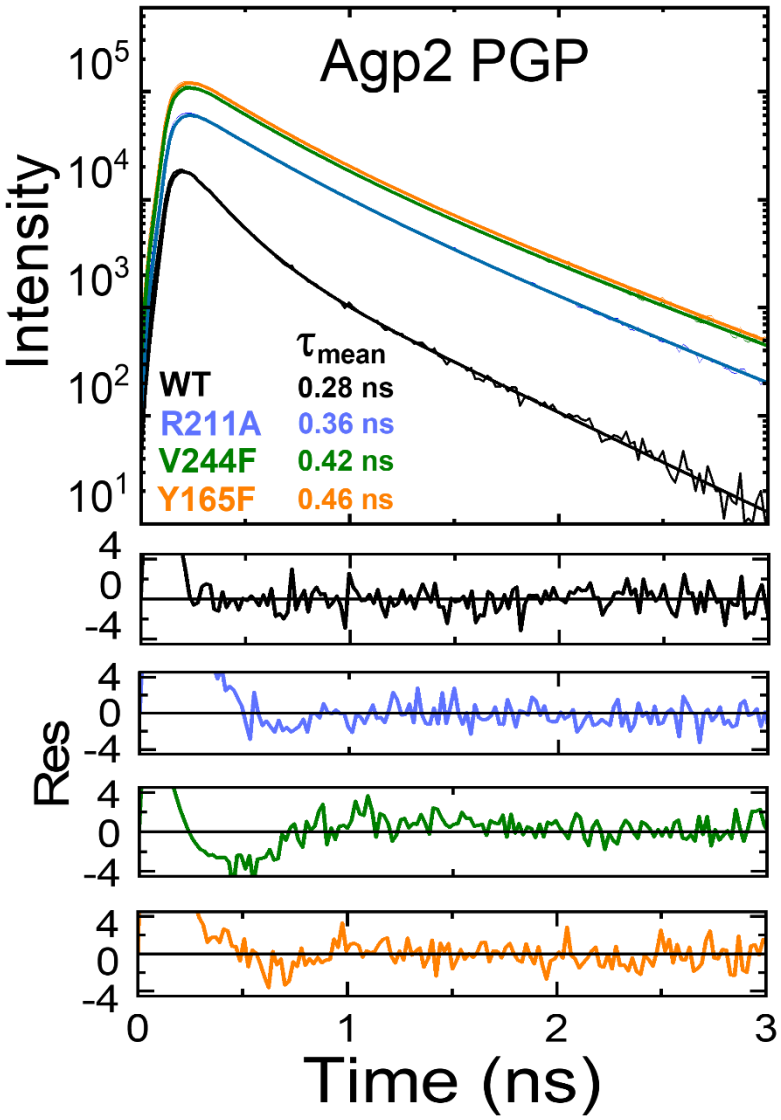

Figure 6-10: Fluorescence lifetime curves of Agp2 PGP WT and its variants. The mean lifetime of each protein is indicated. The fit residuals are given in the lower panel, Agp2 WT and its variants are indicated by color as in the upper panel. The fluorescence lifetimes were measured in the FLIM setup, which is equipped with a white light laser system for tunable excitation. The deconvolution with the instrument response function and the temporal profile of the excitation pulse leads to the larger fit residuals in the time range up to 200 ps. The fit data of each curve are summarized in **Table 6-10**. Conditions: 150 mM NaCl, 50 mM Tris pH 7.8, 19 ºC; λ_{ex} = 640 nm, and λ_{em} = 708±38 nm

The fluorescence lifetime measurement was carried out at temperature 19ºC, in 300 mM NaCl, 50 mM Tris pH 7.8 (**Fig. 6-10**). The samples were illuminated with LED 780 nm for 1 min before each measurement. The collection time was done during 60s with excitation wavelength at 640nm. The curves were fitted using the **Eq. 3-10**, and the fit results were summarized in **Table 6-10**. In contrast to Cph1 and Cph2 variants, the lifetime of Agp2 variants is significantly short. The Agp2 WT has a mean lifetime of 0.28 ns which 3-times and 7-times shorter than the mean fluorescence lifetime of Cph1 PGP and Cph2 GP, respectively. The Agp1 PGP mutants only increases the mean lifetime about 1.6-times longer than wide-type, which are 0.43 ns, 0.45 ns, and 0.44 ns for R211A, V244F, and Y165F, respectively. The first and second amplitude of the fluorescence decay components are almost similar for all variants, α_1 ~ 62-67 %, and α_2 ~ 32-37 %, respectively. While the amplitudes differ to WT with values α_1 ~ 82 %, and α_2 ~ 19 % (**Table 6-10**), which is similar to Cph1 and Cph2 WT variants. However, the higher fluorescent Cph1&Cph2 variants had larger amplitude of the second decay component compared to the first one, opposite to the Agp2 variants, where the first amplitude is larger than the second one. This observation might be explained by the different photocycles between two groups of fluorescent variants. Cph1 and Cph2 variants are locked in the Pr like state, while Agp2 variants are stopped in the Meta-F state. The first amplitude which has shorter lifetime is larger in the variants which partially carry out the photoconversion such Agp2 variants or Cph1 PGP Y263F and Cph1 PGP Y263S. This fact also applies for all the WT samples, which indicates that this fast fluorescence decay component probably represents part of the energy dissipation as a result of photoconversion.

The Agp2 mutant Y165F, which corresponds to position Y176 in Cph1 PGP for which the mutant Y176H significantly enhances the fluorescence quantum yield and fluorescence lifetime, displays no increasing fluorescence. A possible explanation for this difference will be discussed further in chapter 7.

6.6 PAiRFP2 and its mutant

PAiRFP1 and PAiRFP2 are two photoactivatable near-infrared fluorescent proteins (NIR FPs) that are formed by directed molecular evolution from Agp2 PGP, with 15 and 24 amino acid substitutions, respectively (Piatkevich, Subach et al. 2013) (**Fig. 6-11**). PAiRFP2 and the mutant F244V are the targets of this study. All 24 mutants in the Agp2 PGP crystal structure are highlighted in **Fig 6-11**. Three out of 24 substitutions are located in the PAS domain, 11 in the GAF domain, and 10 are in the PHY domain. Except for V244F and A276V, the rest of the residues do not participate in the interaction between the chromophore and the chromophore binding site. While Agp2 PGP shows a parallel (**Fig. 6-11**) orientation of the two crystallographic monomers, Agp2 PAiRFP2 monomers crystallize in a near anti-parallel arrangement (Schmidt, Sauthof et al. 2018). However, the chromophore interaction interface to the surrounding amino acids, especially the potential hydrogen bonds, the hydrophobic interactions, and the water molecules, are

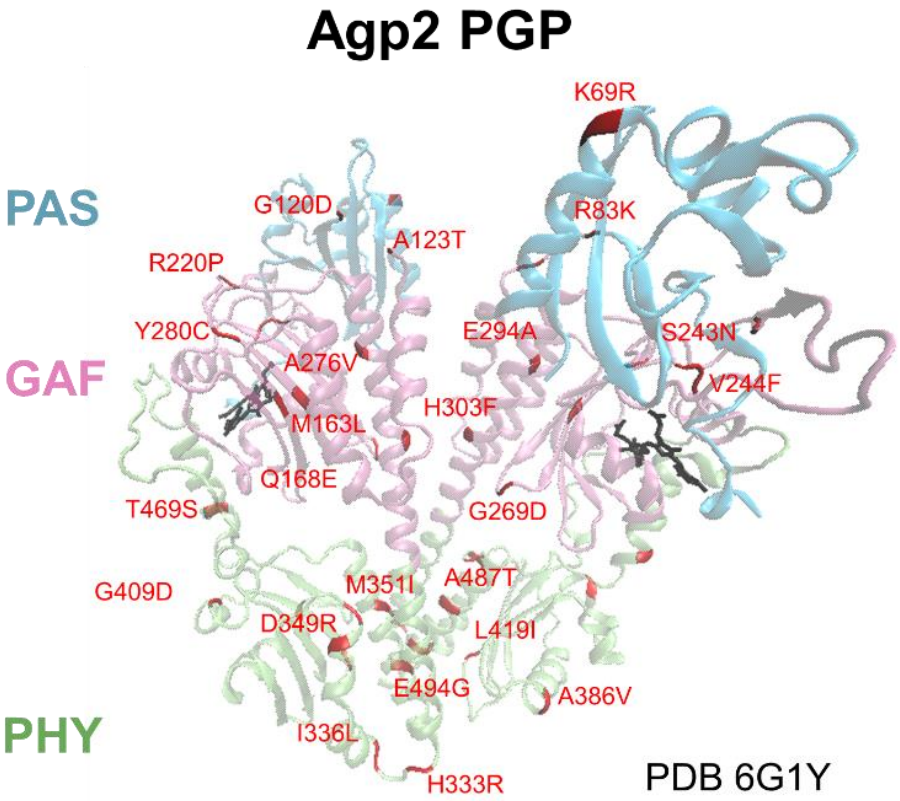

Figure 6-11: Crystal structure of Agp2 PGP. 24 mutants were applied on Agp2 PGP to have the variant PAiRFP2, these substitutions are indicated on crystal structure Agp2 which are K69R, R83K, G120D, A123T, M163L, Q168E, R220P, S243N, V244F, G269D, A276V, Y280C, E294A, H303F, H333R, I336L, D349R, M351I, A386V, G409D, L419I, T469S, A487T, and E494G. PDB code for Agp2 PGP and PAiRFP2 are 6G1Y and 6G1Z, respectively (Piatkevich, Subach et al. 2013).

almost identical for the Pfr states of both Agp2 PGP variants. UV–vis absorption spectra of Agp2 PGP PAiRFP2 in comparison to the wild-type Agp2 PGP construct, the full length Agp2, and the prototypical full length Agp1, display the characteristic spectrum of Pfr but enhanced stability of the final photoproduct state, resulting in slower dark reversion to Pfr compared to Agp2 PGP (**Fig. 6-12**). The half-lives of the photoinduced states of full-length Agp2, Agp2 PGP, and Agp2 PAiRFP2 are 170s (Krieger, Molina et al. 2008), 20s (Krieger, Molina et al. 2008), and 233 min (Piatkevich, Subach et al. 2013), respectively. In fact, in the previous studies, it was assumed that PAiRFP2 performed photoconversion from Pfr to Pr by absorbing in the far-red with a half-life of 233 min (Piatkevich, Subach et al. 2013). However, recently it was proved for PAiRFP2, both by the crystal structure and the resonance Raman spectroscopy that after irritating by far-red light, PAiRFP2 will be trapped in Meta-F and not going to a complete photoconversion to the Pr state (Schmidt, Sauthof et al. 2018). The crystal structure of the PAiRFP2 Meta-F intermediate state with the resolution of 2.16 Å shows the asymmetric unit includes two molecules (Mol A and B), which differ regarding their intermolecular interactions of their N-terminus. While both show overall highly similar topologies compared to the Pfr structure, the overall fold of the protein and specifically the α-helical segment of the tongue remained unchanged but significant structural changes were observed for the chromophore and its binding pocket as reflected by the electron density maps (Schmidt, Sauthof et al. 2018). From Pfr to Meta-F three types of structural changes are taken place in PAiRFP2, first: rearrangement of the extended hydrogen bond network surrounding the chromophore, second: losing the connection of amino acid residues Tyr165, Phe192 and Arg242 to BV via a hydrogen bond network, and third: disordering of the polypeptide backbone of the helical structure of tongue. Therefore, the helical to beta-sheet secondary conformational change is not happening in the Meta-F intermediate state of PAiRFP2, while this conformational change is essential for the formation of the Pr state in the most prototypical phytochrome families (Schmidt, Sauthof et al. 2018). So, this uncompleted photoconversion, as we saw earlier for Agp2 PGP variants, in PAiRFP1 and PAiRFP2 has reduced the dark reversion rate and consequently increases the fluorescence quantum yield to 0.048 ± 0.1 and 0.047 ± 0.1, respectively compared to Agp2 (0.0013) (Piatkevich, Subach et al. 2013).

UV-vis measurements were performed under the same conditions; buffer 300 mM NaCl, 30 mM HEPES 7.8, 20°C. The protein was measured in ambient green light for the dark-adapted state, and it was illuminated for 1 min, using LED 780 nm to measure the illuminated state. **Fig. 6-12A** and **6-12B** show the absorption of PAiRFP2 WT and the mutant F244V in the dark-adapted state (Pfr state), in blue, illuminated state in red and the different spectra in black. The maximum absorption in the dark-adapted state Pfr for WT and F244V are 755 and 754 nm, respectively. The maximum absorption after far-red light illumination is 695 nm for WT and 702 nm for F244V which is closer to the WT and the Agp2 variants. This indicates

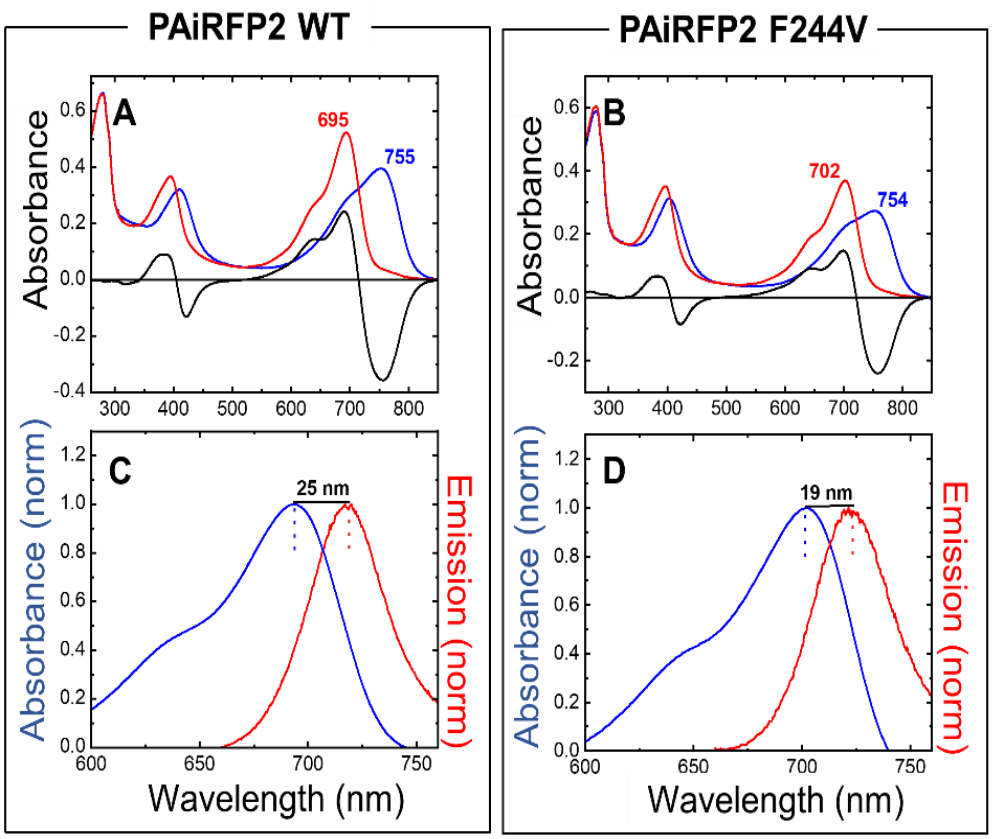

Figure 6-12:(**A-B**) UV-vis absorption spectra of PAiRFP2 WT and its mutant F244V. The dark-adapted (Pfr state) and post-irradiation spectra (far-red light irradiated sample) are shown in blue and red, respectively. The difference spectra are shown in black. λ_{max} values for Pr are indicated. F244V spectra indicates incomplete photoconversion and it seems these variants are locked in Meta-F state (Schmidt 2018). (**C-D**) Steady-state absorption, excitation, and emission spectra of PAiRFP2 WT and its mutant F244V. The absorption (ab) and emission (em) spectra are shown in blue, and red, respectively. The Stokes shift ($\lambda_{max(em)}$- $\lambda_{max(ab)}$) is indicated. The values are summarized in **Table 6-11**. Conditions: 130 mM NaCl, 50 mM HEPES, pH 7.8, 20°C.

Table 6-11: Spectroscopic parameters of PAiRFP2 and its variant F244V for the spectra shown in Fig. 6-12.

PAiRFP2	$\lambda_{max(abs\_Pr)}$ (nm)	$\lambda_{max(abs\_Pfr)}$ (nm)	$\lambda_{max(em)}$ (nm)	Stokes shift (nm)	Φ_f
WT	695	755	720	25	0.047
F244V	702	754	721	19	0.027

the residue V244 is important for the formation of the Pr. The results were summarized in **Table 6-11.** The fluorescence emission measurements were performed under the conditions similar to UV-vis measurement. The fluorescence emission was recorded between 600-760 nm, with excitation wavelength at 640 nm. **Fig. 6-12C** and **6-12D** shows the normalized absorption and emission spectra and the Stokes shift was indicated, which are 25 nm and 19 nm for PAiRFP2 WT and F244V, respectively. The fluorescence quantum yield was calculated based **Eq 2-20.** The results are summarized in **Table 6-11.**

Fig. 6-13 shows the lifetime curves of PAiRFP2 and the mutant F244V with lifetime of 0.42 ns and 0.36 ns respectively. The mutation of F244V, which mutants back to V244 in Agp2, indicated a shorter mean fluorescence lifetime and lower quantum yield compared to PAiRFP2 WT. However, this mutant F244V still has high quantum, yield compared to the Agp2 PGP variants.

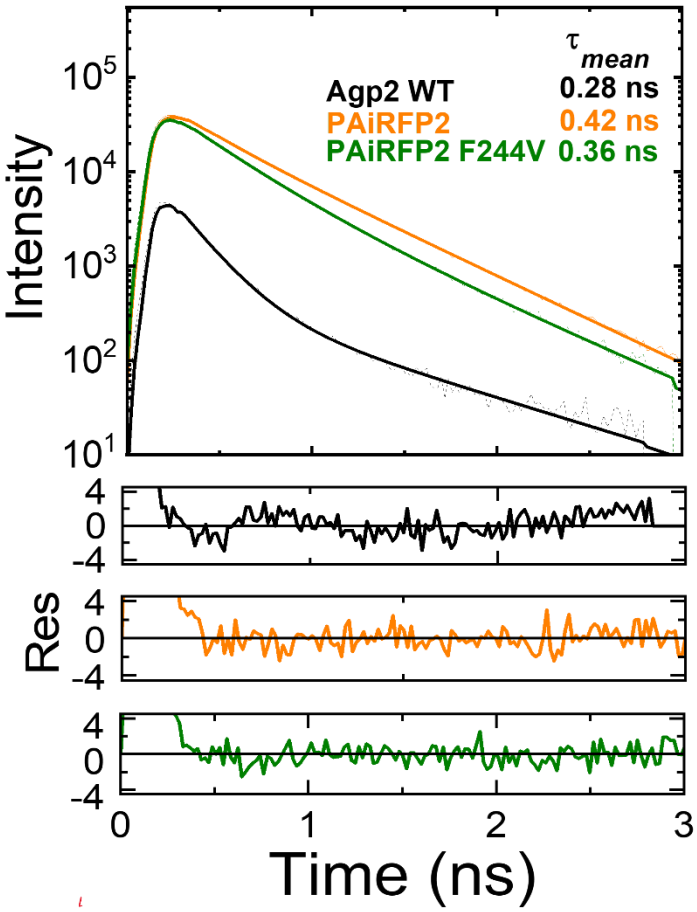

Figure 6-13: Fluorescence lifetime curves of Agp2 WT, PAiRFP2 and PAiRFP2 F244V PGP. The mean lifetimes are given. The fit residuals are shown in the lower panel, WT, PAiRFP2 and PAiRFP2 F244V are indicated by color as in the upper panel. The fluorescence lifetimes were measured in the FLIM setup, which is equipped with a white light laser system for tunable excitation. The deconvolution with the instrument response function and the temporal profile of the excitation pulse leads to the larger fit residuals in the time range up to 200 ps. The fit data of each curve are summarized in **Table 6-12**. Conditions: 130 mM NaCl, 50 mM HEPES, pH 7.8, 19 ºC; λ_{ex} = 640 nm, and λ_{em} = 708±38 nm.

Table 6-12: Fit data from fluorescence lifetime curves of PAiRFP2 variants as shown in Fig. 6-13. The lifetime decay components with τ_1, τ_2, and the related relative amplitudes α_1, α_2 are given. τ_{mean} is calculated as the population weighted mean lifetime according to the **Eq.3-11**, and the reduced chi-square (χ_{red}^2) is given to judge the goodness of the fit.

Sample	τ_1 (ns)	τ_2 (ns)	α_1 (%)	α_2 (%)	τ_{mean} (ns)	χ_{red}^2
PAiRFP2	0.28	0.49	51.74	48.26	0.42	1.08
PAiRFP2 F244V	0.25	0.47	38.15	61.85	0.38	1.01

6.7 Quantum yield and lifetime correlation of fluorescent phytochrome variants

The increases in fluorescence quantum yield and fluorescence lifetime are expected to be correlated. In Cph1&2 variants, the most values for the single and double mutants are well correlated (dotted line to guide the eye in **Fig. 6-14A)**. Interestingly, the WTs of Cph1 PGP, Cph1 PG, and *SyB*-Cph2 show a different correlation and indicate lower radiative rates. For Agp2 PGP variants, we also observe a correlation, while PAiRFP2 WT and its variant F244V show different slopes (**Fig. 6-14B**). The slope revealed the different radiative rates according to the **Eq 2-20.** For those protein data points that are located along the same line, the radiative rate k_r is quite similar and therefore implying a similar fluorescence mechanism.

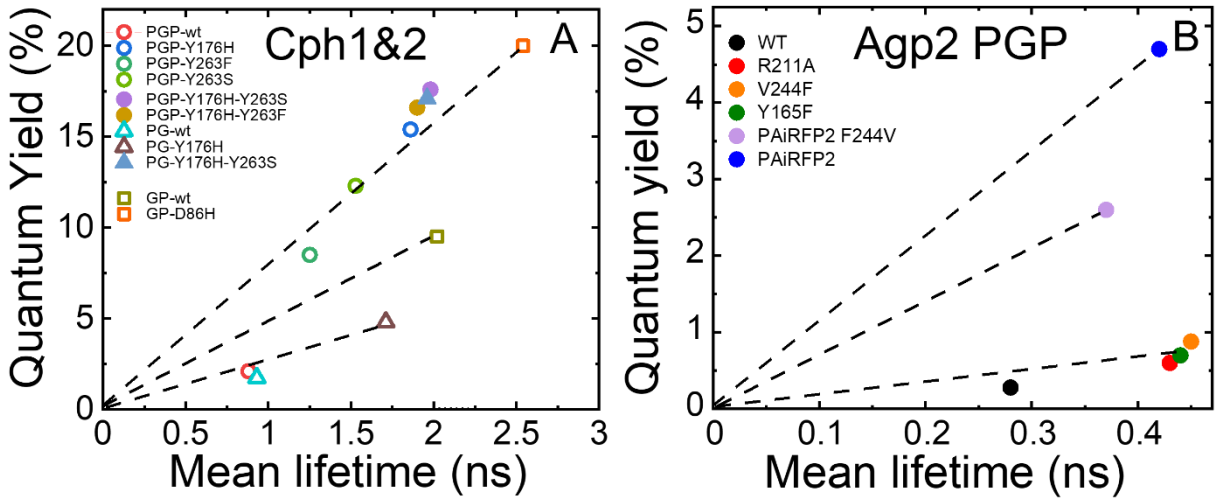

Figure 6-14: **Correlation between fluorescence quantum yield and mean fluorescence lifetime.** Cph1&2 PGP variants **(A)** and Agp2 PGP variants **(B)**. The dotted line is to guide the eye. The slope of this line would correspond to the radiative rate k_r according to the equation $\Phi_f = k_r \cdot \tau$ and indicate a similar k_r for those data points that fall on this line.

6.8 PAiRFP2 in crystal and in solution

During the last few years, the development of the methodology and the equipment could provide complementary data of the static macromolecular X-ray structure. The significant progress has been developed in analyzing crystals with techniques such as ultraviolet–visible light (UV-vis) absorption spectroscopy, fluorescence spectroscopy (Weik et al., 2004), Raman spectroscopy (Carey, 2006), electron

magnetic resonance (Hogbom et al.,2003), extended X-ray absorption fine structure (Pushkar et al., 2008), X-ray absorption near-edge structure, or a combination thereof (e.g., Hough et al., 2008). Indeed, the combination of the structural biology and these complementary techniques will help to understand the function of proteins deeper and more quantitative (De la Mora-Rey & Wilmot, 2007).

Since 1970s (Rossi & Bernhard,1970), single-crystal UV–visible absorbance micro spectrophotometry has been applied to many proteins containing metal centers or chromophores, in order to compare the properties of macromolecules in their crystalline and solution states (Mozzarelli & Rossi, 1996). However, this method has been evolved to monitor the build-up of reaction intermediate states within a crystal, especially for photoactivable or redox proteins (Bourgeois & Royant, 2005). Theses kinetic crystallography studies has been realized the effect of X-rays on the protein structure alteration, particularly in the case of colored proteins. Regarding this fact, it would be essential to check the identical spectroscopic signatures of a given protein in a crystal before and after X-ray data collection (Ravelli & Garman, 2006). Besides UV–visible absorption, fluorescence micro spectrophotometry is a promising technique to assess the relevance of the X-ray crystallography-determined structures of proteins containing endo- or exogenous fluorescent groups. Since 1975, fluorescence steady-state and time-resolved spectroscopy have been performed on slurries of tRNA crystals (Langlois et al., 1975), on myoglobin single crystals of large dimensions (Willis et al., 1991) and on crystalline GFP (Rosell & Boxer, 2003). As the crystals have a high optical density, fluorescence provides a much cleaner signal than absorption. Excitation at given wavelengths could penetrate relatively homogeneously throughout the crystal. However, inner-filtering effects inherent in highly concentrated samples such as protein crystals could make the assessment of the fluorescence emission complicated. Lifetime measurements in crystals are expected to be independent on morphology and concentration compared to steady-state data, therefore it would be beneficial for the comparison of crystal to solution and from crystal to crystal. In previous studies, FLIM was utilized to measure the fluorescence lifetime in crystal and solution of DNA–ethidium bromide (EtBr), EGFP/ECFP (Royant, Carpentier et al. 2007), which revealed different results for each environment. In all cases the mean lifetime in solution was longer than the lifetime in the crystal at room temperature (298 K). This study (Royant, Carpentier et al. 2007) also indicated a longer mean lifetime at 100K compared to 298K both in solution and in crystal which might be related to a decrease of the non-radiative decay when most protein motions are frozen.

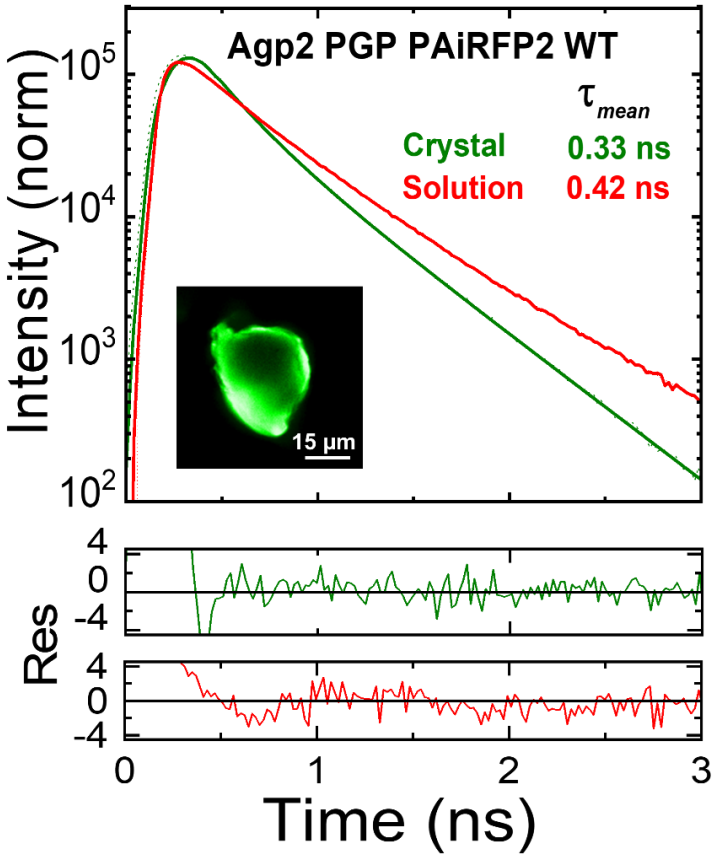

Figure 6-15: Characterization of Agp2 PGP PAiRFP2 in solution and in crystal using FLIM. Fluorescence decay curves in solution and in crystal are shown together with the mean fluorescence lifetimes. The fit residuals are shown in the lower panel. The fluorescence lifetimes were measured in the FLIM setup, which is equipped with a white light laser system for tunable excitation. The deconvolution with the instrument response function and the temporal profile of the excitation pulse leads to the larger fit residuals in the time range up to 200 ps. The inset shows the FLIM image of crystal Agp2 PGP PAiRFP2. Excitation was done at λ_{ex}=640nm and emission was detected with a bandpass of 708±38nm. For the illuminated state the samples were illuminated with LED 780 nm (Thorlabs) before the measurements for 30s. The fit results are summarized in **Table 6-13**. Conditions: 10µM protein in 30mM HEPES, 130mM NaCl pH=7.8, 19°C.

The fluorescence lifetime of PAiRFP2 reveals biexponential decay both in solution and in crystal (see **Fig. 6-15** and **Table 6-13**). The short fluorescence decay times of the protein in crystal and in solution are 0.19 ns, and 0.29 ns with population of 62.15 % and 34.75 %, respectively. And the long fluorescence decay times in crystal and in solution are 0.43 ns, and 0.50 ns with population of 37.85 % and 65.25 %, respectively. Both short and long fluorescence decay times in crystal are faster compared to the counterpart values in solution, although the population of the shorter decay component in crystallized protein is larger than for the protein in solution. Therefore, the calculated mean fluorescence lifetime in crystal is about 21%

smaller than the one solution. This agrees with previous studies such as crystallized EGFP and ECFP which had a fluorescence lifetime decreased by 15–20% compared to the solution. The authors (Royant, Carpentier et al. 2007) interpreted that this reduction indicates a minor quenching effect as the result of the short distance of fluorophores in crystal 30–40 A˚. Also, this decrease could be explained by the effect of precipitant as it increases the viscosity. However, the effect of crystal packing should be considered too.

Table 6-13: Fit data of fluorescence lifetime curves of PAiRFP2 as shown in Fig. 6-15. The lifetime decay components τ_1 , τ_2 and the related relative amplitudes α_1 and α_2 are given. τ_{mean} is calculated as the population weighted mean lifetime according to the **Eq. 3-11**. The reduced chi-square (χ_{red}^2) is given to judge the goodness of the fit.

PAIR2	τ_1 (ns)	τ_2 (ns)	α_1 (%)	α_2 (%)	τ_{mean} (ns)	χ_{red}^2
Crystal	0.19	0.43	62.15	37.85	0.33	1.08
Solution	0.29	0.5	51.74	48.26	0.42	1.01

6.9 *E.coli* cell imaging

In nature, bacteria have been found in diverse environments with highly adaptation to adverse conditions. This unique survival advantages are possible by their ability to modulate metabolic processes. Regarding to this fact, it is essential to investigate some bacterial protein's properties in their cellular environment. To do this important task, here the fluorescence lifetime of double mutants of Cph1 PG was measured in *E.coli* cell, in order to check the fluorescence stability of the protein in its cellular environment. Fluorescence lifetime imaging (FLIM) was carried out using *E.coli* expressing the necessary genes. **Fig. 6-16** shows the decay curves of the protein *in vivo* and *in vitro* with biexponential fit, fit results are summarized in **Table 6-14**. The short fluorescence decay times for *in vitro* and *in vivo* are 0.76 ± 0.05 ns, and 1.17 ± 0.04 ns with amplitude of 9 % and 22 %, respectively. The long fluorescence decay times for *in vitro* and *in vivo* are 2.05 ± 0.01ns, and 2.03 ± 0.01ns with amplitude of about 91% and 78%, respectively. The first fluorescence decay times of *in vitro* is faster the one *in vivo,* while the second decay lifetime is almost identical for both. However, the calculated mean fluorescence lifetime (**Eq. 3-11**) with considering the standard deviation is almost identical *in vivo* with value of 1.90 ± 0.07, and *in vitro* with value of 2.00 ± 0.01. This result indicates a highly stable fluorescence brightness and lifetime within the cellular environment with a minor fluorescence quenching. As it is shown in **Fig**. **6-16,** the *E. coli* shape is not completely rod shape, due to the cell orientation.

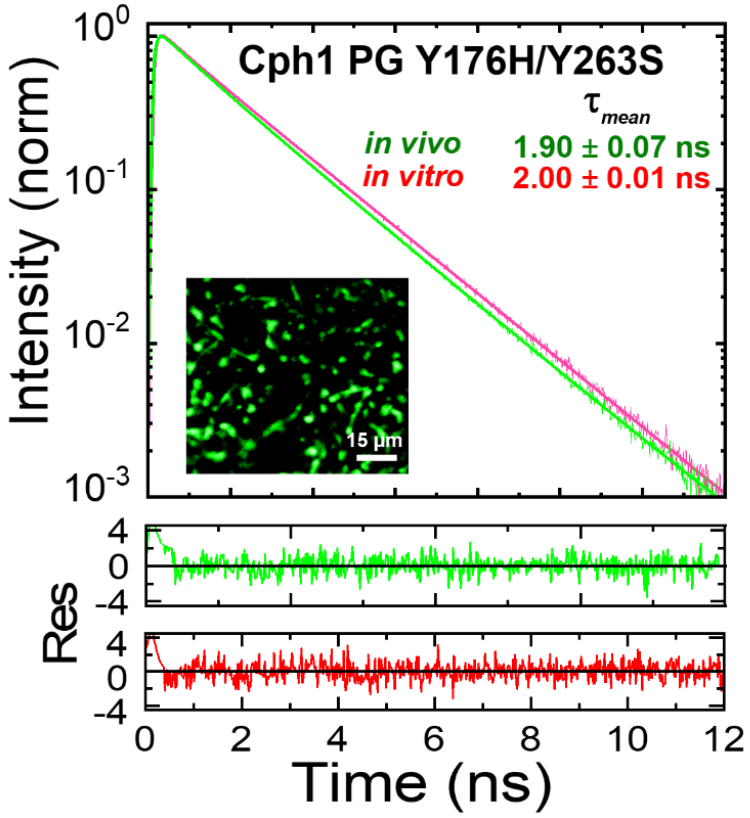

Figure 6-16: Characterization of Cph1 PG Y176H/Y263S in *E.coli* using FLIM. Fluorescence decay curves *in vitro* and *E.coli* are shown together with the mean fluorescence lifetimes and the fit residuals are shown in the lower panel. The fluorescence lifetimes were measured in the FLIM setup, which is equipped with a white light laser system for tunable excitation. The deconvolution with the instrument response function and the temporal profile of the excitation pulse leads to the larger fit residuals in the time range up to 200 ps. The inset shows the FLIM image of *E. coli* cells expressing Cph1 PG Y176H/Y263S. The fit results are summarized in **Table 6-14**. Conditions: 150 mM NaCl, 50 mM Tris pH 8, 19ºC; λ_{ex} = 640 nm, and λ_{em} = 708±38 nm.

Table 6-14: Fit results of fluorescence lifetime decay curves of Cph1 PG Y176H/Y263S *in vivo* and in *E.coli* as shown in Fig. 6-16. The lifetime decay components with τ_1, τ_2, and the related relative amplitudes α_1, α_2 are given. τ_{mean} is calculated as the population weighted mean lifetime according to the **Eq. 3-11**, and the reduced chi-square (χ_{red}^2) is given to judge the goodness of the fit.

Cph1 PG	τ_1 (ns)	τ_2 (ns)	α_1 (%)	α_2 (%)	τ_{mean} (ns)	χ_{red}^2
Y176H/Y263S (*in vitro*)	0.76 ± 0.05	2.05 ± 0.01	8.70 ± 0.48	91.30 ± 0.48	2.00 ± 0.01	1.32
Y176H/Y263S (in *E. coli*)	1.17 ± 0.04	2.03 ± 0.01	22.48 ± 1. 83	77.52 ± 1. 83	1.90 ± 0.07	1.51

6.10 Conclusion

The double tyrosine mutants of Cph1 PGP and Cph1 PG increase fluorescence quantum yield and fluorescence lifetime compared to the single variants. The fluorescence steady-state and time-resolved characterization of single and double conserved tyrosine mutants indicated that the combination of single mutations highly enhance fluorescence. The fluorescence quantum yield in both double mutants Y176H/Y263F and Y176H/Y263S appear synergistic, with values of up to 17%. The fluorescence lifetime also increases from 0.86 ns to about 2 ns. Although removal of the PHY domain reduced fluorescence in the WT and Y176H, for unclear reasons, it hardly affected the Y176H/Y263S mutant.

The Cph1&2 variants have a remarkable higher fluorescence quantum yield and fluorescence lifetime compared to the Agp2 variants. The fluorescence studies of various mutants imply differences in the mechanisms of photoconversion between BV-utilizing bacteriophytochromes, Agp2 PGP variants, and PCB-binding phytochromes, Cph1&2 variants. The fluorescence quantum yield and fluorescence lifetime of Cph1&2 WT (~ 1.8 % and 12.4 %; 0.86 ns and 2.07 ns, respectively) is much larger than Agp1 PGP WT (~ 0.3 %, 0.28 ns). Also, the mutations known to enhance fluorescence which are conserved among of these two groups of phytochrome revealed a different behavior. For example, the mutation of the conserved tyrosine 176 in Cph1 (Y176H), enhance Φ_f to about 14 % in PGP, and 11 % in PG, increasing of about 7 and 6 times, respectively, in comparison to their WT. However, the mutation of this tyrosine in Agp2 PGP, Y165F enhance Φ_f to about 0.7 %, an increase of about 2 times compared to WT. However, PAiRFP2 a variant of Agp2 PGP with 23 rounds of mutation, which was designed for optogenetic tool purpose, enhanced Φ_f to 4.7%. Therefore, the mutations that increase fluorescence quantum yield in one class of phytochromes do not always have the same effects in fluorescence enhancement. Consequently, two classes of phytochromes must be considered as different bases for the development of near-IR fluorophores. The role of the chromophore type, such as BV or PCB, will be investigated and discussed in chapter 7.

7 Results and Discussion Part IV:

The Origin of Fluorescence in Fluorescent Phytochromes

As we saw in chapter 6, the PCB chromophore binding proteins such as Cph1 and Cph2 have a higher quantum yield and a longer fluorescence lifetime compared to the BV-binding proteins such as Agp2 variants. To examine whether the fluorescence quantum yield and lifetime in fluorescent phytochrome are related to the chromophore type, the fluorescent properties of PCB assembling of Agp1 PGP WT (non-covalent assembling) and its variant V249C for a covalent PCB-binding (Borucki, Seibeck et al. 2009), were investigated, and the results was compared to Agp1 PGP WT (BV). Further the variant Y166H in Agp1 PGP was created, in which the equivalent mutant in Cph1, Y176H is known to enhance fluorescence (Fischer and Lagarias 2004). PCB-binding of Agp1 Y166H PGP was characterized for Y166H+PCB (non-covalent binding), and Y166H/V249C-PCB (covalent binding), using the steady-state and the time-resolved fluorescence spectroscopy. There are three conserved tyrosine in the chromophore binding pocket of Cph1, Tyr 176, Tyr 203, and Tyr 263 (**Fig. 7-1A**), which correspond to the residues Tyr 166, Phe 193, and Tyr253 in Agp1 (**Fig. 7-1B**). The mutant F193Y was also created to test the effect of Tyr193, which corresponds to Tyr 203 in Cph1, on enhancing the fluorescence in this variant.

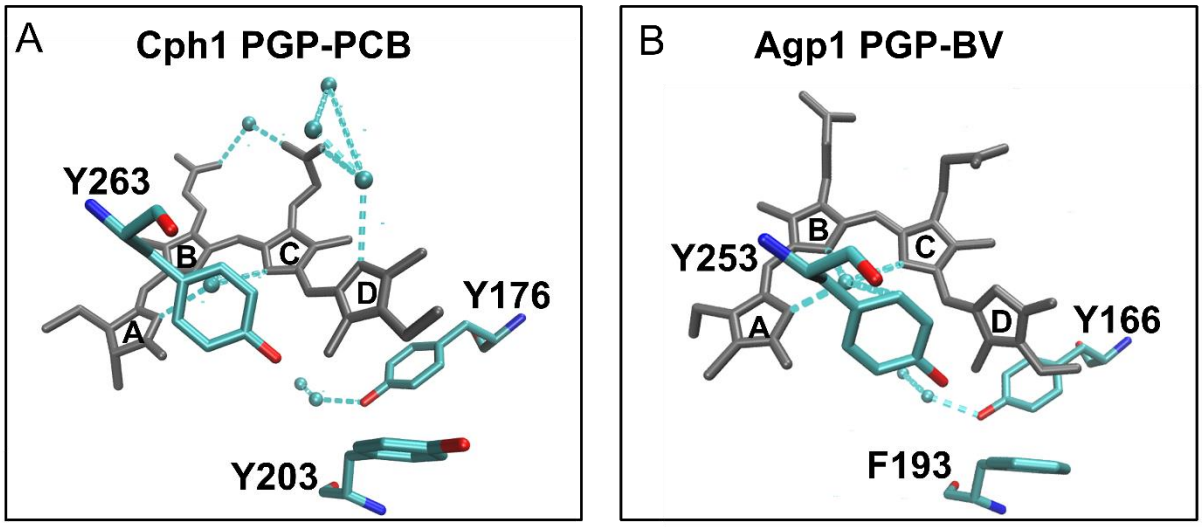

Figure 7-1: The structure of PCB in the chromophore binding pocket in Cph1 PGP (**A**) and the structure of BV in the chromophore binding pocket in Agp1 PGP (**B**) including the water molecules (cyan spheres) and the conserved Tyr (Y176, and Y263 in Cph1, and Y166, and Y253, in Agp1), as well the non-conserved Tyr in Cph1 (Tyr 203) and its equivalent residue F193 in Agp1. The H-bonds are shown as dashed cyan lines. Cph1 PGP PDB: 2VEA, Agp1 PGP PDB: 5I5L. The images of the chromophore binding pocket were created by VMD.

And finally, to test the hypothesis; if the tyrosine acts as a fluorescence quencher of PCB and BV, the fluorescence emission (for a static quenching studying) and fluorescence lifetime (for a dynamic quenching studying) of BSA+ PCB, and BSA+BV were measured in different concentrations of tyrosine in solution.

7.1 The effect of chromophore type on fluorescence emission and fluorescence lifetime

7.1.1 PCB assembly with Agp1 WT (non-covalent) and V249C (covalent)

The steady-state absorption characterization of these two variants were performed in chapter 4 (see chapter 4, **Fig. 4-2**, **Table 4-1**). The fluorescence emission measurements were performed under the same conditions: 12 µM for covalent PCB-binding variants and 22 µM for non-covalent PCB-binding and BV-binding variants in buffer: 300 mM NaCl, 50 mM Tris pH 7.8, 19ºC. The fluorescence emission was recorded between 650-740 nm, with excitation wavelength of 640 nm. **Fig. 7-2B** shows the emission of spectra of the PCB assembling to Agp1 WT (non-covalent) and V249C (covalent), as well as the emission

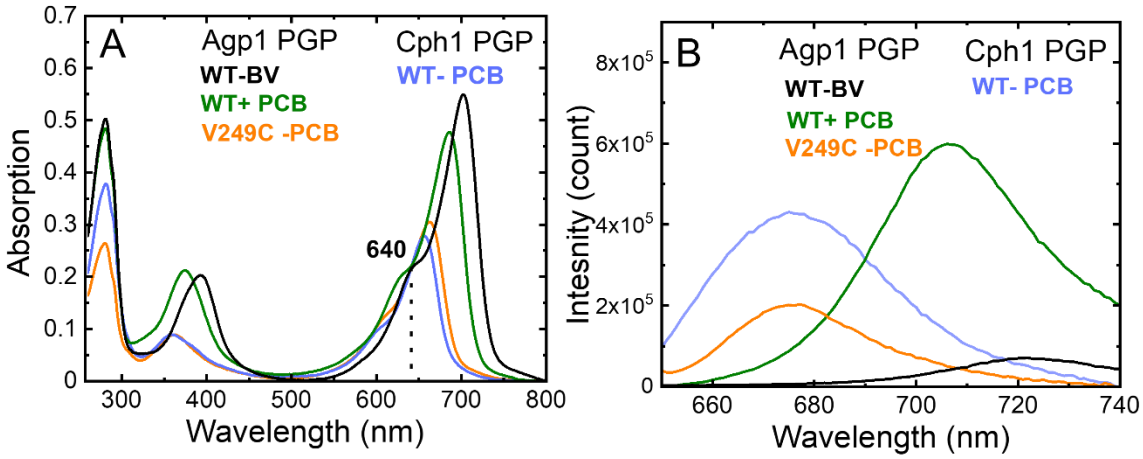

Figure 7-2: Steady-state absorption and fluorescence characterization of PCB-binding to Agp1 PGP WT (non-covalent binding), and its variants V249C (covalent binding) in comparison to the native proteins Agp1 PGP (BV) and Cph1 PGP (PCB). The different variants are indicated by color. (**A)** UV-vis absorption of the samples before the emission measurement, all the sample have the same absorption at the excitation wavelength of 640 nm. **(B)** Fluorescence emission: λ_{ex}= 640 nm, and λ_{em} = 650-740 nm, slit 3. The values are summarized in **Table 7-1.** Condition**:** buffer: 300 mM NaCl, 50 mM Tris pH 7.8, 19ºC, the concentration of the variants was 12 µM for covalent PCB-binding variants and 22 µM for a non-covalent PCB-binding and BV-binding variants.

spectra of Agp1 PGP (BV) and Cph1 PGP (PCB) for a comparison. The absorption spectra of all samples were measured before the emission measurement to have the same absorption at excitation wavelength 640 nm (**Fig. 7-2A**). Further, the fluorescence quantum yield was calculated using the ratio of the integral of emission spectra (**Fig. 7-2B**), and the absorption at the excitation wavelength, which all the samples here have the same absorption value (**Fig. 7-2A**). The fluorescens quantum yield was calculated based on **Eq.2-20**, and Cph1 PGP with Φ_f =0.024 was used as the respected reference (Nagano, Sadeghi et al. 2022). The results were summarized in **Table 7-1**. The fluorescence quantum yield of Agp1 WT (BV) is 0.003 which is higher than value was reported before (0.001) (Zienicke, Chen et al. 2011). The non-covalent assembling of PCB to Agp1 PGP WT increase the Φ_f to 0.032, which is 10 times more fluorescence compared to Agp1 PGP (BV) and about 1.4 times more fluorescence than Cph1 PGP (PCB). However, the covalent binding of PCB to Agp1 PGP V249C with Φ_f = 0.010 does not increase the quantum yield compared to Cph1 PGP (PCB). It sems the covalent bond of PCB in Agp1 PGP V249C is a source of the fluorescence energy dissipation in this variant. Note, in order to calculate the fluorescence quantum yield, the samples were prepared to have the same absorption at the excitation wavelength, 640 nm (**Fig. 7-2A**)

Table 7-1: Spectroscopic parameters of BV and PCB binding to Agp1 PGP WT and its variant V249C (non-covalent and covalent bond) and Cph1 PGP WT, as shown in Fig. 7-2.

Constructs	$\lambda_{max(abs\_Pr)}$ (nm)	$\lambda_{max(em)}$ (nm)	Stokes shift (nm)	Φ_f
Agp1 PGP WT-BV	700	720	20	0.003
Agp1 PGP WT+PCB	685	706	21	0.032
Agp1 PGP V249C-PCB	656	675	19	0.010
Cph1 PGP WT-PCB	658	675	17	0.024

which thereby led to have different chromophore absorption (different protein concentration) for the covalent and non-covalent PCB-binding variants, and covalent BV-binding variants, regarding to their chromophore maximum absorption wavelength, $\lambda_{max,Pr}$ = 654 nm for covalent PCB-binding variants, and $\lambda_{max,Pr}$ = 685-700 nm for non-covalent PCB-binding and covalent BV-binding variants.

Fig. 7-3 shows the decay curves of Agp1 PGP WT (non-covalent) and V249C (covalent), as well as Agp1 PGP (BV) and Cph1 PGP (PCB) for the comparison. All the samples were measured under the same conditions, 12 µM for covalent PCB-binding variants and 22 µM for non-covalent PCB-binding and covalent BV-binding variants in buffer: 300 mM NaCl, 50 mM Tris pH 7.8, 19ºC with excitation wavelength of λ_{ex} = 640 nm (**Fig. 7-2A**), and the emitted photons were collected at the wavelength λ_{em}=708±38 nm. The time-resolved fluorescence lifetime curves were fitted with two decay components according to **Eq. 3-10**, the fit results are summarized in **Table 7-2**, including lifetimes τ_i, amplitudes α_i, and the mean lifetime τ_{mean}. Similar to Cph1 PGP WT and Cph1 PG WT, the Agp1 PGP variants are bound to BV and PCB (both covalent and non-covalent) indicated a higher value of the first amplitude compared to the second one, α_1 ~ 75-80 %, α_2 ~ 20-25% (**Table 7-2**). The fluorescence decay times of Agp1 WT(BV) are 0.14 ns and 0.35 ns.

The fast decay of BV in Agp1 PGP WT indicated a higher non-radiative decay rate which is probably related to the higher flexibility of BV compared to PCB. Beside the intrinsic character of BV and PCB that cause a more flexible of one compared to another, there is another factor that can explain the shorter fluorescence lifetime of PCB in Agp1 compared to Cph1. As the crystal structure reveals for Cph1 PGP, ring D of PCB has a hydrogen bond to a network of water molecular, while crystal structure of Agp1 PGP does not have this water molecules and consequently the hydrogen bond with ring D of BV. When PCB is assembling to Agp1 PGP, the lack of this hydrogen bond network between the water molecule and ring D

might increase the mobility of the ring and consequently shorten the lifetime decay as the result of increasing the non-radiative rate.

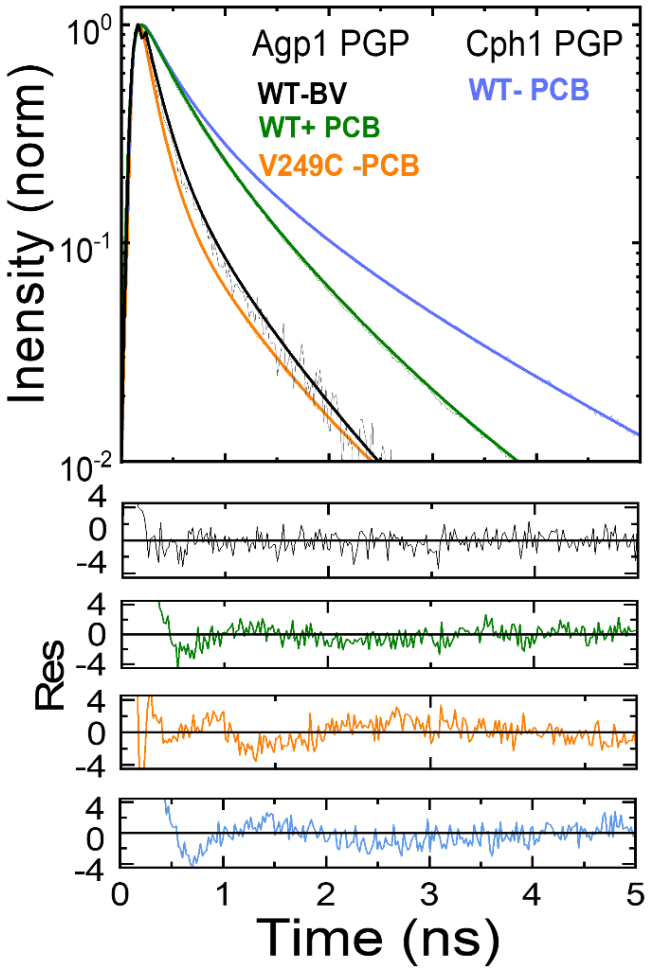

Figure 7-3: Fluorescence lifetime decays of BV and PCB-binding to Agp1 PGP WT and its variant V249C (non-covalent and covalent bond) and Cph1 PGP WT. The residuals are shown below, and the different variants are indicated by color. The curves were measured under the same conditions in the FLIM setup. The fluorescence lifetime decay fit results are summarized in **Table 7-2**. Conditions: 300 mM NaCl, 50 mM Tris pH 7.8, 19 ºC; λ_{ex}= 640 nm, and λ_{em} = 708±38 nm.

Table 7-2: The fluorescence lifetime decay fit results of Fluorescence lifetime decays of BV and PCB-binding to Agp1 PGP WT and its variant V249C (non-covalent and covalent bond). The fluorescence decay components with τ_1, τ_2, and the related relative amplitudes α_1, α_2 are given. τ_{mean} is calculated as the population weighted mean lifetime according to the **Eq. 3-11** The reduced chi-square (χ_{red}^2) is given to judge the goodness of the fit. For comparison the values of Cph1 PGP WT are given (Nagano-Sadeghi 2022). The errors of the decay component values are less than 10% and the errors of the τ_{mean} values are less than 5%.

Constructs	τ_1 (ns)	τ_2 (ns)	α_1 (%)	α_2 (%)	τ_{mean} (ns)	χ_{red}^2
Agp1 PGP WT-BV	0.14	0.35	75.98	24.02	0.30	1.10
Agp1 PGP WT+PCB	0.33	0.81	80.34	19.76	0.50	1.20
Agp1 PGP V249C-PCB	0.19	0.72	74.48	25.52	0.30	1.30
Cph1 PGP WT-PCB	0.34	1.30	76.09	23.91	0.86	0.93

7.1.2 The conserved tyrosine 166 mutant Y166H in Agp1 and its assembly with PCB and BV

The variant Agp1 PGP Y166H was created using site-directed mutagenesis as described in Material and Methods. This variant is aligned with mutant Y176H in Cph1 which was discovered to enhance fluorescence in Cph1 (Fischer and Lagarias 2004). PCB and BV assembling was performed as described in Material and Method, and further the variants were characterized using UV-vis absorption spectroscopy. The steady-state and time resolved fluorescence spectroscopy was performed to investigate the fluorescent properties of these variants. UV-vis absorption measurement for all the samples was performed under the same condition 12 µM for PCB covalent binding variants and 22 µM for PCB non-covalent binding and BV binding variants in buffer: 300 mM NaCl, 50 mM Tris pH 7.8, 19ºC and in background green light. The Pr state for Agp1 Y166H (BV) and for Agp1 Y166H +PCB was generated by saturating irradiation using a 784 nm LED (Conrad Electronic), or alternatively waiting long enough in dark to have back reaction to Pr. For the Pr/Pfr state a 735 nm LED (Conrad Electronic) was used. However, for Agp1 PGP Y166H/V249C-PCB, a 735 nm LED (Conrad Electronic) was used to reach the Pr state and a 680 nm LED (Conrad Electronic) to reach Pr/Pfr, like illumination process of Cph1 PGP variants.

Fig. 7-4 shows the absorption spectra of Pr and Pr/Pfr forms of Agp1 PGP Y166H (BV), and PCB adducts of Agp1 PGP; Y166H (non-covalent) and Y166H/V249C (covalent). The extinction coefficient of 90000 ± 5000 $M^{-1}cm^{-1}$ was used for all the variants (Lamparter, Michael et al. 2002, von Stetten, Seibeck et al. 2007).

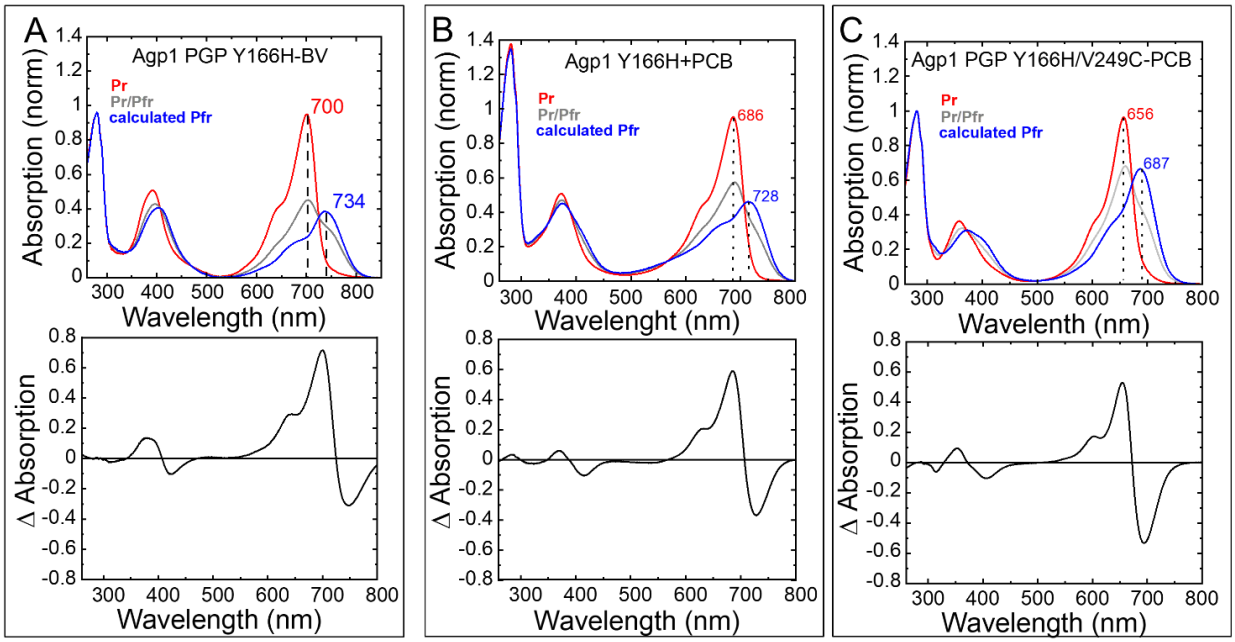

Figure 7-4: UV-vis absorption spectra of BV and PCB adducts of Agp1 PGP variants Y166H and Y166H/V249C. Top panels show the Pr state of the adducts in red, the Pr/Pfr state in gray, and the calculated Pfr state in blue according to **Eq. 4-1**. The absorbance maximum at $\lambda_{max,\,Pr}$ was normalized to 1. The lower panels show the absorption difference between the Pr state and the calculated Pfr state. (**A**) Agp1 PGP Y166H-BV (covalent assembling) (**B**) Agp1 PGP Y166H+PCB (non-covalent assembling) and (**C**) Agp1 PGP Y166H/V249C-PCB (covalent assembling). The values are summarized in **Table 7-3** Conditions: 50 mM Tris buffer pH 7.8, 300 mM NaCl, at 20ºC.

Table 7-3: Chromophore absorption maxima in nanometer for the red absorbing Pr and Pfr band of Agp1 Y166H with bound BV and PCB (covalent and non-covalent) and for Cph1 PGP WT with bound PCB. The *f*-value for calculating the Pfr absorbance spectrum according to **Eq. 4-1 (**see chapter 4**)** is given.

Agp1 PGP	$\lambda_{max(abs),Pr}$ (nm)	$\lambda_{max(abs),Pfr}$ (nm)	*f*	Chromophore type
WT	700	750	0.30	BV
Y166H	700	734	0.30	BV
Y166H	685	728	0.35	PCB (non-covalent)
Y166H/V249C	656	687	0.30	PCB (covalent)

Similar to the PCB binding in WT, the absorption spectra of the Pr forms of the covalent and non-covalent PCB adduct differ in the position of their chromophore band by ~ 30 nm (656 and 686 nm for the covalent and non-covalent PCB adduct, respectively). However, the absorption maximum in the calculated Pfr spectra is blue shifted in Y166H compared to WT (see chapter 4, **Table 4-1**), 16 nm for BV assembling, and 10 nm for covalent PCB assembling, while this value remains the same in non-covalent PCB assembling.

The fluorescence emission was recorded between 650- 740 nm, with excitation wavelength of 640 nm and the condition was similar to UV-vis absorption. **Fig. 7-5B** shows the emission of spectra of PCB-binding to Agp1 Y166H (non-covalent) and Y166H/V249C (covalent), as well as the emission spectra of Agp1 PGP Y166H (BV) for a comparison. The absorption spectra of all samples were measured before the emission measurement to have the same absorption at the excitation wavelength 640 nm (**Fig. 7-5A**). Further, the fluorescence quantum yield was calculated using the ratio of the integral of emission spectra (**Fig. 7-5B**), and the absorption at the excitation wavelength, which all the samples here have the same absorption value (**Fig. 7-5A**). The fluorescens quantum yield was calculated based on **Eq 2-20**, and Cph1 PGP with Φ_f =0.024 was used as the respected reference (Nagano, Sadeghi et al. 2022). The results were summarized in **Table 7-4.** The variant Y166H-BV (covalent) enhanced fluorescence with value of Φ_f = 0.006 compared to WT with value of Φ_f = 0.003 (2-fold enhancement) (**Table 7-4**). The quantum yield of non-covalently bound PCB of Y166H has the same quantum yield value Φ_f = 0.032 as Agp1 PGP WT+PCB Φ_f = 0.032 (**Table 7-1**). While the quantum yield of covalently bound PCB to Y166H, Φ_f = 0.014 is higher than this value in Agp1 PGP V249C-PCB, Φ_f = 0.010.

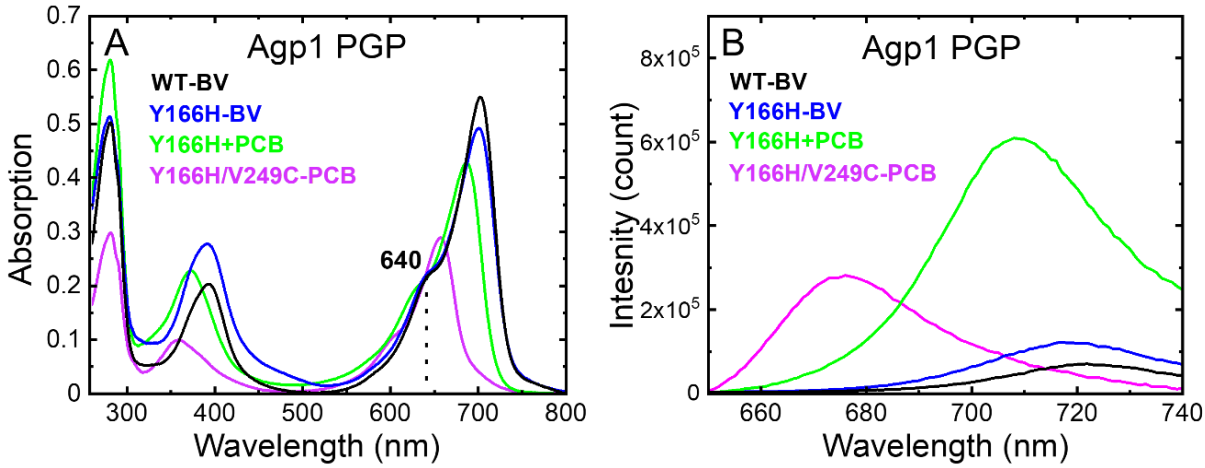

Figure 7-5 Steady-state fluorescence characterization of PCB binding to Agp1 PGP Y166H (non-covalent bond), and its variant V249C (covalent bond) in comparison to Agp1 PGP Y166H (BV) and WT (BV). The different variants are indicated by color. (**A)** UV-vis absorption of the samples before the emission measurement, all the samples have the same absorption at the excitation wavelength of 640 nm. **(B)** Fluorescence emission: λ_{ex}= 640 nm, and λ_{em} = 650-740 nm, slit 3. The values are summarized in **Table 7-4** Condition**:** buffer: 300 mM NaCl, 50 mM Tris pH 7.8, 19ºC, the concentration of the variants was 12 µM for PCB covalent binding variants and 22 µM for PCB non-covalent binding and BV binding variants.

Table 7-4: Spectroscopic parameters of PCB binding to Agp1 PGP Y166H (non-covalent bond), and its variant V249C (covalent bond) in comparison to Agp1 PGP Y166H (BV) and WT (BV) as shown in Figure 7-5.

Agp1 PGP	$\lambda_{max(abs\_Pr)}$ (nm)	$\lambda_{max(em)}$ (nm)	Stokes shift (nm)	Φ_f
WT-BV	700	720	20	0.003
Y166H-BV	700	719	19	0.006
Y166H + PCB	685	710	25	0.032
Y166H/V249C-PCB	656	676	20	0.014

Fig. 7-6 shows the decay curves of Agp1 Y166H (non-covalent) and Y166H/V249C (covalent). All the samples were measured under the same conditions as WT (see **Fig 7-3**). The time-resolved fluorescence lifetime curves were fitted with two decay components according to **Eq. 3-10**, the fit results are summarized in **Table 7-5**, including lifetimes τ_i, amplitudes α_i, and the mean lifetime τ_{mean}. In contrast to the variant Y176H in Cph1 PGP that reduced significantly the first amplitude (18%) compared to WT (76%), none of the Y166H variant had such an effect in Agp1 PGP. The first amplitude reduced slightly (60-63%) compared to WT (75-80%). This might be related to the complete photoconversion in PCB and BV adduct of Agp1 PGP Y166H (**Fig. 7-4**) compared to Cph1 PGP Y176H variant which is blocked in Pr like state. As we discussed above, the photoconversion seems to be correlated to the increase of the non-radiative rate and cause a faster lifetime in phytochrome.

Table 7-5: The fluorescence lifetime decay fit results of PCB binding to Agp1 PGP Y166H (non-covalent bond), and its variant V249C (covalent bond) in comparison to Agp1 PGP Y166H (BV) and WT (BV). The fluorescence decay components with τ_1, τ_2, and the related relative amplitudes α_1, α_2 are given. τ_{mean} is calculated as the population weighted mean lifetime according to the **Eq. 3-11**. The reduced chi-square (χ_{red}^2) is given to judge the goodness of the fit. For comparison the values of Cph1 PGP Y176H are given (Nagano-Sadeghi 2022). The errors of the decay component values are less than 10% and the errors of the τ_{mean} values are less than 5%.

Constructs	τ_1 (ns)	τ_2 (ns)	α_1 (%)	α_2 (%)	τ_{mean} (ns)	χ_{red}^2
Agp1 PGP Y166H-BV	0.18	0.49	61.12	38.88	0.37	1.30
Agp1 PGP Y166H+PCB	0.25	1.16	63.30	36.70	0.58	0.95
Agp1 PGP Y166H/V249C-PCB	0.26	1.34	59.36	36.71	1.10	1.34
Cph1 PGP Y176H-PCB	0.90	2.00	18.02	81.98	1.90	1.27

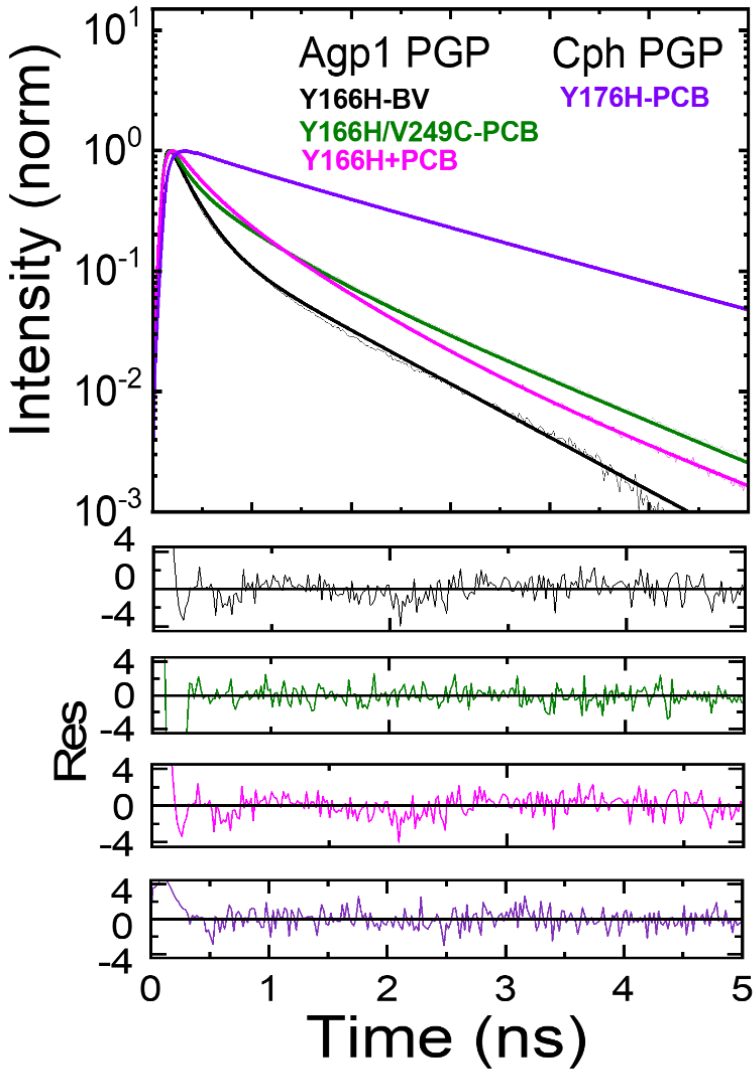

Figure 7-6: **Fluorescence lifetime decays of PCB binding to Agp1 PGP Y166H (non-covalent bond), and its variant V249C (covalent bond) in comparison to Agp1 PGP Y166H (BV), WT (BV) and Cph1 PGP Y176H (PCB).** The residuals are shown below, and the different variants are indicated by color. The curves were measured under the same conditions in the FLIM setup. The fluorescence lifetime decay fit results are summarized in **Table 7-5**. Conditions: 300 mM NaCl, 50 mM Tris pH 7.8, 19ºC; λ_{ex}= 640 nm, and λ_{em} = 708±38 nm.

7.1.3 BV and PCB adducts of Agp1 PGP variant F193Y

Fig. 7-7.C shows the position of Phe193 in the chromophore binding pocket of Agp1 PGP. This residue is aligned with Tyr203 in Cph1 PGP (**Fig. 7-1B**). There are two conserved tyrosine in the chromophore binding pocket of Cph1 PGP and Agp1 PGP which are Tyr166, Tyr253, and Tyr176, Ty263, respectively. The variant F193Y was created to investigate the role of this tyrosine on fluorescence quantum yield. The variant Agp1 PGP F193Y was created using site-directed mutagenesis and PCB and BV assembling was performed as described in Material and Method, and further the variants were characterized using UV-vis absorption spectroscopy. The steady-state and time-resolved fluorescence spectroscopy was performed to investigate the fluorescent properties of these variants. UV-vis absorption measurement for all the samples was performed under the same condition in buffer: 300 mM NaCl, 50 mM Tris/HCl pH 7.8, at 20ºC, and in background green light. The Pr state was generated by saturating irradiation using a 784 nm LED (Conrad Electronic), or alternatively waiting long enough in dark to have back reaction to Pr. For reaching the Pr/Pfr state, a 735 nm LED (Conrad Electronic) was used.

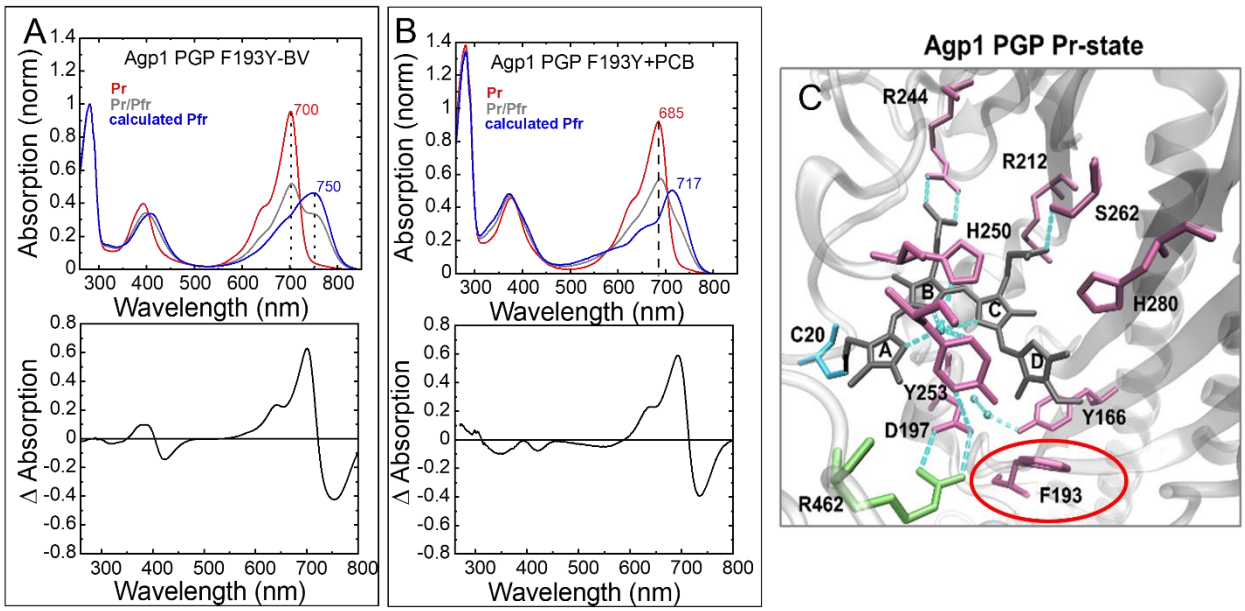

Figure 7-7: UV-vis absorption spectra of BV and PCB adducts of Agp1 PGP variant F193Y. Top panels show the Pr state of the adducts in red, the Pr/Pfr state in gray, and the calculated Pfr state according to **Eq. 4-1** in blue. The absorbance maximum at $\lambda_{max,\,Pr}$ was normalized to 1. The lower panels show the absorption difference between the Pr state and the calculated **(Eq. 4-1)** Pfr state. **(A)** Agp1 PGP F193Y-BV (covalent assembling) **(B)** Agp1 PGP F193Y+PCB (non-covalent assembling) **(C)** Chromophore binding pocket of Agp1 PGP (PDB: 5I5L). The residue F193 is indicated with a red circle. Conditions: 50 mM Tris buffer pH 7.8, 300 mM NaCl, at 20ºC.

Table 7-6: Chromophore absorption maxima in nanometer for the red absorbing Pr and Pfr band of Agp1 PGP F193Y with bound BV and PCB (covalent and non-covalent) and for Cph1 PGP WT with bound PCB. The *f*-value for calculating the Pfr absorbance spectrum according to **Eq. 4-1** is given.

Agp1 PGP	$\lambda_{max(abs),Pr}$ (nm)	$\lambda_{max(abs),Pfr}$ (nm)	*f*	Chromophore type
WT	700	750	0.30	BV
F193Y	700	750	0.30	BV
F193Y	685	717	0.35	PCB (non-covalent)

Fig. 7-4A, B shows the absorption spectra of Pr and Pr/Pfr forms of Agp1 F193Y(BV), and PCB adducts of Agp1 PGP F193Y (non-covalent). The extinction coefficient of 90000 ± 5000 $M^{-1}cm^{-1}$ was used for all the variants (Lamparter, Michael et al. 2002). The chromophore maximum absorption for the red absorbing Pr and Pfr peak for BV and PCB assembling are summarized in **Table 7-6**. The *f*-value is given for calculating the Pfr absorbance spectrum according to **Eq. 4-1 (**see chapter 4**)** which has similar value as WT (**Table 7-6**). The fluorescence emission measurements were performed under the same conditions for both variant: 22 µM in 300 mM NaCl, 50 mM Tris pH 7.8, 19ºC. The fluorescence emission was recorded between 650-740 nm, with excitation wavelength of 640 nm. **Fig. 7-8B** shows the emission of spectra of the PCB is bound to Agp1 F193Y (non-covalent) as well as the emission spectra of Agp1 F193Y (BV), the spectra of Agp1 WT (BV), WT+PCB, and V249C-PCB were shown for a comparison. **Fig. 7-8A** indicates the absorption spectra of the samples before the emission measurement which have the same absorption at excitation wavelength 640 nm. The fluorescence quantum yield was calculated using the ratio of the integral of emission spectra (**Fig. 7-8B**) based on **Eq 2-20**, and Cph1 PGP with Φ_f =0.024 was used as the respected reference (Nagano, Sadeghi et al. 2022). The results were summarized in **Table 7-6.** Interestingly the non-covalent binding of PCB to the mutant Agp1 PGP F193Y increased the quantum yield to Φ_f =0.064 which is around 3 times higher than Cph1 PGP WT. The covalent binding of BV to F193Y has higher quantum yield than WT-BV (Φ_f =0.003) with an increase of about 5-fold yielding Φ_f =0.014. The calculated quantum yield for the PCB adduct (non-covalent) showed a value of 0.064 which is 2-times brighter than the corresponding Agp1 PGP+PCB adduct.

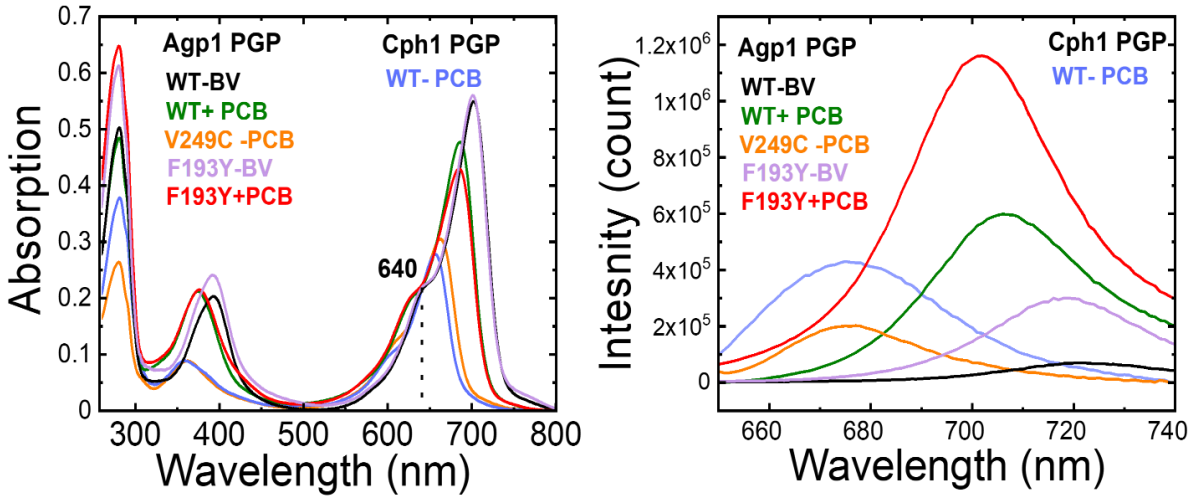

Figure 7-8: Steady-state fluorescence characterization of PCB and BV binding to Agp1 PGP F193Y in comparison to Agp1 PGP WT (BV), Agp1 PGP (WT for non-covalent PCB-binding, and V249C for covalent PCB-binding), and Cph1 PGP WT (PCB). The different variants are indicated by color. **(A)** UV-vis absorption of the samples before the emission measurement, all the samples have the same absorption at excitation wavelength 640 nm. **(B)** Fluorescence emission. λ_{ex}= 640 nm, and λ_{em} = 650-740 nm, slit 3**.** The values are summarized in **Table 7-7.** Condition**:** buffer: 300 mM NaCl, 50 mM Tris pH 7.8, 19ºC, the concentration of the variants was 12 µM for PCB covalent binding variants and 22 µM for PCB non-covalent binding and BV binding variants.

Table 7-7: Spectroscopic parameters of Agp1 PGP WT and its variant F193Y with bound BV and PCB (non-covalent) as shown in Fig. 7-8.

Agp1 PGP	$\lambda_{max(abs\_Pr)}$ (nm)	$\lambda_{max(em)}$ (nm)	Stokes shift (nm)	Φ_f
WT-BV	700	720	20	0.003
WT+PCB	685	706	21	0.032
V249C-PCB	656	675	19	0.010
F193Y-BV	700	720	20	0.014
F193Y+PCB	685	702	17	0.064

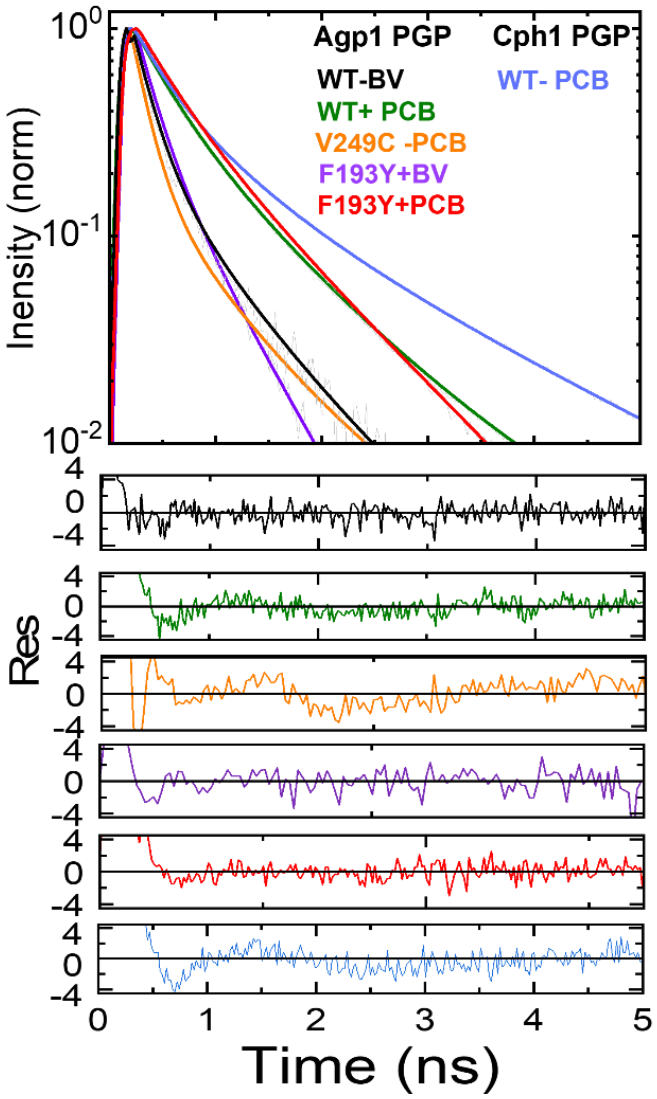

Figure 7-9: Fluorescence lifetime decays of PCB and BV binding to Agp1 PGP F193Y in comparison to Agp1 PGP WT (BV), Agp1 PGP (WT for non-covalent PCB-binding, and V249C for covalent PCB-binding), and Cph1 PGP WT (PCB). The residuals are shown below, and the different variants are indicated by color. The fluorescence lifetime decay fit results are summarized in **Table 7-8**. Conditions: 300 mM NaCl, 50 mM Tris pH 7.8, 19ºC; λ_{ex}= 640 nm, and λ_{em} = 708±38 nm.

Fig. 7-9 shows the decay curves of Agp1 F193Y (BV), F193Y + PCB, the curves WT (BV), WT+PCB, and V249C-PCB, as well as Cph1 PGP (PCB) shown for a comparison. The samples were measured under the same conditions, 12 µM in 300 mM NaCl, 50 mM Tris pH 7.8, 19ºC with excitation wavelength of λ_{ex}=640nm, and the emitted photons were collected at wavelength λ_{em}=708±38 nm. The time-resolved fluorescence lifetime curves were fitted with two decay components according to **Eq. 3-10**, the fit results are summarized in **Table 7-8**, including lifetimes τ_i, amplitudes α_i, and the mean lifetime τ_{mean}. The calculated mean lifetime for F193Y bound with BV, resulted of a close value to WT bound with BV, 0.33ns. However, in the case of non-covalent PCB-binding, the mean lifetime of F193Y indicated a longer mean lifetime with value of 0.67 ns compared to WT. The amplitude of longer lifetime (α_2) increased to 45 % in F193Y+PCB compared to WT (24%). It seems F193Y in Agp1 affects the water molecules distribution in Agp1 PGP, similar to the residue Y203 in Cph1 PGP (**Fig. 7-1**), which might be a reason for a higher quantum yield of Cph1 PGP variants compared to Agp1 variants. As we saw earlier, the covalent bond of PCB reduces quantum yield. This might also be a reason for a higher quantum yield of Agp1 PGP F193Y+PCB compared to Cph1 PGP WT. However, the lifetime of this variant, 0.67 ns, did not increase as much as quantum yield, and it is shorter than the lifetime of Cph1 PGP WT (0.86 ns).

Table 7-8: The fluorescence lifetime decay fit results of PCB and BV binding to Agp1 PGP F193Y in comparison to Agp1 PGP WT (BV), Agp1 PGP (WT for non-covalent PCB-binding, and V249C for covalent PCB-binding). The fluorescence decay components with τ_1, τ_2, and the related relative amplitudes α_1, α_2 are given. τ_{mean} is calculated as the population weighted mean lifetime according to the **Eq. 3-11**. The reduced chi-square (χ_{red}^2) is given to judge the goodness of the fit. The errors of the decay component values are less than 10% and the errors of the τ_{mean} values are less than 5%.

Agp1 PGP	τ_1 (ns)	τ_2 (ns)	α_1 (%)	α_2 (%)	τ_{mean} (ns)	χ_{red}^2
WT-BV	0.14	0.35	75.98	24.02	0.30	1.10
WT+PCB	0.33	0.81	80.34	19.76	0.50	1.20
V249C-PCB	0.19	0.72	74.48	25.52	0.30	1.30
F193Y-BV	0.18	0.48	72.27	27.73	0.33	1.10
F193Y+PCB	0.35	0.84	54.99	45.01	0.67	0.88

7.1.4 Quantum yield and lifetime correlation of PCB and BV binding phytochromes

The correlation between the fluorescence quantum yield and fluorescence lifetime of BV and PCB binding to Agp1 variants are shown in **Fig.7-10**, also the Cph1 PGP WT (PCB) and its variant Y176H shown for a comparison. The fluorescence lifetimes and quantum yield of the variants WT+PCB and Y176H+PCB (non-covalent) are correlated (dotted line to guide the eye in **Fig. 7-10**), in the same line as Cph1 Y176H (PCB). The slope revealed the radiative rate according to the **Eq 2-20**. For those protein data points that are located in the same line, the radiative rate k_r is quite similar and therefore implying a similar fluorescence mechanism. Also, Agp1 V249C-PCB (covalent bond), and F193Y- BV (covalent bond) can be found along the same line as Cph1 PGP WT (PCB). However, F193Y+PCB (non-covalent bond) showed a unique radiative rate compared to the other variants.

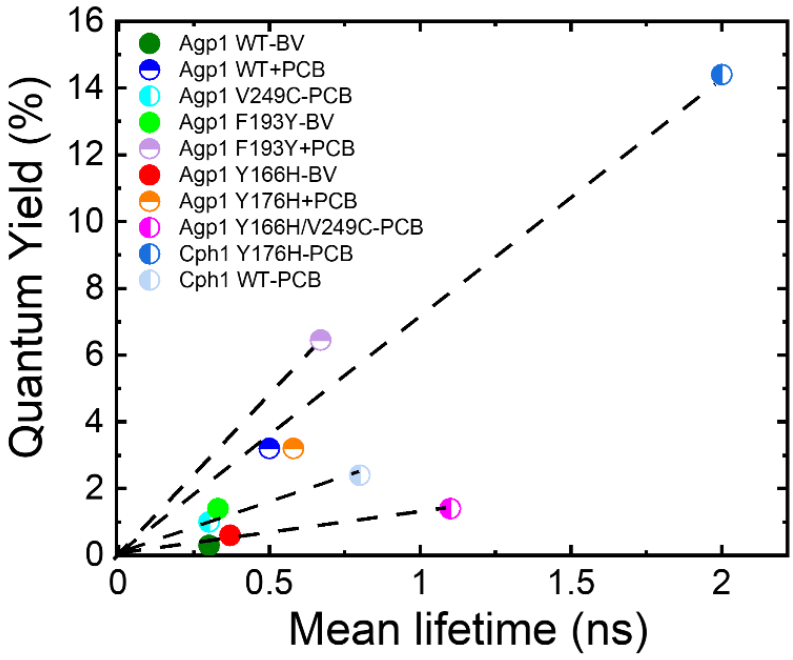

Figure 7-10: Correlation between fluorescence quantum yield and mean fluorescence lifetime. The dotted line is to guide the eye. The slope of this line would correspond to the radiative rate k_r according to the equation $\Phi_f = k_r \cdot \tau$ and indicate a similar k_r for those data points that fall on this line.

7.2 The quenching effect by Tyrosine

7.2.1 The quenching effect in ATTO 655

As shown in the literature, tyrosine can quench the emission of the organic red absorbing dyes, such as ATTO 655. Here we show that besides the static quenching of ATTO 655 with Stern-Volmer quenching constant of K_{SV} = 0.23 ± 0.01, there is also a dynamic quenching with Stern-Volmer quenching constant of K_{SV} = 0.173 ± 0.005 (**Fig. 7-11**).

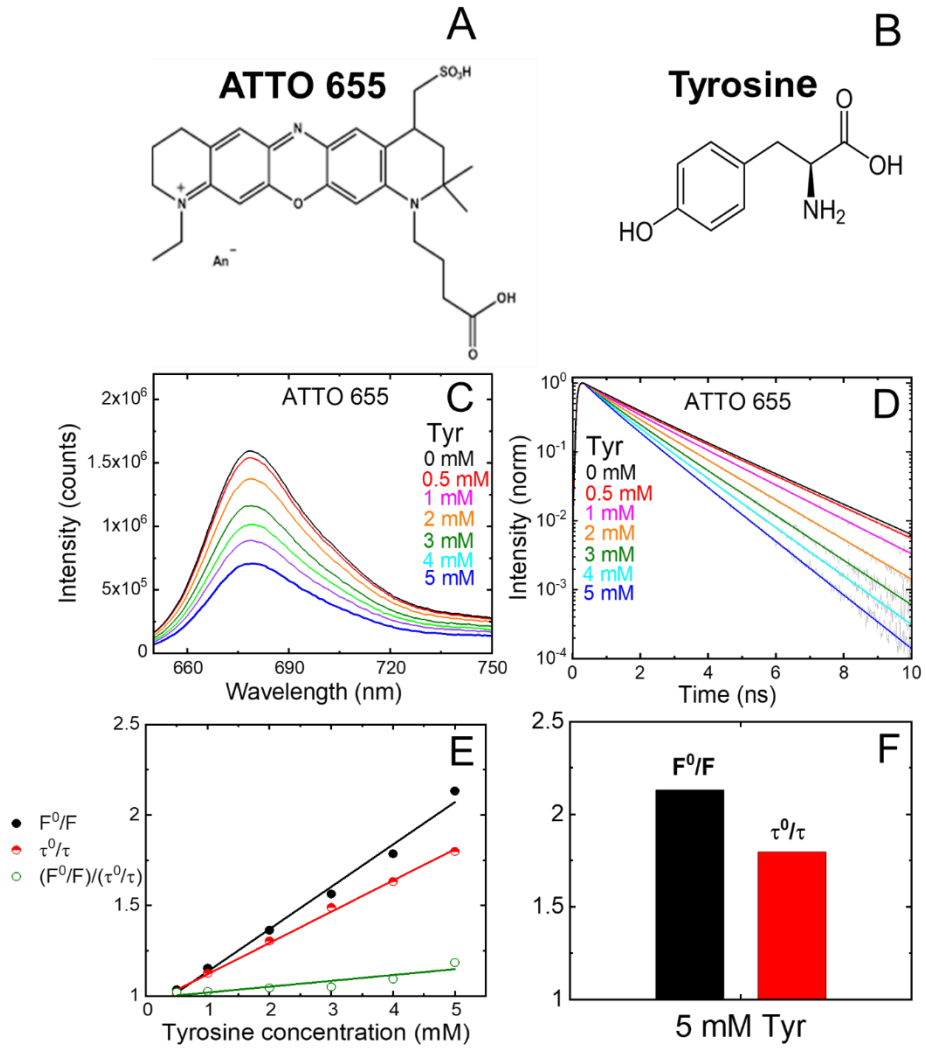

Figure 7-11: Static and dynamic quenching of ATTO 655 by tyrosine. Chemical structure of ATTO 655 (**A**) and tyrosine (**B**). ATTO 655 without tyrosine (0 mM) and with tyrosine concentration 0.5- 5 mM were used to measure emission (**C**) and lifetime (**D**). F is the integral of emission spectra of ATTO 655 with tyrosine and F^0 without tyrosine, and τ is the mean lifetime of ATTO 655 with tyrosine and τ^0 without tyrosine. The Stern-Volmer quenching constant was calculated according to **Eq. 2-27** K_{SV} = 0.23 ± 0.01 for static quenching (F^0/F), and K_{SV}=0.173 ± 0.005 for dynamic quenching (τ^0/τ). Condition: for fluorescence emission: λ_{ex}= 640 nm, and λ_{em}= 650-740 nm, slit 3. PBS buffer pH 7.5, 19ºC, for time-resolved fluorescence: λ_{ex}= 640 nm, and λ_{em} = 708±38 nm, PBS buffer pH 7.5, 19ºC.

7.2.2 The quenching effect by tyrosine in BSA+BV and BSA+PCB

Bovine Serum Albumin (BSA) has 4 hydrophobic pockets to which the PCB and BV can bind to simulate a tetrapyrrole binding protein (**Fig.7-12**). **Fig. 7-13** shows the absorption, emission, and fluorescence lifetime curves of BSA+PCB and BSA+BV.

The fluorescence lifetime of BSA+PCB, 0.48 ns, and the fluorescence lifetime of BSA+BV, 0.20 ns, are shorter than PCB in Cph1 PGP, and BV in Agp1 PGP, respectively.

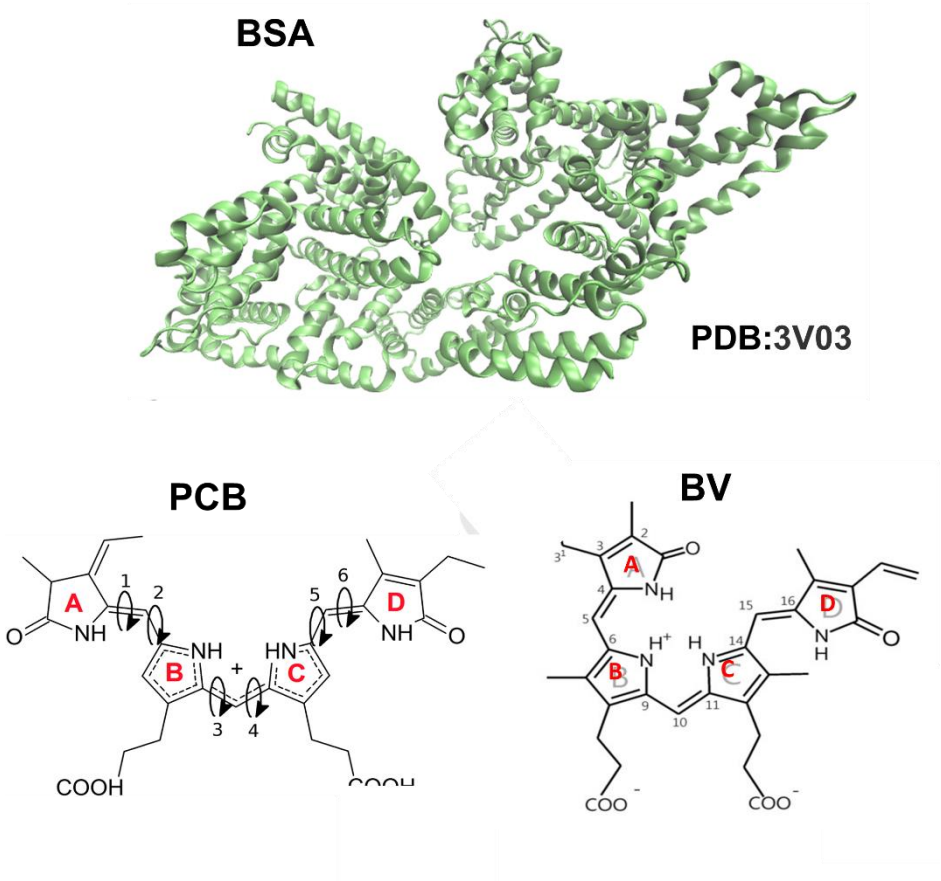

Figure 7-12: Crystal structure of Bovine Serum Albumin (BSA), and chemical structure of PCB and BV. BSA has 4 hydrophobic pockets to which the PCB and BV can bind to simulate a tetrapyrrole binding protein.

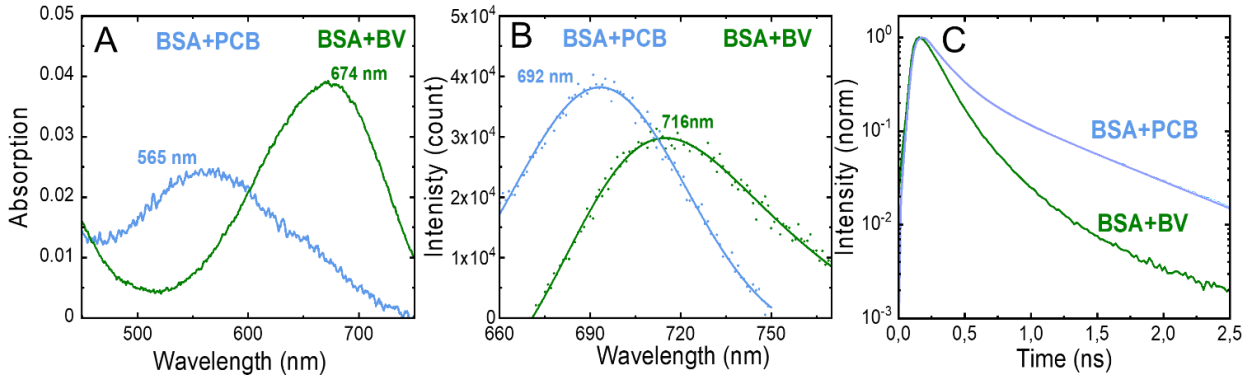

Figure 7-13: Steady-state and time-resolved characterization of PCB and BV assembling to BSA. BSA+PCB is shown in blue, and BSA+BV in green for UV-vis absorption (**A),** emission (**B**), and lifetime (**C**). Conditions: 1µM of PCB or BV + 100 µM BSA in 300 mM NaCl, 50 mM Tris pH 7.8. excitation at 640 nm, 19ºC.

Table 7-7: Spectroscopic parameters of PCB and BV assembling to BSA, as shown in Fig. 7-13.

Constructs	$\lambda_{max(abs\_Pr)}$ (nm)	$\lambda_{max(em)}$ (nm)	Stokes shift (nm)	τ_{mean} (ns)
BSA+BV	674	716	34	0.20
BSA+PCB	565	692	28	0.48

Static and dynamic quenching of BSA+PCB and BSA+BV by tyrosine are shown in **Fig 7-14** and **Fig 7-15**, respectively. The samples were measured under the same condition, 1 µM PCB or BV + 100 µM BSA in PBS buffer pH 7.5, 19ºC. BSA+PCB without tyrosine (0 mM) and with tyrosine concentration 0.5-5 mM were used to measure steady-state fluorescence emission and time-resolve fluorescence lifetime. Integral of emission spectra with tyrosine is shown by F and F^0 without tyrosine. Also, τ is the mean lifetime with tyrosine and τ^0 without tyrosine. The Stern-Volmer quenching constant for static quenching (F^0/F) was calculated according to **Eq. 2-27** with a value of K_{SV} = 0.14 ± 0.05 for BSA+PCB and K_{SV} = 0.20 ± 0.02 for BSA+BV. The Stern-Volmer quenching constant for the dynamic quenching (τ^0/τ) was calculated according to **Eq. 2-30** with a value of K_{SV} = 0.06 ± 0.02 for BSA+PCB and K_{SV} = 0.04 ± 0.01 for BSA+BV. These results show that tyrosine in the immediate environment of respective chromophore can quench fluorescence. Thus, it is expected that tyrosine in the chromophore binding pocket affect the fluorescence of phytochromes. By characterizing BV and PCB in a model binding protein BSA, we observed BSA+BV has a stronger static quenching compared to BSA+PCB, and the dynamic quenching is higher in BSA+PCB.

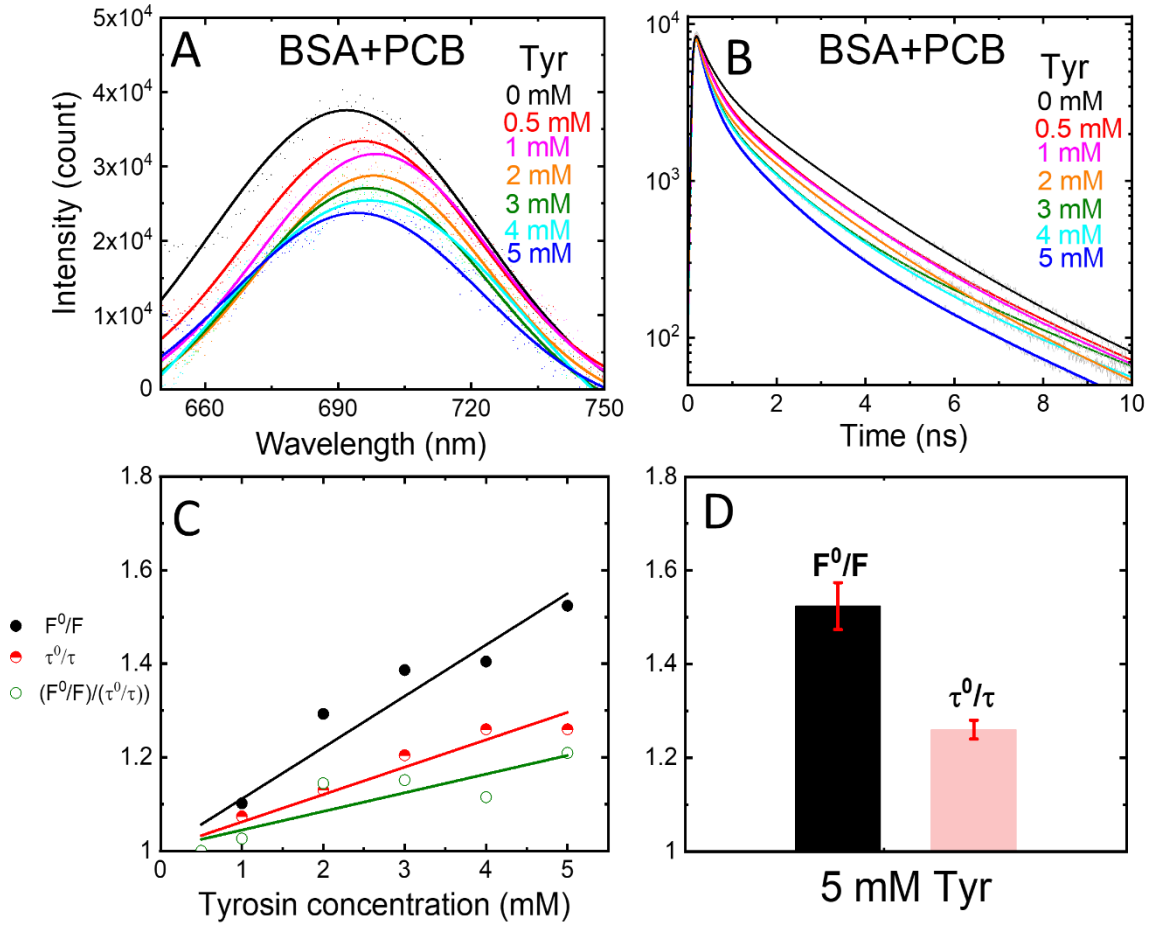

Figure 7-14: Static and dynamic quenching of BSA+PCB by tyrosine. BSA+PCB without tyrosine (0 mM) and with tyrosine concentration 0.5- 5 mM were used to measure emission (**A**) and lifetime (**B**). F is the integral of emission spectra of BSA+PCB with tyrosine and F0 without tyrosine, and τ is the mean lifetime of BSA+PCB with tyrosine and τ^0 without tyrosine. The Stern-Volmer quenching constant was calculated according to **Eq.2-27** K_{SV} = 0.14 ± 0.05 for static quenching (F^0/F), and according to **Eq. 2-30** K_{SV} = 0.06 ± 0.02 for dynamic quenching (τ^0/τ). Condition: Fluorescence emission. λ_{ex}= 640 nm, and λ_{em} = 650-740 nm, slit 3. 1 µM PCB + 100 µM BSA in PBS Buffer pH 7.5, 19ºC.

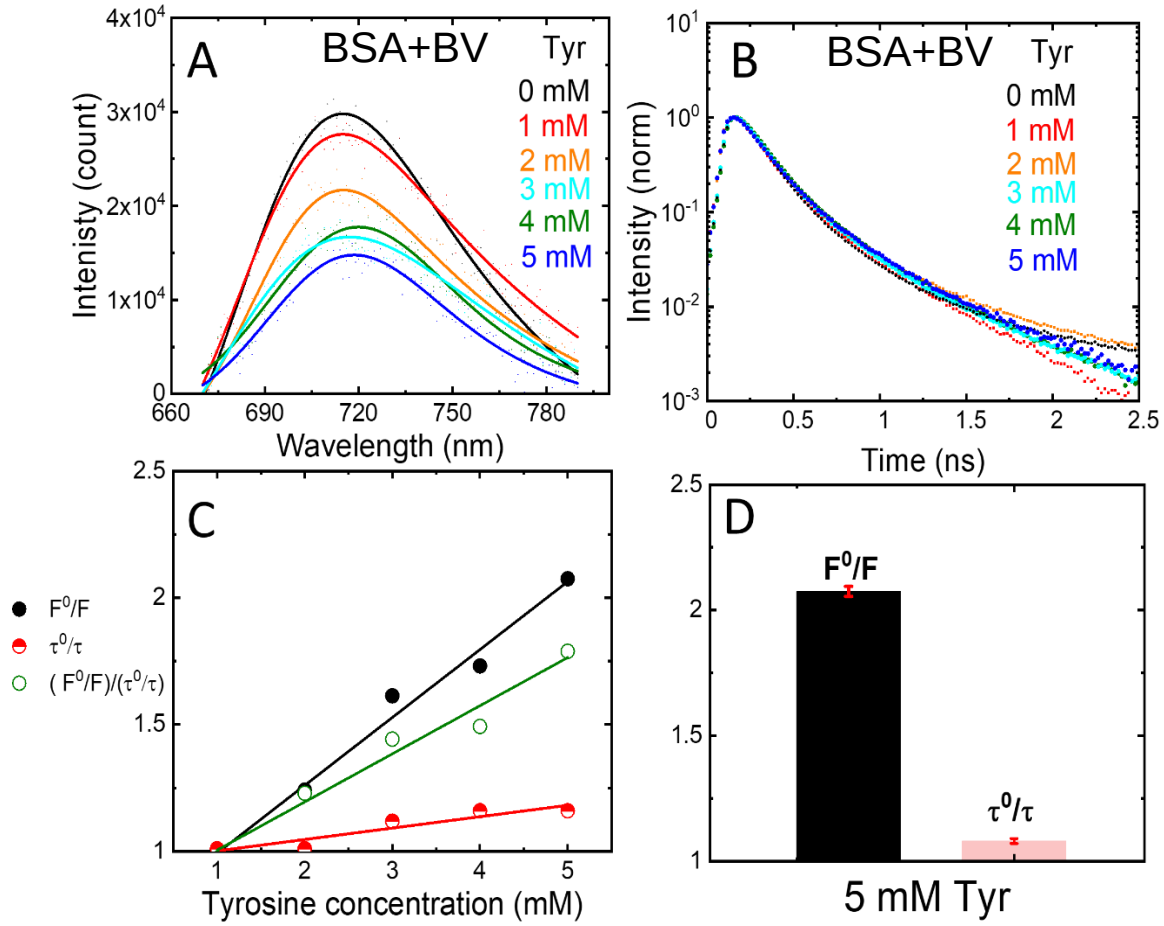

Figure 7-15: Static and dynamic quenching of BSA+BV by tyrosine. BSA+BV without tyrosine (0 mM) and with tyrosine concentration 0.5- 5 mM were used to measure emission (**A**) and lifetime (**B**). F is the integral of emission spectra of BSA+BV with tyrosine and F^0 without tyrosine, and τ is the mean lifetime of BSA+BV with tyrosine and τ^0 without tyrosine. The Stern-Volmer quenching constant was calculated according to **Eq. 2-27** K_{SV} = 0.20 ± 0.02 for static quenching (F0/F), and K_{SV} = 0.04 ± 0.01 for dynamic quenching (τ^0/τ). Condition: Fluorescence emission. λ_{ex}= 640 nm, and λ_{em} = 650-740 nm, slit 3. 1 µM BV + 100 µM BSA in PBS Buffer pH 7.5, 19ºC.

7.3 Conclusion

Non-covalent PCB-binding to Agp1 variants showed a higher fluorescence quantum yield compared to covalent PCB-binding. Both non-covalent and covalent PCB-binding to Agp1 PGP variants increased fluorescence compared to BV-binding Agp1 PGP variants. However, the values which were obtained for fluorescence quantum yield of non-covalent PCB-binding are higher than those values which were obtained for covalent PCB-binding. The covalent PCB-binding to the chromophore seems to dissipate the excitation energy to increase possibly the photoconversion quantum yield. However, the mean fluorescence lifetime is similar for covalent and non-covalent PCB-binding to Agp1 PGP WT, while the mean lifetime of the covalent PCB-binding to Y166H is longer than fluorescence lifetime of the non-covalent PCB-binding to Y166H.

The variant F193Y increased the fluorescence quantum yield in both PCB and BV-binding variants. The residue Phe 193 in Agp1 PGP corresponds to Tyr 203 in Cph1 PGP, in which Phe is missing the hydroxyl group of tyrosine (**Fig.7-1**). This difference can affect the hydrogen bond network or the water molecules distribution, as Agp1 and Cph1 have different water molecules networks in their chromophore binding pocket (**Fig.7-1**). Our results showed the mutant F193Y strongly increased the fluorescence quantum yield in this variant, which indicates the important role of the chromophore binding pocket in fluorescence quantum yield despite of the chromophore type.

Tyrosine might act as a quencher in Agp1 and Cph1. The results from the tyrosine titration of BSA+PCB and BSA+PCB revealed the fact that tyrosine can act as a quencher in these studied samples. In both studied cases, the static and dynamic quenching was observed, although in the case of BSA+BV, the static quenching was higher compared to the static quenching in BSA+PCB.

8 Summery and Outlook

Prototypical phytochromes including Cph1 from the cyanobacterium *Synechocystis* 6803 and Agp1 from *Agrobacterium tumefaciens* act as a biological photo-switch that interconvert between two main states: red (Pr) and metastable far-red (Pfr) states, after absorbing red and far-red light, respectively. The photoconversion in phytochrome is associated with photoisomerization of the bilin chromophore and followed the global structural changes to the cellular output signal which is the C-terminal transmitter (output) module, usually a histidine kinase, in the case of Cph1 and Agp1. During the Pr → Pfr photoconversion, the transient chromophore deprotonation triggers an extensive global structural change to facilitate the protein signaling. However, the photoconversion in phytochrome can be interrupted by the site-directed mutagenesis of the conserved amino acids in the phytochrome chromophore binding pocket which extraordinary enhance the fluorescence quantum yield in several types of phytochromes. Phytochromes as a near-infrared fluorescent probe can be used as an optogenetic tool for *in vivo* imaging. Recently, several near-infrared fluorescent proteins (NIR-FPs) were engineered from biliverdin-binding bacteriophytochromes as well phycocyanobilin-binding phytochromes which are promising probes for

fluorescence microscopy and *in vivo* imaging. However, developing NIR-FPs for higher fluorescence quantum yields and longer fluorescence lifetimes would be an advantage.

This dissertation contained two main parts. The first part including Chapter 4 and 5 focused on the protonation and conformational dynamics of phytochrome and the second part including chapter 6 and 7 studied the fluorescent phytochromes.

The results from the first part showed that the protonation heterogeneity is not related to the photoconversion directly, e.g., more than one p*K* was observed for Cph1 PGP variant Y176H which is blocked the photoconversion in the Pr like state. However, our results suggested that the protonation heterogeneity is more related to the hydrogen bond network of His260 and chromophore PCB, the water molecule, or the other amino acids in the chromophore binding pocket. Also, the protonation heterogeneity was observed only in Agp1 PGP variant V249C with covalent PCB-binding and not in non-covalent PCB-binding variant Agp1 PGP WT. Moreover, the conformational dynamics in far-distance from chromophore (PHY domain) in correlation to the chromophore deprotonation was observed only in Cph1 PGP and not in Agp1 PGP. This is also another evidence, which shows a different mechanism in PCB-binding and BV-binding phytochromes. The present work provided the hypothesis, experiments, and results to understand better the protonation heterogeneity and the chromophore deprotonation and its correlation to the protein conformation dynamic in phytochromes. However, further studies of certain mutants in both Agp1 and Cph1 can help for a deeper understanding of the chromophore deprotonation mechanism in function and structure of phytochromes and its relation to the replacement of BV by PCB during the evolution. One of these variants will be a combination of the single cysteine variant in the PHY domain of C279S/C295S/V364C with the chromophore binding site V249C in the GAF domain in Agp1 PGP, in order to investigate whether the conformational dynamics correlation will be observed in the covalent PCB-binding variant, which showed the protonation heterogeneity. Also, it would be useful to investigate the conformational dynamics and the protonation heterogeneity in Cph1 PGP variant S20C as a binding site for covalent binding of BV, for the comparison to the non-covalent BV-binding of the WT.

In the second part of this dissertation several variants of fluorescent phytochromes were investigated in the steady-state and time-resolved regime. The results from this part indicated a significant higher fluorescence quantum yield and a longer fluorescence lifetime in Cph1&2 variants compared to Agp2 variants. The investigation on the origin of fluorescence in Agp1 variants revealed that the PCB adducts of Agp1 PGP variants increased fluorescence compared to the BV adducts. However, the quantum yield of covalent PCB-binding adducts was lower than non-covalent binding variants and both PCB adducts (covalent and non-covalent) didn’t enhance fluorescence as it was observed for Cph1 PGP (PCB).

However, interestingly the non-covalent PCB-binding of variant F193Y significantly enhanced the fluorescence quantum yield in Agp1 PGP, even more than in WT Cph1 PGP (PCB). This tyrosine in position 193 (Agp1) or 203 (Cph1) might affect the distribution of the second water molecules cluster and further hydrogen bond networks in the vicinity of the ring D, which are missing in native Agp1 PGP. This water molecule network and hydrogen bond networks are shown in the crystal structure of Cph1 PGP. Further mutants such as the double mutant F193Y/V249C and the triple mutant Y166H/F193Y/V249C for covalent PCB-binding would be useful to test our hypothesis about the role of this tyrosine in phytochromes. We expect a further increase of fluorescence in Y166H/F193Y/V249C as much as it was observed for Y176H in Cph1 PGP.

Overall, in this dissertation, a better understanding of the chromophore deprotonation in the Pr state of two groups of PCB-binding and BV-binding phytochrome as well as their effect on the local conformational changes, has been achieved. Our results showed the protonation heterogeneity related to 1) the chromophore type, 2) the hydrogen bond network of the conserved His (260 in Cph1, 250 in Agp1) to the chromophore and the close amino acids, and most importantly, it is not dependent on the photoconversion. Also, our results suggested that chromophore deprotonation in Cph1 PGP is closely associated with a higher intrinsic protein mobility (conformational space) both in proximal and distal protein sites, implying a causal relationship that might be important for the global large protein arrangements and thus intramolecular signal transduction in the photoreceptors after light activation. However, this correlation was not observed in Agp1 PGP. Also, this strong work provided a better understanding of the molecular basis of fluorescence enhancement in phytochrome photoreceptors. Our results suggested that the large difference between fluorescence quantum yield of BV-binding and PCB-binding phytochrome is not only related to the type of the chromophore but also related to the chromophore biding pocket including the conserved amino acids, hydrogen bonds and the water molecule network. This could have a different effect on the chromophore flexibly during the photoconversion in Agp1 and Cph1.

List of Publications

The following publications resulted from this thesis:

Transient Deprotonation of the Chromophore Affects Protein Dynamics Proximal and Distal to the Linear Tetrapyrrole Chromophore in Phytochrome Cph1

Maryam Sadeghi, Jens Balke, Constantin Schneider, Soshichiro Nagano, Johannes Stellmacher, Günter Lochnit, Christina Lang, Chris Weise, Jon Hughes, and Ulrike Alexiev. Biochemistry 2020, 59, 9, 1051–1062. Publication Date: February 18, 2020, https://doi.org/10.1021/acs.biochem.9b00967

I performed the time-resolved anisotropy experiments and analyzed the data, also prepared the apoprotein sample. I contributed to the manuscript writing, discussion, and interpretation of the data, also contributed to the MS analyses.

Improved fluorescent phytochromes for in situ imaging

Soshichiro Nagano, Maryam Sadeghi, Jens Balke, Moritz Fleck, Nina Heckmann1, Georgios Psakis, Ulrike Alexiev. Scientific Reports volume 12, Article number: 5587. Publication Date: April 04, 2022, https://doi.org/10.1038/s41598-022-09169-x

I performed the fluorescence lifetime and flash-spectroscopy experiments and analyzed the data. I contributed to the manuscript writing, discussion, and interpretation of the data.

Acknowledgments

I would like to acknowledge my advisors Prof. Ulrike Alexiev for giving me the opportunity to join her research group. It was a great honor and pleasure to work under her supervision. I truly appreciate her patience, trust, and advice.

I would like to thank Prof. Holger Dau for accepting to be my second supervisor and Prof. Joachim Heberle for accepting to be my second referee.

For financial support I acknowledge SFB 1078, A2 project and DRS for very useful courses.

I feel fortunate to have been in a friendly environment while doing my PhD. Thanks to Robert, Jens, Constantine, Alex, Pier, Victor, Johana, Timm, Jaqueline who helped me learn to do so many different experiments and methods of characterization allowing me to work independently. I learned a lot from all of you during the last six years, while experiencing a new and enjoyable life in Germany. Thanks for always being so nice, supportive, and lovely.

Also, I would like to thank Prof. Jon Hughes, Dr. Soshichiro Nagano from Gießen and Dr. Anastasia Kraskov from TU-Berlin for their scientific collaboration. My special thanks to Norbert Michael and Soshichiro Nagano for teaching me how to work in microbiology lab, and also thanks to Dr. Ramona Schlesinger for letting me to use the cooling incubator, it was indeed a big help in my work.

I appreciate the support of my friends outside of FU-Berlin, who made life more exciting and enjoyable. My especial thanks to Uroš for his support during all of these years, for times that I was working in the lab and not much being available, or I was fully occupied by my challenges. You are wonderful boyfriend and I appreciate a lot what you did to make the life easier for me. Thank you very much, I love you.

Finally, I would like to thank my family for doing their best to help me finding the correct path in life by fully supporting me as I tried to face my problems independently. Of course, I could not reach my goals without you. Thanks to Masoumeh, for being the best sister, for always helping me to overcome my challenges from an early stage of my life, this success won't be achieved without you, I love you.

References

Airan, R. D., K. R. Thompson, L. E. Fenno, H. Bernstein and K. Deisseroth (2009). "Temporally precise in vivo control of intracellular signalling." Nature **458**(7241): 1025-1029.

Alexiev, U. and D. L. Farrens (2014). "Fluorescence spectroscopy of rhodopsins: insights and approaches." Biochim. Biophys. Acta **1837**(5): 694-709.

Alexiev, U. and D. L. Farrens (2014). "Fluorescence spectroscopy of rhodopsins: Insights and approaches." Biochimica et Biophysica Acta (BBA) - Bioenergetics **1837**(5): 694-709.

Alexiev, U., I. Rimke and T. Pohlmann (2003). "Elucidation of the nature of the conformational changes of the EF-interhelical loop in bacteriorhodopsin and of the helix VIII on the cytoplasmic surface of bovine rhodopsin: a time-resolved fluorescence depolarization study." J Mol Biol **328**(3): 705-719.

Alexiev, U., I. Rimke and T. Pöhlmann (2003). "Elucidation of the Nature of the Conformational Changes of the EF-interhelical Loop in Bacteriorhodopsin and of the Helix VIII on the Cytoplasmic Surface of Bovine Rhodopsin: A Time-resolved Fluorescence Depolarization Study." Journal of Molecular Biology **328**(3): 705-719.

Alexiev, U., P. Volz, A. Boreham and R. Brodwolf (2017). "Time-resolved fluorescence microscopy (FLIM) as an analytical tool in skin nanomedicine." European Journal of Pharmaceutics and Biopharmaceutics **116**: 111-124.

Auldridge, M. E., K. A. Satyshur, D. M. Anstrom and K. T. Forest (2012). "Structure-guided engineering enhances a phytochrome-based infrared fluorescent protein." J Biol Chem **287**(10): 7000-7009.

Ayala, F. J. and M. Coluzzi (2005). "Chromosome speciation: Humans, Drosophila, and mosquitoes." Proceedings of the National Academy of Sciences **102**(suppl_1): 6535-6542.

Beale, S. I. (1993). "Biosynthesis of phycobilins." Chemical Reviews **93**(2): 785-802.

Becker, W., B. Su and A. Bergmann (2012). Spatially resolved recording of transient fluorescence-lifetime effects by line-scanning TCSPC, SPIE.

Bhoo, S. H., S. J. Davis, J. Walker, B. Karniol and R. D. Vierstra (2001). "Bacteriophytochromes are photochromic histidine kinases using a biliverdin chromophore." Nature **414**(6865): 776-779.

Borucki, B., S. Seibeck, M. P. Heyn and T. Lamparter (2009). "Characterization of the Covalent and Noncovalent Adducts of Agp1 Phytochrome Assembled with Biliverdin and Phycocyanobilin by Circular Dichroism and Flash Photolysis." Biochemistry **48**(27): 6305-6317.

Borucki, B., D. von Stetten, S. Seibeck, T. Lamparter, N. Michael, M. A. Mroginski, H. Otto, D. H. Murgida, M. P. Heyn and P. Hildebrandt (2005). "Light-induced proton release of phytochrome is coupled to the transient deprotonation of the tetrapyrrole chromophore." J. Biol. Chem. **280**(40): 34358-34364.

Brodwolf, R., P. Volz-Rakebrand, J. Stellmacher, C. Wolff, M. Unbehauen, R. Haag, M. Schäfer-Korting, C. Zoschke and U. Alexiev (2020). "Faster, sharper, more precise: Automated Cluster-FLIM in preclinical testing directly identifies the intracellular fate of theranostics in live cells and tissue." Theranostics **10**(14): 6322-6336.

Buhrke, D., N. N. Tavraz, D. M. Shcherbakova, L. Sauthof, M. Moldenhauer, F. Vélazquez Escobar, V. V. Verkhusha, P. Hildebrandt and T. Friedrich (2019). "Chromophore binding to two cysteines increases quantum yield of near-infrared fluorescent proteins." Sci Rep **9**(1): 1866.

Byrnes, K. R., R. W. Waynant, I. K. Ilev, X. Wu, L. Barna, K. Smith, R. Heckert, H. Gerst and J. J. Anders (2005). "Light promotes regeneration and functional recovery and alters the immune response after spinal cord injury." Lasers in Surgery and Medicine **36**(3): 171-185.

Chen, E., V. N. Lapko, P.-S. Song and D. S. Kliger (1997). "Dynamics of the N-Terminal α-Helix Unfolding in the Photoreversion Reaction of Phytochrome A." Biochemistry **36**(16): 4903-4908.

Dasgupta, J., R. R. Frontiera, K. C. Taylor, J. C. Lagarias and R. A. Mathies (2009). "Ultrafast excited-state isomerization in phytochrome revealed by femtosecond stimulated Raman spectroscopy." Proceedings of the National Academy of Sciences **106**(6): 1784-1789.

Escobar, F. V., C. Lang, A. Takiden, C. Schneider, J. Balke, J. Hughes, U. Alexiev, P. Hildebrandt and M. A. Mroginski (2017). "Protonation-Dependent Structural Heterogeneity in the Chromophore Binding Site of Cyanobacterial Phytochrome Cph1." J. Phys. Chem. B **121**(1): 47-57.
Essen, L.-O., J. Mailliet and J. Hughes (2008). "The structure of a complete phytochrome sensory module in the Pr ground state." Proceedings of the National Academy of Sciences **105**(38): 14709-14714.
Filonov, G. S., K. D. Piatkevich, L.-M. Ting, J. Zhang, K. Kim and V. V. Verkhusha (2011). "Bright and stable near-infrared fluorescent protein for in vivo imaging." Nature Biotechnology **29**(8): 757-761.
Filonov, G. S., K. D. Piatkevich, L. M. Ting, J. Zhang, K. Kim and V. V. Verkhusha (2011). "Bright and stable near-infrared fluorescent protein for in vivo imaging." Nat Biotechnol **29**(8): 757-761.
Fischer, A. J. and J. C. Lagarias (2004). "Harnessing phytochrome's glowing potential." Proc. Natl. Acad. Sci. U. S. A. **101**(50): 17334.
Fischer, A. J. and J. C. Lagarias (2004). "Harnessing phytochrome's glowing potential." Proceedings of the National Academy of Sciences of the United States of America **101**(50): 17334.
Fischer, A. J., N. C. Rockwell, A. Y. Jang, L. A. Ernst, A. S. Waggoner, Y. Duan, H. Lei and J. C. Lagarias (2005). "Multiple Roles of a Conserved GAF Domain Tyrosine Residue in Cyanobacterial and Plant Phytochromes." Biochemistry **44**(46): 15203-15215.
Frankenberg, N. and J. C. Lagarias (2003). "Phycocyanobilin:Ferredoxin Oxidoreductase ofAnabaena sp. PCC 7120: BIOCHEMICAL AND SPECTROSCOPIC CHARACTERIZATION *." Journal of Biological Chemistry **278**(11): 9219-9226.
Frankenberg, N., K. Mukougawa, T. Kohchi and J. C. Lagarias (2001). "Functional Genomic Analysis of the HY2 Family of Ferredoxin-Dependent Bilin Reductases from Oxygenic Photosynthetic Organisms." The Plant Cell **13**(4): 965-978.
Hughes, J. and T. Lamparter (1999). "Prokaryotes and Phytochrome. The Connection to Chromophores and Signaling1." Plant Physiology **121**(4): 1059-1068.
Ihalainen, J. A., H. Takala and H. Lehtivuori (2015). "Fast Photochemistry of Prototypical Phytochromes—A Species vs. Subunit Specific Comparison." Frontiers in Molecular Biosciences **2**.
Kamper, M., H. Ta, N. A. Jensen, S. W. Hell and S. Jakobs (2018). "Near-infrared STED nanoscopy with an engineered bacterial phytochrome." Nature Communications **9**(1): 4762.
Kennedy, M. J., R. M. Hughes, L. A. Peteya, J. W. Schwartz, M. D. Ehlers and C. L. Tucker (2010). "Rapid blue-light–mediated induction of protein interactions in living cells." Nature Methods **7**(12): 973-975.
Kennis, J. T. M. and T. Mathes (2013). "Molecular eyes: proteins that transform light into biological information." Interface Focus **3**(5): 20130005.
Kim, A. J. and J. Hanes (2012). "The emergence of multiple particle tracking in intracellular trafficking of nanomedicines." Biophys. Rev. **4**(2): 83-92.
Kim, P. W., N. C. Rockwell, L. H. Freer, C.-W. Chang, S. S. Martin, J. C. Lagarias and D. S. Larsen (2013). "Unraveling the Primary Isomerization Dynamics in Cyanobacterial Phytochrome Cph1 with Multipulse Manipulations." J. Phys. Chem. Lett. **4**(16): 2605-2609.
Kim, T.-Y., K. Winkler and U. Alexiev (2007). "Picosecond Multidimensional Fluorescence Spectroscopy: A Tool to Measure Real-time Protein Dynamics During Function†." Photochemistry and Photobiology **83**(2): 378-385.
Kirchberg, K., T. Y. Kim, M. Moller, D. Skegro, G. Dasara Raju, J. Granzin, G. Buldt, R. Schlesinger and U. Alexiev (2011). "Conformational dynamics of helix 8 in the GPCR rhodopsin controls arrestin activation in the desensitization process." Proc. Natl. Acad. Sci. U. S. A. **108**(46): 18690-18695.
Kohchi, T., K. Mukougawa, N. Frankenberg, M. Masuda, A. Yokota and J. C. Lagarias (2001). "The Arabidopsis HY2 gene encodes phytochromobilin synthase, a ferredoxin-dependent biliverdin reductase." The Plant cell **13**(2): 425-436.
König, K. (2000). "Multiphoton microscopy in life sciences." Journal of Microscopy **200**(2): 83-104.
Kraskov, A., A. D. Nguyen, J. Goerling, D. Buhrke, F. Velazquez Escobar, M. Fernandez Lopez, N. Michael, L. Sauthof, A. Schmidt, P. Piwowarski, Y. Yang, T. Stensitzki, S. Adam, F. Bartl, I. Schapiro, K.

Heyne, F. Siebert, P. Scheerer, M. A. Mroginski and P. Hildebrandt (2020). "Intramolecular Proton Transfer Controls Protein Structural Changes in Phytochrome." Biochemistry **59**(9): 1023-1037.
Krieger, A., I. Molina, I. Oberpichler, N. Michael and T. Lamparter (2008). "Spectral properties of phytochrome Agp2 from Agrobacterium tumefaciens are specifically modified by a compound of the cell extract." J Photochem Photobiol B **93**(1): 16-22.
Krieger, A., I. Molina, I. Oberpichler, N. Michael and T. Lamparter (2008). "Spectral properties of phytochrome Agp2 from Agrobacterium tumefaciens are specifically modified by a compound of the cell extract." Journal of Photochemistry and Photobiology B: Biology **93**(1): 16-22.
Lagarias, J. C. and H. Rapoport (1980). "Chromopeptides from phytochrome. The structure and linkage of the PR form of the phytochrome chromophore." Journal of the American Chemical Society **102**(14): 4821-4828.
Lamparter, T., N. Michael, O. Caspani, T. Miyata, K. Shirai and K. Inomata (2003). "Biliverdin Binds Covalently to Agrobacterium Phytochrome Agp1 via Its Ring A Vinyl Side Chain*." Journal of Biological Chemistry **278**(36): 33786-33792.
Lamparter, T., N. Michael, F. Mittmann and B. Esteban (2002). "Phytochrome from Agrobacterium tumefaciens has unusual spectral properties and reveals an N-terminal chromophore attachment site." Proceedings of the National Academy of Sciences **99**(18): 11628-11633.
Levskaya, A., A. A. Chevalier, J. J. Tabor, Z. B. Simpson, L. A. Lavery, M. Levy, E. A. Davidson, A. Scouras, A. D. Ellington, E. M. Marcotte and C. A. Voigt (2005). "Engineering Escherichia coli to see light." Nature **438**(7067): 441-442.
Levskaya, A., O. D. Weiner, W. A. Lim and C. A. Voigt (2009). "Spatiotemporal control of cell signalling using a light-switchable protein interaction." Nature **461**(7266): 997-1001.
Macháčková, I. (1994). "Kendrick, R.E., Kronenberg, G.H.M.:Photomorphogenesis in plants. 2nd Edition." Biologia Plantarum **36**(4): 564-564.
Mailliet, J., G. Psakis, K. Feilke, V. Sineshchekov, L.-O. Essen and J. Hughes (2011). "Spectroscopy and a High-Resolution Crystal Structure of Tyr263 Mutants of Cyanobacterial Phytochrome Cph1." Journal of Molecular Biology **413**(1): 115-127.
Mailliet, J., G. Psakis, K. Feilke, V. Sineshchekov, L. O. Essen and J. Hughes (2011). "Spectroscopy and a high-resolution crystal structure of Tyr263 mutants of cyanobacterial phytochrome Cph1." J Mol Biol **413**(1): 115-127.
Mattis, J., K. M. Tye, E. A. Ferenczi, C. Ramakrishnan, D. J. O'Shea, R. Prakash, L. A. Gunaydin, M. Hyun, L. E. Fenno, V. Gradinaru, O. Yizhar and K. Deisseroth (2012). "Principles for applying optogenetic tools derived from direct comparative analysis of microbial opsins." Nature Methods **9**(2): 159-172.
Mayerhöfer, T. G., S. Pahlow and J. Popp (2020). "The Bouguer-Beer-Lambert Law: Shining Light on the Obscure." ChemPhysChem **21**(18): 2029-2046.
Möller, M. and U. Alexiev (2009). "Surface Charge Changes upon Formation of the Signaling State in Visual Rhodopsin†." Photochemistry and Photobiology **85**(2): 501-508.
Montgomery, B. L. and J. C. Lagarias (2002). "Phytochrome ancestry: sensors of bilins and light." Trends in Plant Science **7**(8): 357-366.
Murphy, J. T. and J. C. Lagarias (1997). "The phytofluors: a new class of fluorescent protein probes." Current Biology **7**(11): 870-876.
Nagano, S., P. Scheerer, K. Zubow, N. Michael, K. Inomata, T. Lamparter and N. Krauß (2016). "The Crystal Structures of the N-terminal Photosensory Core Module of Agrobacterium Phytochrome Agp1 as Parallel and Anti-parallel Dimers." J Biol Chem **291**(39): 20674-20691.
Nieder, J. B., E. A. Stojković, K. Moffat, K. T. Forest, T. Lamparter, R. Bittl and J. T. M. Kennis (2013). "Pigment–Protein Interactions in Phytochromes Probed by Fluorescence Line Narrowing Spectroscopy." The Journal of Physical Chemistry B **117**(48): 14940-14950.

Oka, Y., T. Matsushita, N. Mochizuki, T. Suzuki, S. Tokutomi and A. Nagatani (2004). "Functional Analysis of a 450–Amino Acid N-Terminal Fragment of Phytochrome B in Arabidopsis." The Plant Cell **16**(8): 2104.
Piatkevich, K. D., F. V. Subach and V. V. Verkhusha (2013). "Engineering of bacterial phytochromes for near-infrared imaging, sensing, and light-control in mammals." Chemical Society reviews **42**(8): 3441-3452.
Piatkevich, K. D., F. V. Subach and V. V. Verkhusha (2013). "Far-red light photoactivatable near-infrared fluorescent proteins engineered from a bacterial phytochrome." Nature Communications **4**(1): 2153.
Rockwell, N. C., L. Shang, S. S. Martin and J. C. Lagarias (2009). "Distinct classes of red/far-red photochemistry within the phytochrome superfamily." Proceedings of the National Academy of Sciences of the United States of America **106**(15): 6123-6127.
Royant, A., P. Carpentier, J. Ohana, J. McGeehan, B. Paetzold, M. Noirclerc-Savoye, X. Vernede, V. Adam and D. Bourgeois (2007). "Advances in spectroscopic methods for biological crystals. 1. Fluorescence lifetime measurements." Journal of Applied Crystallography **40**(6): 1105-1112.
Ruban, A. V. (2014). "Evolution under the sun: optimizing light harvesting in photosynthesis." Journal of Experimental Botany **66**(1): 7-23.
Rumfeldt, J. A., H. Takala, A. Liukkonen and J. A. Ihalainen (2019). "UV-Vis Spectroscopy Reveals a Correlation Between Y263 and BV Protonation States in Bacteriophytochromes." Photochemistry and Photobiology **95**(4): 969-979.
Sadeghi, M., J. Balke, C. Schneider, S. Nagano, J. Stellmacher, G. Lochnit, C. Lang, C. Weise, J. Hughes and U. Alexiev (2020). "Transient Deprotonation of the Chromophore Affects Protein Dynamics Proximal and Distal to the Linear Tetrapyrrole Chromophore in Phytochrome Cph1." Biochemistry **59**(9): 1051-1062.
Sadeghi, M., J. Balke, C. Schneider, S. Nagano, J. Stellmacher, G. Lochnit, C. Lang, C. Weise, J. Hughes and U. Alexiev (2020). "Transient Deprotonation of the Chromophore Affects Protein Dynamics Proximal and Distal to the Linear Tetrapyrrole Chromophore in Phytochrome Cph1." Biochemistry.
Schmidt, A., L. Sauthof, M. Szczepek, M. F. Lopez, F. V. Escobar, B. M. Qureshi, N. Michael, D. Buhrke, T. Stevens, D. Kwiatkowski, D. von Stetten, M. A. Mroginski, N. Krauß, T. Lamparter, P. Hildebrandt and P. Scheerer (2018). "Structural snapshot of a bacterial phytochrome in its functional intermediate state." Nature Communications **9**(1): 4912.
Schmidt, P., T. Gertsch, A. Remberg, W. Gärtner, S. E. Braslavsky and K. Schaffner (1998). "The Complexity of the Pr to Pfr Phototransformation Kinetics Is an Intrinsic Property of Native Phytochrome*." Photochemistry and Photobiology **68**(5): 754-761.
Schröder, G. F., U. Alexiev and H. Grubmüller (2005). "Simulation of Fluorescence Anisotropy Experiments: Probing Protein Dynamics." Biophysical Journal **89**(6): 3757-3770.
Shu, X., A. Royant, M. Z. Lin, T. A. Aguilera, V. Lev-Ram, P. A. Steinbach and R. Y. Tsien (2009). "Mammalian Expression of Infrared Fluorescent Proteins Engineered from a Bacterial Phytochrome." Science **324**(5928): 804.
Sineshchekov, V., L. Koppel', B. Esteban, J. Hughes and T. Lamparter (2002). "Fluorescence investigation of the recombinant cyanobacterial phytochrome (Cph1) and its C-terminally truncated monomeric species (Cph1Δ2): implication for holoprotein assembly, chromophore–apoprotein interaction and photochemistry." Journal of Photochemistry and Photobiology B: Biology **67**(1): 39-50.
Sineshchekov, V., J. Mailliet, G. Psakis, K. Feilke, J. Kopycki, M. Zeidler, L. O. Essen and J. Hughes (2014). "Tyrosine 263 in cyanobacterial phytochrome Cph1 optimizes photochemistry at the prelumi-R -> lumi-R step." Photochem Photobiol **90**: 786-795.
Sineshchekov, V. A. (1995). "Evidence for the existence of two phytochrome A populations." Journal of Photochemistry and Photobiology B: Biology **28**(1): 53-55.
Sineshchekov, V. A. (1995). "Photobiophysics and photobiochemistry of the heterogeneous phytochrome system." Biochimica et Biophysica Acta (BBA) - Bioenergetics **1228**(2): 125-164.

Smith, H. (2000). "Phytochromes and light signal perception by plants--an emerging synthesis." Nature **407**(6804): 585-591.
Song, C., L. O. Essen, W. Gartner, J. Hughes and J. Matysik (2012). "Solid-state NMR spectroscopic study of chromophore-protein interactions in the Pr ground state of plant phytochrome A." Mol. Plant **5**(3): 698-715.
Song, C., G. Psakis, J. Kopycki, C. Lang, J. Matysik and J. Hughes (2014). "The D-ring, not the A-ring, rotates in Synechococcus OS-B' phytochrome." J. Biol. Chem. **289**(5): 2552-2562.
Song, C., G. Psakis, C. Lang, J. Mailliet, W. Gärtner, J. Hughes and J. Matysik (2011). "Two ground state isoforms and a chromophore D-ring photoflip triggering extensive intramolecular changes in a canonical phytochrome." Proceedings of the National Academy of Sciences of the United States of America **108**(10): 3842-3847.
Strickland, D., X. Yao, G. Gawlak, M. K. Rosen, K. H. Gardner and T. R. Sosnick (2010). "Rationally improving LOV domain–based photoswitches." Nature Methods **7**(8): 623-626.
Su, Y.-s. and J. C. Lagarias (2007). "Light-Independent Phytochrome Signaling Mediated by Dominant GAF Domain Tyrosine Mutants of *Arabidopsis* Phytochromes in Transgenic Plants." Plant Cell **19**(7): 2124.
Takala, H., A. Björling, O. Berntsson, H. Lehtivuori, S. Niebling, M. Hoernke, I. Kosheleva, R. Henning, A. Menzel, J. A. Ihalainen and S. Westenhoff (2014). "Signal amplification and transduction in phytochrome photosensors." Nature **509**: 245.
Takala, H., H. K. Lehtivuori, O. Berntsson, A. Hughes, R. Nanekar, S. Niebling, M. Panman, L. Henry, A. Menzel, S. Westenhoff and J. A. Ihalainen (2018). "On the (un)coupling of the chromophore, tongue interactions, and overall conformation in a bacterial phytochrome." J Biol Chem **293**(21): 8161-8172.
Terry, M. J., P. J. Linley and T. Kohchi (2002). "Making light of it: the role of plant haem oxygenases in phytochrome chromophore synthesis." Biochemical Society Transactions **30**(4): 604-609.
Toh, K. C., E. A. Stojkovic, I. H. van Stokkum, K. Moffat and J. T. Kennis (2011). "Fluorescence quantum yield and photochemistry of bacteriophytochrome constructs." Phys Chem Chem Phys **13**(25): 11985-11997.
Ulijasz, A. T., G. Cornilescu, D. von Stetten, S. Kaminski, M. A. Mroginski, J. Zhang, D. Bhaya, P. Hildebrandt and R. D. Vierstra (2008). "Characterization of two thermostable cyanobacterial phytochromes reveals global movements in the chromophore-binding domain during photoconversion." The Journal of biological chemistry **283**(30): 21251-21266.
van Thor, J. J., B. Borucki, W. Crielaard, H. Otto, T. Lamparter, J. Hughes, K. J. Hellingwerf and M. P. Heyn (2001). "Light-induced proton release and proton uptake reactions in the cyanobacterial phytochrome Cph1." Biochemistry **40**: 11460.
van Thor, J. J., B. Borucki, W. Crielaard, H. Otto, T. Lamparter, J. Hughes, K. J. Hellingwerf and M. P. Heyn (2001). "Light-induced proton release and proton uptake reactions in the cyanobacterial phytochrome Cph1." Biochemistry **40**(38): 11460-11471.
Velazquez Escobar, F., P. Piwowarski, J. Salewski, N. Michael, M. Fernandez Lopez, A. Rupp, B. M. Qureshi, P. Scheerer, F. Bartl, N. Frankenberg-Dinkel, F. Siebert, M. Andrea Mroginski and P. Hildebrandt (2015). "A protonation-coupled feedback mechanism controls the signalling process in bathy phytochromes." Nature Chemistry **7**(5): 423-430.
Velazquez Escobar, F., D. von Stetten, M. Günther-Lütkens, A. Keidel, N. Michael, T. Lamparter, L.-O. Essen, J. Hughes, W. Gärtner, Y. Yang, K. Heyne, M. A. Mroginski and P. Hildebrandt (2015). "Conformational heterogeneity of the Pfr chromophore in plant and cyanobacterial phytochromes." Frontiers in Molecular Biosciences **2**: 37.
Volz, P., R. Brodwolf, C. Zoschke, R. Haag, M. Schäfer-Korting and U. Alexiev (2018). "White-Light Supercontinuum Laser-Based Multiple Wavelength Excitation for TCSPC-FLIM of Cutaneous Nanocarrier Uptake." Zeitschrift für Physikalische Chemie **232**(5-6): 671-688.

Volz, P., N. Krause, J. Balke, C. Schneider, M. Walter, F. Schneider, R. Schlesinger and U. Alexiev (2016). "Light and pH-induced Changes in Structure and Accessibility of Transmembrane Helix B and Its Immediate Environment in Channelrhodopsin-2." Journal of Biological Chemistry **291**(33): 17382-17393.
von Stetten, D., S. Seibeck, N. Michael, P. Scheerer, M. A. Mroginski, D. H. Murgida, N. Krauss, M. P. Heyn, P. Hildebrandt, B. Borucki and T. Lamparter (2007). "Highly Conserved Residues Asp-197 and His-250 in Agp1 Phytochrome Control the Proton Affinity of the Chromophore and Pfr Formation." Journal of Biological Chemistry **282**(3): 2116-2123.
von Stetten, D., S. Seibeck, N. Michael, P. Scheerer, M. A. Mroginski, D. H. Murgida, N. Krauss, M. P. Heyn, P. Hildebrandt, B. Borucki and T. Lamparter (2007). "Highly Conserved Residues Asp-197 and His-250 in Agp1 Phytochrome Control the Proton Affinity of the Chromophore and Pfr Formation*." Journal of Biological Chemistry **282**(3): 2116-2123.
Wagner, J. R., J. Zhang, D. von Stetten, M. Gunther, D. H. Murgida, M. A. Mroginski, J. M. Walker, K. T. Forest, P. Hildebrandt and R. D. Vierstra (2008). "Mutational analysis of *Deinococcus radiodurans* bacteriophytochrome reveals key amino acids necessary for the photochromicity and proton exchange cycle of phytochromes." J. Biol. Chem. **283**(18): 12212-12226.
Wagner, J. R., J. Zhang, D. von Stetten, M. Gunther, D. H. Murgida, M. A. Mroginski, J. M. Walker, K. T. Forest, P. Hildebrandt and R. D. Vierstra (2008). "Mutational analysis of *Deinococcus radiodurans* bacteriophytochrome reveals key amino acids necessary for the photochromicity and proton exchange cycle of phytochromes." J Biol Chem **283**(18): 12212-12226.
Wan, S., J. A. Parrish, R. R. Anderson and M. Madden (1981). "Transmittance of nonionizing radiation in human tissues." Photochemistry and photobiology **34**(6): 679-681.
Weissleder, R. (2001). "A clearer vision for in vivo imaging." Nature Biotechnology **19**(4): 316-317.
Wu, S.-H. and J. C. Lagarias (2000). "Defining the Bilin Lyase Domain: Lessons from the Extended Phytochrome Superfamily." Biochemistry **39**(44): 13487-13495.
Wu, X.-J., K. Chang, J. Luo, M. Zhou, H. Scheer and K.-H. Zhao (2013). "Modular generation of fluorescent phycobiliproteins." Photochemical & Photobiological Sciences **12**(6): 1036-1040.
Zienicke, B., L.-Y. Chen, H. Khawn, M. A. S. Hammam, H. Kinoshita, J. Reichert, A. S. Ulrich, K. Inomata and T. Lamparter (2011). "Fluorescence of Phytochrome Adducts with Synthetic Locked Chromophores." Journal of Biological Chemistry **286**(2): 1103-1113.
Zienicke, B., I. Molina, R. Glenz, P. Singer, D. Ehmer, F. V. Escobar, P. Hildebrandt, R. Diller and T. Lamparter (2013). "Unusual spectral properties of bacteriophytochrome Agp2 result from a deprotonation of the chromophore in the red-absorbing form Pr." The Journal of biological chemistry **288**(44): 31738-31751.

Appendix

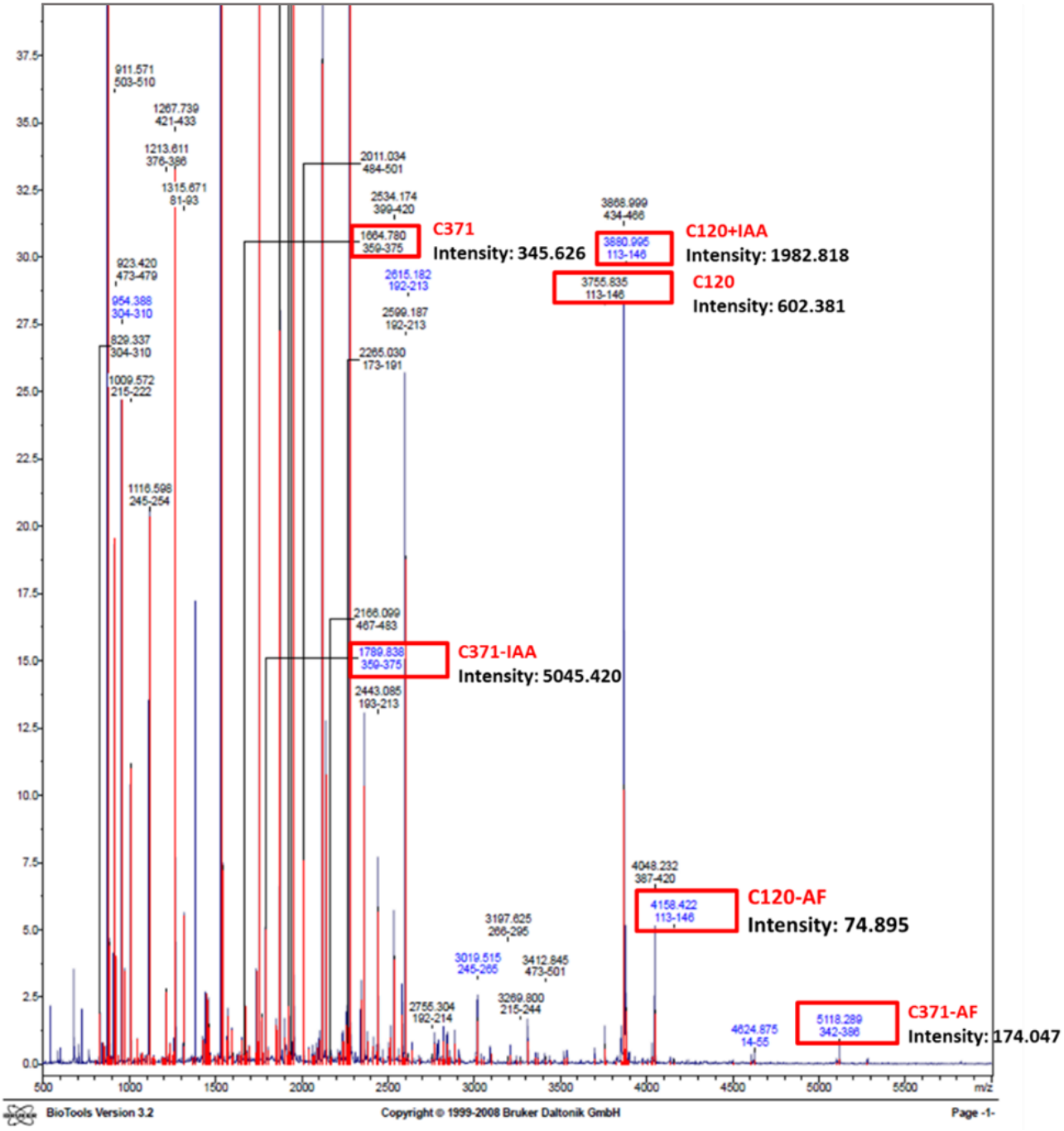

Figure A1: MS analysis of Cph1-PGP -AF. The intensity and the mass of the peptides which include C371-IAA, C371-AF, and C120-AF are marked with red.

Table A1: Cph1 tryptic peptides detected by MALDI-MS sorted by their position in the protein sequence. *Peak #* indicates the peak number in the spectrum shown in Fig. S1; *M+H (expt)* is the mass determined experimentally; *M+H (calc)* is the peptide mass calculated from the Cph1 protein sequence; *ppm* is the relative deviation of the experimental mass from the theoretical value given in parts per million; *intensity* gives the intensity value from the mass spectrum for the respective peak; *#MC* is the maximal number of allowed missed cleavages by trypsin (incomplete cleavage); *position* gives the start and the end of the peptide; *peptide sequence* shows the underlying Cph 1 peptide sequence, and *modifications* lists side chain modifications taken into account in the peptide assignment.Search parameters used: Peptide tolerance: 150 ppm, specificity: Trypsin/P, optional modifications: N-ethylmaleimide (NEM,) 5-iodoacetamidofluorescein (5-IAF).

Peak #	M+H (expt)	M+H (calc)	ppm	Intensity	#MC	Position	Peptide sequence	Cysteine Modifications
194	4.624.875	4.624.492	83	137	0	014-055	QLETLAIHTAHLIQPHGLVVVLQEPDLTISQISAN**C**TGILGR	C49 NEM
9	886.435	886.463	-32	4420	0	056-063	SPEDLLGR	
99	1.951.928	1.951.976	-25	47666	0	064-080	TLGEVFDSFQIDPIQSR	
46	1.315.671	1.315.722	-38.76	663.491	0	81 - 93	LTAGQISSLNPSK	
79	1.753.782	1.753.837	-31.43	42.174.456	0	98 - 112	VMGDDFVIFDGVFHR	
80	1.769.789	1.769.832	-24.19	1.755.126	0	98 - 112	VMGDDFVIFDGVFHR	
182	3.880.995	3.880.831	42.244	1.982.818	0	113 - 146	NSDGLLV**C**ELEPAYTSDNLPFLGFYHMANAALNR	C120 NEM
191	4.158.422	4.158.852	-103.5	74.895	0	113 - 146	NSDGLLV**C**ELEPAYTSDNLPFLGFYHMANAALNR	**C120-IAF**
175	3.755.835	3.755.783	13.813	602.381	0	113 - 146	NSDGLLVCELEPAYTSDNLPFLGFYHMANAALNR	
62	1.539.741	1539.78	-25.16	7.247.262	0	155 - 166	DFYDVIVEEVRR	
121	2265.03	2265.06	-13.48	783.111	1	173 - 191	VMLYRFDENNHGDVIAEDK	
68	1.602.641	1.602.703	-39	298.068	1	178 - 191	FDENNHGDVIAEDK	
141	2.615.182	2.615.219	-14.38	246.053	0	192 - 213	RDDMEPYLGLHYPESDIPQPAR	
144	2.755.304	2.755.326	-7.93	225.742	1	192 - 214	RDDMEPYLGLHYPESDIPQPARR	
140	2.599.187	2.599.225	-14.35	18.767.377	2	192 - 213	RDDMEPYLGLHYPESDIPQPAR	
130	2.443.085	2.443.123	-15.91	5.699.839	1	193 - 213	DDMEPYLGLHYPESDIPQPAR	
140	2.599.187	2.599.225	-14.35	18.767.377	0	193 - 214	DDMEPYLGLHYPESDIPQPARR	
141	2.615.182	2.615.219	-14.38	246.053	1	193 - 214	DDMEPYLGLHYPESDIPQPARR	
166	3269.8	3.269.816	-4.892	110.718	1	215 - 244	LFIHNPIRVIPDVYGVAVPLTPAVNPSTNR	
20	1.009.572	1.009.594	-21.96	11.033.526	1	215 - 222	LFIHNPIR	
123	2.279.189	2.279.239	-22.22	43.297.877	0	223 - 244	VIPDVYGVAVPLTPAVNPSTNR	
159	3.019.515	3.019.539	-7.793	1.606.118	0	245 - 265	AVDLTESILRSAYHCHLTYLK	
32	1.116.598	1.116.626	-25.29	20.363.386	1	245 - 254	AVDLTESILR	
93	1.921.826	1.921.931	-54.38	2.176.281	0	255 - 265	SAYHCHLTYLK	
163	3.197.625	3.197.671	-14.47	140.218	0	266 - 295	NMGVGASLTISLIKDGHLWGLIACHHQTPK	
96	1.937.672	1.937.944	-140.4	384.921	1	280 - 295	DGHLWGLIA**C**HHQTPK	C289 NEM
7	873.481	873.519	-44.12	48.800.021	0	296 - 302	VIPFELR	
16	954.388	954.414	-26.76	25.226.176	0	304 - 310	A**C**EFFGR	C305 NEM
3	829.337	829.366	-35.01	1930.18	0	304 - 310	ACEFFGR	
110	2.120.919	2.120.977	-27.3	37.227.899	0	311 - 328	VVFSNISAQEDTETFDYR	
56	1.464.743	1.464.806	-43.08	1.388.157	0	329 - 341	VQLAEHEAVLLDK	
196	5.118.289	5.118.439	-29.27	174.047	0	342 - 386	MTTAADFVEGLTNHPDRLLGLTGSQGAAI**C**FGEKLILVGETPDEK	**C371-IAF**
89	1.874.805	1874.87	-34.54	27.302.294	2	342 - 358	MTTAADFVEGLTNHPDR	
82	1.789.838	1.789.915	-43.02	5045.42	0	359 - 375	LLGLTGSQGAAI**C**FGEK	C371 NEM
72	1664.78	1.664.868	-52.73	345.626	0	359 - 375	LLGLTGSQGAAICFGEK	
39	1.213.611	1.213.667	-46.26	2.678.918	0	376 - 386	LILVGETPDEK	
61	1.532.781	1.532.822	-26.96	43.839.352	0	387 - 398	AVQYLLQWLENR	
189	4.048.232	4.048.049	45.087	1.881.463	0	387 - 420	AVQYLLQWLENREVQDVFFTSSLSQIYPDAVNFK	
134	2.534.174	2.534.245	-28	3901.73	1	387 - 420	EVQDVFFTSSLSQIYPDAVNFK	
196	5.118.289	5.117.602	134.25	174.047	0	421 - 466	SVASGLLAIPIARHNFLLWFRPEVLQTVNWGGDPNHAYEATQEDGK	
45	1.267.739	1.267.773	-26.79	33.265.674	2	421 - 433	SVASGLLAIPIAR	
180	3.868.999	3.868.847	39.284	10.246.094	0	434 - 466	HNFLLWFRPEVLQTVNWGGDPNHAYEATQEDGK	
144	2.755.304	2.755.259	16.122	225.742	1	442 - 466	PEVLQTVNWGGDPNHAYEATQEDGK	
112	2.166.099	2.166.182	-38.19	250.195	0	467 - 483	IELHPRQSFDLWKEIVR	
170	3.412.845	3.412.863	-5.211	176.442	2	473 - 501	QSFDLWKEIVRLQSLPWQSVEIQSALALK	
13	923.42	923.462	-46	3997.27	2	473 - 479	QSFDLWK	
101	2.011.034	2.011.122	-43.7	7.627.675	0	484 - 501	LQSLPWQSVEIQSALALK	
12	911.571	911.604	-36.2	19.536.075	0	503 - 510	AIVNLILR	

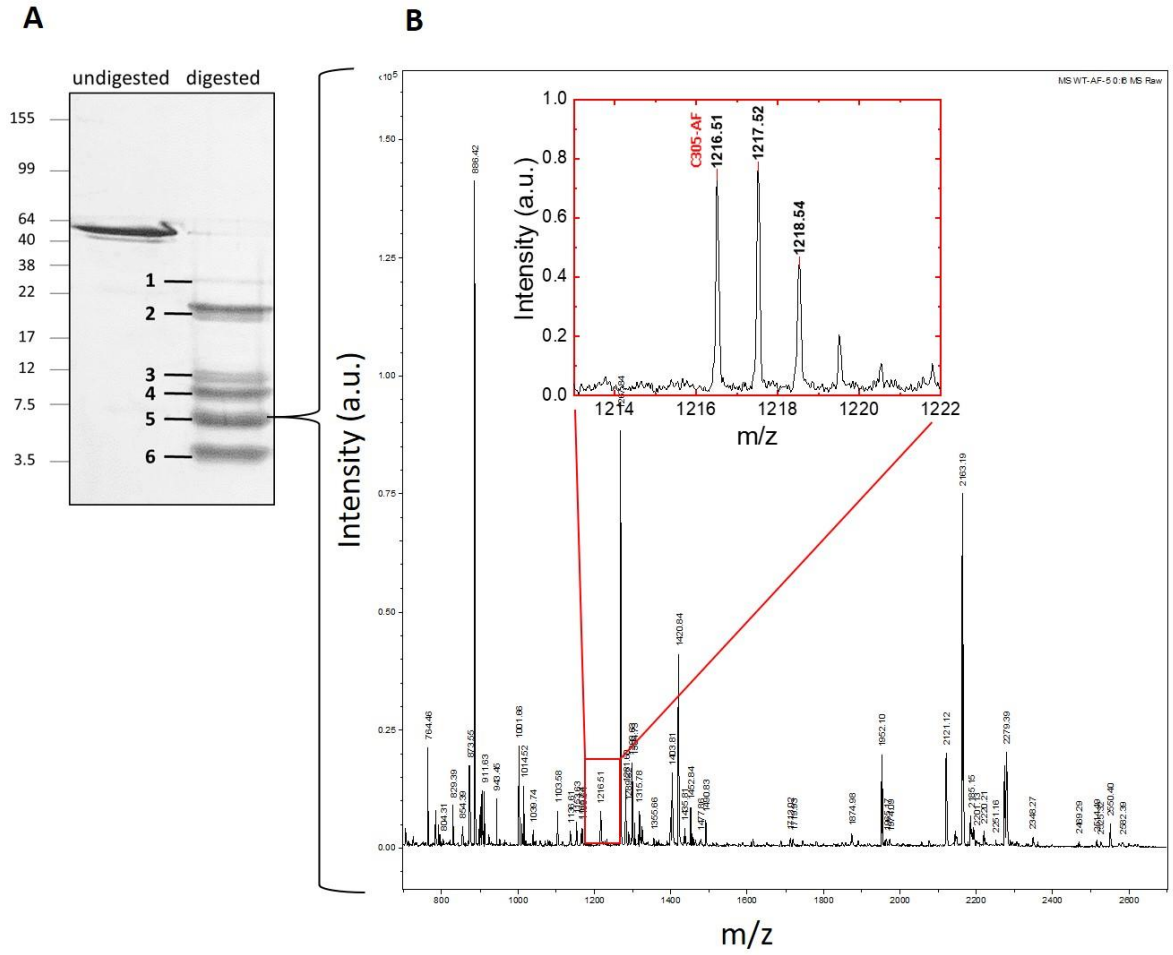

Figure A2: **MS analysis of Cph1-PGP-C371S-AF**. A) 10-20% acrylamide gradient SDS-PAGE of Cph1-PGP-C371S-AF undigested and in-solution digested with Lys-C. B) Mass spectrum of in-gel digest of fraction 5 with Trypsin in the m/z range of 700-2700. C) Mass spectrum zoom into the m/z region from 1213 to 1222. The mass 1216.51 can be identified with the peptide pos. 304-310 (sequence ACEFFGR theoretical mass 829.37 Da) with the cysteine residue 'C305' modified with IAF (+387. 07 Da).

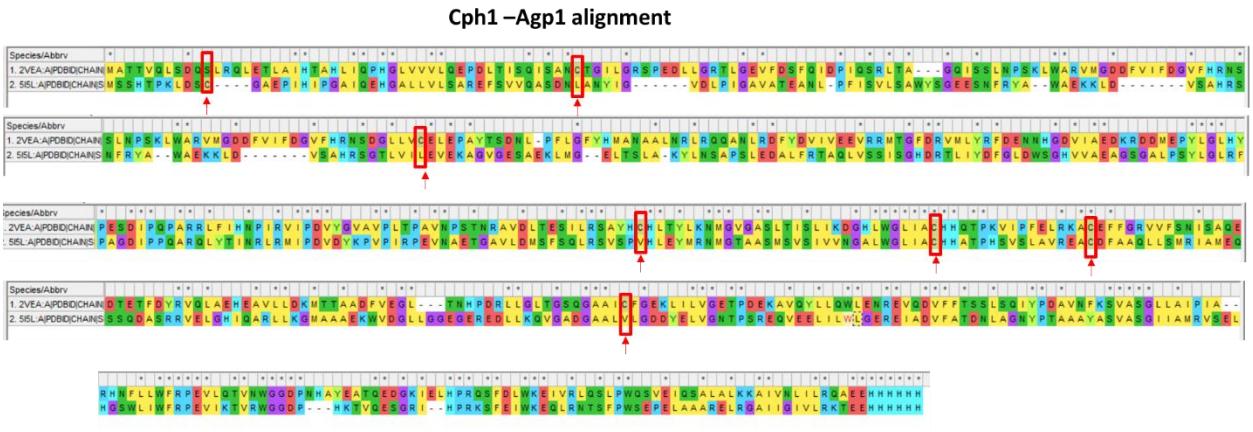

Figure A3: **Agp1 PGP and Cph1 PGP amino acids alignment.** The cysteines and their equavlent amin acids are shown with a red frame.

Selbstständigkeitserklärung

Name: Sadeghi
Vorname: Maryam

Ich erkläre gegenüber der Freien Universität Berlin, dass ich die vorliegende Dissertation selbstständig und ohne Benutzung anderer als der angegebenen Quellen und Hilfsmittel angefertigt habe. Die vorliegende Arbeit ist frei von Plagiaten. Alle Ausführungen, die wörtlich oder inhaltlich aus anderen Schriften entnommen sind, habe ich als solche kenntlich gemacht. Diese Dissertation wurde in gleicher oder ähnlicher Form noch in keinem früheren Promotionsverfahren eingereicht.

Berlin, den 05.05.2022